



**Multiscale Mechano-Morphology of Soft Tissues: A Computational  
Study with Applications to Cancer Diagnosis and Treatment**

Javier Palacio Torralba

Submitted for the degree of Doctor of Philosophy

Heriot-Watt University

School of Engineering and Physical Sciences

March 2016

The copyright in this thesis is owned by the author. Any quotation from the thesis or use of any of the information contained in it must acknowledge this thesis as the source of the quotation or information.

## **ABSTRACT**

Cooperation of engineering and biomedical sciences has produced significant advances in healthcare technology. In particular, computational modelling has led to a faster development and improvement of diagnostic and treatment techniques since it allows exploring multiple scenarios without additional complexity and cost associated to the traditional trial-and-error methodologies.

The goal of this thesis is to propose computational methodologies to analyse how the changes in the microstructure of soft tissues, caused by different pathological conditions, influence the mechanical properties at higher length scales and, more importantly, to detect such changes for the purpose of quantitative diagnosis and treatment of such pathologies in the scenario of drug delivery. To achieve this objective different techniques based on quasi-static and dynamic probing have been established to perform quantitative tissue diagnosis at the microscopic (tissue) and macroscopic (organ) scales. The effects of pathologies not only affect the mechanical properties of tissue (e.g. elasticity and viscoelasticity), but also the transport properties (e.g. diffusivity) in the case of drug delivery. Such transport properties are further considered for a novel multi-scale, patient-specific framework to predict the efficacy of chemotherapy in soft tissues. It is hoped that this work will pave the road towards non-invasive palpation techniques for early diagnosis and optimised drug delivery strategies to improve the life quality of patients.

## ACKNOWLEDGEMENTS

Words cannot express my gratitude to my supervisors Dr Yuhang Chen and Prof Bob Reuben for giving me the opportunity to pursue my PhD at Heriot-Watt, for their continuous support, guidance, patience and invaluable advice. Thanks Yuhang and Bob.

I would like to take this opportunity to thank the e-Finger team for the valuable contributions. In particular I would like to thank Dr Daniel W. Good (University of Edinburgh, Edinburgh, UK), Dr Steven Hammer (Heriot-Watt University, Edinburgh, UK), Dr Grant D. Stewart (Cambridge Cancer centre, Cambridge, UK) and Prof. S. Alan McNeill (Western General Hospital, NHS Lothian, Edinburgh, UK)

I had the opportunity to share the time as a Ph.D. candidate with the fantastic people in the research group. Thanks Ben, Frank, Solenn, Jess, Judith, Swati, Anurag and Antonio. You made this experience much more interesting and fun.

I would like to thank Elizabeth Jiménez Aguilar, Ray Manneh and Mario Martínez López from Hospital 12 de Octubre in Madrid (Spain) for sharing critical data for this thesis, often with very tight deadlines, and for the enlightening discussions.

Nasim Mammadov helped perform the experiments in Section 3.7 of Chapter 3 for which I am really grateful.

This doctoral thesis could not have been carried out without the James-Watt scholarship that Heriot-Watt University awarded to me. Furthermore both the Heriot-Watt Annual Fund and the Institute of Mechanical, Process and Energy Engineering (IMPEE) also awarded me a grant to partially fund a conference travel which has led to an interesting collaboration. I am absolutely grateful for the confidence that was deposited in me.

I am really grateful to my friends for the good moments we always share even when we are a bit far away.

Last, but certainly not least, I would like to thank my family for their unconditional support.

## DEDICATION

To my family.



**“Knowing is not enough; we must apply. Willing  
is not enough; we must do.”**

Johann Wolfgang von Goethe

# LIST OF PUBLICATIONS

The following journal papers and conference presentations have been made during my Ph.D. candidature:

## **Journal Publications**

1. **J. Palacio-Torralba**, M. Martínez López, D. W. Good, G. D. Stewart, S. Alan McNeill, R. L. Reuben and Y. Chen. A multiscale patient-specific approach to drug delivery into solid tumours: towards personalized treatment. *To be submitted*.
2. **J. Palacio-Torralba**, D. W. Good, G. D. Stewart, S. Alan McNeill, R. L. Reuben and Y. Chen. A multiscale, mechano-morphological approach to soft tissue diagnosis: application to prostate cancer diagnosis using support vector machines. *To be submitted*.
3. **J. Palacio-Torralba**, D. W. Good, G. D. Stewart, S. Alan McNeill, R. L. Reuben and Y. Chen. A novel approach to quantitatively estimate the location, depth and volume of a nodule in a soft tissue using mechanical palpation. *To be submitted*.
4. **J. Palacio-Torralba**, D. W. Good, G. D. Stewart, S. Alan McNeill, R. L. Reuben and Y. Chen. A Novel Method for Rapid and Quantitative Mechanical Assessment of Soft Tissue for Diagnostic Purposes. *To be submitted*.
5. **J. Palacio-Torralba**, S. Hammer, D. W. Good, S. Alan McNeill, G. D. Stewart, R. L. Reuben and Y. Chen. Patient Specific Modelling of Palpation-based Prostate Cancer Diagnosis: Effects of Pelvic Cavity Anatomy and Intrabladder Pressure. International Journal for Numerical Methods in Biomedical Engineering (2016).
6. **J. Palacio-Torralba**, S. Hammer, D. W. Good, S. Alan McNeill, G. D. Stewart, R. L. Reuben and Y. Chen. Quantitative diagnostics of soft tissue through viscoelastic characterization using time based instrumented palpation. Journal of the Mechanical Behavior of Biomedical Materials (2015).

## **Conference Proceedings**

1. J. Abolle Okoyeagu, **J. Palacio-Torralba**, Y. Chen, R. Reuben Acoustic Emission Source Identification in Pipes Using Finite Element Analysis. 31<sup>st</sup> Conference of the European Working Group on Acoustic Emission (EWGAE), September 2014.

## **Conferences and Presentations**

1. **J. Palacio-Torralba**, M. Martínez, K. George, D.W. Good, R. Malathi, J. Krishnan, R. L. Reuben, Y. Chen. A multiscale patient-specific approach to drug delivery into solid tumors: towards personalized treatment. *22<sup>nd</sup> Congress of the European Society of Biomechanics*, Lyon, France, 2016.
2. **J. Palacio-Torralba**, E. Jiménez Aguilar, B. Esfandiar Jahromi, S.A. McNeill, G.D. Stewart, R.L. Reuben, Y. Chen. Patient specific modelling and quantitative tissue quality assessment for prostate cancer diagnosis. *21<sup>st</sup> Congress of the European Society of Biomechanics*, Prague, Czech Republic, 2015.
3. **J. Palacio-Torralba**, R. L. Reuben, Y. Chen. Patient Specific Modelling and diagnostic through instrumented mechanical palpation. *Simulia UK Academic Forum*, Glasgow, UK, 2015.
4. **J. Palacio-Torralba**, R. L. Reuben, Y. Chen. A Quantitative Tool for Soft Tissue Diagnostic using Dynamic Palpation with Application to Prostate Cancer. *12th International Symposium on Computer Methods in Biomechanics and Biomedical Engineering*, Amsterdam, Netherlands, 2014.
5. **J. Palacio-Torralba**, R. L. Reuben, Y. Chen. Soft tissue diagnosis using mechanical palpation. *BOSE User Group Meeting*, Sheffield, UK, 2014.
6. **J. Palacio-Torralba**, R. L. Reuben, Y. Chen. Quantitative Diagnostics of Prostate Cancer using Mechanical Palpation. *2nd UK National Conference on Patient-Specific Modelling*, Edinburgh, UK, 2014.
7. **J. Palacio-Torralba**, R. L. Reuben, Y. Chen. Quantitative Diagnostics of Prostate Cancer using Dynamic Palpation. *11th World Congress on Computational Mechanics*, Barcelona, Spain, 2014.
8. **J. Palacio-Torralba**, D. Timms, R. L. Reuben, Y. Chen. A Novel Framework for Diagnostics of Prostatic Cancerous Nodules using Mechanical Palpation. *5th International Conference on Mechanics of Biomaterials and Tissues*, Sitges, Spain.
9. **J. Palacio-Torralba**, R. L. Reuben, Y. Chen. Anisotropic, heterogeneous and cellular materials: From microarchitecture to macro-level response. *Telford-UKIERI workshop*, Edinburgh, UK.

# ACADEMIC REGISTRY

## Research Thesis Submission



Name:	Javier Palacio Torralba		
School/PGI:	Engineering and Physical Sciences		
Version: <small>(i.e. First, Resubmission, Final)</small>	Final	Degree Sought (Award <b>and</b> Subject area)	Ph.D. Mechanical Engineering

### Declaration

In accordance with the appropriate regulations I hereby submit my thesis and I declare that:

- 1) the thesis embodies the results of my own work and has been composed by myself
- 2) where appropriate, I have made acknowledgement of the work of others and have made reference to work carried out in collaboration with other persons
- 3) the thesis is the correct version of the thesis for submission and is the same version as any electronic versions submitted\*.
- 4) my thesis for the award referred to, deposited in the Heriot-Watt University Library, should be made available for loan or photocopying and be available via the Institutional Repository, subject to such conditions as the Librarian may require
- 5) I understand that as a student of the University I am required to abide by the Regulations of the University and to conform to its discipline.

\* Please note that it is the responsibility of the candidate to ensure that the correct version of the thesis is submitted.

Signature of Candidate:		Date:	
-------------------------	--	-------	--

### Submission

Submitted By <i>(name in capitals)</i> :	JAVIER PALACIO TORRALBA
Signature of Individual Submitting:	
Date Submitted:	

### For Completion in the Student Service Centre (SSC)

Received in the SSC by <i>(name in capitals)</i> :			
1.1 Method of Submission <i>(Handed in to SSC; posted through internal/external mail):</i>			
1.2 E-thesis Submitted ( <b>mandatory for final theses</b> )			
Signature:		Date:	

# TABLE OF CONTENTS

<b>CHAPTER 1 Introduction</b>	1
Contents	1
1.1 Motivation	1
1.2 Thesis scope and structure	3
<b>CHAPTER 2 Multiscale Modelling of Soft Tissue and Mechanics-based Diagnosis: the State of the Art</b>	8
Contents	8
2.1 Summary	9
2.2 Soft tissue hierarchy and heterogeneity	9
2.3 Viscoelasticity in soft tissue	12
2.3.1 An introduction to viscoelasticity	12
2.3.2 Characterization of viscoelastic parameters	13
2.4 Homogenization and multiscale modelling– a necessary simplification	15
2.5 Patient specific modelling – a complication to medical diagnosis	19
2.6 Soft tissue diagnostics	20
2.7 Drug delivery	24
2.8 Bridging the gaps	27
<b>CHAPTER 3 A novel palpation-based method to detect hard cancerous nodules in soft tissues – the computational framework and experimental validation</b>	30
Contents	30
3.1 Summary	30
3.2 2D computational models	31
3.3 Material characterization and validation	35
3.4 Nodule characterization: decoupling the size and depth	38
3.5 Quantitative characterization of cancerous nodules: 2D analysis	43
3.6 Feasibility study – tumour geometry	47
3.7 Experimental Validation	49
3.8 Concluding remarks	55
<b>CHAPTER 4 Quantitative tissue quality assessment through viscoelastic characterization using instrumented palpation</b>	56
Contents	56
4.1 Summary	56
4.2 Viscoelastic modelling and characterization	57
4.3 Finding the limits of dynamic characterization: the clinically significant range of testing frequencies	62
4.4 Sensitivity analysis: size, depth and position	65

4.5	An ex-vivo, patient-specific example.....	69
4.6	Concluding remarks.....	73
<b>CHAPTER 5 A novel method for rapid, quantitative, mechanical assessment of soft tissue for diagnostic purposes – a viscoelastic ‘rule of mixtures’ .....</b>		<b>76</b>
Contents.....		76
5.1	Summary.....	76
5.2	Effective viscoelastic properties 1D formulation .....	77
5.3	Tissue heterogeneity - quantitative cancer diagnosis .....	80
5.4	The rule of mixtures: 1D analysis.....	83
5.5	Parametric analysis: 2D heterogeneous materials .....	86
5.5.1	Effect of $t_{exp}$ .....	86
5.5.2	Effect of Young’s Modulus .....	86
5.6	Quantitative diagnosis of prostate cancer: a practical study.....	87
5.7	Concluding remarks.....	91
<b>CHAPTER 6 Patient Specific Modelling of Palpation-based Prostate Cancer Diagnosis: Effects of Pelvic Cavity Anatomy and Intrabladder Pressure .....</b>		<b>93</b>
Contents.....		93
6.1	Summary.....	93
6.2	Selection of patients and their pathophysiological conditions .....	94
6.3	Modelling the pelvic cavity .....	95
6.4	Influence of subject-specific features in IDRE.....	99
6.5	Influence of intrabladder pressure: is it possible to increase its sensitivity preparing the patient?.....	102
6.6	The pelvic bone: to model or not to model.....	105
6.7	Concluding remarks.....	109
<b>CHAPTER 7 A multiscale, mechano-morphological approach to soft tissue mechanics: application in prostate cancer diagnosis.....</b>		<b>111</b>
Contents.....		111
7.1	Summary.....	111
7.2	Modelling patient histological data .....	112
7.3	Homogenization formulation.....	114
7.4	Tissue diagnosis using SVM .....	119
7.5	Comparison between the traditional and new method.....	120
7.6	Effects of RVE size in the distribution of the mechanical properties .....	123
7.7	Inter-patient difference in tissue elasticity.....	127
7.8	Support Vector Machines: A tool for quantitative tissue diagnosis. ....	128
7.9	Concluding remarks.....	130

<b>CHAPTER 8 Heterogeneity in Tissue Diffusivity: An Application in Drug Delivery</b>	133
Contents	133
8.1 Summary	133
8.2 Histology modelling: homogenisation of diffusivity	134
8.3 Formulation of pharmacodynamics – modelling of tissue response	139
8.4 Numerical homogenization of tissue diffusivity	141
8.5 Sensitivity analysis	145
8.5.1 A preliminary analysis of diffusion in soft tissues	145
8.5.2 Intravenous drug delivery – sensitivity analysis	148
8.5.3 Bolus injection – sensitivity analysis	152
8.6 Concluding remarks	159
<b>CHAPTER 9 Looking back and working forward</b>	162
Contents	162
9.1 Looking back	162
9.2 Working forward	167
<b>Bibliography</b>	171

# LISTS OF FIGURES

<b>Figure 2-1.</b> Histological sample stained with haematoxylin and eosin show the multiscale nature of soft tissue. (a) The bigger acini of a healthy prostate are clearly visible compared to the smaller ones in blue shown at the bottom of (a) and (b), which are malignant cells (M). A closer look into the cancerous area is shown in (c) and (d) where a blood vessel and blood cells are shown. ....	11
<b>Figure 2-2.</b> Schematic of multiscale modelling for the example of lung tissue [76]. The data predicted on respective scales flow upscale/downscale and <i>vice versa</i> to improve the fidelity of the model. ....	17
<b>Figure 2-3.</b> (a) Example of a hierarchical, multiscale structure built from multiple representative volume elements (RVE). (b) The average behaviour, represented by the thick solid line, may of sufficient use for certain applications when the high frequency local challenges [78]. ....	18
<b>Figure 2-4.</b> Schematic of the transrectal and transperineal approaches for prostate biopsy. Up to 20 tissue samples are often collected from the sample. However the risk of false negatives is always present[102]. ....	22
<b>Figure 2-5.</b> (a) The e-Finger is an example of a soft tissue palpation device [125]. (b) Rolling indentation system proposed by Sangpradit et al.[43] (c) Indentation system described by Ahn et al.[126]. ....	24
<b>Figure 2-6.</b> Examples of thermoliposomes, drug carriers activated by temperature [136]. ....	26
<b>Figure 3-1.</b> The 2D plain strain computational model. Plain strain is chosen for the 2D models since they represent better the experiments often done to characterize anomalies within soft tissues using palpation [43, 111]. ....	33
<b>Figure 3-2.</b> Different nodule topologies are considered to test the effectiveness of the proposed methodology. (a) and (b) are built from intersecting circle in different sizes; (c) tumour nodule is in a random shape; (d) represents a circular nodule of cancerous tissue surrounded by regions where the boundary between cancerous and healthy tissue is unclear; and (e) is an example comparable to the 3D validation test. ....	35
<b>Figure 3-3.</b> The tissue phantom and experimental set up. (a) The locations where palpation is performed. (b) The computational model of the palpation test with a circular nodule inside. A convergent mesh with over 300000 linear tetrahedral elements with hybrid formulation were used. (c) The nodule inside the phantom and (d) a view of the entire phantom. ....	37
<b>Figure 3-4.</b> Healthy and cancerous force feedback profiles obtained during the palpation experiment using a 10mm deep indentation. The point where the difference is larger is used to locate the tumour. ....	39
<b>Figure 3-5.</b> (a) Venn's diagram of the procedure to identify the depth and size of the proposed methodology. In this case a single point is found as a solution. (b) When the areas of plausible solutions do not converge into a single point it is considered that the solution belongs to an area close to the three circles. ....	41
<b>Figure 3-6.</b> Schematic of the methodology proposed to identify depth and size of nodules in soft tissues. In the first phase the nodule is located comparing the force feedback with a computational one where the sample is considered to be healthy. The identification phase requires performing sweeping palpation at different depths of indentation and	



obtaining the second derivatives of the force feedback curves. The second derivative at the position where the nodule was located is then plotted against a set of benchmark simulations with nodules of different sizes located at different depths. The points where these curves intersect, which are represented by the symbols ■, ▲ and ● define a new set of curves that plotted in a Diameter-Depth graph allow to identify the size and depth of the nodule in the soft tissue. ....42

**Figure 3-7.** The limitations diagnosis based on analysis of force feedback from a single indentation are illustrated here. (a) Example of nodules used to determine the region of feasible force feedback in the palpation test. The possible combinations of nodule depth and sizes are represented in (b) and the arrows show the path of Nodule Depth and Diameter follow to build the aforementioned envelope. (c) The envelope of reaction forces for a depth of indentation of 1 mm and 10 mm is shown here. For any given force an infinite number of combinations of nodule diameter and depth exist, as shown in segment D, which result in the same force feedback. ....44

**Figure 3-8.** Two different scenarios are considered in this example with a 16mm diameter nodule located at 30 mm from the surface (a) and a 30 mm diameter one located at 50 mm from the surface (b). ....45

**Figure 3-9.** Diameter of the tumour against the second derivative of the force profile at the centre of the tumour for a depth of indentation of 1 mm (a), 5 mm (b) and 10 mm (c). The different depths of the tumour are 30, 35, 40, 45, 50 and 60 mm. The point of intersection is (30, 16). The diameter of the tumour was 16 mm and the depth 30 mm. (d). The point of intersection is (50, 30). The diameter of the tumour was 30mm and the depth 50 mm (e). ....46

**Figure 3-10.** Summary of the 2D shapes used to test the proposed methodology and the estimated nodule depths and sizes. Convergent meshes were used with over 40000 linear quadrilateral and triangular elements to model the different scenarios. It should be noted that the volume of the nodule does not seem to play a significant role in the accuracy of the predictions. ....48

**Figure 3-11.** Results of the sweeping palpation in the healthy (a) and cancerous (b) samples and the fitted neo-Hookean model. Comparison of the healthy sample and the sample with a nodule embedded (c). ....50

**Figure 3-12.** (a), (b) and (c) show the results for the second derivative obtained with computational simulations where nodules of different sizes are located at different depths (4, 8, 9, 10, 11 and 12 mm). (d) and (e) show the nodule depth and size identification in the real and simulated model respectively. It should be noted here that the prediction areas should be considered areas that provide the approximate depth and size of the nodule. The accuracy of the predictions will depend on a number of factors including the uncertainty during the characterization of the mechanical properties, the spatial resolution of the indentation procedure, which depends mainly on the number of indentations performed on the surface of the sample, and the number of computational benchmark tests used. As mentioned in section 3.2. the depths of indentation used are arbitrary; however it is limited by the signal to noise ratio for low depths of indentation and by patient discomfort and pain management for large depths of indentation. ....53

**Figure 4-1.** Prony series approximation of the normalized stress relaxation obtained from the model [44], using one or two terms. It can be observed that results using two terms present better fitting for both short and long term behaviours simultaneously. ....59

**Figure 4-2.** Mechanical behaviour of tissues with different viscoelastic parameters subjected to dynamic palpation. (a) Evolution of relative amplitude with respect to

frequency; and (b) phase shift between displacement and force signals, where phase lag of prostatic and cancerous tissues are also shown. ....	64
<b>Figure 4-3.</b> Amplitude and phase shift from Zener model using fitted parameters. ....	64
<b>Figure 4-4.</b> Sensitivity analysis of the proposed method. (a) Schematic diagram; (b) stress distribution when indentation occurs with a 2mm radius nodule located at the centre of the prostate 12.5mm below its surface; (c) at mean depth; and (d) at maximum depth. Unit of plotted stress is MPa. To obtain these results a convergent mesh with 33826 linear quadrilateral elements and 34277 nodes was used.....	67
<b>Figure 4-5.</b> Sensitivity analysis for laterally-located nodules.....	68
<b>Figure 4-6.</b> Sensitivity analysis: changing the depth, size and position of the cancerous nodule. (a) Evolution of model parameters when size of cancerous nodules varies. (b) and (c) show evolution of model parameters when depth of cancerous nodules varies in models with medium and big size nodule, respectively.....	69
<b>Figure 4-7.</b> 3D prostate model obtained from the excised prostate specimen. (a) 3D prostate model from MRI scan; (b) 8 indentation sites at posterior surface; (c) Force feedback recorded during the indentation of the healthy prostate and the one with a cancerous nodule; and (d) smoothed data where viscoelastic parameters are fitted and obtained.....	70
<b>Figure 4-8.</b> Tissue quality index (TQI) for the prostate with a cancerous nodule and the healthy one at 8 indentation sites. Convergent meshes with over 500000 linear tetrahedral elements were used to model the mechanical palpation .....	71
<b>Figure 5-1.</b> Illustration of the models used to derive and to test the framework. (a) Biphase heterogeneous viscoelastic material and (b) the equivalent homogeneous material. (c) shows the 2D heterogeneous viscoelastic material with a random distribution of cancerous tissue (red) with a volume fraction of 60%.....	79
<b>Figure 5-2.</b> Flowchart of the proposed methodology. First a creep or stress relaxation experiment is carried out and the displacement or force feedback fitted to obtain the apparent time constant. The rule of mixtures is obtained using the mechanical properties from the healthy and cancerous tissues. The volume fraction of healthy tissue is read directly from the graph for the apparent time constant. ....	80
<b>Figure 5-3.</b> Five samples from prostatic tissue (including the whole prostate and surrounding fascia) are considered to analyse the proposed diagnostic methodology. Red and grey indicate cancerous tissue and healthy prostatic tissue respectively. The volume fraction of healthy tissue is 72% in Sample 1, 19% in Sample 2, 40% in Sample 3, 53% in Sample 4, and 87% in whole tissue sample. Convergent hybrid tetrahedral meshes with the number of elements ranging from 65380 for the smallest sample (Sample 4) up to 1061676 elements for the complete prostate were used.....	82
<b>Figure 5-4.</b> Comparison of the average time constant values obtained for different materials and relaxation times. The error bars show the confidence interval for six standard deviations. (a) Average time constants for the 1D model with times of experiment of 50s and 5s for different volume fractions of healthy tissue. (b) Comparison of the rules of mixtures predicted by the proposed methodology and the results obtained from the computational models for the 2D sample. (c) Increasing the stiffness ratio between both materials causes a minimal variation in the calculated average properties for a time of experiment of 0.9s. (d) The rules of mixtures become steep for short $t_{exp}$ when ratios of 100:1 in the time constants and 1:2 in the Young's modulus are considered. (e) Increasing the Young's modulus ratio to 5:1 requires shorter times of experiment to	

obtain better results. Ten time values on logarithmic timescale between 0 and 50s were used to analyse the effects of both shorter and longer testing times. .... 85

**Figure 5-5.** Comparison of the observed time constants and volume fraction with the predicted ones. (a) Results from the volume fraction estimation of each phase in the different samples. (b) and (c) show the comparison between the predicted law of mixtures and the observed values for a relaxation time of 5s and 10s. .... 89

**Figure 6-1.** Typical MR images of the three patients selected for the study, showing patient-specific structural features. B and P indicate the location of the bladder and prostate, respectively. (a) Patient 1: an enlarged prostate compresses the bladder; (b) Patient 2: the inferior of the bladder is tightly wrapped around the superior part of the prostate; (c) Patient 3: prostate contains holes (H) due to brachytherapy treatment. .... 95

**Figure 6-2.** Computational model where organs are embedded in a box of fascia. The displacement of the anterior side of the box is constrained. .... 98

**Figure 6-3.** Schematic of the 3D reconstructed model of Patient 2. The arrow indicates the direction of indentation. .... 99

**Figure 6-4.** Reconstructed 3D models of three selected patients from MRI scans. (a) Patient 1; (b) Patient 2; and (c) Patient 3. Convergent hybrid, tetrahedral meshes were used in the model with 1198539 elements for Patient 1, 922988 for Patient 2 and 1022059 for Patient 3. .... 100

**Figure 6-5.** Changes in palpation force of three patients during IDRE subjected to (a) high intrabladder pressure and (b) low intrabladder pressure when the pelvic bone is considered. .... 102

**Figure 6-6.** Displacement fields in mm of three patients subjected to IDRE when LIBP is present. (a) Patient 1; (b) Patient 2; and (c) Patient 3. In these cases, the pelvic bone is not modelled and the prostate is assumed to be healthy and the pelvic bone is not modelled. .... 103

**Figure 6-7.** Reaction forces of Patients 1 (a), 2 (b) and 3 (c) under LIBP and HIBP conditions without the presence of the pelvic bone. .... 104

**Figure 6-8.** Displacement fields of Patients 1, 2 and 3, comparing the influence of the pelvic bone in IDRE under HIBP condition. The prostate is assumed to be completely healthy. (a) and (b): Patient 1 with and without pelvic bone, respectively; (c) and (d): Patient 2 with and without pelvic bone, respectively; (e) and (f): Patient 3 with and without pelvic bone, respectively. .... 107

**Figure 6-9.** Comparison of the palpation forces of all three patients under low intrabladder pressure (left column) and high intrabladder pressure (right column) conditions. (a) and (b): Patient 1; (c) and (d): Patient 2; and (e) and (f): Patient 3. The results show a significant difference when the pelvic bone is not present. .... 108

**Figure 7-1.** The apparent mechanical properties are obtained for two different patients. (a) shows the a histological sample from Patient's 1 prostate stained with haematoxylin and eosin (H&E). The cancerous nodule is located at the posterior left side and marked with 'C'. NA indicates an example of an RVE which would not be unacceptable since it contains part of the background. (b) shows a histological images stained with H&E from Patient 2. This patient has two different cancerous nodules located in the left and right sides of the prostate. .... 114

**Figure 7-2.** (a) Example of a periodic mesh where nodes in all the faces have a matching node at the opposite faces. (b) shows an arbitrary mesh where some nodes (for instance c) do not have a matching node on the opposite face. .... 116

<b>Figure 7-4.</b> Von Mises stress distribution in MPa when the traditional method (a) and the new method (b) are used to impose periodic boundary conditions in a tensile test with 80 control points.....	122
<b>Figure 7-5.</b> Convergence results toward the traditional PBC solution for increasing number of control points. (a) shows the results for the component $C_{11}$ and (b)-(d) for $C_{12}$ , $C_{22}$ and $C_{33}$ respectively.....	122
<b>Figure 7-6.</b> Average mechanical properties of the healthy and cancerous RVE's from patient 1(a) and 2(b) and their respective standard deviations.....	124
<b>Figure 7-7.</b> Comparison of the relative frequency of the magnitude of components $C_{11}$ and $C_{22}$ of the stiffness tensor for different RVE sizes and different conditions: healthy and cancer for Patient 1.....	126
<b>Figure 7-8.</b> Inter-patient comparison of the relative frequency of the apparent mechanical properties of RVE for different sizes when only cancerous tissue is considered. ....	127
<b>Figure 7-9.</b> Inter-patient comparison of the relative frequency of the apparent mechanical properties of RVE for different sizes when only healthy tissue is considered.....	128
<b>Figure 8-1.</b> The histological samples of patient's 1 and 2 used to estimate the apparent tissue diffusion are shown in (a) and (b). NA indicates an unacceptable area to calculate the apparent diffusion tensor since it contains part of the background. C indicates the cancerous areas.....	136
<b>Figure 8-2.</b> The histological samples are divided into regions of interest to be analysed. Acini are clusters of cells that contain fluid. For the purpose of the analysis in this chapter the diffusivity properties of such fluid are considered like those of water. The diffusivity properties of the solid phase are calculated from Eq. 8-1.....	138
<b>Figure 8-3.</b> The histological sample from patient 3 used to illustrate the proposed framework is presented here. (a) shows the histological slice of patient 3 with visible blood vessels. The image shows the multiscale nature of the tissue and therefore the need to obtain apparent mechanical properties to reduce computational time. Images (b) and (c) show the homogenized model and the position of the blood vessels. In (c) the area where the bolus injection is applied is highlighted. Convergent meshes with 156225 3-node linear diffusion elements are used to model the drug diffusivity.....	141
<b>Figure 8-4.</b> Statistical distribution of the diffusivity results for the different sizes of RVE considered (i.e. small and large), conditions (i.e. cancer and healthy), drugs (i.e. Paclitaxel and Doxorubicin), patients (Patient 1 and Patient 2) and diffusivity tensor components ( $D_{11}$ and $D_{22}$ ). ....	142
<b>Figure 8-5.</b> Comparison of the diagonal components of the effective diffusivity tensor and their distribution for two different RVEs Patient 1(a-b) and Patient 2(c-d) when the drug used is Doxorubicin. Although the results are anisotropic the distribution along the symmetry line (where $D_{11} = D_{22}$ ) is relatively symmetric. This suggests that the average behaviour of the tissue could be approximately isotropic.....	144
<b>Figure 8-6.</b> Comparison of the diagonal components of the effective diffusivity tensor and their distribution for two different RVEs Patient 1(a-b) and Patient 2(c-d) when Paclitaxel is used as a chemotherapeutic agent. The results are qualitatively similar to those shown in Fig. 8-5 for Doxorubicin. Although the results are anisotropic the distribution along the symmetry line (where $D_{11} = D_{22}$ ) is relatively symmetric. This suggests that the average behaviour of the tissue could be approximately isotropic....	145

---

<b>Figure 8-7.</b> A simple model (a) is used to illustrate how drugs with different apparent diffusivities may influence significantly the profile of the drug concentration along the Analysis Line (b) but cancer volume fraction evolution remains similar (c) over time.....	146
<b>Figure 8-8.</b> Simplified model to illustrate the role of the diffusivity of blood vessels in drug delivery efficacy. The models with and without the blood vessel are depicted in (a) and (b) respectively. The drug concentration along the analysis line is significantly greater when no blood vessel is present (c) which results in a reduced population of cancerous cells (d).....	148
<b>Figure 8-9.</b> The drug profile considered is sinusoidal. The results for Paclitaxel and Doxorubicin are very similar independently of the concentration used. ....	149
<b>Figure 8-10.</b> Evolution of cancer volume fraction for different initial concentration of cancerous cells. The prophylactic effect of chemotherapy is only visible for the highest concentration.....	150
<b>Figure 8-11.</b> Evolution of cancerous cell population when the replication rate of cells is increased.....	150
<b>Figure 8-12.</b> Evolution of the population of cancerous cell when the ability of cancerous cell to repair, $\epsilon_m$ , is increased. ....	151
<b>Figure 8-13.</b> Evolution of cancer volume fraction for different cell cycle arrest for cancer and healthy cells.....	151
<b>Figure 8-14.</b> Comparison of cancer volume fraction evolution over time when two different amplification factors and drugs are considered.....	153
<b>Figure 8-15.</b> A comparison of the influence of the initial concentration of cancerous cells in cancer volume fraction over time.....	154
<b>Figure 8-16.</b> Impact on cancer volume fraction evolution over time of the ability of cancerous cells to repair themselves when Paclitaxel and Doxorubicin are administered.....	155
<b>Figure 8-17.</b> Comparison of cancer volume fraction evolution over time when two different drugs and cancerous cell replication rate, $r_m$ are considered. ....	156
<b>Figure 8-18.</b> (a) A different drug concentration controlled by two exponentials is considered in this section. Evolution of cancerous volume fraction when the drug is following a sinusoidal or exponential law via a bolus (b) or through the blood vessels (c).....	157
<b>Figure 8-19.</b> Drug concentration is shown in (a) and (b) 4 hours and 80 hours after the beginning of the treatment when a sinusoidal bolus injection is considered. The evolution of the cancer status is shown in (c) and (d) after the same period respectively. The area where the bolus sinusoidal injection was applied is identified by the high concentration in (a-b) and by a large reduction in the population of cancerous cells in (d) compared to the same area in (c). ....	158

---

# LISTS OF TABLES

---

<b>Table 3-1.</b> Mechanical properties of the prostatic tissue reported in the literature. ....	34
<b>Table 3-2.</b> Parameters of the second order model used to model the mechanical behaviour of the healthy prostatic tissue and the cancerous nodule. ....	34
<b>Table 3-3.</b> Results of material model characterization for the healthy and cancerous material phantoms when the units used are Newtons for force and millimeters for length and $E$ is the Young's modulus .....	50
<b>Table 4-1.</b> Material parameters for cancerous and healthy tissues fitted using Prony series. $D_1/\tau_1$ are related to the short-time behaviour and $D_2/\tau_2$ to the long-term.....	59
<b>Table 4-2.</b> Viscoelastic parameters of the equivalent Zener model. ....	65
<b>Table 4-3.</b> Viscoelastic parameters of the healthy and cancerous prostate at 8 indentation sites. The parameter $\tau$ serves as a better indicator of the tissue quality than $a$ or $b$ . ....	72
<b>Table 5-1.</b> Cancerous tissue volume fraction, observed time constants in the histological samples and predicted time constants using the proposed rule of mixture. ....	90
<b>Table 6-1.</b> Variation of intrabladder pressure (IBP) subjected to different volumes of urine. Data were taken from Chiumello et al. [161], where IBP was used as an indicator of intra-abdominal pressure. ....	96
<b>Table 6-2.</b> Mechanical properties and material models used for tissues considered in this study... ..	97
<b>Table 7-1.</b> Summary of the number of samples and sizes considered throughout the study... ..	114
<b>Table 7-2.</b> Results of the average stiffness tensor for different RVE sizes in Patient 1. All the elements are shown to depict the quasi orthotropic behaviour of the material. Terms $C_{31}, C_{32}, C_{13}$ and $C_{23}$ are much smaller than the rest and close to zero. ....	125
<b>Table 7-3.</b> Results of the average stiffness tensor for different RVE sizes in patient 2. All the elements are shown to depict the quasi orthotropic behaviour of the material. ....	125
<b>Table 8-1.</b> Summary of the number of samples and sizes considered throughout the study... ..	137

---

# LIST OF ABBREVIATIONS

<b>CT</b>	Computed tomography
<b>DRE</b>	Digital Rectal Examination
<b>ECG</b>	Electrocardiogram
<b>EEG</b>	Electroencephalogram
<b>FE</b>	Finite Element
<b>HIBP</b>	High Intrabladder Pressure
<b>IBP</b>	Intrabladder Pressure
<b>IDRE</b>	Instrumented Digital Rectal Examination
<b>KUBC</b>	Kinematic Uniform Boundary Conditions
<b>KVFD</b>	Kelvin Voigt Fractional Derivative
<b>LIBP</b>	Low Intrabladder Pressure
<b>MRI</b>	Magnetic Resonance Imaging
<b>MW</b>	Molecular Weight
<b>PBC</b>	Periodic Boundary Conditions
<b>PSA</b>	Prostate Specific Antigen
<b>RVE</b>	Representative Volume Element
<b>SUBC</b>	Static Uniform Boundary Conditions
<b>SVM</b>	Support Vector Machine
<b>TQI</b>	Tissue Quality Index
<b>TURP</b>	Transurethral resection of the prostate

# CHAPTER 1

## Introduction

### Contents

---

1.1	Motivation.....	1
1.2	Thesis scope and structure .....	3

---

#### 1.1 Motivation

Perhaps the most significant recent advances in improving the life of humanity are attributable to cooperation between engineers and medical and biological scientists. Increasingly, computational modelling has become a key tool in biomedical practice and research, in such areas as surgery planning [1], clinician training [2] and preventive medicine [3]. Other biomedical and biological areas, such as tissue engineering [4], biomaterials research [5] and cell mechanics [6] have also been advanced using the *in-silico* approach. Major advantages of computational modelling include faster evaluation of parameters that can be easily controlled (compared to experimentation) and examined individually for sensitivity analysis, thus offering unique time and cost-effective capabilities over the traditional trial-and-error approach.

Despite recent advances in biochemistry and diagnostic imaging, early diagnosis of pathologies in soft tissues still remains challenging and often requires a biopsy to ascertain the presence of pathology and its grade. However, such procedures are often invasive and not free from risks such as infection and haemorrhage. In addition, they can



only be carried out in well-equipped medical centres. Considering that a large part of the global human population is in the developing countries where appropriate and timely diagnosis may be inaccessible due to the lack of resources, a simple, less-invasive and cost-effective method for soft tissue diagnosis is urgently required.

The mechanical properties of soft tissues have been shown to be subject to different physiopathological conditions such as cancer [7], liver fibrosis [8], kidney hydration level [9] or even age [10]. These changes, often observed at organ level [11-13], have been attributed to variations at lower length scales assessed under histopathological analysis [14]. Palpation, where the practitioner looks for abnormalities such as nodules, changes in roughness and lumps, has been successfully used for centuries as a diagnostic technique. However, palpation remains qualitative to this day, largely relying on the practitioner's experience and is open to inter-clinician variations. Although various devices and methodologies have been proposed to detect such changes, and so to avoid, or at least reduce, the number of invasive diagnostic procedures, quantitative diagnosis using palpation remains challenging. More importantly, inter-patient differences including those due to previous treatments or different anatomical structures further complicate diagnosis. Such patient-specificity could greatly affect the diagnostic effectiveness and so must be taken into account for generic applicability. Furthermore, some aspects of treatment could benefit from patient specific modelling. For example, current models for assessment of the efficacy of drug delivery [15, 16] are often one dimensional and do not consider the unique features of each patient such as details of the vascular network or microstructural changes due to pathological conditions thus leading to treatments that may not necessarily optimized with respect to the conditions of individual patient.

## **1.2 Thesis scope and structure**

This thesis has two major goals. The first is to establish new methodologies for soft tissue diagnosis, with specific reference to instrumented palpation applied to prostate cancer. The second goal is to establish a computational framework to test the efficacy of chemotherapeutic treatment. Fulfilling these objectives will pave the way towards early diagnosis of soft tissues and optimal treatment design. The ultimate impact of this work could be critical for pathologies such as cancer where early diagnosis significantly increases the life expectancy of patients, more so if the treatment at this stage can be made more effective. The methodologies presented here are expected, in the long term, to reduce the number of unnecessary biopsies performed on patients, leading to less invasive procedures, reduced medical costs and lower risk of infection. Additionally those patients requiring drug treatment would benefit from optimised treatments customised for their specific pathological conditions. It should be highlighted here that the two aforementioned objectives, namely tissue diagnosis and drug treatment, are linked by an analysis which takes into account the heterogeneous, hierarchical nature of soft tissue, whose changes under different pathophysiological conditions are also investigated in this thesis.

The objectives of this thesis are, therefore:

- to develop a methodology for quantitative tissue quality assessment using mechanical indices;
- to establish a robust diagnostic framework to determine position, depth and size of harder nodules in soft tissues;
- to analyse how changes in the microstructure of soft tissues influence the macroscopic mechanical properties;
- to investigate the effects of patient-specific structural features affect mechanical response, specifically during a digital rectal examination procedure;

- to research the influence of patient-specific tissue microstructure on drug delivery to target sites

The rest of this doctoral thesis is structured to elaborate how these objectives are met, as follows:

## **Chapter 2: Multiscale Modelling of Soft Tissue and Diagnosis: State of the Art**

This chapter reviews the state of the art of the topics investigated in this thesis. First a brief survey of soft tissue microstructure and the changes caused by pathological conditions are discussed with an emphasis on prostate cancer. Secondly, existing methods to characterize and model the mechanics of soft tissues considering its heterogeneous and multiscale nature are reviewed. Then, the necessity for patient-specific modelling is discussed within the framework of diagnosis and treatment of soft tissue diseases. Finally, the current challenges in soft tissue diagnosis and treatment are highlighted, and the potential impact of meeting the thesis objectives discussed.

## **Chapter 3: A novel palpation-based method to detect hard cancerous nodules in soft tissues – the computational framework and experimental validation**

In this chapter, a novel methodology to determine the size, shape and depth of hard nodules in soft tissue using palpation is presented. This methodology does not require *a priori* knowledge of any of the three targets; depth, size and geometry of the inclusion. First the methodology is tested using 2D examples with idealised geometries. It is then validated using gelatine phantoms with tissue-mimicking mechanical properties. The analysis carried out in this chapter suggests that the differences in the viscoelastic behaviour of cancerous and healthy tissues could be exploited as a critical diagnostic index for quantitative assessment of tissue quality, a matter which is further investigated in Chapter 4.

## **Chapter 4: Quantitative tissue quality assessment through viscoelastic characterization using instrumented palpation**

A framework for tissue quality assessment based on the changes in the apparent time constant observed during dynamic palpation is presented in this chapter. The methodology is described and tested on 2D specimens, and then on clinically-relevant patient-specific models of prostate, reconstructed from MRI. The capacity of dynamic palpation to measure the changes in viscoelastic properties is assessed. A diagnostic framework is proposed to measure elastic and viscous behaviours simultaneously using a reduced set of viscoelastic parameters, giving a reliable index for quantitative assessment of tissue quality. The approach is illustrated on prostate models reconstructed from MRI scans of prostate. The examples show that the change in viscoelastic time constant between healthy and cancerous tissue is a key index for quantitative diagnostics using point probing. Although the proposed methodology allows quantitative diagnosis of nodules in soft tissues, it does not allow the volume fraction of cancerous tissue to be obtained. Since this would be of particular interest in clinical diagnosis, e.g. in surgery, medication or palliative care, a new method to predict the volume fraction of cancerous tissue using its apparent viscoelastic parameters is presented in the next chapter.

## **Chapter 5: A novel method for rapid, quantitative, mechanical assessment of soft tissue for diagnostic purposes – a viscoelastic ‘rule of mixtures’**

In this chapter a methodology is presented to obtain a rule of mixtures that relates the apparent time constant of a tissue sample to the fractions of its components. A rule of mixtures, which relates tumour volume fraction to the apparent mechanical properties, is obtained by minimizing the difference between the strain energy of a heterogeneous system and an equivalent homogeneous one subjected to a creep or stress relaxation test. The fraction of each tissue component is then predicted by comparing the observed time constant with that calculated from the rule of mixtures. Next, the methodology is tested

in a clinically relevant scenario: instrumented digital rectal examination and examination during a laparoscopic procedure.

## **Chapter 6: Patient Specific Modelling of Palpation-based Prostate Cancer**

### **Diagnosis: Effects of Pelvic Cavity Anatomy and Intrabladder Pressure**

The analysis done in the foregoing parts of the thesis and the literature suggest that patient-specificity is critical to the accuracy of clinical diagnosis. In this chapter, a computational framework that takes into account some patient-specific features relevant to instrumented palpation is proposed, using the example of prostate cancer diagnostics using palpation taking into account specific features of both the prostate and the surrounding pelvic cavity. The effects of patient specific anatomical structures on palpation outcome are studied in three selected patients with different pathophysiological conditions whose pelvic cavities are reconstructed from MRI scans. In particular, the role of intrabladder pressure in the outcome of digital rectal examination is investigated with the objective of providing guidelines to practitioners to enhance the effectiveness of diagnosis. Furthermore, the presence of the pelvic bone is assessed to examine the necessity of including such a patient-specific feature in the proposed computational framework.

## **Chapter 7: A multiscale, mechano-morphological approach to soft tissue mechanics: application in prostate cancer diagnosis**

The study presented so far has been carried out at either organ or tissue scale. However, in order to better understand how changes in the microstructure influence the apparent behaviour at higher scales it is essential to investigate lower scales (e.g. tissue microstructure). In this chapter, a methodology to predict the apparent mechanical properties of soft tissue microstructures is presented. The influence of pathological conditions on the apparent stiffness are analysed and compared with results obtained at different length scales with the aim of establishing a framework for multiscale modelling.

Furthermore, the use of support vector machines as a tool to perform diagnosis based on the mechanical properties of soft tissues is also presented.

### **Chapter 8: Heterogeneity in Tissue Diffusivity: An Application in Drug Delivery**

Following on from some of the findings of Chapters 5 and 7 (i.e. that apparent properties are greatly affected by microstructural changes in tissue), this chapter aims to investigate how the pathophysiological conditions influence the diffusivity and therefore the efficacy of drug delivery. Specifically, a computational framework to analyse the effectiveness of a chemotherapeutic treatment for solid tumours is presented. The apparent diffusivity of two commonly-used drugs for prostate cancer (i.e. paclitaxel and doxorubicin) in healthy and cancerous tissues is estimated from the histopathological samples from various patients. The proposed methodology is then coupled with a mathematical model for predicting the fate of cancerous cells as a result of the treatment, in order to estimate its outcome. Following on from this, the efficacy of different strategies for drug delivery (e.g. intravenous infusion and bolus injection) is investigated.

### **Chapter 9: Looking back / working forward**

In this chapter, the work carried out in the thesis is summarized and the main conclusions are highlighted. Future work is proposed to pursue the benefits of computational modelling in clinical practice and, ultimately, realise the aim of tangible benefits to human health. In particular, further research directions are suggested that would potentially enhance the outcome of tissue diagnosis using instrumented palpation. Additionally, the basis of a novel patient-specific platform for drug delivery into soft tissue is sketched.

# CHAPTER 2

## Multiscale Modelling of Soft Tissue and Mechanics-based Diagnosis: the State of the Art

### Contents

---

2.1	Summary .....	9
2.2	Soft tissue hierarchy and heterogeneity .....	9
2.3	Viscoelasticity in soft tissue.....	12
2.3.1	An introduction to viscoelasticity .....	12
2.3.2	Characterization of viscoelastic parameters.....	13
2.4	Homogenization and multiscale modelling– a necessary simplification .....	15
2.5	Patient specific modelling – a complication to medical diagnosis .....	19
2.6	Soft tissue diagnostics .....	20
2.7	Drug delivery .....	24
2.8	Bridging the gaps .....	27

---

## 2.1 Summary

SECTION TITLE	OBJECTIVE
2.2 Soft hierarchy and heterogeneity	Establish the hierarchical, heterogeneous, viscoelastic nature of soft tissues and how changes in their microstructure influence the apparent properties at higher length scales
2.3 Soft tissue characterization	Survey the current methodologies for characterizing viscoelastic materials with emphasis on soft tissue
2.4 Viscoelastic modelling	Review viscoelastic models for soft tissues
2.5 Homogenization and multiscale modelling– a necessary simplification	Review the different computational approaches to homogenize and treat multiscale modelling problems required for soft tissue modelling
2.6 Patient specific modelling – a complication to medical diagnosis	Establish the need for patient specific modelling to obtain the accuracy required in clinical practice
2.7 Soft tissue diagnosis	Review the state of the art for methods for soft tissue diagnosis and their limitations
2.8 Drug delivery	Review the current methods for analysing and predicting the outcome of drug delivery strategies
2.9 Conclusion	Identify the gaps in knowledge to be addressed in the thesis

## 2.2 Soft tissue hierarchy and heterogeneity

Biological tissues are heterogeneous, hierarchical, visco-elasto-plastic materials whose mechanical properties have been proved to change subject to physiological conditions such as swelling and menstruation as well as pathological conditions such as the presence of cancer and ageing.

Viscoelasticity in biological tissue was first recognized by Bayliss and Robertson [17] in cat lungs. The time-dependent behaviour of tissue has been attributed to the movement of fluid within its microstructure in such tissues as cartilage or liver [18, 19] and also to the lubricating effect that the proteoglycan matrix exerts between the collagen fibrils that



occurs, for example, in arterial tissue [20]. The mechanical behaviour of collagen is also known to vary with strain rate [21], and is believed to contribute significantly to the viscoelastic response of tissues such as lung [22], liver [23], prostate [7] and skin [24]. Breast tissue has been observed to exhibit viscoelastic properties which vary with such conditions as hormonal balance or cancer [25-28]. The viscoelastic behaviour of brain tissue [29, 30] has been shown to vary with such pathological conditions as multiple sclerosis [31], cancer and ageing [10]. Liver tissue also exhibits a certain viscoelasticity [32] that has been observed to vary subject to conditions such as fibrosis [12], water content [19] and preservation time [14]. Arteries have been reported to have a rate dependent behaviour where the response is often anisotropic and nonlinear [33, 34]. In cartilage, viscoelasticity, which is responsible for energy dissipation, is a desirable property that allows the stress associated with physiological load to be less damaging [35]. Furthermore it has been shown that the energy dissipated is sufficient to increase the temperature of healthy cartilage so that proteoglycans and hyaluronic acid can be produced [36]. Muscle tissue also exhibits an anisotropic viscoelastic behaviour that becomes nonlinear at large strains [37, 38]. Changes in the mechanical properties of kidney tissue under different hydration conditions, and different cancer phenotypes have also been reported in the literature [9, 39].

Prostate tissue, the particular focus of this thesis makes a useful case study for structure-property relationships. Conditions such as prostatitis, benign prostate hyperplasia (BPH) and prostate cancer (PCa) are also known to influence the elastic and viscoelastic properties of the prostate gland [7, 40]. Fig. 2-1 shows histological images of a prostate at different magnifications. The hierarchical and multiscale nature of the tissue is clearly visible therein, where large acini can be found from the upper (non-cancerous) part and a homogeneous structure (at the magnification used) is present in the lower (cancerous) part. However, with increased magnification, as illustrated in Fig. 2-1 (b), it is seen that

the apparently homogeneous cancerous nodule visible in Fig. 2-1(a) also contains smaller acini indicating the presence of prostate cancer. A further detailed look at the tissue as shown in Fig. 2-1 (c) clearly reveals the heterogeneity of acini in the cancerous nodule, which is associated with the clinical prognosis for the patient through the Gleason score [41]. Such changes in the acini size would influence not only the amount of liquid within the tissue but also its transport properties which have been related to viscoelasticity [18, 19]. Thus, there is a huge potential to use viscoelasticity as an index in the diagnostic assessment of soft tissue, not only for prostate, but also more generally in terms of a number of positive or negative physiological or pathological axes. Compared to traditional methods for tissue diagnosis based on elastic indices [42, 43] viscoelasticity introduces at least two further parameters (i.e. time constants and long term modulus) that could provide more accurate and specific diagnosis.

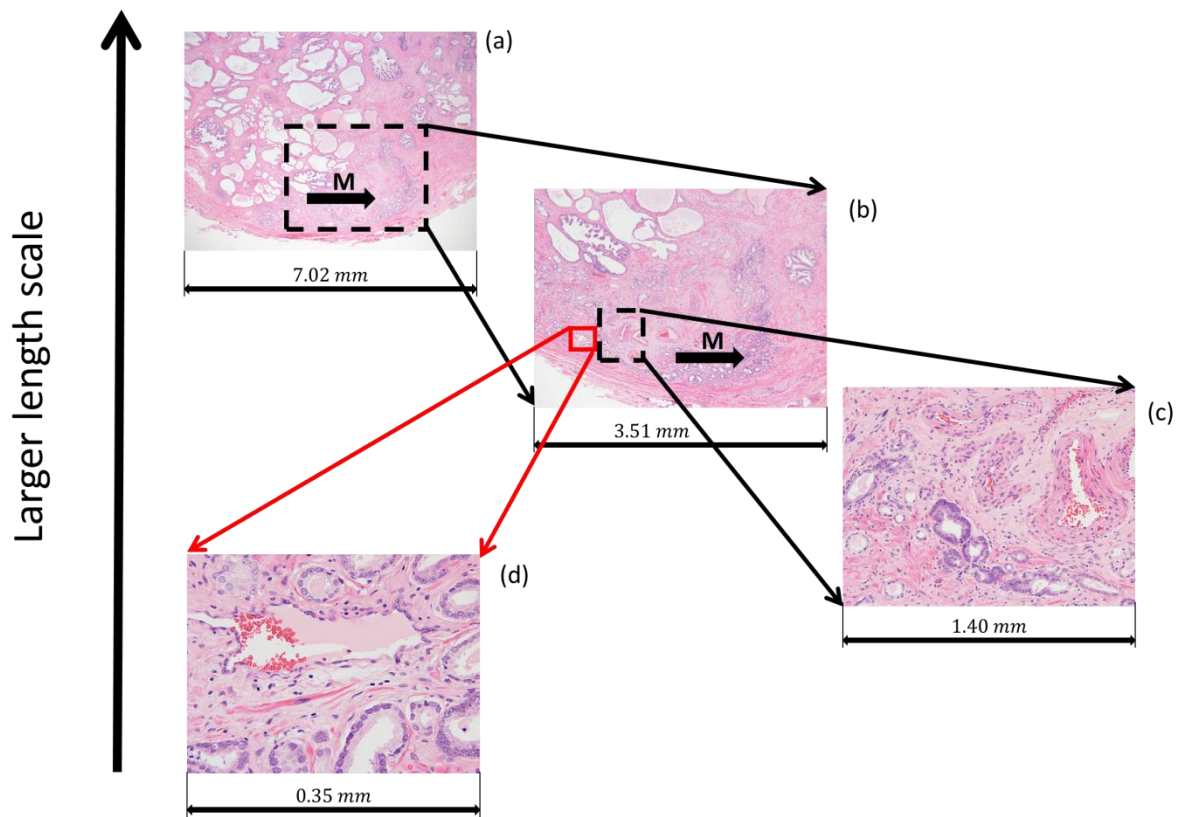


**Figure 2-1.** Histological sample stained with haematoxylin and eosin show the multiscale nature of soft tissue. (a) The bigger acini of a healthy prostate are clearly visible compared to the smaller ones in blue shown at the bottom of (a) and (b), which are malignant cells (M). A closer look into the cancerous area is shown in (c) and (d) where a blood vessel and blood cells are shown.

## 2.3 Viscoelasticity in soft tissue

### 2.3.1 An introduction to viscoelasticity

A wide range of materials such as biological tissues and polymers present certain inelastic behaviours such as creep, which causes the strain to increase when the stress is held constant; stress relaxation, where the stress decreases with time when the strain is maintained constant; hysteresis or phase lag between the applied stress and strain which causes energy dissipation; strain-dependent properties such as an increase in the apparent stiffness at high strain rates. Different models that reproduce such behaviours have been proposed. The simplest models are the Maxwell model which consists of an elastic spring (Eq. 2-1) and a purely viscous dashpot (Eq. 2-2) in series and the Kelvin-Voigt model where the dashpot and spring are in parallel.

$$\sigma_{elastic}(t) = E \cdot \epsilon(t) \quad (2-1)$$

$$\sigma_{viscous}(t) = \eta \cdot \frac{d\epsilon(t)}{dt} \quad (2-2)$$

In Eqs. 2-1 and 2-2  $\sigma$  is the stress,  $E$  is the Young's modulus,  $\epsilon$  is the strain,  $t$  is the time and  $\eta$  the viscosity of the dashpot. However, these models cannot reproduce creep and stress relaxation respectively. The standard linear model or Zener combines a Maxwell model with an elastic spring in parallel which is adequate to reproduce both creep and stress relaxation. Such model can be generalized and include several dashpot-spring units in parallel to account for more complex viscoelastic behaviours. A further generalization of these models includes the use of fractional derivatives for the dashpot as shown in Eq. 2-3.

$$\sigma_{viscous}(t) = \eta \cdot \frac{d\epsilon(t)}{dt^\alpha} \quad (2-3)$$

Although fractional derivative models have been used to model certain tissues such as prostate [44] they require numerically solving Riemann-Liouville [45] or Caputo [46]

integrals which is a complex and computationally intensive task [47] especially for large models. It should be noted here that most commercial software for structural finite element simulations implement Prony series. Compared to other models previously mentioned, Prony series are widely used to model complex creep and stress relaxation behaviours and due to its simple analytical formulation shown in Eq. 2-4 easier to fit.

$$E(t) = E_0 \cdot \left(1 - \sum_{i=1}^n p_i \cdot \left(1 - e^{\frac{-t}{\tau_i}}\right)\right) \quad (2-4)$$

### 2.3.2 Characterization of viscoelastic parameters

Characterization of viscoelasticity for biological tissue requires the entire history of deformation when its time dependent behaviour is not negligible. Two different approaches are often adopted, i.e. creep/stress relaxation (quasi-static) and dynamic tests. The results from quasi-static tests are often correlated by means such as Prony series[48], although other fitting techniques have been used, including a more generalized transfer function (between stress and strain) in Laplace space [49], or using splines [50]. These tests are capable of retrieving the instantaneous and the long-term moduli. In dynamic tests, the sample (usually in tensile/-compressive configurations) is often loaded with a pre-defined displacement function, such as a sinusoid. The amplitude of the force response and phase lag between the displacement and force signals can then be measured over a range of frequencies. In such tests, different techniques can be used to identify the corresponding transfer functions to relate the stress and strain in Laplace space [49, 51]. It should be noted here that the two types of tests, in fact, measure the same thing, where the transfer function obtained from a stress relaxation/creep test mathematically dictates the dynamic behaviour that would be measured in the frequency test, and *vice versa*. Therefore, the ranges of time and frequency that are used may influence measurement outcome. For example, using higher frequencies or shorter times allows the detection of the smaller time constants that define the behaviour in the early stage of stress relaxation,

whereas lower frequencies provide information for higher time constants that characterize the long-term response.

The time constants obtained from models such as Prony series define the characteristics of amplitude and phase-shift, but overfitting of a single data set using an excessive number of time constants can lead to undesired, sometimes entirely artificial, characteristics at certain ranges of frequency. Therefore, it is critical to find the balance between the fitting error and the number of fitting parameters. Ideally the results of both dynamic and quasi-static tests should be fitted at the same time to avoid overfitting; however this would increase the complexity of testing making it inapplicable to clinical tissue diagnostics.

### **2.3.2 Viscoelastic modelling in soft tissue**

The elasticity of biological tissue has been thoroughly discussed in reviews [52-54] and can be described using such models as the 8-chain model [55] or other phenomenological continuum models including Mooney-Rivlin [6], Ogden [30] and Holzapfel-Gasser-Ogden (HGO) [34]. The origin of viscoelasticity in biological tissues is still unclear [18, 19] and therefore there are relatively few physics-based models. Amongst these, Parker [56] has proposed a model where a perfect cube with a fluid microchannel inside is subjected to uniaxial loading and shows viscoelastic behaviour. The fact that such a model is able to mimic the viscoelasticity in soft tissues highlights their hierarchical and multiscale nature. Another category of theoretical models, often referred to as recruitment models, consists of multiple Maxwell elements arranged so that, when a given element reaches the allowable strain, the following element starts to deform. Such models, whose physical basis can be traced to a tissue made out of multiple fibres with varying stiffness and length (e.g. elastin and fibrin), have proven successful, for example, in modelling lung tissue where stress relaxation follows a power law [57]. In some scenarios, viscoelasticity is also modelled using Prony series [58] and Kelvin-Voigt fractional

derivative (KVFD) [32]. Of particular note is the work of Holzapfel and co-workers [20, 33, 34, 59], who proposed a range of viscoelastic models based on a strain energy density function of fibre-reinforced anisotropy that successfully predicts the viscoelasticity in soft tissues such as arterial walls. Such models are particularly interesting as they are currently used in clinical practice. Peña et al.[60] has also modelled the viscoelastic behaviour of vascular tissue including softening due to damage. Anisotropic viscoelastic models have also been proposed to predict the behaviour of heart valves [61]. Bergström and Boyce [55, 62] described tissue viscoelasticity using the interaction between two networks, one related to the elasticity and the other to the viscous behaviour. Although both networks have the same deformation gradient, the velocity gradient in the viscous network is decomposed into elastic and viscous velocity tensors [55, 62]. It should be noted here that, although it is possible to model complex behaviours using viscoelasticity, especially when dynamic loading is applied, the model complexity and computational time increase significantly. Furthermore, the number of parameters is increased, which can lead to higher uncertainty levels and therefore reduced relevance in clinical practice.

## **2.4 Homogenization and multiscale modelling— a necessary simplification**

In the context of continuum mechanics materials such as composites or biological tissues are often modelled as homogenous material, with effective properties ‘averaged’ from microstructures at lower length scales. Often these methodologies consider the existence of a representative volume element (RVE) whose apparent properties are estimated as ‘homogenized’ values and used to predict mechanical behaviour at a higher length scale. This implies the existence of a unit cell in a periodic microstructure or an infinite volume (in practice, very large compared to the size of the unit cell) containing a large set of representative volume elements [63]. Fig. 2-2 shows a flowchart typically used in multiscale modelling where data is interchanged between different length scales of the model. Such averaging techniques have been developed for heterogeneous engineering

materials for years [64]. For example, analytical models, such as the series (or Reuss) and parallel (or Voigt) models, have been proposed to determine the effective properties of heterogeneous materials and are often used to estimate upper and lower bounds of effective properties [65, 66]. Such models, usually expressed as a relationship that involves the volume fractions of the constituent phases and their respective properties, are often referred to as '*rule of mixtures*'. Hamilton and Crosser [67] proposed an analytical model for composite materials when the topology of the inclusions is known, and Landauer [68] when unknown. Of special interest is the work by Hashin and Shtrikman [69] in the 1960s, shown in Fig. 2-3, who mathematically derived upper and lower bounds of effective properties such as conductivity and Young's modulus using asymptotic homogenization irrespective of the topology of the microstructure. Theoretical bounds for viscoelastic materials were also derived in the late 90s [70]. Despite their advantages, including ease of use and low computational cost, analytical models have certain limitations such as oversimplified physics and an inability to tackle more complex problems including fluid-structure interaction, contact and viscoplasticity [64]. In this regard, numerical methods have proven useful especially for more complex scenarios such as in determining the effective properties when contact occurs within microstructures [71] and also for thermo-coupled problems [72]. Various methodologies that estimate the effective properties of viscoelastic materials have been proposed in the Fourier [73], time [74] and Laplace [75] domains, respectively.

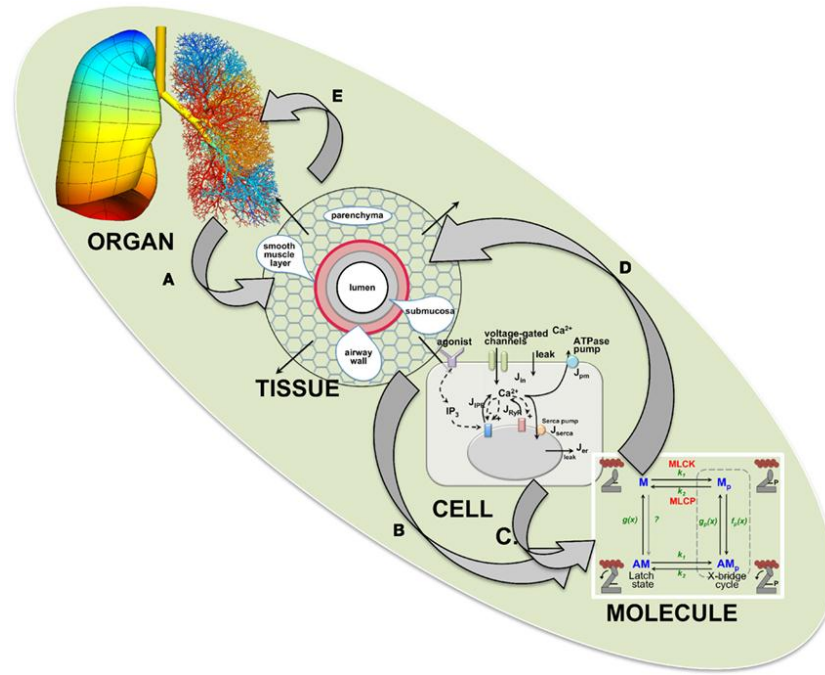


**Figure 2-2.** Schematic of multiscale modelling for the example of lung tissue [76]. The data predicted on respective scales flow upscale/downscale and *vice versa* to improve the fidelity of the model.

Computational approaches such as the self-consistency method have also been developed to take into account the topology of the sample and also non-linear behaviours including plasticity, viscoelasticity or damage [77]. Although such algorithms can handle complex behaviours, they often require multiple finite element problems to be solved iteratively. Therefore, the estimation of effective properties and hence a rule of mixture for heterogeneous materials may become a computationally intensive task.

Fig. 2-3 (a) illustrates the example of a structure composed of a large number of RVEs. Each of these unit cells contains a pore and a solid inclusion. By imposing certain boundary conditions on such an RVE, it is possible to obtain the apparent mechanical properties, as illustrated in Fig. 2-3(b), using computational methods such as asymptotic homogenization. Three main types of boundary conditions are commonly used for this purpose, namely kinematic uniform boundary conditions (KUBC), stress uniform boundary conditions (SUBC) and periodic boundary conditions (PBC). KUBCs consist of applying a prescribed displacement field and often provide upper bounds for the



apparent stiffness, whereas SUBCs often result in a lower bound by imposing a force field. PBCs consider and average the compression or shear field in each principal direction so that displacements on the boundaries are periodic [63].

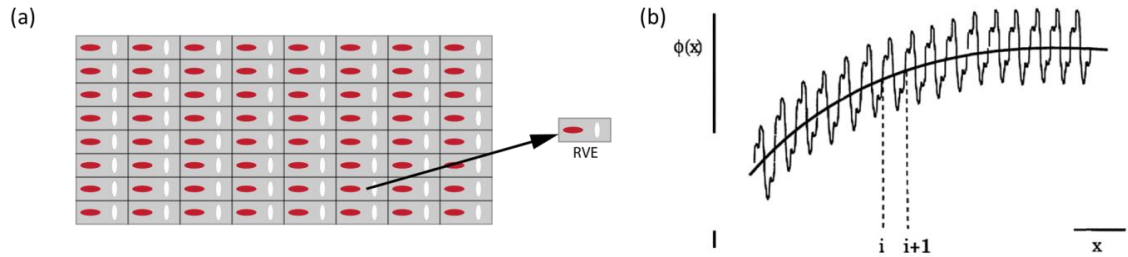


**Figure 2-3.** (a) Example of a hierarchical, multiscale structure built from multiple representative volume elements (RVE). (b) The average behaviour, represented by the thick solid line, may of sufficient use for certain applications when the high frequency local challenges [78].

To impose such periodic boundary conditions in a finite element regime, meshes with matching nodes at opposite sides of the RVE (in either 2D or 3D) are often used. However, obtaining such periodic meshes may become a difficult task or require extremely refined meshes especially when the geometry is complex, such as it might be when reconstructed from medical images. Different methods have been reported in the literature to overcome such a complication. A Lagrange polynomial and spline interpolation has been proposed to eliminate the need for matching nodes at the boundaries [79]. Another method, developed for composites, was proposed by Tyrus et al. [80] using cubic interpolants along the boundaries to reduce the number of constraints and therefore the computational cost. However, this method requires periodicity to be imposed onto the intersection of the inclusions with the RVE therefore making it less capable of modelling biological tissues, which often are not symmetric. The approaches presented so far have certain limitations regarding the topologies that can be handled or the necessity to modify the stiffness matrix of the problem which can be difficult in

commercial finite element software. Furthermore, there can be a significant increment in the number of degrees of freedom required to interpolate the displacement fields using the Lagrange polynomials or splines leading to a significant increase in the computational time.

## **2.5 Patient specific modelling – a complication to medical diagnosis**

Patient specific models use inputs (i.e. material properties, geometry, loadings etc.) from the very patient for whom a treatment, diagnosis or any other procedure is being investigated, instead of using average values estimated for all people or certain groups based on gender, age, ethnicity or other factors. Nowadays, it is widely accepted that patient specificity plays a vital role in the effectiveness of predictive modelling [81-83] and so it is of great importance to examine the sensitivity of any biomechanical model to patient-specific parameters, especially when quantitative information is required for clinical diagnosis.

There are some examples in the literature of how patient-specific modelling has successfully enhanced clinical diagnosis and treatment. Bone tissue has attracted significant interest in the past decade due to the social and economic impact of diseases including osteoporosis and osteoarthritis as well as in the correction of traumas, e.g. hip fracture. Garijo et al. [84] used artificial neural networks, support vector machines and linear regression to predict loads in bone when taking into account patient specific features such as proximal femur geometry. Kerner et al. [85] investigated whether bone loss following total hip arthroplasty could be explained by strain remodelling using patient-specific geometries and bone densities. For osteoporosis, Schileo et al. [86] proposed a framework which included patient specific geometries and material properties based on tissue density and Young's modulus to predict the strain in bones and, consequently, the probability of fracture. Other examples of patient-specific modelling include planning of clinical treatment such as radiotherapy and cryosurgery. The side

effects of radiotherapy, for example, can be mitigated by predicting the movement of the healthy organs that surround the malignant tissue. In this context, Scaife et al. [87] developed a framework, which takes patient uniqueness (e.g. topology) into account, to determine the position and absorbed dose to the rectum during radiation treatment to avoid unnecessarily extreme exposures. In the area of cryosurgery, where probes are used to cool tissues down below a certain threshold, (e.g. for prostate cancer surgery), Zhang et al. [88] modelled the temperature distribution taking into account patient-specificity in thermal properties as well as the heating from the urethral warming catheter, which is inserted to reduce the risk of damage to the urethral tissue. This approach allows a safer and more reliable approach since it is possible to control the temperature of the tissues to avoid damage. As a result the malignant tissue can be eliminated while maintaining the integrity of surrounding healthy tissue and adjacent structures.

Patient specific modelling has recently also proven successful in other clinical scenarios [89, 90]. Gasser and co-workers proposed a systematic approach to estimate the risk of rupture of abdominal aorta aneurysms which has already been translated into clinical practice [91]. In this framework, the geometry of the blood vessels was obtained from the patient using CT scans, despite the use of average values for the mechanical properties. Patient specific models have greatly assisted in understanding the mechanisms behind the rupture of aortic aneurysms [92] and consequently the prediction of rupture risk [93], thus making a significant contribution in preventive cardiovascular medicine.

## **2.6 Soft tissue diagnostics**

Various techniques that exploit the changes in the mechanical properties of the tissue subject to pathophysiological conditions have emerged to help clinical tissue diagnosis. X-ray, computerized axial tomography (CAT), magnetic resonance imaging (MRI), positron emission tomography (PET) and other medical imaging techniques provide critical information on structural anomalies for different types of tissues and have been

extremely successful in detecting pathological conditions such as neoplasms or aneurysms. In addition to being able to detect anomalies in prostate, these techniques allow the surrounding structures such as the seminal vesicles [94] and bladder [95] also to be examined. However, they may not be appropriate for certain groups of patients such as pacemaker carriers or infants and it is often economically infeasible to apply them to large numbers of patients. Elastography (in the form of trans-rectal ultrasound) has also been widely used to help detect prostate cancer [13, 23, 96, 97] and is based on the relative displacements caused by the difference in stiffness in the tissue. However, it is still challenging to relate the elastographic image of the tissue to the underlying pathological conditions especially when multiple conditions such as in Benign Prostate Hyperplasia and cancer are present [98].

Biopsies are often used as the standard procedure to assess the presence and extent of different pathologies in soft tissues and have seen a significant improvement during the last three decades, e.g. in prostate cancer diagnostics. Prior to the 1980s, most prostate biopsies were performed using a needle which was directly guided by the clinician [99], largely relying on their experience of the anatomy. In the early 90s the technique was improved by the introduction of transrectal ultrasound (TRUS) and the sextant approach. The procedure is often repeated 10 to 12 times (up to 20) at different locations of the prostate, the samples then undergoing histological examination. Although increasing the number of samples and their coverage can lead to higher confidence levels of around 20% [100], biopsies can still give false negative results (as the TRUS does not necessarily identify all prostate cancer regions and the needle only samples small cores) [99, 101]. Other disadvantages such as pain and discomfort for the patient and the possibility of complications including rectal bleeding and haematuria [101] further reduce the effectiveness of such diagnostic methods. Fig. 2-4 shows the schema of this invasive

procedure, where the needle is often inserted close to structures such as the urethra or the sphincter, thus increasing the surgical risk to the patient.

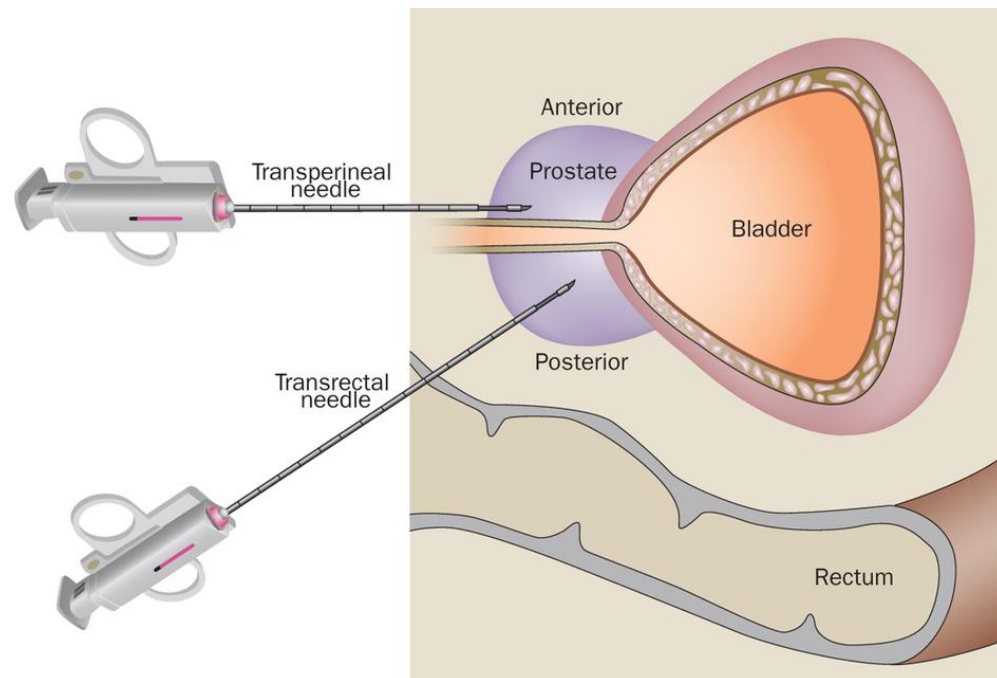


**Figure 2-4.** Schematic of the transrectal and transperineal approaches for prostate biopsy. Up to 20 tissue samples are often collected from the sample. However the risk of false negatives is always present[102].

Palpation is widely used in primary diagnosis of conditions such as appendicitis, haemorrhoids and breast cancer as well as prostate and testicular cancer. However it remains a qualitative diagnostic method that largely relies on the practitioner's experience, which often leads to subjective diagnosis greatly affected by inter-clinician variations. Such uncertainties result in less accurate diagnosis that may lead to suboptimal treatments, which can be critical for life threatening diseases such as cancer. Instrumented palpation would allow the recording of quantitative data and could also be more sensitive than traditional palpation. Therefore, disease could be diagnosed at an earlier stage before it spreads to other organs and, consequently, improved prognosis for the patient. Significant work has been done to improve the clinical efficacy of palpation-based diagnostic methods [8, 42, 44, 103-107]. This has led to the development of

methodologies to identify areas suspected of being malignant and to offer the possibility of diagnosing diffuse and/or indolent tumours [108], which is indeed one of the motivations of this thesis.

Efforts have also been made to develop palpation devices such as rolling and sweeping probes [109-111] to test elasticity [8, 42, 44, 112, 113] in a variety of tissues such as swine brain *in vivo* [114], porcine [115] and human liver and skin [116, 117], as well as soft tissue from lower limb extremities [118, 119]. Unfortunately, the effects of the depth and size of a nodule in the force feedback are coupled; a small nodule near the surface would result in a similar force feedback to a bigger one deeper inside. De-coupling these effects is of critical importance for clinical applications since depth and tumor location have been related to the progression of disease and therefore its prognostic outcome [120]. Furthermore, those aspects can affect the chosen treatment and the surgical margin in any intervention, and therefore should be considered before proceeding with any treatment. In some attempts at quantitative diagnosis using mechanical palpation, only simple geometries of cancerous nodules such as cylindrical [43, 121] or rectangular [109] were considered. Artificial neural networks have also been employed to predict not only the size and depth of anomalies but also their mechanical properties [121]. However, such an approach relies on *a priori* knowledge of the stress distribution in the tissue, which remains a difficult (if not impossible) task, especially in biological tissues with rate-dependent behaviour where loading history is usually unknown. More recently, viscoelasticity has been considered as a possible index for tissue quality assessment [7, 44] in diseases such as breast cancer, prostate cancer (PCa) [122], benign prostate hyperplasia [40], liver fibrosis [123] and pancreatic diseases [124]. Fig. 2-5 illustrates a few examples of devices for instrumented mechanical palpation

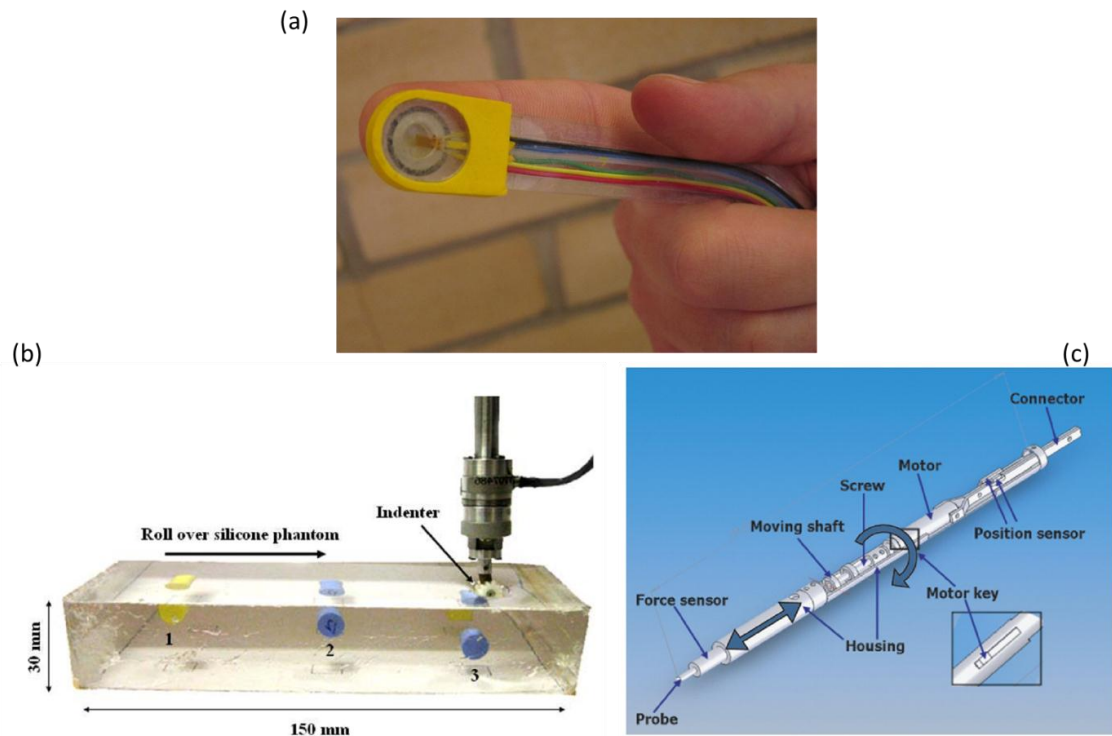


**Figure 2-5.** (a) The e-Finger is an example of a soft tissue palpation device [125]. (b) Rolling indentation system proposed by Sangpradit et al.[43] (c) Indentation system described by Ahn et al.[126].

In addition to the aforementioned diagnostic methods, concentration of prostate-specific antigen (PSA) in blood is commonly used as a primary test for prostate cancer [127]. However, PSA levels vary in each patient subject to various factors such as prostate manipulation (for instance during digital rectal examination), ejaculation and certain drugs such as finasteride [128]. It has also been reported recently that the presence of certain tumours in the prostate does not influence the PSA levels [127], therefore making it an unreliable diagnostic index.

## 2.7 Drug delivery

Although the synergies of engineering and biomedical sciences have proven useful to improve soft tissue diagnosis, other fields, such as treatment optimization, offer further potential for enhancement. In particular, delivery of chemotherapeutic agents is challenging due to the need to administer the drugs at the highest possible concentration to eliminate the malignant cells without causing undesirable side effects.

Solid tumours are often found in breast, colon, rectum, lung and prostate. The treatment options for such cancers include radiotherapy [87], surgery [129], brachytherapy [130] and chemotherapy [131] among others. Compared to other types of cancers such as lymphoma or leukaemia, chemotherapy in solid tumours is less successful due to the different barriers the drug needs to overcome before encountering the cancerous cells, for example blood vessels and increased interstitial pressure. However chemotherapy is often used as a primary treatment when surgery or radiotherapy are not adequate or used as adjuvant treatment due to their prophylactic action against cancer progression [132]. Two medical approaches are commonly used to deliver drugs into these challenging tumours: oral and intravenous delivery where the drug travels through the bloodstream and bolus administration where the drug is directly inserted into the tumour. In the first case, the drug travels through the whole body thus interacting not only with the cancerous cells but also with the healthy ones. Other drug delivery methodologies include nanoparticles [133] and thermosensitive liposomes [134] as shown in Fig. 2-6.

Independently of the method used to deliver the drug to the tumour site, it needs to reach the cancerous cells, often with diffusion as the main driving force, given the increased interstitial fluid pressure often found in solid tumours which limits convection [135]. Diffusivity of drugs in solid tissues has been related to the molecular weight of the drug. However, it also depends on the pathophysiological conditions which influence vascular density, interstitial fluid pressure and tissue microstructure on a patient specific basis. Therefore such parameters need to be incorporated into any model that is aimed to be used in clinical practice due to the high accuracy required.



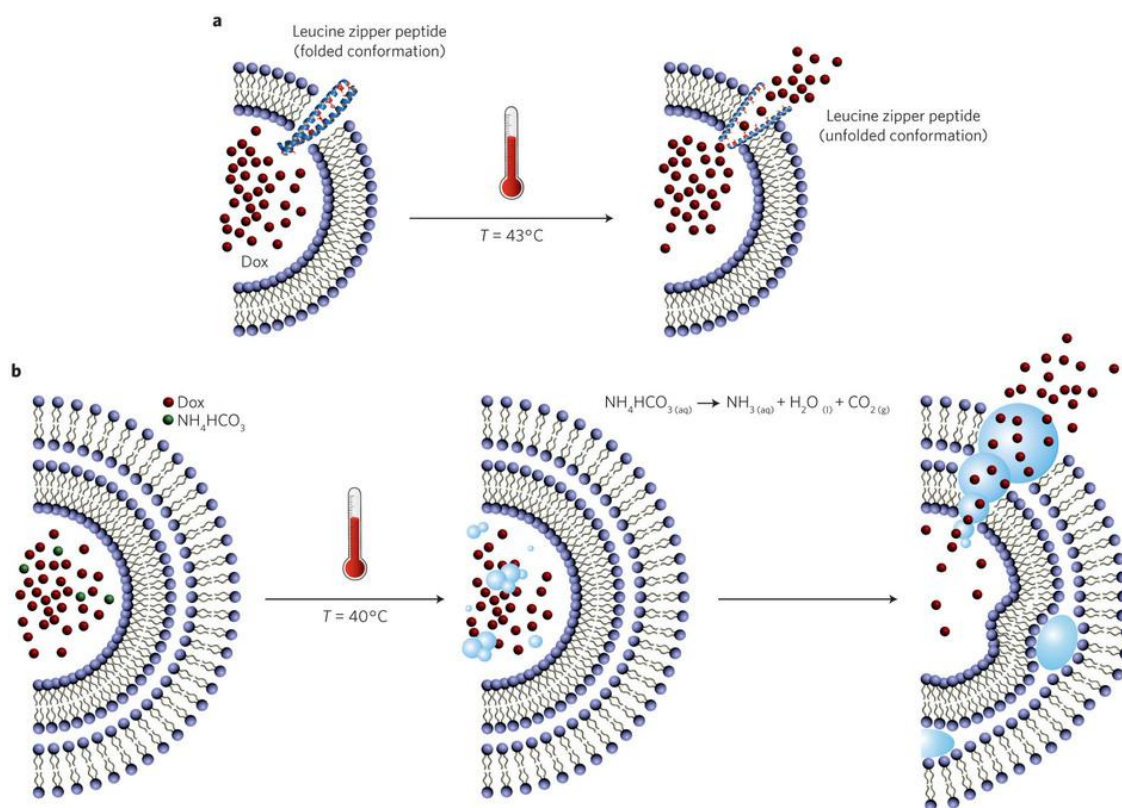


**Figure 2-6.** Examples of thermoliposomes, drug carriers activated by temperature [136].

Mathematical and numerical modelling has become a useful tool to investigate drug delivery in clinical practice and drug trials [15]. Traditional approaches to analyse drug delivery are based on *in-vitro* , *in-vivo* (in animals) observations and also those from human biopsies [137]. Compared to such approaches, mathematical and numerical modelling offers as the potential to reduce the amount of experimental work and/or reduced ethical compromises. However, many models do not consider the geometry of the underlying microstructure and use one dimensional models [16]. Also, the diffusivity and other parameters are estimated for bulk material and are often considered to be isotropic. Little experimental or computational validation is found in the literature and the underlying microstructure has proven to change under different physiopathological conditions [14].

Although tissue diffusivity plays a critical role in the efficacy of drug delivery, determining the effects of the drugs on the cells is crucial. The mechanisms by which drugs interact with cancerous cells are complex. Multiple mathematical models that

consider drug concentration and biological parameters such as cell replication and apoptosis rate have been proposed at cell [16] and tissue [138] scales to predict whether a cell population will proliferate or not. However, the input for such models does not consider patient-specific features such as tumour or blood vessel network topology. Therefore, obtaining a realistic, quantitatively accurate map of how the drugs travel through the tissue and interact with healthy and cancerous cells is a complex, possibly insurmountable task. Therefore, such techniques might not be appropriate for predicting the outcome of a treatment before actually administering it to the patient, making it unlikely that they can be used to optimise treatment.

Finding a solution is critical due to the possible life threatening side effects of chemotherapy which can include cardiotoxicity, hepatotoxicity and damage to bone marrow [139]. Such effects can limit drug dosage and can cause cancerous cells to develop resistance, mutating to adapt to their environment after repeated treatments [138], with potentially fatal consequences. Currently, chemotherapy treatments are often administered following rigid dose and schedule protocols, which are only changed in the event of cancer progression or unbearable toxicity for the patient [138]. Better analytical tools could illuminate the way towards optimal, patient-specific based drug protocols, which could replace the current approach, which essentially is based maximising, as opposed to optimising dosage in an attempt to avoid under-treatment.

## **2.8 Bridging the gaps**

Considering the mission and objectives of this thesis and the literature review carried out in this chapter it is considered that the following topics require further investigation:

- It is necessary to analyse systematically how the changes in the microstructure of soft tissues influence their properties at higher scales. This would allow measurements at organ scale (e.g. elastography, palpation) often done in clinical practice to be related to tissue condition, thus providing an invaluable tool for qualitative and quantitative

diagnosis. Such analysis will be carried out by investigating the mechanical properties of the tissue microstructures from various patients and at various length scales subject to different pathological conditions. This will provide a framework for qualitative tissue diagnosis (i.e. cancerous or healthy) with a certain degree of confidence. In addition, performing such analysis at different length scales could lead to an optimisation of the probe size and probed volume and therefore define the optimal probing parameters for novel diagnostic devices;

- Less invasive, palpation-based methods for soft tissue diagnosis have proved to be promising in detection of prostate cancer. However, quantifying the size and depth of the nodules in soft tissues using palpation is still challenging without *a priori* knowledge of quantitative information such as geometry and topology. To illuminate this, different approaches will be investigated- **i)** Sweeping palpation to determine the location, size and depth of hard nodules in soft matrices; **ii)** dynamic palpation to perform quantitative tissue quality assessment and; **iii)** quasi-static probing to determine the cancerous volume fraction in tissue. This paves the way for a less invasive, and, more importantly, quantitative characterization of the pathological stage.
- The importance of patient-specific modelling at various length scales is widely acknowledged, yet this is not often found in the contexts of prostate cancer diagnosis using palpation and treatment using drug delivery. A patient specific framework will be presented here to analyse the influence of inter-patient variation on the outcome of digital rectal examination. Furthermore, the importance of modelling certain components from the reconstructed MRI models will be discussed. The value of such work is that it can result in guidelines for the clinical and modelling communities on how they might optimize their procedures and computational efficiency, respectively.

- Different frameworks to analyse drug delivery into soft tissues have been proposed, but are often based on over-simplified geometries and do not consider critical patient specific features such as the microstructure or the blood vessel network. This lack of detail, coupled with the rigid, static medical protocols used for chemotherapy lead to suboptimal treatments of life threatening diseases such as cancer. To address this, a framework that combines a microstructural patient-specific model with a cell dynamics model will be presented to evaluate the efficacy of chemotherapeutic treatments *in-silico* before any drug is administered to the patient. The diffusivity of various drugs in soft tissues will be analysed in different patients and at various length scales.

This thesis will address the aforementioned four topics which, together, lead to a novel computational framework that can provide less invasive, quantitative and optimal solutions to soft tissue diagnosis and treatment.

# CHAPTER 3

## **A novel palpation-based method to detect hard cancerous nodules in soft tissues – the computational framework and experimental validation**

### **Contents**

---

3.1	Summary .....	30
3.2	2D computational models .....	31
3.3	Material characterization and validation .....	35
3.4	Nodule characterization: decoupling the size and depth.....	38
3.5	Quantitative characterization of cancerous nodules: 2D analysis.....	43
3.6	Feasibility study – tumour geometry .....	47
3.7	Experimental Validation .....	49
3.8	Concluding remarks .....	55

---

### **3.1 Summary**

Palpation has been successfully used for centuries as a diagnostic tool where the practitioner examines the tissue looking for lumps, changes in roughness etc. Recently the need of non-invasive, more effective early detection systems has led to the development of new medical devices that measure the force feedback during instrumented palpation. Recording the force feedback has various advantages such as allowing the analysis of tissue stiffness evolution over a certain period of time thus obtaining a quantitative diagnosis. Although this represents a significant progress over manual palpation, determining the size and depth of nodules in soft tissues still remains

challenging. Several techniques have been proposed to address this problem, however, they require *a priori* knowledge of the mechanical properties of the tissues (e.g. healthy and cancerous), the geometry of the organ and either the size or the depth of the inclusion. A further constraint of these techniques is that they are limited to cylindrical nodules.

This chapter presents a novel methodology using sweeping palpation that eliminates three of the limitations from most existing methods: the shape of the nodule can be unknown and even arbitrary and it is not necessary to know the size or depth of the nodule *a priori*. It is hoped that such methodology can be used to detect a wide range of diseases such as prostate or breast cancer. The chapter is organized as follows: first the existing methodologies in the literature are reviewed; the proposed methodology and validation procedure are then presented; finally the results of the numerical and experimental validation are shown.

### **3.2 2D computational models**

A 2D *in silico model* is used to demonstrate the feasibility of the proposed methodology, as shown in Fig. 3-1(a). It consists of a 100mm sided square domain with a cancerous nodule located inside. Indentation is performed at the upper surface at 40 equally spaced locations, with depths of 1, 5 and 10mm, respectively. It should be noted here that the number of indentations along the surface and the depths of indentation would be constrained in the clinical framework. A high number of indentation points would result in long, uncomfortable and expensive procedures. Similarly very deep indentations would result in discomfort or pain for the patient or even damage to the organ. Therefore a balance needs to be found between the optimal parameters for the test (i.e. deep indentation for low signal to noise ratio) and the limitations imposed by patient discomfort (i.e. duration of the test). The 10mm diameter probe used for performing such indentation is considered as a rigid body. A vertical displacement is applied on the indenter and the force feedback is recorded. The contact between the indenter and the tissue is considered

frictionless [109]. The bottom of the model is constrained to mimic an *ex vivo* experiment where the tissue sample lies on a flat testing platform [112, 121].

Similar to most biological tissues, prostate tissue exhibits certain viscoelasticity [40, 44], where its apparent stiffness depends on the loading rate [42, 44]. However, little data can be found in the literature since characterization of such rate dependent properties is rather difficult both *in-vivo* (due to patient discomfort, ethical requirements, patient specific anatomical features etc.) and *ex-vivo* (due to dehydration, cell death etc.). Compared to other biological tissues characterization of the mechanical properties of the prostate presents certain challenges. If the characterization is to be done *in-vivo* the rectal wall is a barrier if the transrectal approach is used. In the case of the transurethral approach the urethra would stop the direct testing of the tissue. Therefore invasive procedures where tissue is cut or destroyed would be required to directly test the tissue. However, they would represent a risk for the patient due to complications such as infections or urine retention after the procedure and therefore should be avoided. Nevertheless, under certain loading conditions, the mechanical behaviour can be considered elastic and modelled using an equivalent modulus, especially when the strain rate (or frequency in dynamic characterization) is very low or very high. In those cases the viscous component becomes negligible and the behaviour can be modelled using either so-called long-term or instantaneous modulus.

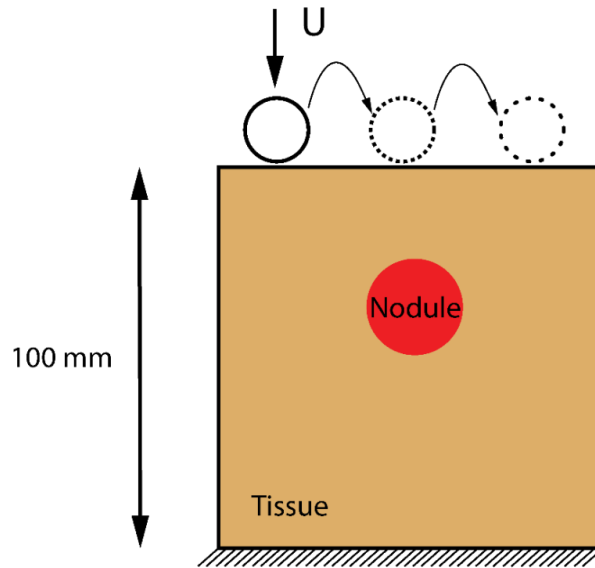


**Figure 3-1.** The 2D plain strain computational model. Plain strain is chosen for the 2D models since they represent better the experiments often done to characterize anomalies within soft tissues using palpation [43, 111].

This approach, which simplifies the experiments and simulations, has been widely used in the literature [112, 140]. However, some studies have shown that for large strains the elastic behaviour of the prostate may no longer be linear [13], which has also been modelled for tissue diagnosis purpose [115]. Table 3-1 summarises the values of elastic properties of prostatic tissue reported in the literature, where the wide range is due to inter-patient variations and different experimental conditions.

In this chapter, without loss of generality, healthy and cancerous tissues are modelled as incompressible homogeneous elastic materials, with Young's moduli of 20kPa and 40kPa, respectively. Such values are within the range often published as demonstrated in Table 3-1. The elastic behaviour of both tissues is fitted using the Levenberg-Marquardt algorithm with a second order Ogden strain energy density shown in Eq. 3-1 and finite strains are considered in the model solved in ABAQUS (Dassault Systemes, Vlizy-Villacoublay, France). The parameters used are shown in Table 3-2.

$$\Psi = \sum_{i=1}^2 \frac{2\mu_i}{\alpha_i^2} \cdot (\bar{\lambda}_1^{\alpha_i} + \bar{\lambda}_2^{\alpha_i} + \bar{\lambda}_3^{\alpha_i}) + \sum_{i=1}^2 \frac{1}{D_i} \cdot (J_{el} - 1)^{2i} \quad (3-1)$$



The material parameters to be fitted are  $\mu_i, \alpha_i$  and  $\bar{\lambda}_1, \bar{\lambda}_2, \bar{\lambda}_3$  are the principal stretches.

**Table 3-1.** Mechanical properties of the prostatic tissue reported in the literature.

Young's Modulus (kPa) Healthy Tissue	Young's Modulus (kPa) Cancerous Tissue	Poisson's ratio	Reference	Type of Study (C = Computational, E= Experimental)
12	200	0.499	[109]	C,E
30	90	0.495	[140]	C
16±5.7	40±15.9	0.49-0.5	[44]	E
3	19		[110]	C,E
41	135		[42]	C,E
10 ~ 29	11-38		[126]	E

**Table 3-2.** Parameters of the second order model used to model the mechanical behaviour of the healthy prostatic tissue and the cancerous nodule.

Tissue	$\mu_1$	$\alpha_1$	$\mu_2$	$\alpha_2$	$D_1$	$D_2$
Prostate	0.02119	2.244	-0.01120	-1.081	0	0
Cancerous Nodule	0.04238	2.244	-0.02240	-1.081	0	0

Four different geometries are considered in this study. First a geometry composed of two intersecting circles in different diameters is considered as shown in Figs. 3-2(a) and 3-2(b). This is to model a scenario where tumour nodules appear from two different locations or grow around the urethra [141]. Then an arbitrarily shaped tumour is considered to test the ability of the method to diagnose diffused tumour [141], as shown in Fig. 3-2(c). Additionally an interfacial layer between the nodule and the healthy tissue is included, as shown in Fig. 3-2(d), where a solid tumour is surrounded by a mix of healthy and cancerous islands. Such a scenario is often found in clinical diagnosis, where

it is difficult to draw a clear boundary between healthy and cancerous tissue without histopathological analysis. Finally, a rectangular tumour is considered in Fig. 3-2(e) as scenario comparable to the 3D one used for validation.

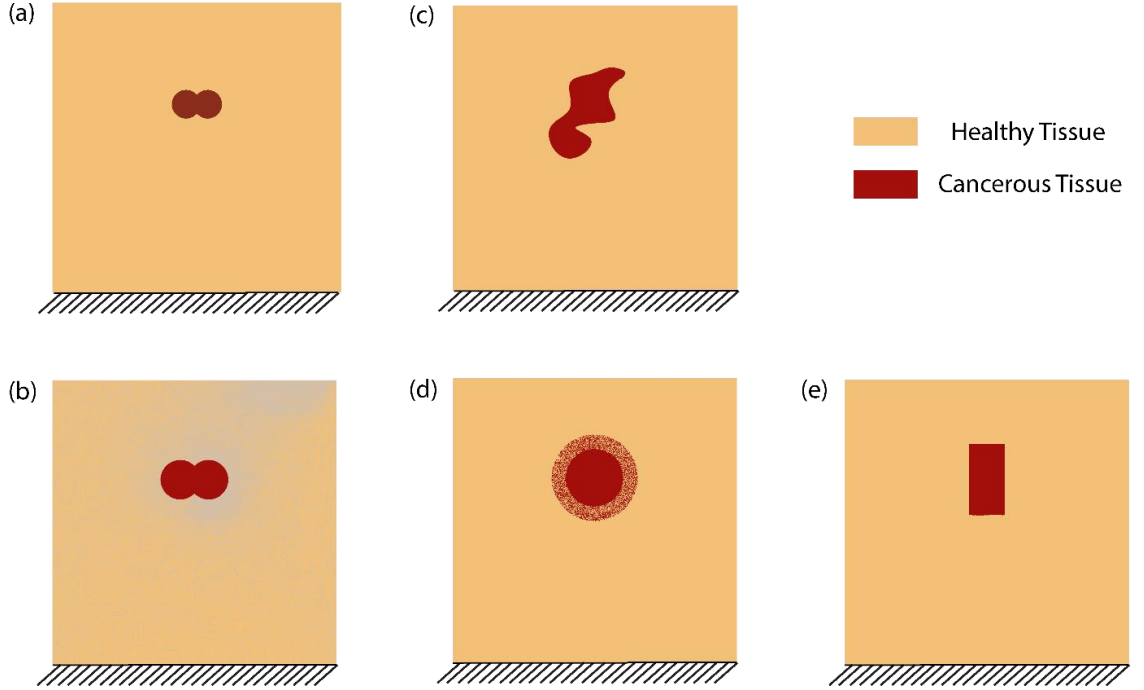


**Figure 3-2.** Different nodule topologies are considered to test the effectiveness of the proposed methodology. (a) and (b) are built from intersecting circle in different sizes; (c) tumour nodule is in a random shape; (d) represents a circular nodule of cancerous tissue surrounded by regions where the boundary between cancerous and healthy tissue is unclear; and (e) is an example comparable to the 3D validation test.

### 3.3 Material characterization and validation

A phantom made of gelatine which mechanically mimics the prostatic tissue is used to validate the proposed diagnostic framework. This material has been widely used for prostate surgery training [142] and ultrasound diagnosis [143] because of its similar mechanical properties to the prostatic tissue. To make the phantom a fixed amount of gelatine powder (36g) is mixed with different volumes of boiling water (e.g. 250ml for cancerous sample and 300ml for healthy) in a container. Red food colorant is used to dye the cancerous nodule to make it visible within the ‘healthy’ gelatine in light yellow. The mix is then slowly stirred to avoid bubble formation until it becomes transparent and homogeneous. After cooling to room temperature the samples are stored at 4°C for 18-20

hours. They are then removed from the container and cut into samples with dimensions of  $100(\text{length}) \times 31(\text{height}) \times 60(\text{width})$  mm. Before testing, the phantoms are left for 90 minutes to reach room temperature. To fabricate the phantom with the embedded tumour nodule a first layer of gelatine is created following the procedure described above. Before the gelatine completely solidifies, a cancerous nodule (20 mm long, 12 mm wide and 12 mm height) is placed in the middle of the healthy sample. The cancer volume results in  $2880 \text{ mm}^3$  which is within the range of nodule volume often found in prostate cancer patients[144]. It should be noted here that tumour shape is chosen so that it is relatively simple to manufacture and measure its volume so that it can be later modelled for numerical validation. The container is filled with liquid gelatine solution (i.e. healthy sample) and left to cool to room temperature. The surface of the cancerous nodule is located 10mm below the surface of the sample as tumours are often found near the posterior surface of the prostate[144]. Fig. 3-3(a) shows the positions where the samples are tested with an indentation system - Mach-1 V500css (Biomomentum Inc, Laval, Canada). Figs. 3-3(b) and 3-3(c) show the phantom where the ‘cancerous’ nodule (in red) is placed inside the ‘healthy tissue’.

A 10mm diameter hemispherical indenter as shown in Fig. 3-3 (a) is used to indent the phantom sequentially at each position (10, 30 and 50mm from the side), with three different indentation depths (i.e. 2, 4 and 6mm), respectively. The force feedback during a 150s relaxation test is used to characterize the long term modulus. It should be noted here that the number of indentation sites and the depths of indentation are chosen within certain constraints. The indentation sites must be separated using a sufficient distance so that the influence of inelastic effects such plasticity or long term viscoelastic behaviours, which are not considered in the finite element model, are negligible. In clinical practice this criterion would also reduce the testing time which would help to reduce patient discomfort and testing costs. The range of useful indentation depths is constrained by the

ability of the system to detect contact reliably with an adequate signal to noise ratio for small depths of indentation and by patient discomfort for large depths of indentation. In the case of this particular phantom a further constraint is that no damage can be caused so that the mechanical properties remain constant.

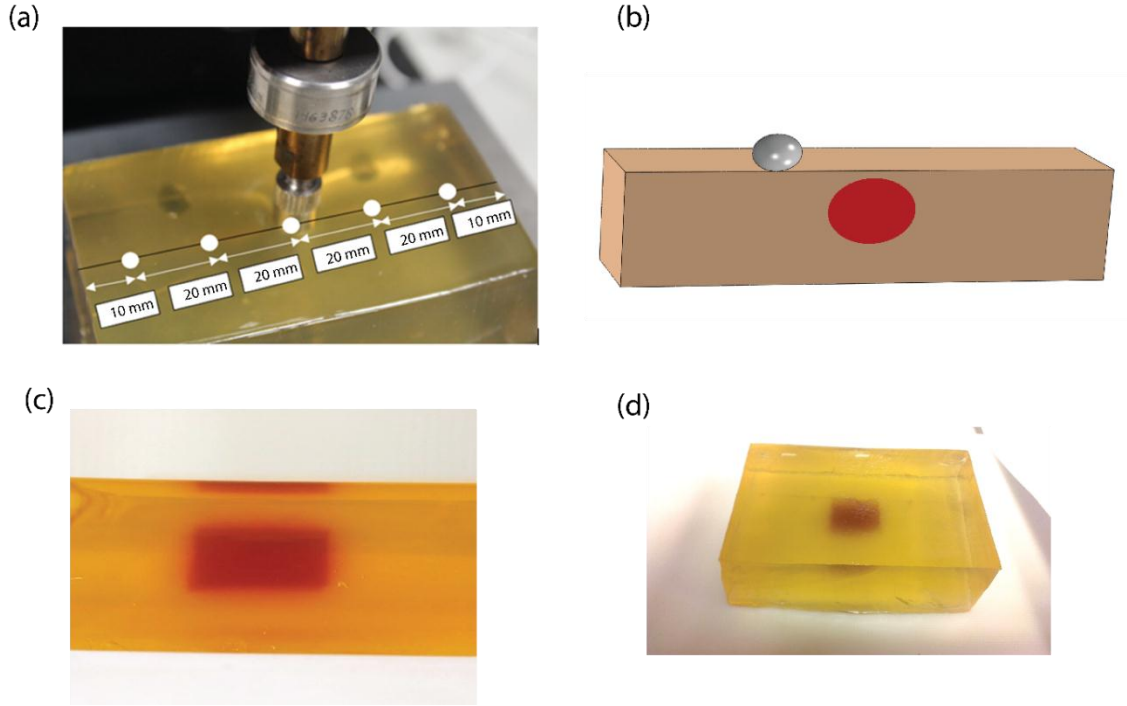


**Figure 3-3.** The tissue phantom and experimental set up. (a) The locations where palpation is performed. (b) The computational model of the palpation test with a circular nodule inside. A convergent mesh with over 300000 linear tetrahedral elements with hybrid formulation were used. (c) The nodule inside the phantom and (d) a view of the entire phantom.

Symmetry boundary conditions are considered and only half of the sample is modelled to reduce both the experimental and computational effort as shown in Fig. 3-3(b). In total 9 tests (i.e. using three different depths and three different indentation sites) are considered to fit the mechanical behaviour of the phantom. The indentation test is modelled with Abaqus (Dassault Systemes, Vlizy Villacoublay, France) using a material considered incompressible and neo-Hookean, for both mechanical characterization of gelatine and the proposed diagnostic framework. Because of material incompressibility, elements with hybrid formulation, where the hydrostatic pressure is also considered as a variable, are used. The material parameter  $C_1$  that characterizes the incompressible neo-Hookean

material model (Eq. 3-1) is obtained from the minimization problem in Eq. 3-2. which is solved using Levenberg-Marquardt's algorithm [145].

$$\Psi = C_1(\bar{I} - 3) \quad (3-1)$$

$$\min \sum_{depth=1}^n \sum_{pos=1}^m (F^{pos,depth}_{FEA}(C_1) - F^{pos,depth}_{Exp})^2 \quad (3-2)$$

Levenberg-Marquardt's algorithm is a non-linear least-squares method often used to fit experimental data to a given analytical equation. The algorithm is an improvement of the well-known Gauss-Newton non-linear least squares estimator shown in Eq. 3-3.

$$x_{n+1} = x_n + (J_f^T \cdot J_f)^{-1} \cdot J_f^T \cdot (y_i - f(y_i, x)) \quad (3-3)$$

where  $J_f$  is the Jacobian of the analytical function to be fitted,  $f(y_i, x)$ . The superscript  $T$  denotes the matrix transpose,  $y_i$  denotes each experimental observation and  $x$  is the optimal set of parameters to be found. To improve the algorithm's efficiency a modification is introduced so that larger steps are taken in the directions with lower gradients as shown in Eq. 3-4.

$$x_{n+1} = x_n + (J_f^T \cdot J_f + \lambda \cdot \text{diag}(J_f^T \cdot J_f))^{-1} \cdot J_f^T \cdot (y_i - f(y_i, x)) \quad (3-5)$$

where  $\lambda$  is the damping parameters that has to be chosen specifically for each problem and, in this application, it is fixed at  $10^{-6}$  which is proved to be both accurate and fast in benchmark tests.

### 3.4 Nodule characterization: decoupling the size and depth

The methodology proposed to determine the size and depth of a nodule is described in this section. It consists of two stages: nodule locating and nodule identification. To determine the location of the nodule it has been previously proposed [43, 109] to find the

location where the difference between the force feedback from the palpation and the force feedback from a healthy sample calculated, e.g. from a computational model, is maximum. It should be noted that this procedure only requires the force feedback at a single depth of indentation. However, as mentioned in the previous section, the force feedback would be recorded at multiple depths of indentation to allow, as it will be later explained, to determine the size and depth of a nodule. Although the force feedback curves are similar when far away from the nodule they become significantly different (leading to different curvature of the fitted force feedback curve) close to the nodule location, as shown in Fig. 3-4. It is hypothesized and later validated that such variations in the curvature of the force feedback profile can be affected by both nodule size and depth, thus making the diagnosis possible.

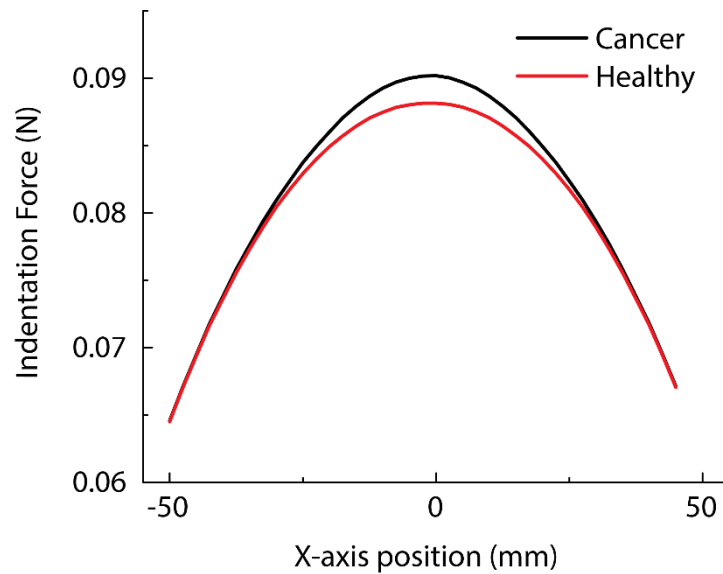


**Figure 3-4.** Healthy and cancerous force feedback profiles obtained during the palpation experiment using a 10mm deep indentation. The point where the difference is larger is used to locate the tumour.

Once the location of the nodule (i.e. along horizontal axis) is known the nodule characterization process starts. The proposed methodology consists of reducing the space of possible solutions until the solution is found. The first limitation to the solution space is the geometry of the sample (i.e. a spherical nodule cannot have a larger radius than the

organ itself), which is self-explanatory. The solution space is further reduced using the second derivative of the force profile obtained from computationally probing a set of benchmark samples at multiple indentations depths. Such *in silico* tests are carried out with circular nodules of different sizes located at different depths where the nodule is located. In each test the force feedback is recorded at different indentation depths (i.e. 1, 5 and 10mm), respectively. The second derivative (with respect to the indentation positions, i.e. horizontal axis) of the force feedback is then calculated from the force feedback data fitted using smoothing splines. The value of the second derivative at the position where the nodule is located (i.e. maximum force feedback) is plotted against the diameter of the nodule for different nodule depths at different indentation depths. Finally, the experimental value of the second derivative where the tumour is located is plotted against indentation depth in *in silico* models. The intersection points are then plotted in a depth-diameter diagram where that intersection indicates the depth and size of the nodule. For arbitrary nodule shapes, the proposed algorithm identifies the equivalent depth and radius of the circle (in 2D) or sphere (in 3D) that best represents the nodule (in terms of having equivalent force feedback). The equivalent radius of the nodule in 3D ( $R_{equivalent}^{3D}$ ) and 2D ( $R_{equivalent}^{2D}$ ) are defined as

$$R_{equivalent}^{3D} = \sqrt[3]{\frac{3 \cdot V_{nodule}}{4 \cdot \pi}} \quad (3-3)$$

$$R_{equivalent}^{2D} = \sqrt{\frac{A_{nodule}}{\pi}} \quad (3-4)$$

where  $V_{nodule}$  and  $A_{nodule}$  denote the nodule's volume and area respectively. Ideally the solution region would be a single point as shown in Fig. 3-5 (a). However, due to irregular geometries of the cancerous nodule and the prostate model, as well as the noise from computational and experimental tests, the possible solution space may not converge to a single point. In that case only an area of possible solutions (i.e. a few possible combinations of size and depth of the cancerous nodule) can be identified, as illustrated

in Fig. 3-5(b). Therefore instead of a single solution a few feasible solutions can be obtained using the proposed method. The proposed two-step diagnosis algorithm is summarized in Fig. 3-6.

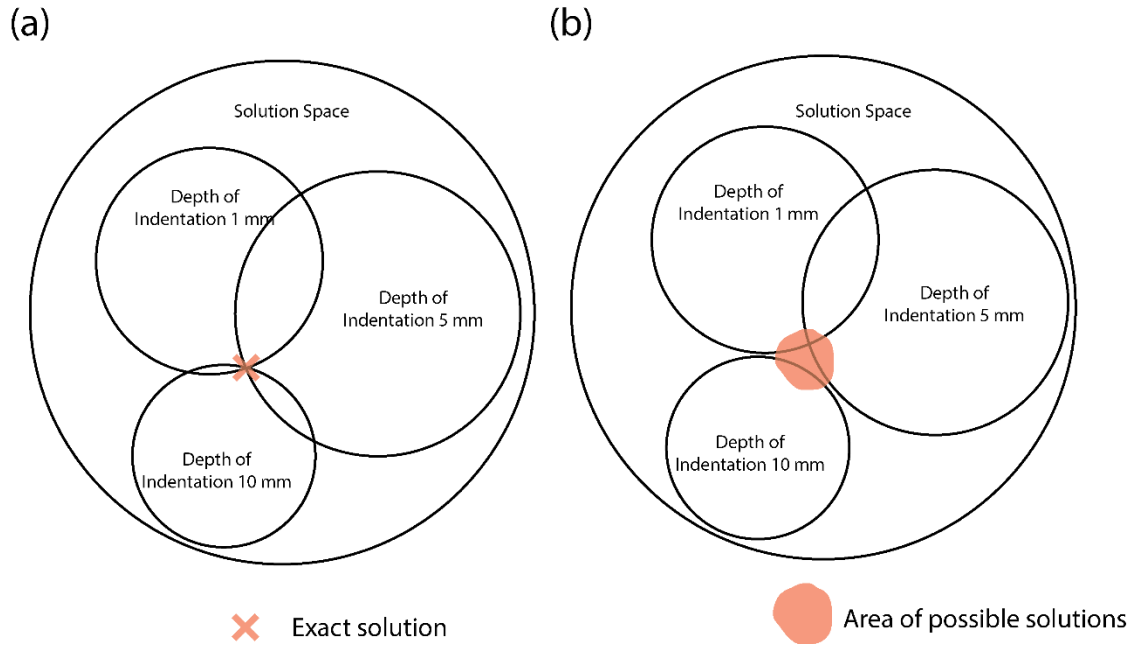


**Figure 3-5.** (a) Venn's diagram of the procedure to identify the depth and size of the proposed methodology. In this case a single point is found as a solution. (b) When the areas of plausible solutions do not converge into a single point it is considered that the solution belongs to an area close to the three circles.



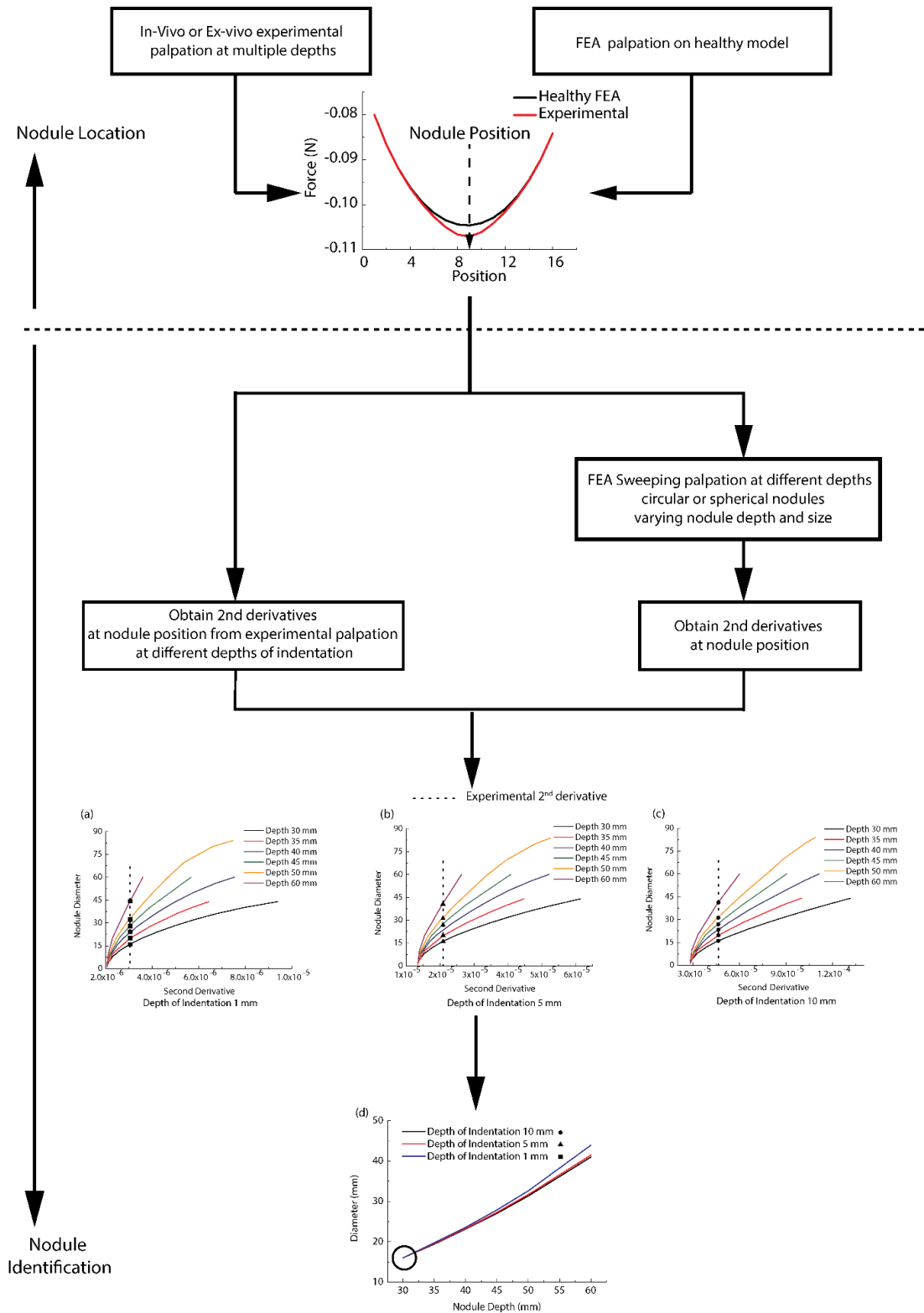


**Figure 3-6.** Schematic of the methodology proposed to identify depth and size of nodules in soft tissues. In the first phase the nodule is located comparing the force feedback with a computational one where the sample is considered to be healthy. The identification phase requires performing sweeping palpation at different depths of indentation and obtaining the second derivatives of the force feedback curves. The second derivative at the position where the nodule was located is then plotted against a set of benchmark simulations with nodules of different sizes located at different depths. The points where these curves intersect, which are represented by the symbols ■, ▲ and ● define a new set of curves that plotted in a Diameter-Depth graph allow to identify the size and depth of the nodule in the soft tissue.

### 3.5 Quantitative characterization of cancerous nodules: 2D analysis

The aim of this section is twofold. It is firstly shown that a single depth measurement is insufficient to determine the size and depth of a cancerous nodule in soft tissue. Then an example that demonstrates the proposed methodology to estimate the depth and size of a nodule without *a priori* knowledge of nodule location and geometry is presented.

One of the major challenges to identify the size and depth of nodules in soft tissue is that small nodules close to the surface subject to palpation would give similar force feedback to that of bigger ones located deeper inside. A parametric study with circular tumours with the maximum diameter allowable at each depth as shown in Figs. 3-7(a) and 3-7(b) is conducted to illustrate the coupling effect of size and depth (i.e. force feedback affected by both size and depth of the nodule). Such extreme scenarios allow to build the area of possible solutions for the force feedback. Fig. 3-7(c) shows the maximum force feedback ‘envelope’ obtained from such simulations for different combinations of tumour depth and size subject to indentations depth of 1 and 10 mm on top of the tumour. For any given force feedback the solution of the nodule depth and size is not unique- different combinations of the depth and size exist that result in the same force feedback as illustrated in Fig. 3-7. Therefore it is not possible to know the size and depth of the nodule from a measurement using just a single indentation depth. These results highlight a critical problem associated with such measurements, especially when the ratio between nodule diameter and nodule depth is low. Large tumours located deep into the prostate, whose progression could be faster and therefore have a worse prognosis, could be identified as a smaller, superficial, more benign tumour. This could lead to overestimate, or even worse, underestimate nodule size and therefore provide an inadequate diagnosis and treatment.

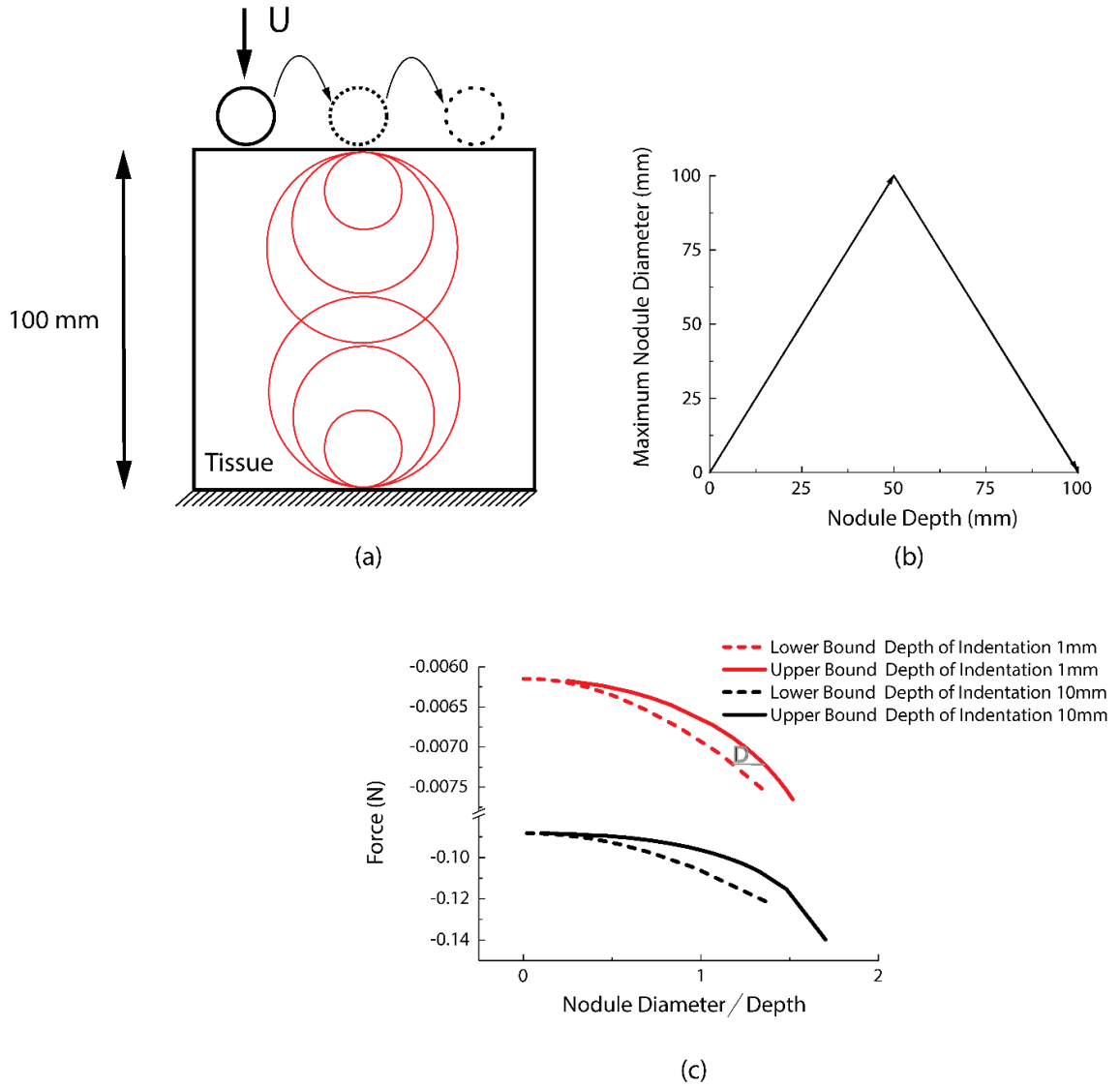


**Figure 3-7.** The limitations diagnosis based on analysis of force feedback from a single indentation are illustrated here. (a) Example of nodules used to determine the region of feasible force feedback in the palpation test. The possible combinations of nodule depth and sizes are represented in (b) and the arrows show the path of Nodule Depth and Diameter follow to build the aforementioned envelope. (c) The envelope of reaction forces for a depth of indentation of 1 mm and 10 mm is shown here. For any given force an infinite number of combinations of nodule diameter and depth exist, as shown in segment D, which result in the same force feedback.

Two examples are shown here to demonstrate the proposed methodology as shown in Fig. 3-8. First the location is identified at the point where the difference between measured force feedback and the force feedback calculated in a completely healthy *in silico* model is maximum. The second derivative of the force feedback is calculated and plotted against the second derivative of the force feedback calculated *in silico* for the benchmark tests as shown in Figs. 3-9 (a)-(c). Figs. 3-9(d) and 3-9(e) show the results of two examples that contain circular tumours in diameters of 16mm and 20mm located at 30 and 60mm depth,

respectively. It can be seen that all depth-size curves intersect at one point which indicates the predicted depth and size of the nodule.

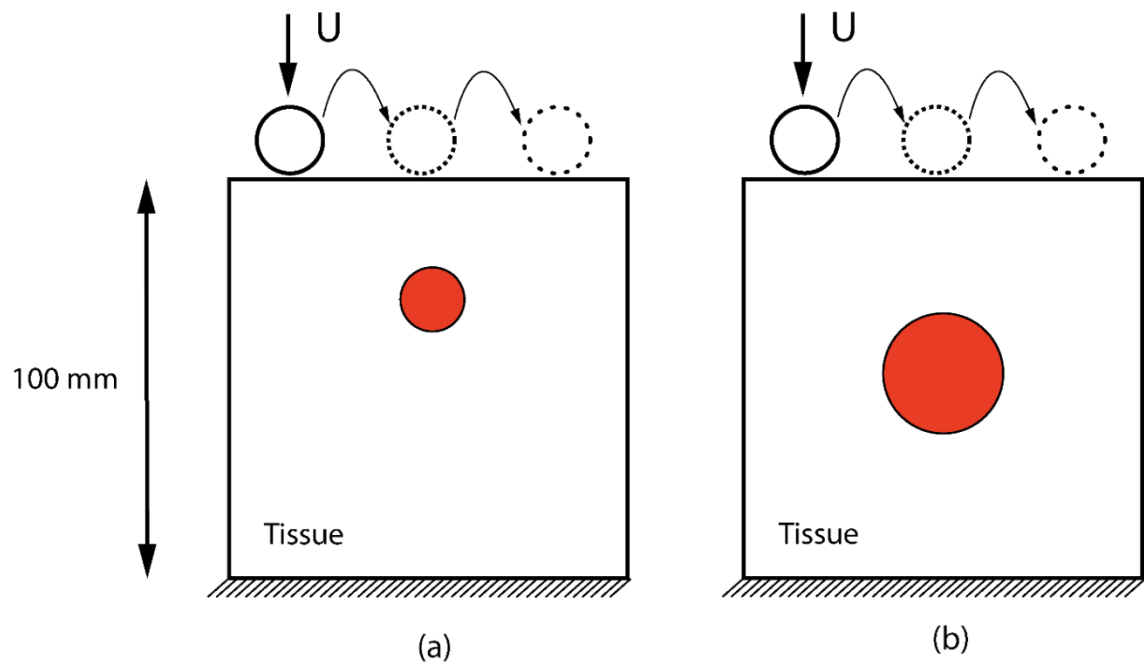


**Figure 3-8.** Two different scenarios are considered in this example with a 16mm diameter nodule located at 30 mm from the surface (a) and a 30 mm diameter one located at 50 mm from the surface (b).

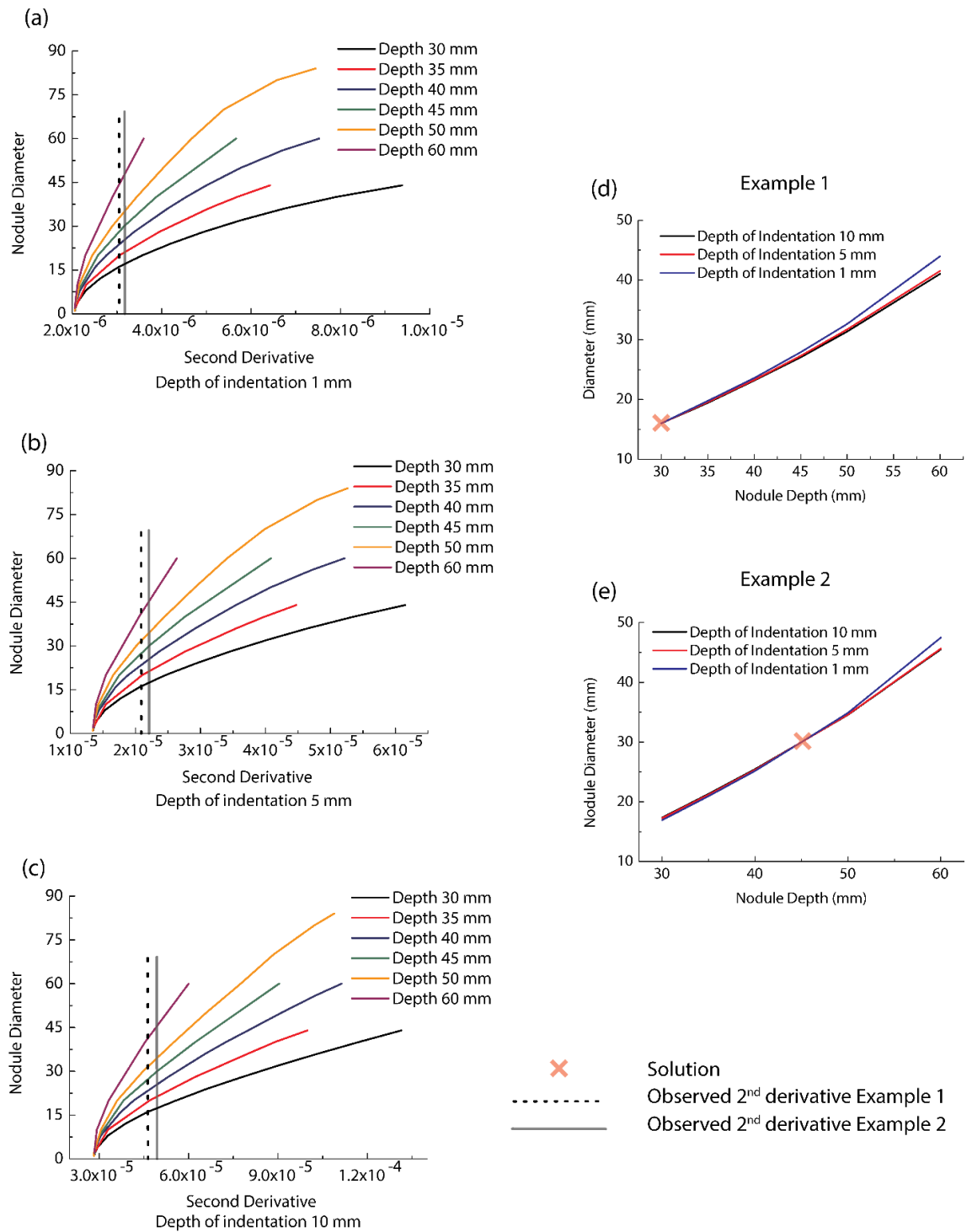


**Figure 3-9.** Diameter of the tumour against the second derivative of the force profile at the centre of the tumour for a depth of indentation of 1 mm (a), 5 mm (b) and 10 mm (c). The different depths of the tumour are 30, 35, 40, 45, 50 and 60 mm. The point of intersection is (30, 16). The diameter of the tumour was 16 mm and the depth 30 mm. (d). The point of intersection is (50, 30). The diameter of the tumour was 30mm and the depth 50 mm (e).

### 3.6 Feasibility study – tumour geometry

In this section the proposed methodology to determine the depth and size of cancerous nodules in soft tissue is applied to tumours with different, even irregular, geometries which are more relevant to what can be found in clinical cases. Figs. 3-10 (a) and 3-10 (b) show the results for the identification of nodules with shapes similar to those encountered in the prostate close to the urethra. The area is estimated with an error below 25% and the error drops below 13% if the equivalent radius of the tumour is considered to evaluate the results defined in Eq. (3-2). It is worth highlighting that the estimated depth is close to the centre of the circular inclusions. In Fig. 3-10(c) a nodule with an irregular shape, as often found in prostate cancer, is presented. In this example the area is estimated with a 10.23% error, demonstrating the applicability of the proposed methodology in diagnosis without *a priori* knowledge of the tumour geometry. In Fig. 3-10(d), another scenario is considered where the tumour boundary is not well defined. The tumour area and depth are underestimated in this case. However, such a scenario is uncommon in prostate cancer [141]. Finally, a rectangular nodule is considered and the error in estimation is 12.58%. The solution for these cases is obtained using three different depths of indentation: 1, 5 and 10mm to show how they intersect at a single point. Literature shows that most tumours have an irregular shape due to the ‘stochastic’ distribution and growing patterns, which has been attributed to the complex topology of the stroma in the gland of prostate [141]. It should be noted here that the proposed algorithm identifies depth and radius of the circle that best represents the nodule inside the tissue. The aim of this methodology is not to recognize multiple nodules, instead it rather aims at early diagnosis which often starts with the appearance of a single nodule. Motivated by the work presented in this chapter, methods to quantify the volume fraction of cancerous tissue will be further developed and presented in Chapters 4 and 5.

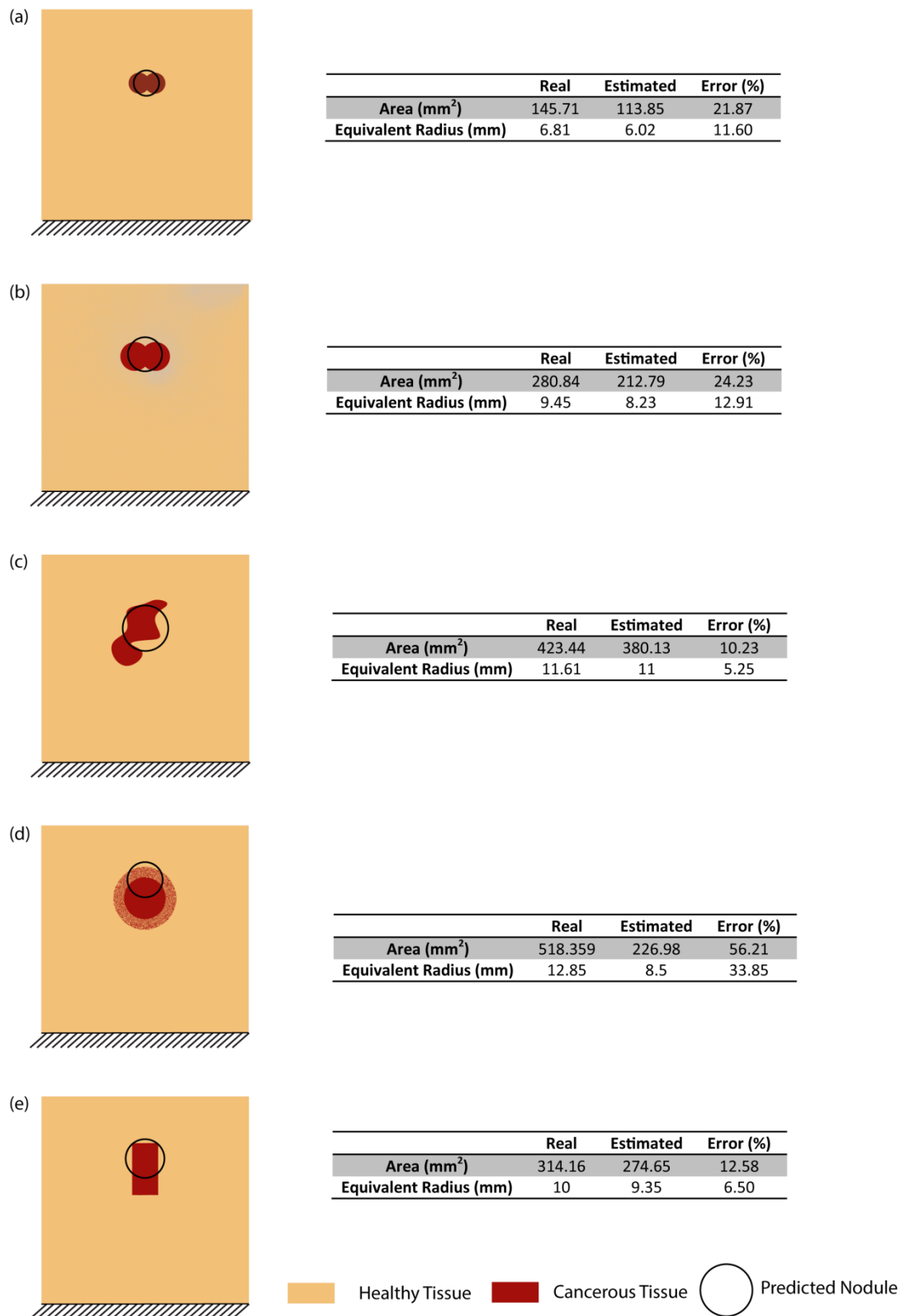


**Figure 3-10.** Summary of the 2D shapes used to test the proposed methodology and the estimated nodule depths and sizes. Convergent meshes were used with over 40000 linear quadrilateral and triangular elements to model the different scenarios. It should be noted that the volume of the nodule does not seem to play a significant role in the accuracy of the predictions.

### 3.7 Experimental Validation

In this section the methodology is validated with a gelatine phantom that mimics the mechanical properties of healthy and cancerous tissue. First the mechanical properties of the phantom which are required for the numerical models are obtained. Figs. 3-11 (a) and (b) show the force feedback obtained from the experimental palpation used to fit the neo-Hookean model which results in a Young's modulus of 28.1 *kPa* and 39.5 *kPa* for the healthy and cancerous tissues, respectively. The parameters estimated with the methodology aforementioned and the errors are shown in Table 3-2. It should be noted that the maximum fitting errors (16.7% and 18.45% for healthy and cancer respectively) occur in both cases at the middle point of the sample subject to the lowest depth of indentation. The influence of finding the contact in low depth indentations and especially in soft materials should be noted here. The deformation and force feedback during the contact-finding step may be comparable to the total deformation thus leading to a source of error.

Once the mechanical properties of the phantom are known, the process to identify the nodule size and depth begins. The force feedback of the sweeping palpation, where the cancerous nodule (20×12×12 mm located at a depth of 10 mm), is shown in Fig. 3-11(c) and compared with the healthy sample. It is necessary to note that the force feedback for the 2mm indentation is slightly higher for the healthy than for the cancer sample. This, as aforementioned, is attributed to the difficulties of robustly finding the contact in the indentation procedure. Such effect is less noticeable for cases using deeper indentation depths because the force feedback caused by the deformation is significantly larger than the forces recorded during the contact-finding step. This would be of critical relevance in clinical diagnosis and imposes a further constraint to the methodologies used to diagnose, especially during surgery when blood clots or other debris may complicate finding a robust contact detection. The next step to identify the nodule depth and size is to fit the



force feedback from the sweeping indentation with a smoothing spline and obtain the second derivative.

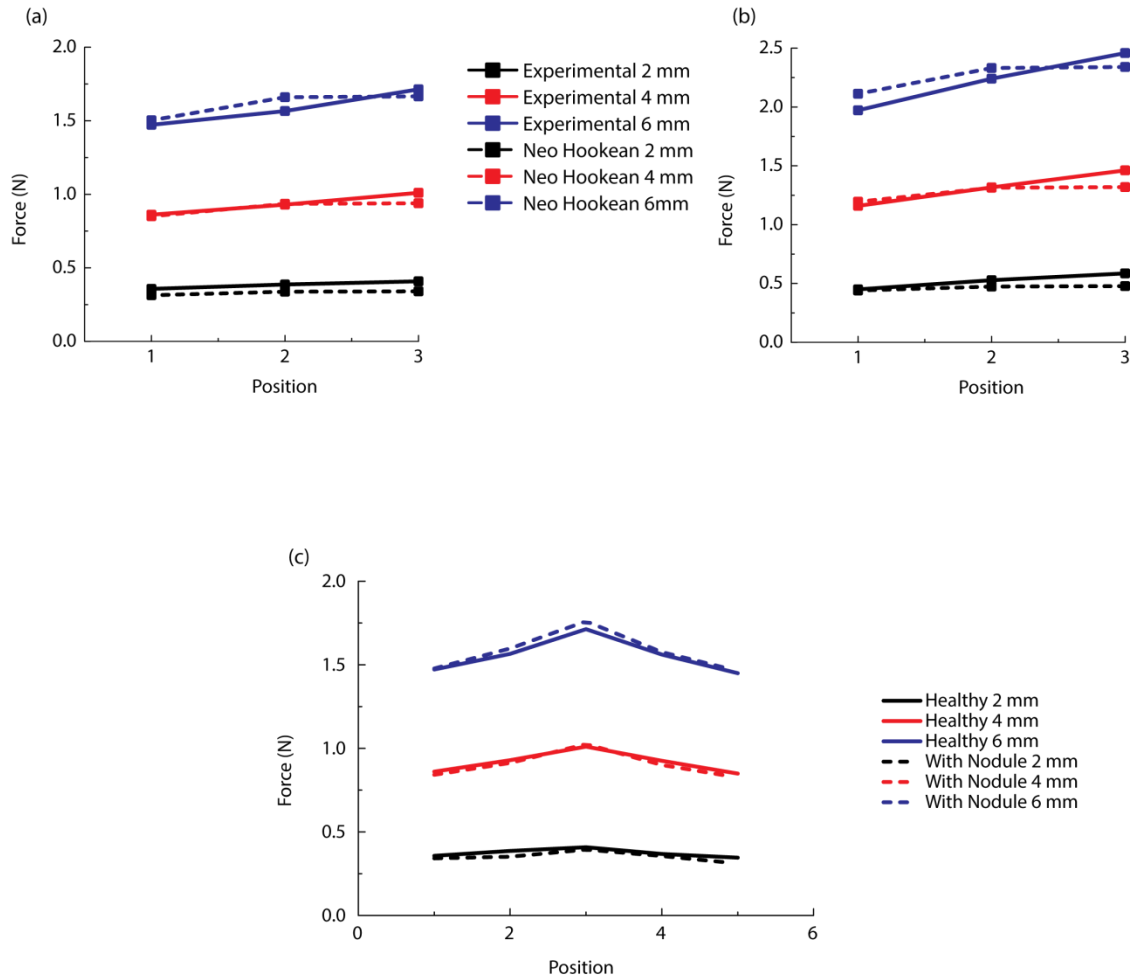


**Figure 3-11.** Results of the sweeping palpation in the healthy (a) and cancerous (b) samples and the fitted neo-Hookean model. Comparison of the healthy sample and the sample with a nodule embedded (c).<sup>1</sup>

**Table 3-3.** Results of material model characterization for the healthy and cancerous material phantoms when the units used are Newtons for force and millimeters for length and E is the Young's modulus

	C1	Max Error	Min Error	Mean Error	E (kPa)
Healthy	4.6898e-3	16.7%	0.6%	6.82%	28.1
Cancer	6.5872e-3	18.45%	0.22%	6.65%	39.5

<sup>1</sup> The palpation experiment shown here was performed by Mr Nasim Mammadov as part of his 4<sup>th</sup> Year undergraduate project, of which I am a co-supervisor. I designed the experiments so that the results were reproducible *in silico*.

By comparing the healthy and cancerous force feedback from the sweeping palpation, the tumour nodule is calculated to be in position 3 as shown in Fig. 3-11 (c). The next step consists of performing multiple *in silico* sweeping indentation tests with spherical nodules of different sizes located in position 3 (i.e. the centre of the sample) at different depths (in this example 4, 8, 9, 10, 11 and 12 mm nodule depths are considered). The second derivative of the computed force feedback is then plotted in Figs. 3-12 (a), (b) and (c) for depths of indentation 2, 4 and 6mm respectively. It should be noted here that the number of nodule depths considered for the benchmark tests is arbitrary. Increasing the number of depths chosen would result in an increased resolution of the diameter-depth figures (e.g. Figs 3.12 (a) and 3.12 (b)). However, the associated computational cost would significantly increase. Regarding the number of indentation depth used a similar situation is found. Increasing the number of indentation depths would result in improved accuracy with increased computation time. Therefore it is necessary to find a balance between accuracy and the applicability of the method in clinical practice where time constraints are imposed, among other, by the cost of examination. In this particular application using 6 nodule depths and 3 depths of indentation was enough to define the solution area.

In contrast to the results obtained with the spherical tumours in Section 3.5, the lines in the depth-radius figures do not intersect at one point. In this example two possible solution regions, highlighted in grey circles, are obtained where the three curves get closer as seen in Fig. 3-12(d). An average of such solutions is used as the prediction of the nodule depth and size. This leads to an estimated radius of 9.05mm, depth of 10mm, and volume of  $3115.1 \text{ mm}^3$ . For comparison the original volume of the ‘cancerous’ gelatine is  $2880 \text{ mm}^3$  therefore the error is 8.16%. It is important to remark some sources of uncertainty in numerical modelling. To reduce the computational cost, only a few benchmark scenarios (i.e. different depths and sizes of circular tumours) are modelled, and the results in the 2<sup>nd</sup> derivative-radius graphs interpolated linearly. Therefore, certain sensitivity in the

obtained depth and size is expected. For instance, at depth 11mm the three lines also get close. If that point is used, i.e. nodule radius of 10 mm, the nodule volume of 4188 mm<sup>3</sup> would be overestimated by 45%. If the lines do not intersect in a single point or do not intersect, the solution point is chosen as that point where the curves in the nodule radius-nodule depth diagram become closer. When multiple solution points are identified then the average of such solutions could be considered as the predicted nodule depth and size.

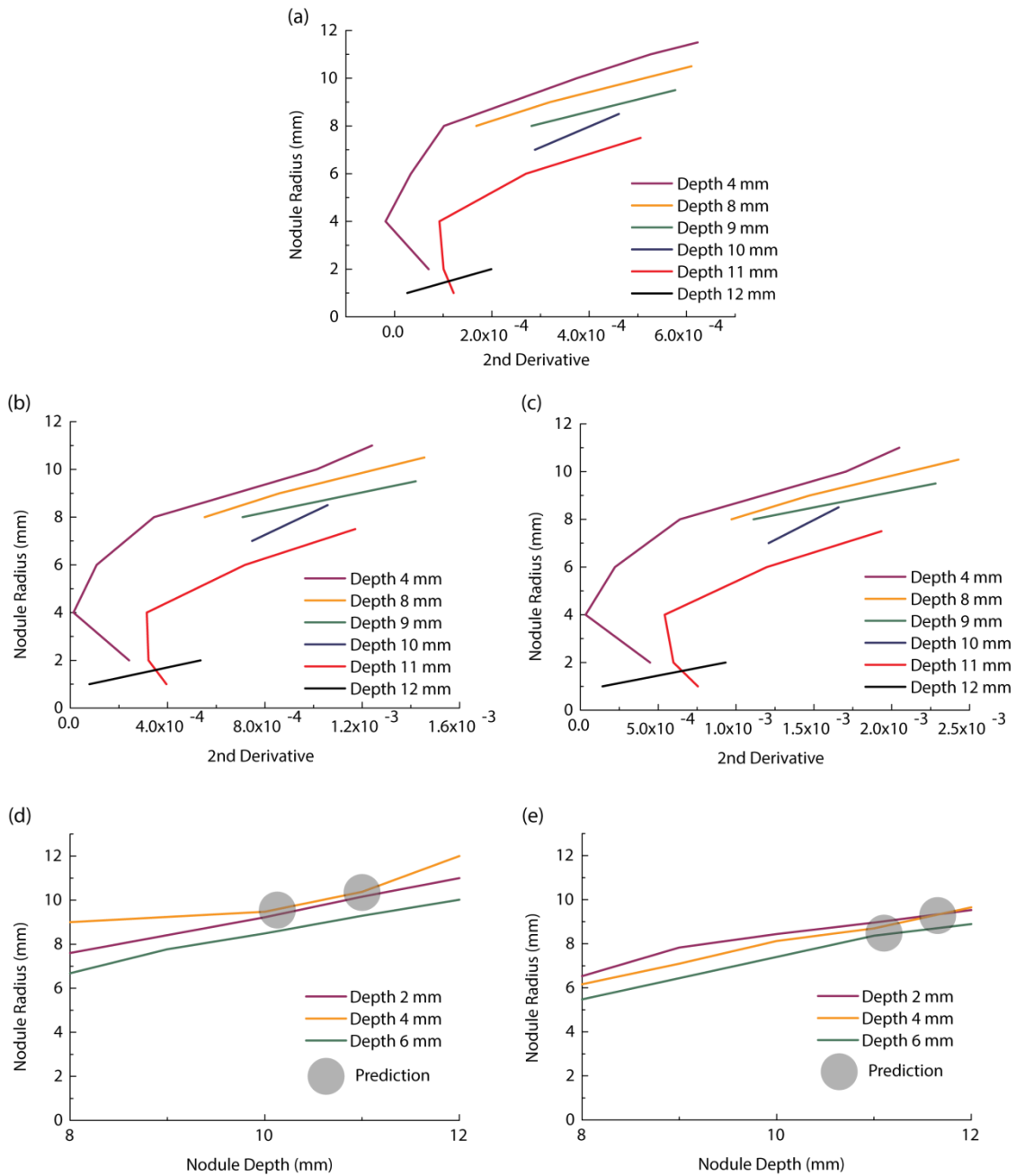


**Figure 3-12.** (a), (b) and (c) show the results for the second derivative obtained with computational simulations where nodules of different sizes are located at different depths (4, 8, 9, 10, 11 and 12 mm). (d) and (e) show the nodule depth and size identification in the real and simulated model respectively. It should be noted here that the prediction areas should be considered areas that provide the approximate depth and size of the nodule. The accuracy of the predictions will depend on a number of factors including the uncertainty during the characterization of the mechanical properties, the spatial resolution of the indentation procedure, which depends mainly on the number of indentations performed on the surface of the sample, and the number of computational benchmark tests used. As mentioned in section 3.2. the depths of indentation used are arbitrary; however it is limited by the signal to noise ratio for low depths of indentation and by patient discomfort and pain management for large depths of indentation.

To summarise, different sources of uncertainty can be identified in the examples presented here. First, the inaccuracy in finding the contact point (i.e. when the indenter

‘feels’ the contact) leads to, to a certain extent, inaccurate measurement of the indentation depth. Secondly, in the *in silico* model the contact is considered frictionless, however it has been showed that friction between the indenter and the tissue influences significantly the force feedback in indentation experiments [146]. Therefore this parameter should be examined on a patient-to-patient basis. Thirdly, in the validation experiment, tumour location is not perfectly accurate due to the nature of how the phantom is made. Furthermore, as aforementioned the limited number of indentation sites may introduce error since the fitting of the force feedback data becomes worse conditioned. Reducing the size of the indenter could be a possible solution but in that case other problems may appear such as rupture of the tissue/phantom or localized stress that reduces the testing area therefore making deeper nodules undetectable. Lastly, compared to previous work in nodule characterization [43, 109, 121], the ratio between the cancerous and healthy stiffness considered in this paper is lower, thus making the diagnosis even more challenging.

To eliminate the sources of error that the experimental set up introduces, a computational model of the sweeping palpation test is carried out to analyse the accuracy of the proposed methodology in a best case scenario without any of the uncertainty sources aforementioned, i.e. the indentation depth and the mechanical properties of the *in silico* phantom are obviously the same as in the computational models used in the benchmark tests. The identification results of such *in silico* model are shown in Fig. 3-12(e). A depth of 11mm is obtained for an equivalent radius of 8.6733mm which leads to a volume of  $2733 \text{ mm}^3$  and therefore an error of 5.1%. As in the previous case the reduced number of benchmark tests considered causes a relatively low number of points in the nodule radius- nodule depth graph. Therefore the resolution of the method is reduced. If the solution is considered to be depth 11.5 mm and radius 9.05 mm the estimated volume would be  $3104 \text{ mm}^3$  with an error of 7.78%.

### 3.8 Concluding remarks

Literature shows the need of a diagnostic algorithm to determine the depth and size of hard nodules in soft tissues using instrumented palpation. A methodology based on sweeping indentation and finite element analysis to characterize the size and depth of cancerous nodules without *a priori* knowledge of their topology was proposed in this Chapter. This methodology could therefore be used as a diagnostic tool in a great variety of tissues such as breast, prostate, liver, kidney etc., not only useful for primary diagnosis but also capable of providing real-time solution to the nodule characterization during surgical procedures. The methodology is validated using gelatine phantoms and both the size and depth of the nodule are estimated simultaneously. The methodology proposed here has certain limitations in its current form. First it is necessary to know the mechanical properties of healthy and cancerous tissues. Furthermore the magnitude of the errors caused by the uncertainties in tissue characterization needs further analysis. This can be problematic as it is subjected to inter-patient variation, i.e. patient-specificity. It is hoped to validate the methodology *in-vivo* once the instrumented DRE prototype becomes available.

## Quantitative tissue quality assessment through viscoelastic characterization using instrumented palpation

### Contents

4.1	Summary .....	56
4.2	Viscoelastic modelling and characterization.....	57
4.3	Finding the limits of dynamic characterization: the clinically significant range of testing frequencies.....	62
4.4	Sensitivity analysis: size, depth and position.....	65
4.5	An ex-vivo, patient-specific example .....	69
4.6	Concluding remarks .....	73

### 4.1 Summary

Qualitative and quantitative analysis of the elastic properties of soft tissue have been proven useful in clinical diagnosis as discussed in Chapters 2 and 3. However, the behaviour of most biological tissues has a viscous component which may change in the presence of various pathophysiological conditions. In this chapter a framework based on dynamic palpation for characterizing tissue viscoelastic properties as a diagnostic index of its pathological condition is presented. Compared to other methods that require parameters from different viscoelastic material models, a set of generalized and simplified parameters are adopted for quantitative tissue assessment. One of the main advantages of this methodology is it is less influenced by the depth of the cancerous nodule compared

to those methodologies based on elastic indexes. Therefore, it is not required to have *a priori* knowledge of tissue microstructure from e.g. histology. The methodology and its sensitivity are explored using 2D prostate models. The proposed method is then applied to a 3D model obtained from an MRI scan of an excised prostate. It is expected that this methodology can be applied to diagnose a wide range of diseases which influence the viscoelastic properties such as multiple sclerosis, cancer and liver fibrosis.

## 4.2 Viscoelastic modelling and characterization

The Zener model is one of the simplest rheological models for characterizing both creep and stress relaxation of viscoelastic materials and is adopted here to demonstrate the use of time constants in characterizing rate-dependent behaviour for quantitative tissue diagnostics. The model consists of a spring in parallel with a spring-dashpot series couple [51, 147], and its stress ( $\sigma$ )-strain( $\epsilon$ ) relationship can be expressed as

$$\frac{d\sigma}{E_2 \cdot dt} + \frac{\sigma}{\eta} = \left(1 + \frac{E_1}{E_2}\right) \cdot \frac{d\epsilon}{dt} + \frac{E_1}{\eta} \cdot \epsilon \quad (4-6)$$

where  $E_1$  denotes the stiffness of the single spring, and  $E_2$  and  $\eta$  the stiffness and damping coefficients of the spring-dashpot couple, respectively. When the system is subjected to a uniaxial dynamic force  $F=\sin(w \cdot t)$ , the stress  $\sigma$  is  $\sin(w \cdot t)/A$ , where  $A$  is the area,  $w$  the angular frequency and  $t$  the time. Eq. (4-1) then reads as

$$c \cdot \cos(w \cdot t) + b \cdot \sin(w \cdot t) = s \cdot \frac{d\epsilon}{dt} + a \cdot \epsilon \quad (4-7)$$

To simplify the notation:  $a=E_1/\eta$ ;  $b=1/(\eta \cdot A)$ ;  $c=w/A \cdot E_2$  and  $s=1+E_1/E_2$ . The solution of Eq. (4-2) becomes:

$$\epsilon(t) = K_1 \cdot e^{\frac{-E_1 \cdot t}{\eta \cdot s}} + P \cdot \sin(w \cdot t) + Q \cdot \cos(w \cdot t) \quad (4-8)$$

where



$$P = \frac{c \cdot s \cdot w + b \cdot a}{a^2 + s^2 \cdot w^2} \quad Q = \frac{a \cdot c - b \cdot s \cdot w}{a^2 + s^2 \cdot w^2}$$

And  $K_1$  is to be obtained from initial conditions. It is important to note that if a dynamic displacement is used as the input, then the resulting differential equation is symmetrical, i.e. the typology of Eq. (4-2) is the same except the values of  $a$ ,  $b$ ,  $c$  and  $s$  therefore the solution of stress to a relaxation test will be of the same form as Eq. (4-3).

Using Prony series, the transfer function of a viscoelastic material can be described as:

$$\sigma(t) = \int_0^t G(t - \tau) \cdot \frac{du(\tau)}{d\tau} \cdot d\tau \quad (4-9)$$

$$G(t) = 1 - \sum_{i=1}^n D_i \cdot (1 - e^{-\frac{t}{\tau_i}}) \quad (4-10)$$

which indicate that, to describe the behaviour of a viscoelastic material, it is necessary to know the stress history.

The mechanical properties of prostatic tissue are known to change in the presence of benign prostatic hyperplasia (BPH) and cancer [13]. For the sake of simplicity, mechanical properties of normal prostatic and cancerous tissue obtained from stress relaxation tests by Hoyt et al.[44] are adopted in this chapter. The relaxation curve is fitted using normalized Prony series as shown in Fig. 4-1, using least squares approximation with a sufficient number of points based on the Kelvin Voigt Fractional Derivative (KVFD) model [44]. The least number of terms in Eq. (4-10) to adequately fit the data is found to be two; using a single term only allows fitting to either short or long time but not both. Table 4-1 shows the corresponding viscoelastic parameters, where  $D_i$  and  $\tau_i$  are the constants to be determined in Eq. (4-10).

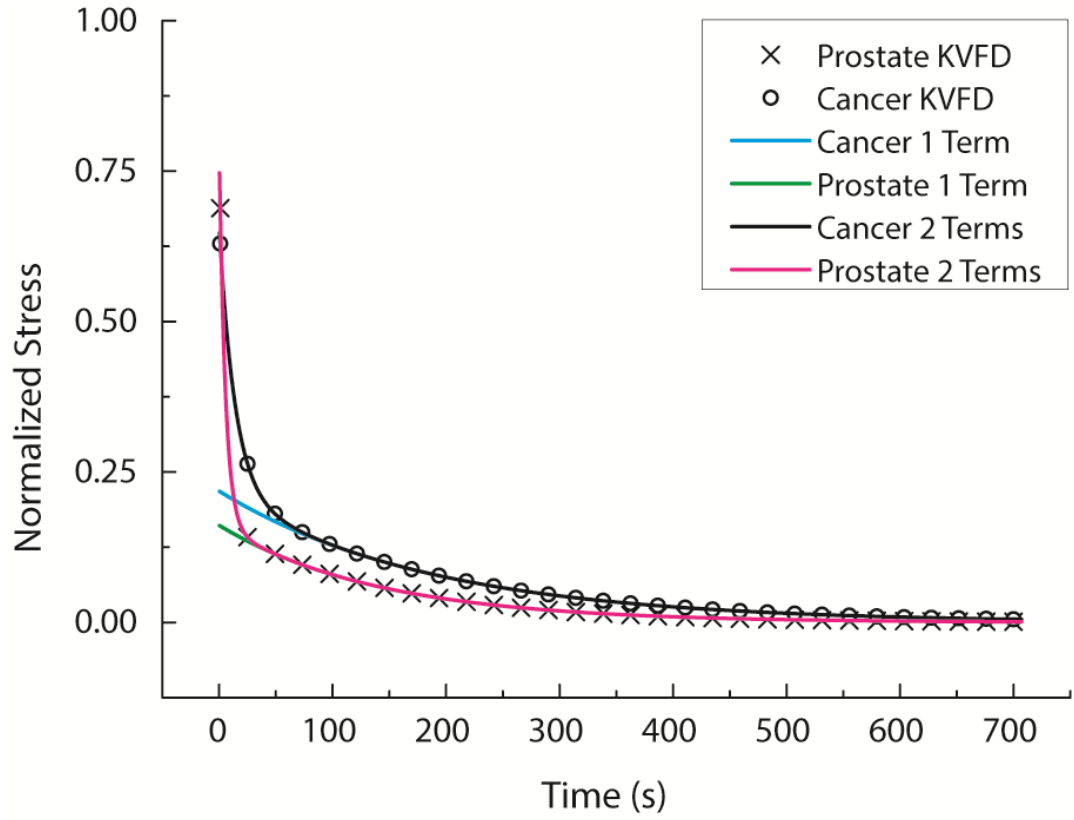


**Figure 4-1.** Prony series approximation of the normalized stress relaxation obtained from the model [44], using one or two terms. It can be observed that results using two terms present better fitting for both short and long term behaviours simultaneously.

**Table 4-1.** Material parameters for cancerous and healthy tissues fitted using Prony series.  $D_1/\tau_1$  are related to the short-time behaviour and  $D_2/\tau_2$  to the long-term.

	KVFD model [44]		Prony Series (Fitted)			
	$\eta$ (kPa · s $^\alpha$ )	$\alpha$	$D_1$	$D_2$	$\tau_1$ (s)	$\tau_2$ (s)
<b>Healthy</b>	$8.7 \pm 3.4$	$0.22 \pm 0.04$	0.4432	0.2182	13.87	187.6
<b>Cancer</b>	$3.6 \pm 1.3$	$0.23 \pm 0.03$	0.63337	0.16144	5.4981	140.63

Dynamic characterization of tissue viscoelasticity is usually performed by constructing phase and amplitude diagrams with respect to a range of frequencies and obtaining the parameters using a certain viscoelastic model [51, 148]. Alternatively, the storage and

loss moduli that relate to the elastic and viscoelastic components can also be obtained in the same way [143, 149].

In its simplest form, mechanical palpation involves imposing displacement as an input from an indenter and measuring the corresponding reaction force. Without loss of generality, a sinusoidal displacement with a compressive mean position is chosen so that separation between tissue and indenter can be minimized. A smoothed mean value of the force signal  $f(t)$  is obtained using a weighted local regression algorithm (LOESS) [150]. By fitting  $f$  with a series of exponential functions as described below, a set of parameters, i.e.  $a_i$ ,  $t_i$ ,  $b_i$ , can be obtained.

$$f(t) = \underbrace{\sum_{n=0}^{i-1} (a_n \cdot e^{-\frac{t}{t_n}} + b_n)}_{n \leq i-1} + \overbrace{a_i \cdot e^{-\frac{t}{t_i}} + b_i}^{n=i} + \underbrace{\sum_{n=i+1}^N (a_n \cdot e^{-\frac{t}{t_n}} + b_n)}_{n \geq i-1} \quad (4-11)$$

The parameters ‘ $a$ ’ and ‘ $b$ ’ are related to the material elasticity;  $b$ , in particular, being an index for the long-term elastic modulus. It should be mentioned here that the duration of palpation is critical in determining the reduced set of parameters. From Eq. (4-6) it can be seen that, for a given time of palpation, a specific time constant (i.e.  $t_i$ ) will predominantly influence the viscous behaviour of the material. Time parameters significantly higher than  $t_i$  (i.e.  $n \geq i+1$ ) can be considered constants since their behaviours over short testing time are indistinguishable from an instantaneous modulus. On the other hand, smaller time parameters (i.e.  $n \leq i-1$ ) will make the exponential term tend to unity which means those terms will be included in the behaviour described by the long-term modulus  $b_i$ . In both cases,  $b$  becomes an important index for apparent elasticity of the tissue.

A 1D model is created first to conduct theoretical analysis that allows a better understanding of tissue viscoelasticity in both transient and steady state. A sinusoidal displacement is applied at one end of the model, which is fully fixed at the other. The cross-sectional area is  $A$ , Young's modulus  $E$  and the length  $L$ . For the sake of simplicity, it is assumed in this section that the viscoelasticity of prostatic tissue can be modelled by a Prony series with one time constant ( $\tau_1$ ), which after normalization is given by:

$$E(t) = 1 - E_1 \cdot \exp\left(-\frac{t}{\tau_1}\right) \quad (4-12)$$

where  $E_1$  is the fraction of stiffness lost after complete relaxation. When subjected to a certain displacement, the reaction force is described as

$$\begin{aligned} F(t) &= \frac{A}{L} \cdot \int_0^t \left(1 - E_1 \cdot e^{-\frac{t-\xi}{\tau_1}}\right) \cdot \frac{d(\sin(w \cdot \xi))}{d\xi} \cdot d\xi \\ &= \frac{A}{L} \left( \sin(wt) - \frac{E_1 \tau_1 w \left( \cos(wt) - e^{-\frac{t}{\tau_1}} + \tau_1 w \sin(wt) \right)}{1 + \tau_1^2 w^2} \right) \end{aligned} \quad (4-13)$$

Once the steady state is achieved the mechanical behaviour is then governed by two oscillatory terms: a sine and a cosine, the latter of which accounts for the phase shift between input and output signals. The amplitude of the oscillations in steady state can be calculated as:

$$Amplitude = \sqrt{\psi^2 + \xi^2} \quad (4-14)$$

where  $\psi$  and  $\xi$  are the coefficients of the sine and cosine terms in Eq. (4-8) respectively, normalized with respect to  $E$ ,  $A$  and  $L$ . The phase shift is calculated as

$$\Delta\phi = \arctan \frac{\xi}{\psi} \quad (4-15)$$

Finite element models are created to demonstrate the effectiveness of the proposed method in quantitative tissue diagnostics. A 2D model representing a cross-section of *ex vivo* prostate sample, which is constrained at the bottom surface, is created first, as shown in Fig. 4-4. An indenter with a 10 mm diameter hemispherical tip is modelled as a rigid solid, to which a sinusoidal displacement is applied. The prostate palpation is then modelled in ABAQUS (Dassault Systemes, Vlizy-Villacoublay, France). The material behaviour is adjusted with a second order Ogden strain energy density function to mimic a linear viscoelastic material with an elastic modulus of 17 kPa for healthy tissue and 34 kPa for cancerous tissue. The mesh under the indenter is refined to allow a better solution to the contact problem and inertial effects are taken into account using a tissue density of 1000 kg/m<sup>3</sup> [151].

A 3D prostate model is also created to provide a more realistic evaluation of the proposed methodology. The model is based on a prostate specimen, excised using the laparoscopic radical prostatectomy approach, from a patient undergoing surgery for localized prostate cancer.<sup>2</sup> After removal of the prostate, a 7-Tesla magnetic resonance imaging (MRI) is performed on the fresh specimen, where a resolution of 0.31 mm in the sagittal and coronal planes and 1.5mm in the axial plane is adopted. In total, 44 images are obtained to reconstruct the 3D model using Scan-IP (Simpleware Ltd., Exeter, UK).

### **4.3 Finding the limits of dynamic characterization: the clinically significant range of testing frequencies**

Clinical tissue diagnostics is a major challenge due to various complex constraints such as time, available number of samples, patient discomfort and pathological conditions.

---

<sup>2</sup> This is to acknowledge Dr. Maurits Jansen and Mr. Ross Lennen from the Edinburgh Preclinical Imaging magnetic resonance imaging facility at the University of Edinburgh/British Heart Foundation (BHF) Centre for Cardiovascular Science, for performing MRI scans on the prostates used in this study.

Therefore, it is critical to select the optimal measures (such as phase-shift and/or amplitude), and to choose the optimal parameters, such as frequency and number of measurement points. The 1D dynamic analysis is carried out using different time parameters across the available frequency range in order to identify the optimal range of frequency over which a dynamic measurement should be performed. The range of frequency starts at 1Hz, since lower values would lead to excessively long examinations. The upper limit is determined by those which produce undesirable dynamic behaviour and, in the extreme, data loss due to indenter lift-off if the sample is unable to recover back to its original shape when the indenter retracts.

Fig. 4-2 shows the amplitude and phase response diagrams subject to a sinusoidal displacement over a range of frequency using various viscoelastic parameters. It can be seen in Fig. 4-2(a) that viscous behaviour is negligible at low frequencies and therefore the mechanical behaviour of the material becomes rate-independent. Under such conditions the behaviour can be characterized using the long-term modulus. Increasing the strain rate (frequency) increases the force amplitude and also the apparent stiffness until a plateau is reached. Materials with time constants  $\tau$  in the range of 1 to 10s exhibit primarily the instantaneous modulus when subjected to frequencies in excess of 1Hz. The range of frequency where viscoelastic behaviour of such materials exhibits is found to be between 0.001 and 1 Hz, as shown in Fig. 4-2. Therefore, the identification of the tissues which exhibit time constants consistent with the measurements of Hoyt et al. ( $\tau_{Healthy} = 5.49\text{ s}$  and  $\tau_{Cancer} = 13.87\text{ s}$ ) would need to be based on their (quasi-)elastic behavior since frequencies lower than 1Hz are not clinically practical. Such quasi-elastic behaviour can also be observed in the phase lag diagram shown in Fig. 4-2(b), which tends to zero in the range of higher frequency ( $> 1\text{ Hz}$ ). To distinguish materials using phase lag their time constants should be at least one order magnitude different. More importantly, to

observe a noticeable phase shift, the material needs to have at least one time constant in the range of 0.001s to 1s.

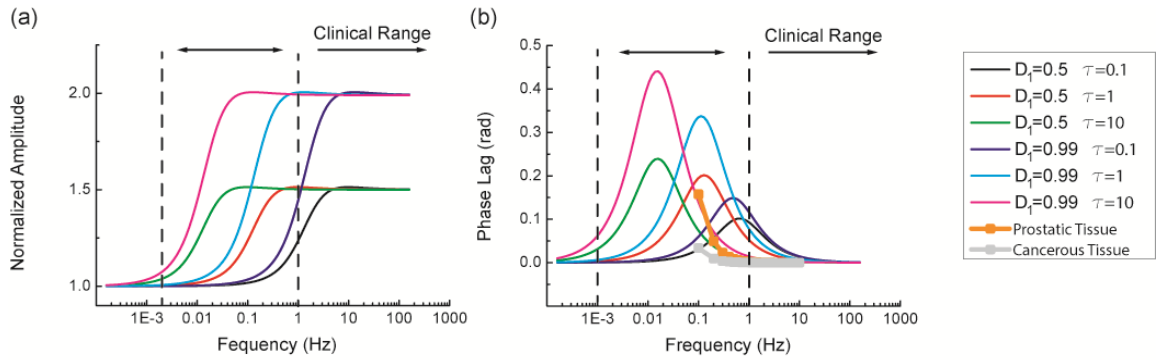


**Figure 4-2.** Mechanical behaviour of tissues with different viscoelastic parameters subjected to dynamic palpation. (a) Evolution of relative amplitude with respect to frequency; and (b) phase shift between displacement and force signals, where phase lag of prostatic and cancerous tissues are also shown.

Fig. 4-3 shows the amplitude and phase lag behaviour of the prostatic and cancerous tissue when the dynamic behaviour is fitted using a Zener model. The parameters of the Zener model are estimated by least squares fitting, using the quasi steady-state solutions to the reaction force from input (displacement) frequency at 0.1, 1, 10 and 100Hz for both Prony and Zener models. Fitting the results, which are shown in Table 4-2, over a wide range of frequencies allows characterization of the dynamic behaviour with a reduced risk of overfitting.

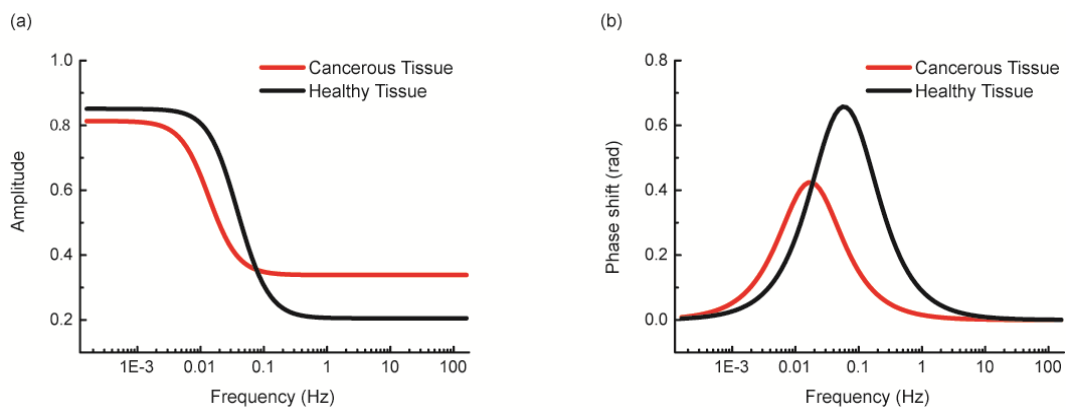


**Figure 4-3.** Amplitude and phase shift from Zener model using fitted parameters.

**Table 4-2:** Viscoelastic parameters of the equivalent Zener model.

<b>Zener Model Parameters (<math>R^2 &gt; 0.99</math>)</b>				
	$E_1(\text{N/m})$	$E_2(\text{N/m})$	$\tau(\text{s})$	$\eta(\text{N/m}\cdot\text{s})$
<b>Healthy</b>	1.175	3.6985	4.9538	18.3216
<b>Cancer</b>	1.2294	1.7239	10.2925	17.7432

The viscoelastic behaviour predicted by the Zener model is similar to that obtained using Prony series, where a quasi-elastic response is evident at the extremes of high and low frequencies illustrated by constant amplitudes and negligible phase lag. The transition between the two states can be considered as the range of frequency in which dynamic measurements of viscoelastic properties can be made. The parameter that dictates this behaviour is the time constant  $\tau = \eta/E_2$ , so it can be seen that the ranges that give good sensitivity in dynamic palpation run between 0.001 Hz and 0.1Hz for the case of amplitude and between 0.001 and 1Hz for the case of phase lag.

In this particular case, phase shift only becomes significant at frequencies below about 1Hz using parameters from Hoyt et al. [44]. In that case, unfortunately, the reaction force obtained will only depend on the long-term modulus and therefore only elasticity will be measured, losing most of the viscous information that the material presents.

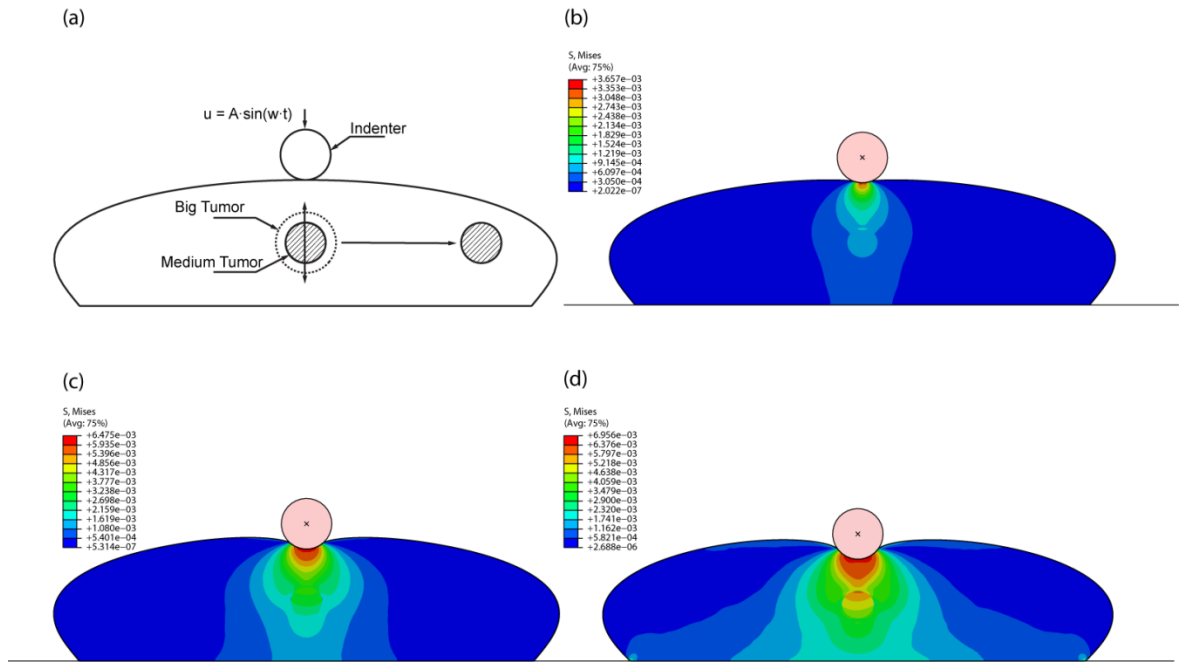
#### **4.4 Sensitivity analysis: size, depth and position**

In a practical application of tissue diagnostics using mechanical probing, it would be rather difficult to perform palpation across the entire surface. Therefore a grid of test points would normally be used to assess the accessible surface. It is useful to explore the



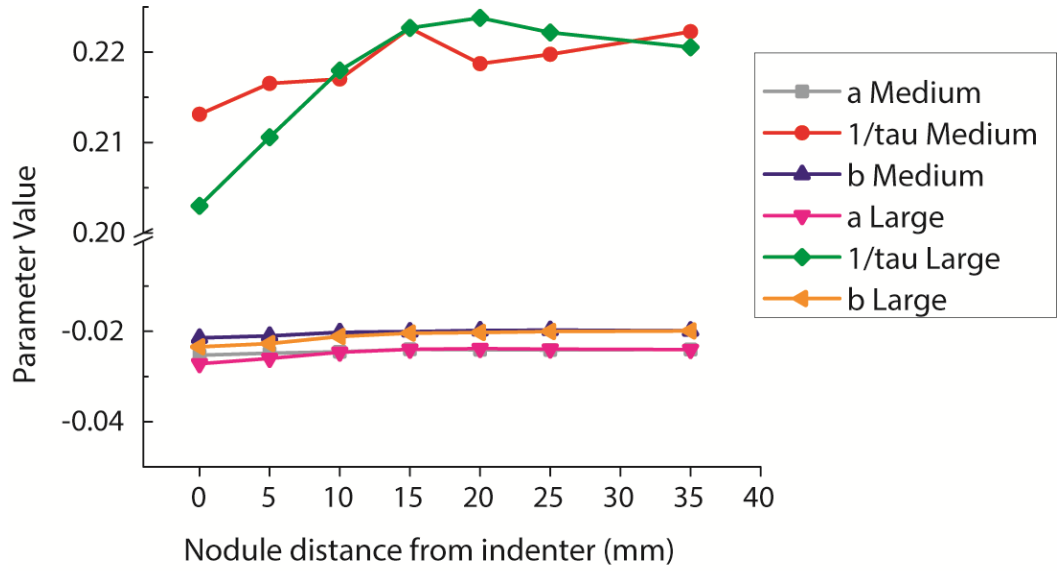
sensitivity of the proposed method with respect to various diagnostic indices, such as position, depth and size of the cancerous nodule.

In this section the proposed method is applied to a 2D model with a representative cross-section of prostate sample where size, depth and position of the cancerous nodule vary. The displacement is applied to the prostate through an indenter, as illustrated in Fig. 4-4, where stress distribution at different stages of indentation are plotted, including initial contact in Fig. 4-4(b), mean position of indentation in Fig. 4-4(c) and deepest indentation point in Fig. 4-4(d). The stress becomes higher underneath the indenter and around the cancerous nodule when the indentation progresses, leading to higher stress over a larger area and hence a higher reaction force, although there is a limit of how deep an indentation can be made before discomfort occurs. Increasing the mean depth of indentation for a given nodule size and position also increases the measured apparent stiffness,  $b$ , due to the increased strain and also the larger contact area of the indenter. Finally, excessively deep indentation could cause an artificial increase in the measured stiffness due to the mechanical constraint at the bottom.



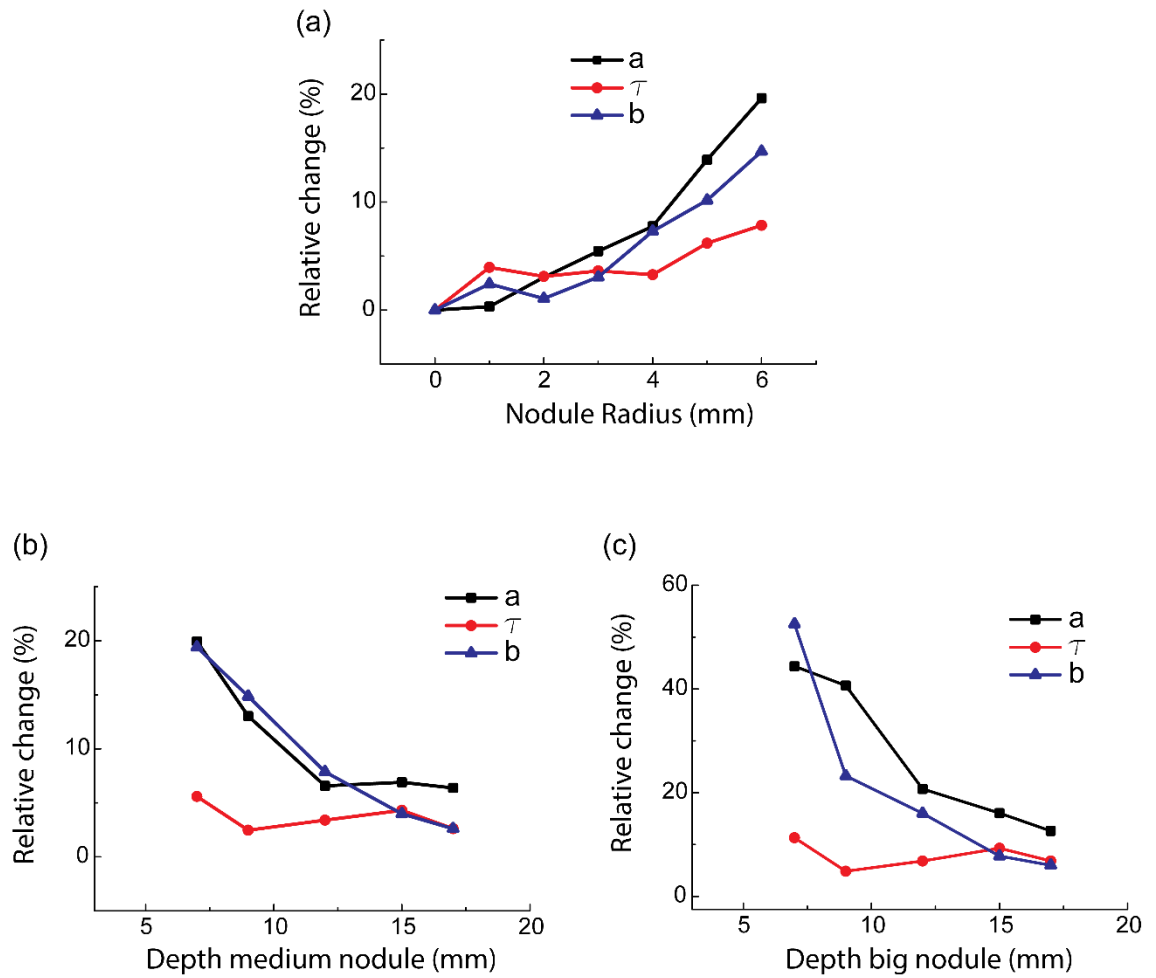
**Figure 4-4.** Sensitivity analysis of the proposed method. (a) Schematic diagram; (b) stress distribution when indentation occurs with a 2mm radius nodule located at the centre of the prostate 12.5mm below its surface; (c) at mean depth; and (d) at maximum depth. Unit of plotted stress is MPa. To obtain these results a convergent mesh with 33826 linear quadrilateral elements and 34277 nodes was used.

Fig. 4-5 illustrates the changes in viscoelastic parameters  $a$ ,  $b$  and  $\tau$  when two different sizes of nodule (large, 6 mm in radius, and medium, 4 mm in radius, both located at 12.5mm under the surface) shift horizontally in 5mm increments away from the indenter. The influence of nodule size to parameters ‘a’ and ‘b’ is smaller than with  $\tau$  and therefore they become less adequate for the purpose of diagnosis. As shown, there is little discrimination when the nodule is far away from the indenter, which is to be expected since the influence to the stress distribution caused by a distant nodule is small. Therefore, in order to assess tissue quality, a sufficient number of indentations needs to be used for lateral resolution/discrimination. This also constraints the spatial resolution of the procedure since, in practice, only a limited number of palpations can be done to avoid an excessively long procedure.



**Figure 4-5.** Sensitivity analysis for laterally-located nodules.

The effects of size and depth of the cancerous nodule is explored in Fig. 4-6, and found to be substantial on both parameters  $a$  and  $b$ . The depth and size of cancerous nodule are, in fact, coupled in the elastic response, which means that a smaller nodule close to the surface will lead to similar force feedback to a larger nodule located deeper inside. Therefore, the elasticity itself in this case is unable to discriminate between size and depth, although changes in  $\tau$  (from now referred as Tissue Quality Index or TQI in this chapter) remains less affected in both cases, which implies that using relative changes of both tissue elastic and viscous behaviours may lead to successful decoupling of depth and size of cancerous nodule, thus making quantitative diagnostics possible.



**Figure 4-6.** Sensitivity analysis: changing the depth, size and position of the cancerous nodule. (a) Evolution of model parameters when size of cancerous nodules varies. (b) and (c) show evolution of model parameters when depth of cancerous nodules varies in models with medium and big size nodule, respectively.

#### 4.5 An ex-vivo, patient-specific example

In this section the proposed method will be applied to a 3D prostate model shown in Fig. 4-7(a), which is reconstructed from an excised prostate with the cancerous nodule at the posterior side. The palpation area used in the model was at the posterior side of the prostate (to model digital rectal examination) and was sequentially indented at 8 sites as shown schematically in Fig. 4-7(b). These indentation sites were selected to maximize the area to be tested across the entire surface whilst maintaining good contact between indenter and prostate. The anterior surface was constrained to mimic the *ex vivo* boundary conditions during an actual mechanical indentation. Figs. 4-7(c) and (d) show the recorded

force in both healthy and cancerous samples and the fitted smoothed data used to determine the reduced set of parameters for tissue quality assessment. It is evident that the displacement and force signals are hardly distinguishable and the difference becomes negligible especially when steady-state is reached. This again indicates that only using phase shift and/or amplitude may not be sufficient for quantitative tissue assessment.

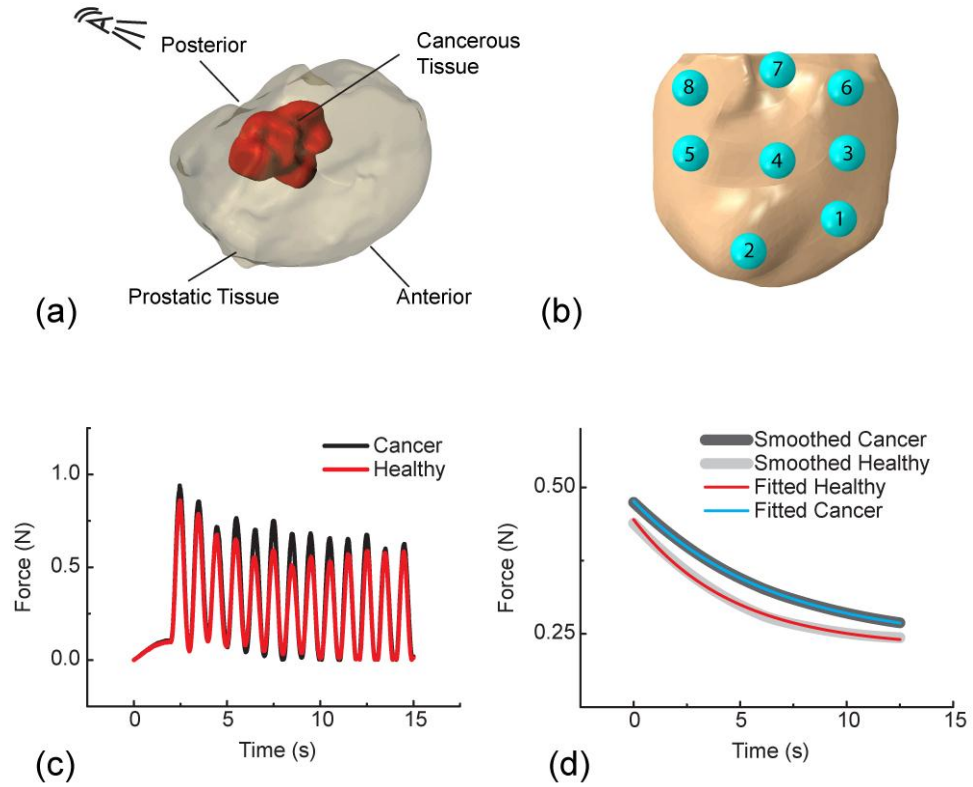


**Figure 4-7.** 3D prostate model obtained from the excised prostate specimen. (a) 3D prostate model from MRI scan; (b) 8 indentation sites at posterior surface; (c) Force feedback recorded during the indentation of the healthy prostate and the one with a cancerous nodule; and (d) smoothed data where viscoelastic parameters are fitted and obtained.

In order to examine the applicability of proposed method in 3D, two models are created here: one with cancerous nodule inside which has the same viscoelastic parameters used earlier in Fig. 4-4; another one which is fully healthy (i.e. material properties of healthy tissue assigned to the cancerous nodule). The resulting viscoelastic parameters (i.e.  $a$ ,  $b$  and  $\tau$ ) of the entire prostate are shown for both cases in Table 4-3. It is important to note here that, even in the healthy case, the reduced set of parameters does not remain constant at all probe points due to the curvature of the surface which changes the contact area and

hence tissue response in the tissue-indenter contact zone, thus the force feedback. Nevertheless, at probe points 5, 6 and 8, close to the nodule, the viscoelastic properties results in a stiffer and slower response (i.e. with higher time constant) than when the prostate is considered to be completely healthy. It is worth highlighting that, as shown in Fig. 4-8, the tissue quality index offers a unique capability of quantitatively characterizing the location and extent of cancerous nodules inside the prostate.

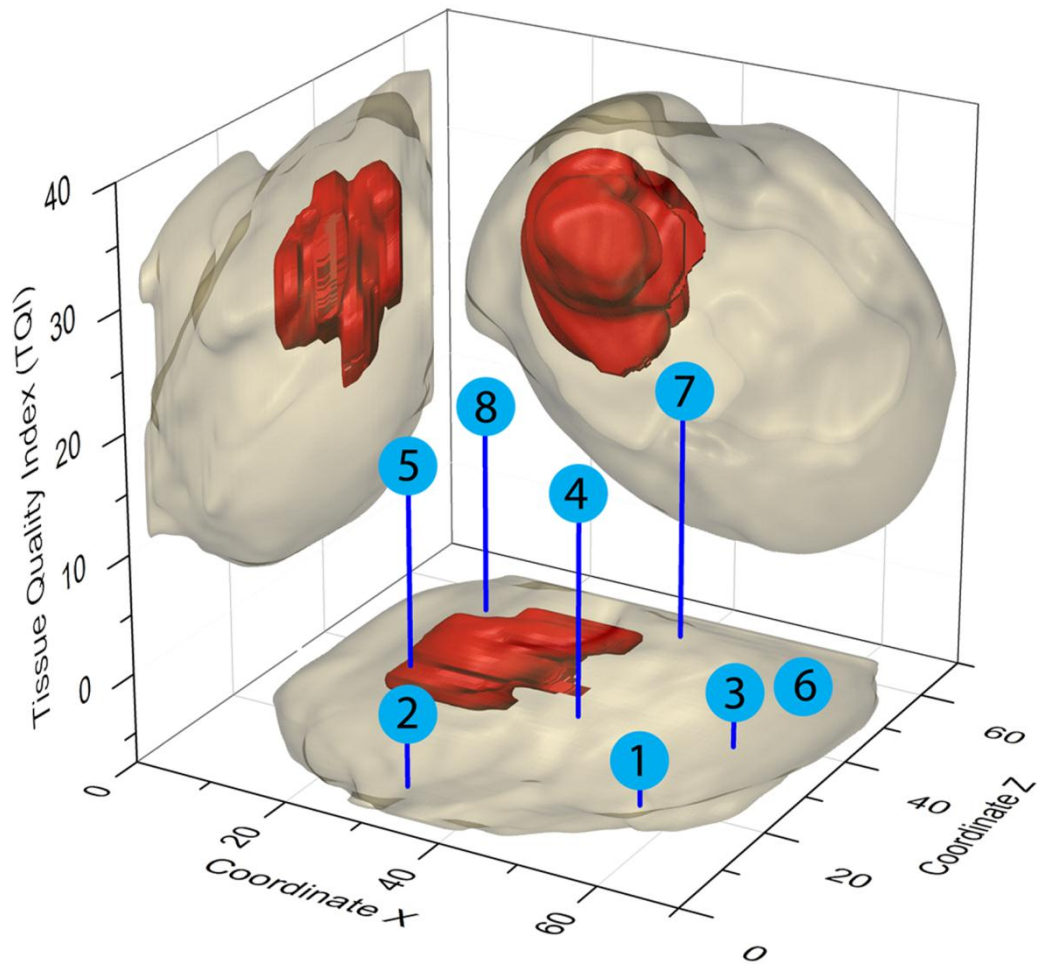


**Figure 4-8.** Tissue quality index (TQI) for the prostate with a cancerous nodule and the healthy one at 8 indentation sites. Convergent meshes with over 500000 linear tetrahedral elements were used to model the mechanical palpation

**Table 4-3.** Viscoelastic parameters of the healthy and cancerous prostate at 8 indentation sites. The parameter  $\tau$  serves as a better indicator of the tissue quality than  $a$  or  $b$ .

Position	Cancerous Prostate			Healthy Prostate			Relative Change (%)		
	$a$	$\tau$	$b$	$a$	$\tau$	$b$	$\Delta a(\%)$	$\Delta \tau(\text{TQI})(\%)$	$\Delta b(\%)$
1	0.30	5.88	0.35	0.30	6.25	0.34	1.52	-3.62	-2.04
2	0.31	6.25	0.31	0.31	6.67	0.31	0.06	-1.10	-2.23
3	0.29	8.33	0.27	0.29	9.09	0.26	1.32	-2.31	-3.51
4	0.37	5.88	0.42	0.36	5.26	0.41	-2.22	11.41	-1.33
5	0.26	7.14	0.44	0.25	6.67	0.27	-7.23	10.16	-38.35
6	0.24	7.69	0.25	0.25	8.33	0.24	1.55	-7.43	-5.04
7	0.31	6.67	0.32	0.28	5.88	0.31	-8.97	14.29	-3.96
8	0.25	8.33	0.27	0.23	7.69	0.22	-5.16	10.71	-16.96

#### 4.6 Concluding remarks

Based on the strong evidence from literature that the viscoelasticity of soft tissue is often affected by pathological conditions such as cancer, this paper used published data of viscoelasticity of cancerous and healthy prostatic tissue, to establish a novel framework of quantitative diagnostics for soft tissue based on its viscoelasticity using dynamic palpation.

The proposed method features diagnostic procedures that can be used to obtain elastic and viscous behaviours simultaneously, with the viscoelastic parameters being able to characterize the cancerous nodule, thus becoming a more reliable index for quantitative assessment of tissue quality. The method is illustrated in a 3D prostate model reconstructed from a MRI scan of an excised prostate specimen. It is shown that the change of viscoelastic time constant could be a key indicator for quantitative diagnostics of tissue pathological conditions, i.e. presence of cancerous nodule. It should be noted here that obtaining the mechanical properties of the healthy and cancerous tissue is a challenging task on a patient specific basis. Two approaches are proposed here. First a database with the mechanical properties of healthy and cancerous tissues for different age ranges could be created and used as benchmark values. To avoid the difficulties of obtaining the mechanical properties from *in-vivo* digital rectal examinations (i.e. patient discomfort, uncertainties caused by the rectal wall) the mechanical test could be performed, for instance, during surgery to remove the prostate. However, this approach would not be patient-specific and, therefore, would impact negatively on the accuracy of the methodology. Instrumented palpation offers the unique capability of recording the data from the patient over time. Therefore it would be possible to record and analyse the changes in the mechanical properties of the healthy tissue and use standard values for the cancerous tissue.



The method presented here has certain advantages in a clinical context such as reduced duration of examination and less invasiveness. Due to the reduced influence of tumour depth that the proposed methodology exhibits compared to the methodologies based on elastic indexes the method presented here could become useful to solve the curse of size and depth coupling. The proposed method is not limited to a particular material model or scale, thus becoming useful for tissue where defining a single time constant is not trivial. It is important to mention that the objective of this methodology is not to provide a detailed description of the viscoelastic behaviour. For that purpose frequency testing as well as stress relaxation should be undertaken. Instead this study aims at providing a methodology to identify the presence of cancerous nodule in the framework of tissue diagnostics.

Assessment of other pathological conditions, such as benign prostate hyperplasia (BPH) and prostatitis, will depend on their elastic properties and also the difference in viscoelastic time constant in comparison to healthy tissue. Selection of the indenter size and shape as well as indentation depth also requires further investigation to maximize the capability to assess tissue quality with sufficient resolution whilst still satisfying clinical constraints. Although the proposed methodology is a clear step forward in quantitative analysis of tissue quality, estimating the volume fraction of cancerous tissue in tissue still remains challenging and critical in clinical practice. A methodology to address such challenge will be presented in next chapter.

As it stands the proposed methodology has certain limitations. First healthy tissue is considered here as a homogenous media, however, certain heterogeneity is expected as shown in Chapter 7 which could introduce noise in the system thus hindering the diagnosis. That might be critical if the range of viscoelastic behaviours found in the healthy tissue overlapped with that of the cancerous tissue. Testing the proposed framework in more samples would allow a more in-depth analysis of the robustness of

the methodology. However, that is a complex task since obtaining MRI scans with the sufficient resolution is a complex and expensive task which is expected to be carried out in the future. A further limitation of this methodology for *in-vivo* prostate analysis is the presence of the rectal wall which, although thin, may influence the measurements. Testing of other organs such as the skin would not present such a challenge.

# CHAPTER 5

## **A novel method for rapid, quantitative, mechanical assessment of soft tissue for diagnostic purposes – a viscoelastic ‘*rule of mixtures*’**

### **Contents**

---

5.1	Summary .....	76
5.2	Effective viscoelastic properties 1D formulation.....	77
5.3	Tissue heterogeneity - quantitative cancer diagnosis.....	80
5.4	The rule of mixtures: 1D analysis .....	83
5.5	Parametric analysis: 2D heterogeneous materials.....	86
5.5.1	Effect of $t_{exp}$ .....	86
5.5.2	Effect of Young’s Modulus.....	86
5.6	Quantitative diagnosis of prostate cancer: a practical study .....	87
5.7	Concluding remarks .....	91

---

### **5.1 Summary**

Pathophysiological conditions such as cancer, sclerosis and inflammation have been shown to alter the tissue microstructure. Such changes influence the apparent properties of tissue and can be used for diagnostic purposes as demonstrated in previous chapters. Although different techniques have been proposed to detect anomalies within tissues using palpation, performing a quantitative estimation of nodules (e.g. volume and distribution) is still challenging and important for clinical diagnosis. It can be a particularly difficult task when procedures such as sweeping palpation, elastography or

MRI are not available. Various mathematical models have been proposed to estimate the apparent stiffness using the volume fractions of each phase and vice-versa. In particular some notable mathematical studies such as the Hashin-Shtrikman bounds have been found to effectively determine the space of apparent mechanical properties independently of the topology of each constituent. As discussed in the previous chapter viscoelasticity plays an important role in tissue diagnostics. Therefore, it could be of interest to determine the volume fraction of each phase (i.e. healthy and cancerous) in a tissue from the apparent viscoelastic properties. This would be relevant not only for quantitative tissue diagnostic but also for computational modelling of hierarchical viscoelastic materials. The methodology described in this chapter proposes that a creep or stress relaxation test of a biphasic material can be approximated by a biphasic simple system whose analytical solution is known. The problem is then reduced to finding the mechanical properties of a homogeneous material that mimics the behaviour of the heterogeneous one over a certain period of time. Solving such minimization problem for a number of volume fractions for each phase leads to a predicted ‘rule of mixtures’ between the apparent time constant and the volume fraction of each constituent. The methodology is further consolidated using histological samples of prostatic tissue with different nodule topologies and volume fractions.

## 5.2 Effective viscoelastic properties 1D formulation

A one-dimensional formulation of the rule of mixtures will be presented here to estimate the effective properties of heterogeneous viscoelastic tissue subjected to creep or stress relaxation over a specific range of time  $t_{exp}$  to determine one apparent time constant over that period by fitting a one term Prony series as shown in Eq. 5-1. A creep test simulation on a biphasic (e.g. healthy and cancerous tissues) rod with unit length is considered as shown in Fig. 5-1(a), the volume fractions of each material being represented by the lengths  $l$  and  $1 - l$ , respectively. Although a number of models such as KVFD [152],

Zener [10], power laws [153] and recruitment models [57] have been used to model the creep and stress relaxation tests of soft biological materials this paper describes the material viscoelasticity, without loss of generality, using a single-term Prony series:

$$E(t) = E_0 \left( 1 - D \cdot \left( 1 - e^{-\frac{t}{\tau}} \right) \right) \quad (5-16)$$

where  $E_0$  denotes the instantaneous modulus,  $\tau$  the relaxation time and  $D$  the fraction of stiffness loss over  $\tau$ . The displacement at the free end where a constant force  $F$  is applied is given by

$$u_{heterogeneous}(t) = \frac{F}{A} \left( \frac{l^c}{E_c(t)} + \frac{1 - l^c}{E_h(t)} \right) \quad (5-17)$$

where  $A$  is the cross-sectional area of the rod,  $l_c$  the length (fraction) of the cancerous material,  $E_c(t)$  and  $E_h(t)$  the instantaneous effective moduli of the cancerous and healthy materials, respectively. The displacement of the equivalent homogeneous system shown in Fig. 5-1(b) is

$$u_{homogeneous}(t) = \frac{F}{A \cdot E(t)_{homogeneous}} \quad (5-18)$$

To determine the effective properties of the homogeneous system, the Hill principle needs to be satisfied [154], i.e. the strain energy must be equivalent to that in the heterogeneous system.

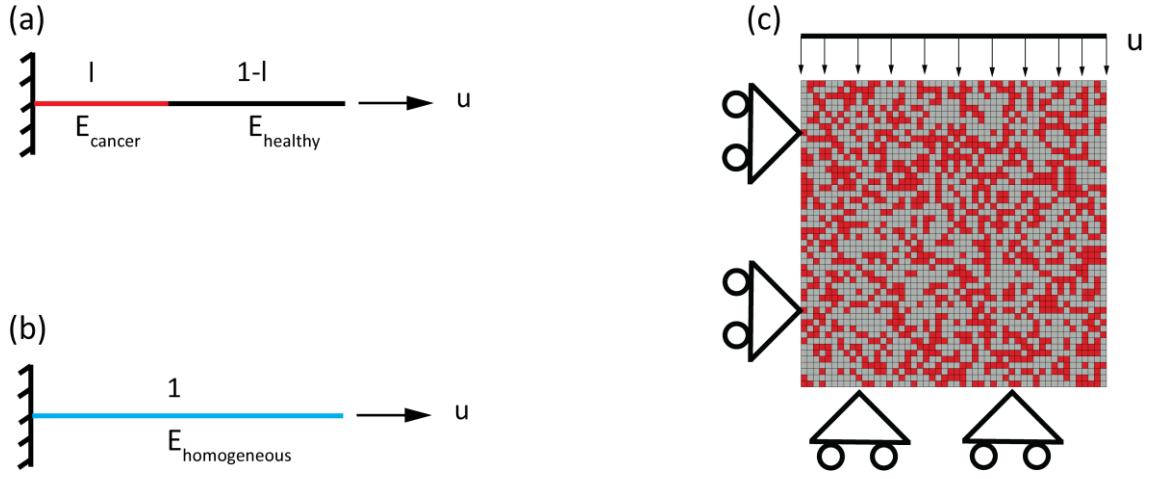


**Figure 5-1.** Illustration of the models used to derive and to test the framework. (a) Biphase heterogeneous viscoelastic material and (b) the equivalent homogeneous material. (c) shows the 2D heterogeneous viscoelastic material with a random distribution of cancerous tissue (red) with a volume fraction of 60%.

Since the stress is constant along the rod, the problem is then to solve the minimization of the difference between displacements at the free end of the heterogeneous and homogeneous systems over  $t_{exp}$ ,

$$\min \int_0^{t_{exp}} (u_{heterogeneous} - u_{homogeneous})^2 dt \quad (5-19)$$

where  $E_0, \tau$  and  $D$  are constrained to be positive. The proposed methodology assumes that the tissue behaviour is equivalent to a heterogeneous system whose analytical solution is known. The time of the experiment  $t_{exp}$ , however, needs to be chosen *ad hoc* - it depends on the mechanical properties of each constituent and the practical application (e.g. taking into account such factors as patient discomfort and examination cost). In the exemplar case described here, the integral in Eq. (5-4) was evaluated numerically using the trapezoidal method with a time step of 50ms, and the minimization problem was solved using a sequential quadratic programming algorithm. The flowchart for quantifying the volume fraction of each material is summarized in Fig. 5-2.

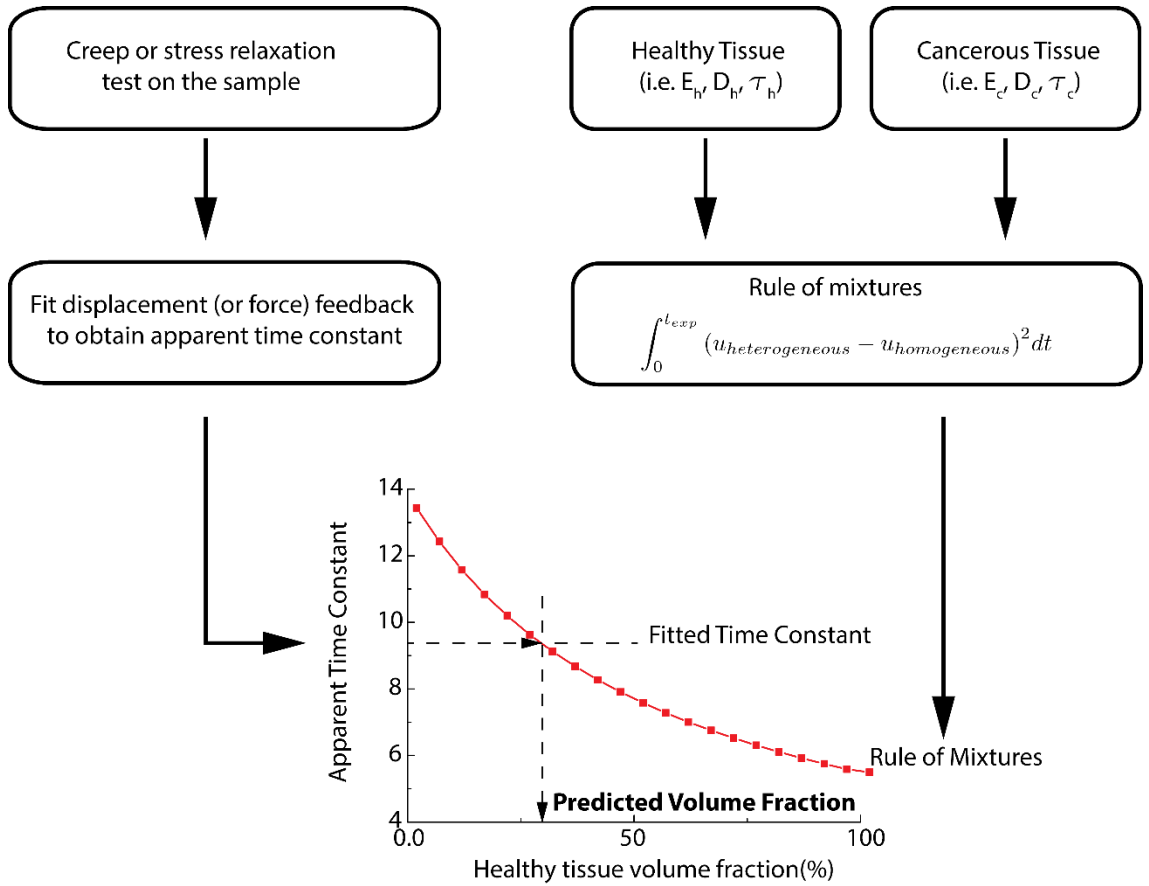


**Figure 5-2.** Flowchart of the proposed methodology. First a creep or stress relaxation experiment is carried out and the displacement or force feedback fitted to obtain the apparent time constant. The rule of mixtures is obtained using the mechanical properties from the healthy and cancerous tissues. The volume fraction of healthy tissue is read directly from the graph for the apparent time constant.

### 5.3 Tissue heterogeneity - quantitative cancer diagnosis

In this section the methodology to predict the volume fraction of both cancerous and healthy prostatic tissues is presented. A 2D biphasic model is created and meshed with bilinear plane stress finite elements as shown in Fig. 5-1(c). Each element is randomly assigned with material properties that represent either cancerous or healthy tissue to estimate the possible bounds of effective properties. Specifically, 10 random samples were used and the simulated stress relaxation experiment performed using various volume fractions (20%, 40%, 60% and 80% healthy tissue). Different ratios between Young's moduli and time constants of the two constituents were considered to evaluate the

algorithm subject to various experiment times,  $t_{exp}$ . Stiffness ratios (i.e. healthy:cancerous) of 1:2 and 1:5 were selected as they are typical of those found in the literature [13]. For the time constant, ratios of 1:10 and 1:100 were used, which, although higher than those reported [44], give an opportunity to analyse the sensitivity of the procedure in scenarios where the changes of the tissue viscoelasticity under different pathological conditions are extreme (e.g. when stones are present in the gallbladder or kidneys [155]).

To further evaluate the proposed methodology in the scenario of quantitative cancer diagnosis, a prostatic tissue model was reconstructed from an actual histological section prepared from a patient who had undergone a radical prostatectomy.<sup>3</sup> The boundary between benign and malignant tissue was determined by the uropathologist. Histological images were segmented and the geometry was built and meshed using Scan-IP (Simpleware Ltd., Exeter, UK). To test the proposed framework in a clinically relevant scenario, samples from 3 different locations of the prostate are considered in this analysis, shown in Fig. 5-3. Sample 1 contains 28% of cancerous tissue and serves as a test for an extreme width-to-length ratio, whereas sample 2 consists of 81% of cancer. It is, in fact, a subdomain of Sample 1 with the same cancer inclusion but reduced fraction of healthy tissue. Both samples were chosen from the lateral side of prostate to represent the scenario of palpation during minimally invasive radical prostatectomy (MIRP). In Sample 3 the malignant tissue accounts for 60% of the total tissue volume and was chosen to test the proposed methodology in a sample where no direct contact between the probe and the malignant tissue exists. Sample 4 was chosen from the posterior region and contains 47% of cancerous tissue, Samples 3 and 4 representing palpation at the posterior of the prostate which is the area accessible using digital rectal examination (DRE). Finally, the whole

---

<sup>3</sup> This is to acknowledge Dr. M O'Donnell (Consultant Uropathologist, Western General Hospital, UK) for the pathohistological analysis of the images used in this Chapter.



histology, which contains 87% of healthy tissue, was also tested. It should be noted that the histology has been simplified over how a pathologist would normally grade cancer to give a measure of cancerous volume fraction over a range from low to relatively high. This allows an evaluation of the proposed methodology for quantitative diagnosis in the biphasic case. More importantly, the samples are chosen in a way that the cancerous nodules have different geometries and topologies, which allows the effectiveness of volume fraction estimation of cancerous tissue to be assessed in real tissue scenarios.

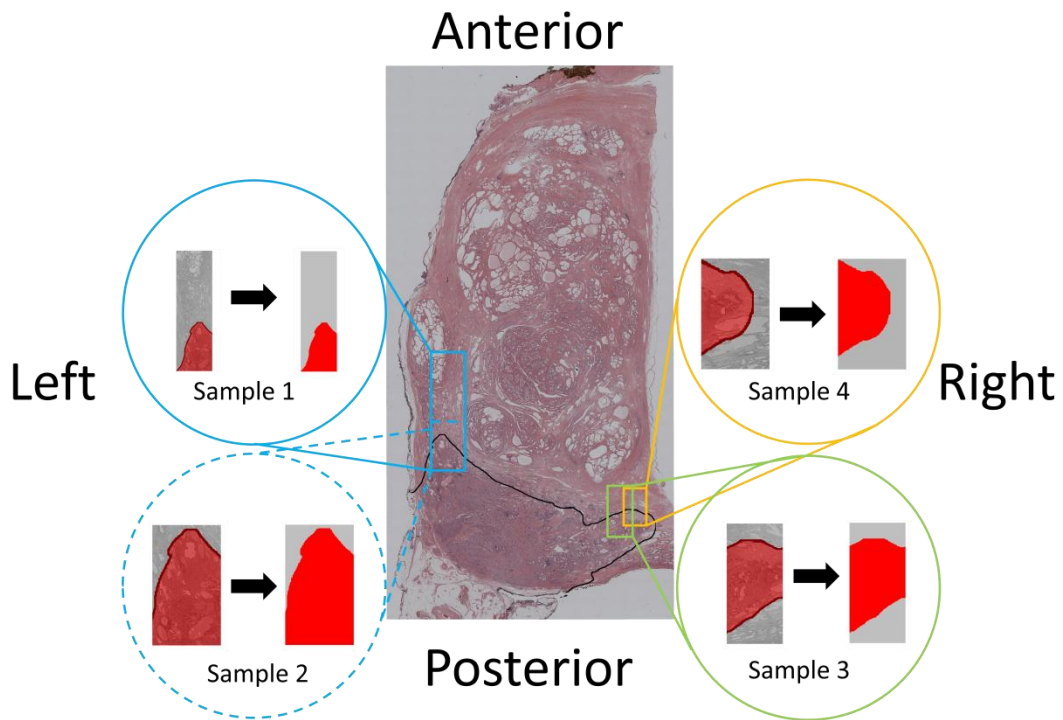


**Figure 5-3.** Five samples from prostatic tissue (including the whole prostate and surrounding fascia) are considered to analyse the proposed diagnostic methodology. Red and grey indicate cancerous tissue and healthy prostatic tissue respectively. The volume fraction of healthy tissue is 72% in Sample 1, 19% in Sample 2, 40% in Sample 3, 53% in Sample 4, and 87% in whole tissue sample. Convergent hybrid tetrahedral meshes with the number of elements ranging from 65380 for the smallest sample (Sample 4) up to 1061676 elements for the complete prostate were used.

DRE is a diagnostic procedure where the practitioner palpates the prostate through the rectum looking for lumps and assessing stiffness and motility. New devices that record the force feedback during DRE have been recently developed to perform quantitative tissue diagnosis [106, 109, 156]. To model instrumented DRE here, symmetry boundary

conditions were applied at the anterior and right boundaries and the sample was palpated from the posterior side. To simulate the wider implications of palpation diagnosis during a minimally invasive surgical intervention, symmetry boundary conditions were used at the anterior and right boundaries and the sample was palpated from the left side. Finite strains were considered and a neo-Hookean strain energy density function was chosen to model tissue elasticity with Young's moduli of 17kPa and 34kPa for healthy and cancerous tissue, respectively [44]. Without loss of generality a ratio of 1:2 was considered for both the material time constant and Young's modulus between healthy and cancerous tissue. Such a ratio concurs with elasticity reported for prostatic tissue [13, 42]. The model, as illustrated in Fig. 5-1(c), was solved using the finite element method in Abaqus (Dassault Systemes, Vlizy-Villacoublay, France). The proposed methodology allows the estimation of the viscoelastic properties of the equivalent homogeneous material. However, only the effective time constant is studied here for the purpose of quantitative diagnosis since it has already proven effective in assessing tissue quality [19, 157].

#### **5.4 The rule of mixtures: 1D analysis**

In this section the 1D model is analysed and the rule of mixtures that relates the apparent time constant to the fraction of each constituent is presented. Fig. 5-3(a) shows the effective time constant of the heterogeneous material obtained from computational (observed) and mathematical (predicted) models, respectively. The time constant found in the finite element analysis decays with the amount of cancerous tissue and only small variations are observed between results over times  $t_{exp}$  of 5 and 50s. However, the difference between the predicted and computational effective time constant increases when  $t_{exp}$  becomes longer. For shorter  $t_{exp}$ , the predicted time constants are smaller than the observed ones because there is insufficient time for the exponential term in Eq. (1) to be significant for longer time constants. Finding an optimal  $t_{exp}$  is therefore critical for

the purpose of diagnosis. Such optimization of  $t_{exp}$  would require a balance between the accuracy of the procedure and practicality such as patient discomfort and diagnostic constraints in clinical practice. It is worth pointing out that the example  $t_{exp}$  of 5s, which is a reasonable time for clinical use, predicts the effective time constant with a maximum error of 5.44% between the predicted and observed results.

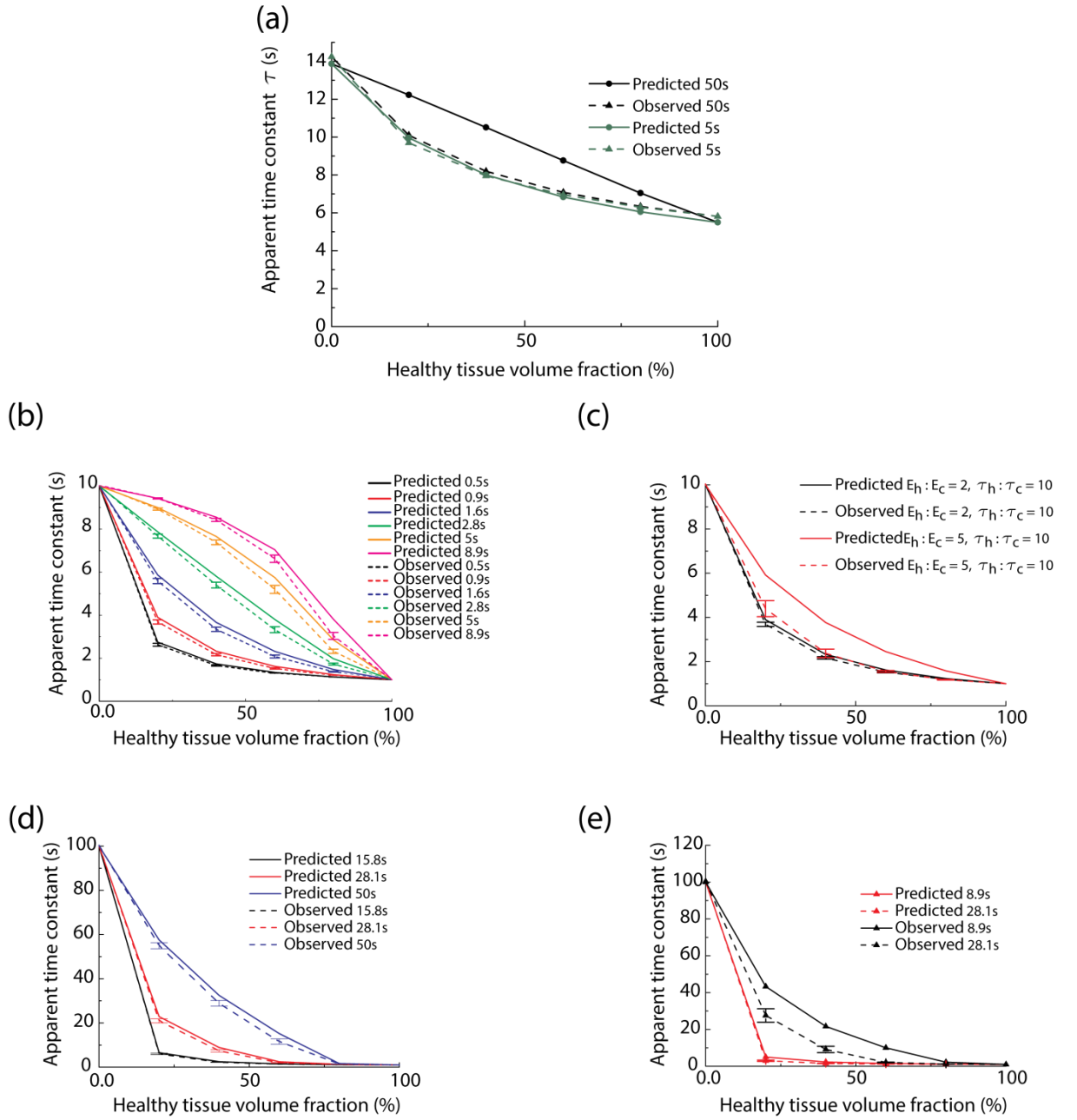


**Figure 5-4.** Comparison of the average time constant values obtained for different materials and relaxation times. The error bars show the confidence interval for six standard deviations. (a) Average time constants for the 1D model with times of experiment of 50s and 5s for different volume fractions of healthy tissue. (b) Comparison of the rules of mixtures predicted by the proposed methodology and the results obtained from the computational models for the 2D sample. (c) Increasing the stiffness ratio between both materials causes a minimal variation in the calculated average properties for a time of experiment of 0.9s. (d) The rules of mixtures become steep for short  $t_{exp}$  when ratios of 100:1 in the time constants and 1:2 in the Young's modulus are considered. (e) Increasing the Young's modulus ratio to 5:1 requires shorter times of experiment to obtain better results. Ten time values on logarithmic timescale between 0 and 50s were used to analyse the effects of both shorter and longer testing times.

## 5.5 Parametric analysis: 2D heterogeneous materials

### 5.5.1 Effect of $t_{exp}$

In this section the influence of different relaxation times  $t_{exp}$  in the effective time constant is explored. Long testing times would be economically infeasible and may lead to patient discomfort. Very short testing times, especially if the sampling rate of the force feedback is low, would result in insufficient number of data, since there is a risk of overfitting which could reduce the accuracy and significance of prediction. Fig. 5-4(b) shows the effective time constants obtained from the observed and predicted models over a range of experimental  $t_{exp}$  and also illustrates the upper and lower limits of the effective time constants for each  $t_{exp}$  used. It is important to note here that the diagnostic sensitivity can be effectively improved by taking advantage of the shape of curve of the rule of mixtures. For longer  $t_{exp}$ , the curve becomes concave thus allowing a better sensitivity for tissue quality prediction when small percentages of tumour is present, since small variations in the percentage of cancerous tissue will result in large changes in the observed effective time constant, and *vice versa*. This would offer the opportunity for more accurate diagnostic procedures by performing multiple consecutive tests using different  $t_{exp}$  to improve the diagnostic sensitivity.

### 5.5.2 Effect of Young's Modulus

In this section the influence of the ratio between the Young's moduli of cancerous and healthy tissue is analysed. This is of special relevance to tissue diagnosis where it has been shown that different physiological and pathological conditions could give rise to changes in tissue elasticity [7, 27, 125] and is also important when taking into account patient-specificity and more complex tissue microstructures than the simple biphasic one considered here.

Fig. 5-4(c) shows the observed and predicted effective stiffness when the ratio between the Young's moduli of healthy and cancerous tissues is 2 and 5, respectively. This allows a better understanding of the capacity of the proposed methodology in quantifying the amount of cancerous tissue in organs when the stiffness ratio between the healthy and cancerous tissues is higher such as in breast carcinoma [13]. The predicted and observed effective time constants match well when the stiffness ratio is 2. However, when the stiffness ratio increases to 5, a difference of up to 50% can be seen between the estimated and observed effective time constants. Figs. 5-4(d) and (e) show the rule of mixtures when the stiffness ratio for healthy and cancerous materials is 2 and 5, respectively, and the time constant ratio between the healthy and cancerous tissues is 100 ( $E_h = 20 \text{ kPa}$ ,  $\tau_h = 1 \text{ s}$ ;  $E_c = 40 \text{ kPa}$  or  $100 \text{ kPa}$ ,  $\tau_c = 100 \text{ s}$  - the subscripts  $h$  and  $c$  indicating healthy and cancerous, respectively). In the first case ( $E_h:E_c=1:2$ ) the observation and estimation match well in most cases, whereas a good match can only be found for smaller  $t_{exp}$  when the stiffness ratio increases as illustrated in Fig. 5-4(e). This is caused by the viscoelastic effects being indistinguishable from the long-term elastic modulus over short times of observation.

## 5.6 Quantitative diagnosis of prostate cancer: a practical study

In this section the proposed methodology is used to estimate the amount of cancerous tissue in a histological sample of prostatic tissue. The relaxation time observed from the FE analysis is compared with that calculated using the proposed rule of mixtures. The samples were tested along two different directions; the anteroposterior axis to model the DRE and the radial margin to simulate palpation conducted during the MIRP surgery.

A summary of the results can be found in Table 5-1. Fig. 5-5(a) shows the observed volume fraction of cancerous tissue in all 5 samples through numerical tests, alongside predicted ones subjected to experimental times of 5 and 10s, respectively. In Samples 1, 2 and 3 the error between the real volume fractions of cancerous tissue and the predicted

ones with  $t_{exp} = 10s$  is smaller than those predicted with  $t_{exp} = 5s$ , for both lateral and posterior testing. However, for Sample 4 and the whole prostate such trend is not clear. A possible reason for this behaviour is that the differences caused by tissue topology, direction of indentation, sample's aspect ratio etc., to some extent, mask the influence of  $t_{exp}$  in this particular example, where the time constant and Young's moduli between healthy and cancerous tissue are relatively close. Therefore as opposed to the examples shown in the previous section where the cancer distribution was random and the differences between the mechanical properties of each tissue constituents were higher, determining an optimal time of experiment ( $t_{exp}$ ) within a clinically relevant framework is complex in this particular scenario. Variations between the tissue volume predicted in the lateral and posterior examination are relatively close with a maximum difference of 8% and a minimum of 0.5%. Figs. 5-5 (b) and (c) show the observed and predicted time constants for the samples considered. It should be noted that in both cases the lateral palpation better predicts the volume fraction of healthy tissue, which might be due to the fact that the cancerous tissue is closer to the probing sites therefore the influence of its presence is higher. In summary, the tests indicate that the best approach for diagnosis would be the one where the measurement is made as close as possible to cancerous tissue, regardless of the direction used to characterize the tissue. The possibility of examining the tissue from any direction would be of particular importance in interventions where only the diseased parts of the organ have to be resected, for instance in the liver, kidney and pancreas. The method would help identify the surgical margin if a test is done at those positions close to the area of suspected malignancy to maximize the sensitivity of the procedure.

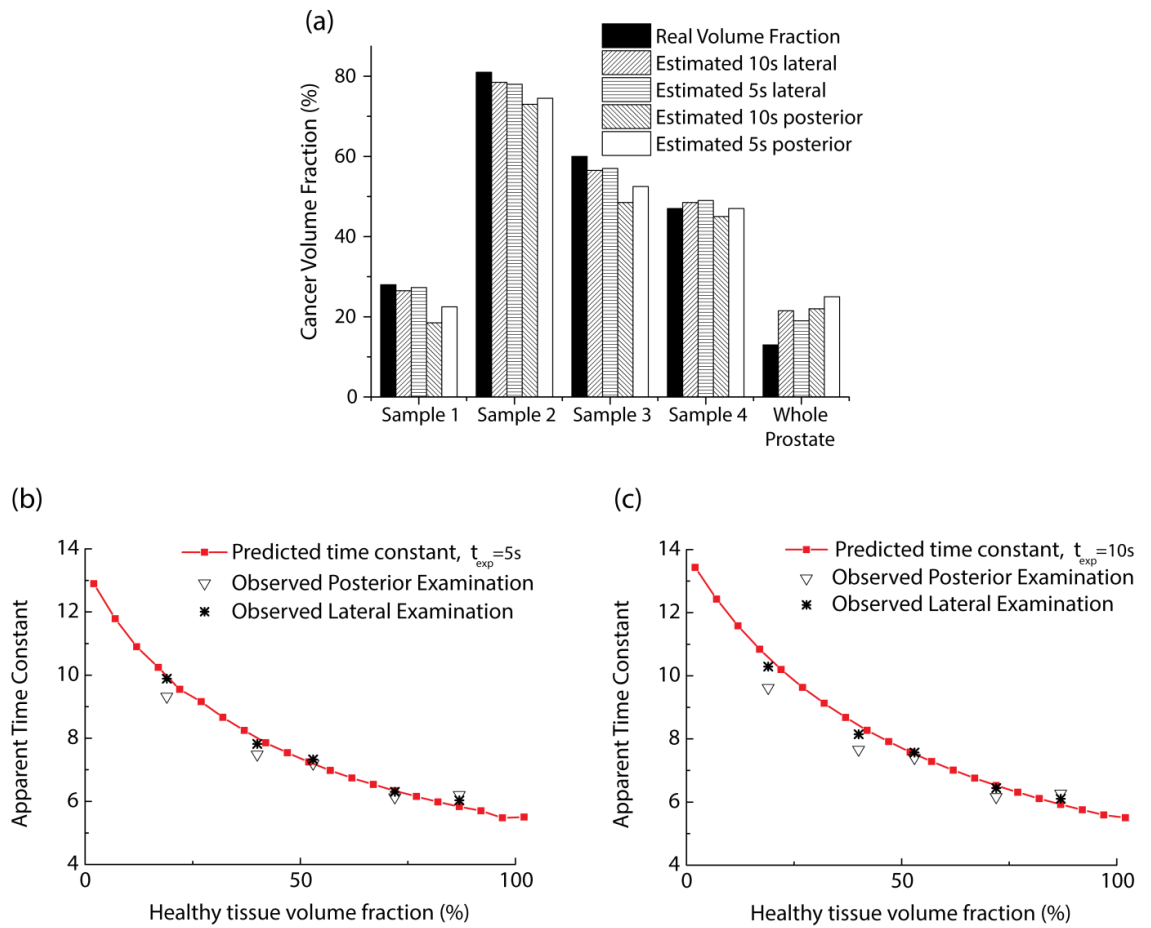


**Figure 5-5.** Comparison of the observed time constants and volume fraction with the predicted ones. (a) Results from the volume fraction estimation of each phase in the different samples. (b) and (c) show the comparison between the predicted law of mixtures and the observed values for a relaxation time of 5s and 10s.



**Table 5-1.** Cancerous tissue volume fraction, observed time constants in the histological samples and predicted time constants using the proposed rule of mixture.

Sample	$\tau_{Observed}^{5s}(s)$	$\tau_{Observed}^{10s}(s)$	$V_{Predicted}^{5s}(\%)$	$V_{Predicted}^{10s}(\%)$	$V_{Real}(\%)$	$Error^{5s}(\%)$	$Error^{10s}(\%)$
Sample 1 Posterior	6.13	6.16	22.5	18.5	28	5.5	9.5
Sample 1 Lateral	6.3	6.44	27.3	26.5	28	1.7	1.5
Sample 2 Posterior	9.32	9.62	74.5	73	81	6.5	8
Sample 2 Lateral	9.89	10.29	78	78.5	81	3	2.5
Sample 3 Posterior	7.49	7.66	52.5	48.5	60	7.5	11.5
Sample 3 Lateral	7.82	8.15	57	56.5	60	3	3.5
Sample 4 Posterior	7.2	7.4	47	45	47	0	2
Sample 4 Lateral	7.33	7.57	49	48.5	47	2	1.5
Whole Prostate Posterior	6.21	6.27	25	22	13	12	9
Whole Prostate Lateral	6.03	6.1	19	21.5	13	6	8.5

## 5.7 Concluding remarks

Based on the work carried out in Chapter 4, this Chapter presents a quantitative framework of tissue diagnosis to predict the volume fraction of cancerous tissue in a sample where the underlying histology is unknown. The proposed framework is based on the hypothesis that the quasi-static behaviour of a complex viscoelastic heterogeneous sample can be approximated by a homogeneous system with a known analytical solution. From that solution, a rule of mixtures that quantify the relationship between the volume fraction of each tissue constituent and the apparent mechanical properties is obtained. Compared to the other tissue diagnostic techniques such as those based on the inverse FE analysis as reviewed in Chapters 2.5 and 2.6, the proposed method is significantly faster and subsequently more applicable particularly for clinical diagnosis and certain experimental purposes where testing duration is an important parameter. Considering a stress relaxation or a creep experiment leads to the same solution, so the practitioner may choose one to use depending on the tissue type and available equipment. The methodology has been tested using a wide range of mechanical properties through the rule of mixtures to validate its potential applicability for quantitative diagnosis of different biological tissues. Different aspect ratios of histological samples and volume fractions of tumour were considered and the methodology has proven robust to variations in such parameters. This methodology, based as it is on non-invasive mechanical palpation, could be used to assess the quality of a large variety of tissues reducing the necessity of invasive and expensive procedures such as biopsies, MRI scans and CT scans whose side effects are not negligible. More importantly, it could become a useful tool in early diagnosis of life threatening diseases that change the mechanical properties of the tissues, such as cancer, liver fibrosis or amyotrophic lateral sclerosis. The methodology presented here is, as it stands, limited since it requires an *a priori* knowledge of the mechanical properties of each component. Obtaining such mechanical properties could

become troublesome on a patient-to-patient basis. Future work will aim to provide benchmark values that could be used for different groups of patients as it has been done for other tissues such as the aorta [158].

# CHAPTER 6

## Patient Specific Modelling of Palpation-based Prostate Cancer Diagnosis: Effects of Pelvic Cavity Anatomy and Intrabladder Pressure

### Contents

---

6.1	Summary .....	93
6.2	Selection of patients and their pathophysiological conditions.....	94
6.3	Modelling the pelvic cavity.....	95
6.4	Influence of subject-specific features in IDRE .....	99
6.5	Influence of intrabladder pressure: is it possible to increase its sensitivity preparing the patient? .....	102
6.6	The pelvic bone: to model or not to model .....	105
6.7	Concluding remarks .....	109

---

### 6.1 Summary

The influence in tissue diagnosis of the mechanical properties of tissue and organ structure has been discussed in previous chapters. However, other features such as the anatomical structure can also significant influence the outcome of a diagnostic procedure such as the digital rectal examination (DRE). A possible approach would be to model all the organs and interactions among them. This however can be a complex and time consuming task thus making the technique less useful for clinical practice. More importantly it could introduce a significant amount of uncertainty due to the large number

of parameters required for such models. As a result determining which organs and mechanical interactions should be modelled is critical - this has not been thoroughly explored in literature. Other parameters such as intrabladder pressure (IBP) can also influence the outcome of the procedure. IBP can be easily controlled during the patient preparation for the procedure therefore could be potentially used to improve the procedure's sensitivity. The highlights of this chapter include: **i)** analysis of inter-patient variations in three patients whose structural features, diagnosis and previous treatment are significantly different; **ii)** evaluation of the influence of IBP in the outcome of digital rectal examination to provide guidelines to practitioners on how to improve the procedure; and **iii)** investigation of the influence of modelling the pelvic bone for the purpose of DRE.

## **6.2 Selection of patients and their pathophysiological conditions**

Three male patients with different anatomical and pathological conditions were selected in this chapter to investigate how patient-specificity influences the outcome of the instrumented digital rectal examination for prostate cancer diagnosis.<sup>4</sup> Fig. 6-1 shows representative MR images of all three patients. From Fig. 6-1(a) it can be seen that Patient 1 has an enlarged prostate which suggests adenomatous hyperplasia. An imprecise marginal area suspected of being malignant was identified at the vertex and in the anterior zone. A distinctive anatomical feature of this patient is an enlarged prostate that compresses the bladder causing pollakiuria, a condition that results in high frequency of urination. The MRI scan of Patient 2 in Fig. 6-1(b) shows invasion of cancerous tissue into the peripheral and posteriocentral zones, which suggests a neoplastic process prolonged to the periurethral zone. Ganglionar and indeterminate iliac bone lesions can also be observed in the scan, although they are not modelled in this study. For Patient 3,

---

<sup>4</sup> The MRI scans were kindly provided by Ms Elizabeth Jiménez Aguilar from the Department of Medical Oncology at Hospital 12 de Octubre in Madrid (Spain). The help of Dr. Ray Manneh is greatly appreciated.

the clinical history indicates that brachytherapy was conducted, where cancerous tissue was destroyed by the effect of radioactive seeds inserted into the tissue. The MRI scan shown in Fig. 6-1(c) indicates loss of central-peripheral differentiation of the gland as well as thinning of the posterior right capsular limits, continued with the seminal vesicles and neurovascular plexus. Ganglionic disease and right sacral bone lesions are also present but not modelled. These observations are consistent with recurrent prostate cancer with at least stage T3b (tumour spread to the seminal vesicles), N1 (cancerous cells present in the lymph nodes) and M1b (metastasis to the bone), using the TNM (Tumour size, nearby lymph node involvement, distant metastasis) classification [159]. T2-weighted, 1.5-Tesla MRI scans, with a resolution of 3.0 mm in the axial plane (all Patients) and 0.7813 mm resolution (Patients 1 and 2) and 0.651mm (Patient 3) in the sagittal and coronal planes were used to reconstruct the 3D model in ITK-SNAP [160].

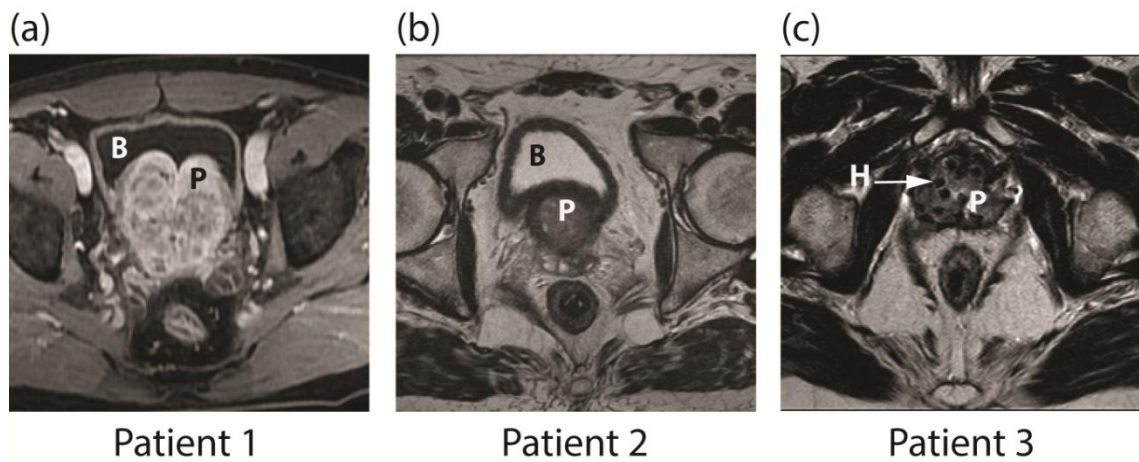


**Figure 6-1.** Typical MR images of the three patients selected for the study, showing patient-specific structural features. B and P indicate the location of the bladder and prostate, respectively. (a) Patient 1: an enlarged prostate compresses the bladder; (b) Patient 2: the inferior of the bladder is tightly wrapped around the superior part of the prostate; (c) Patient 3: prostate contains holes (H) due to brachytherapy treatment.

### 6.3 Modelling the pelvic cavity

The male pelvic cavity contains the end part of the large intestine, the urinary bladder, the prostate, the seminal vesicles and the pelvic bone plus some other, minor anatomical structures. Its patient-specific modelling presents various challenges, depending on the

clinical application, including decisions on; which organ(s) to model, how they interact with each other, and also the initial conditions of tissue (presence of disease, cavity filling, pre-stress etc.). The models proposed in this chapter aims to understand the effects of patient-specific features in IDRE and to present a diagnostic framework for patient specific modelling of prostatic diseases. Intrabladder pressure (IBP) and the pathological condition of the prostate are key parameters and their influence on the effectiveness of IDRE will be investigated in this study. Moreover, the effectiveness of inclusion of the pelvic bone in the *in silico* IDRE model will be assessed. It should be noted here that, although there are a few clinical parameters that can be used to optimize the procedure, such as the position of the patient during the examination, the margin of potential clinical usefulness is limited due to patient discomfort. IBP, however, can be easily managed during clinical examinations. This can be controlled by the patients themselves prior to the examination or with the help of a catheter. Table 6-1 shows the different IBPs that were adopted in this study to model a full and empty bladder [161], respectively. Bladders of all three patients were emptied prior to the MRI scan and the reconstructed 3D organs are considered as undeformed and unstressed.

**Table 6-1.** Variation of intrabladder pressure (IBP) subjected to different volumes of urine. Data were taken from Chiumello et al. [161], where IBP was used as an indicator of intra-abdominal pressure.

Volume of saline(ml)	IBP (mmHg)	IBP (MPa)
50	9.5	$1.267 \cdot 10^{-3}$
200	27.1	$3.613 \cdot 10^{-3}$

In the rest of this chapter, the pressure corresponding to a bladder content of 50 ml urine will be referred to as low intrabladder pressure (LIBP) and the content of 200 ml as high intrabladder pressure (HIBP). During normal activities, the rectum is subjected to a certain internal pressure [162]. However, due to the insertion of the instrumented system

(or finger, in the case of digital rectal examination), it will be considered to be at ambient pressure during the procedure.

Like most biological tissues, the fascia, bladder, prostate and rectum exhibit viscoelastic behaviour [44, 163-165]. Nevertheless, under certain loading conditions, their mechanical behaviour can be considered to be elastic; especially when the strain rate is very low as is the case for DRE, where the viscous component can be neglected. Subjected to such a quasi-static loading the observed stiffness is often referred to long-term modulus. This assumption, which simplifies the experiments and modelling, has been widely used in the literature [109, 121, 140] and will be used in this chapter. To ensure numerical stability, the mechanical properties of the tissues are modelled by non-linear hyperelastic strain energy density functions that mimic the behaviour shown in Table 6-2.

**Table 6-2.** Mechanical properties and material models used for tissues considered in this study.

Material	Equivalent Young's Modulus (kPa)	Hyperelastic Model	Reference
Rectum	10	Neo-Hookean	[166]
Healthy Prostatic Tissue	17	Ogden 2 <sup>nd</sup> order	[44]
Cancerous Prostatic Tissue	34	Ogden 2 <sup>nd</sup> order	[44]
Bladder	15	Neo-Hookean	[166]
Fascia	15	Neo-Hookean	[166]
Bone	$\sim 6 \times 10^6$	Neo- Hookean	[167]

The organs in consideration are embedded in a ‘box’ of fascia. The size of this box (300×300×300 mm) is chosen to be comparable to the size of patient’s pelvic cavity, big enough so that the effect from boundary conditions that prevent rigid body motions becomes negligible whilst keeping the computational cost to a minimum. In this study, it is considered that the patient is bent at the waist over towards a table during examination.



Therefore, in the proposed model, the displacement at the anterior side of the box is constrained. Fig. 6-2 shows the organs of patient 2 embedded in the box and the anterior side that is constrained.

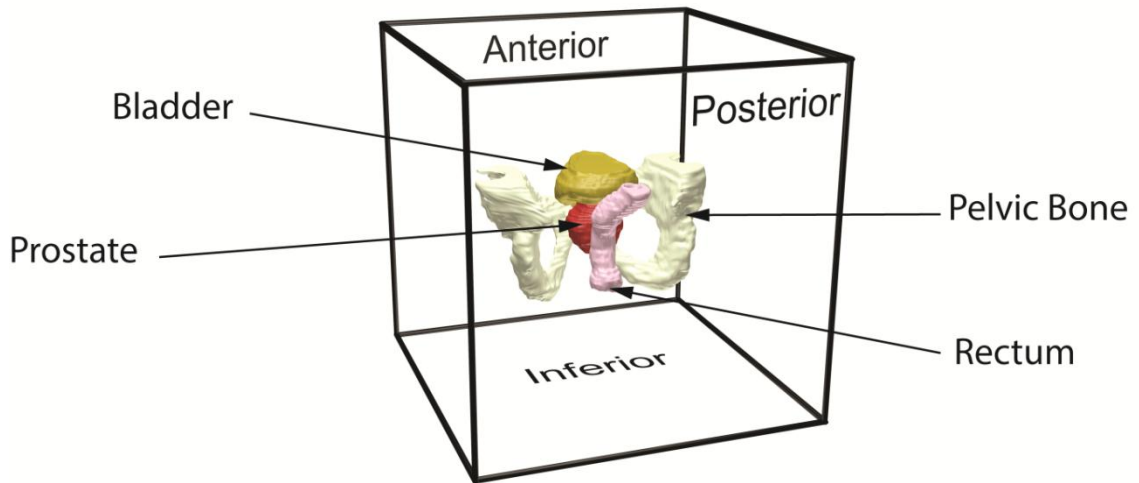


**Figure 6-2.** Computational model where organs are embedded in a box of fascia. The displacement of the anterior side of the box is constrained.

The patient-specific models were simulated in ABAQUS (Dassault Systemes, Vlizy-Villacoublay, France). The organs were meshed with linear hybrid tetrahedral elements where the hydrostatic pressure is considered as an independent variable and coupled with the displacement using the constitutive model, which is required to model such quasi-incompressible materials accurately and an implicit quasi-static solver was used. A 5mm radius spherical indenter as a part of the instrumented palpation system was modelled as a discrete rigid solid, meshed with 3 node triangular and 4 node bilinear quadrilateral facets as shown in Fig. 6-3. The connection of the indenter to other parts of the instrumented palpation system was not modelled in this study, since it often only consists of a cable in a small diameter [125]. Surface to surface contact considering finite strains was used to simulate the interaction between the indenter and the rectal wall. The palpation was simulated under displacement control with a maximum allowable displacement of 5 mm.

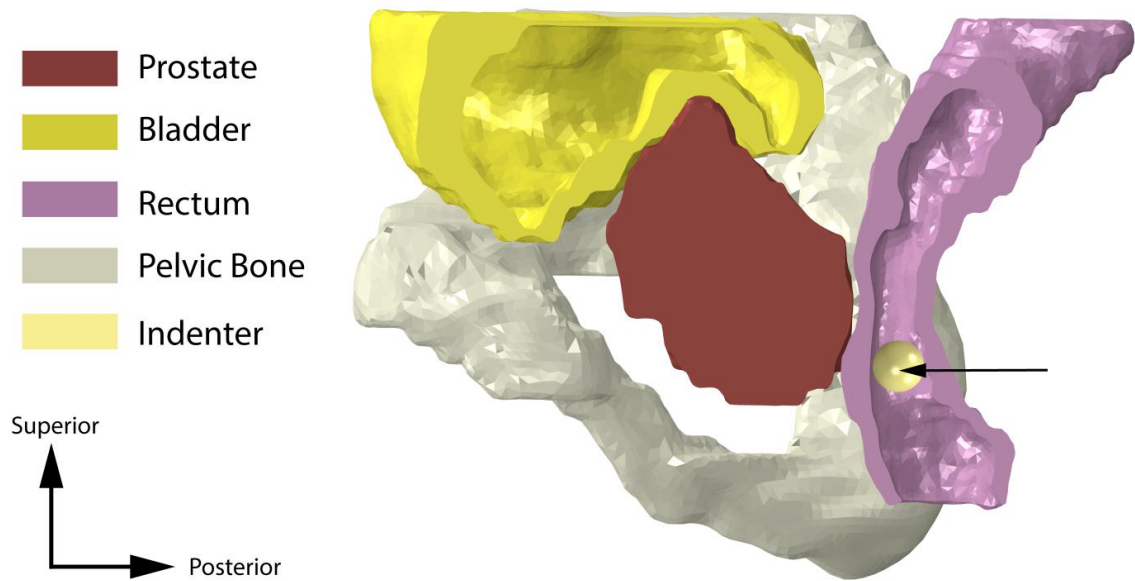


**Figure 6-3.** Schematic of the 3D reconstructed model of Patient 2. The arrow indicates the direction of indentation.

Two modelling scenarios will be considered: completely healthy and completely cancerous prostate. This will allow the determination of two extreme cases of the force feedback diagrams in instrumented digital rectal examination as well as investigating how the resolution of the procedure (the distance between the force feedback curves for the cancerous and healthy scenarios) varies for different patients and IBPs. It should be noted here that considering intermediate scenarios where a cancerous nodule is present within the prostate would not help to provide general guidelines on how to improve the outcome of the diagnostic procedure due to the patient-specific nature of the nodule shape and location.

#### **6.4 Influence of subject-specific features in IDRE**

In this section, in order to isolate the anatomical and pathological patient-specificity, the presence of the pelvic bone is not considered (still illustrated). Fig. 6-4 shows the reconstructed 3D models of the three patients from the MRI scans. It can be seen in Fig. 6-4 (a) that the bladder of Patient 1 wraps around the enlarged prostate. Patient 2 has a

different structure where the bladder sits above the prostate, as shown in Fig. 6-4 (b). Patient 3 has, again, different anatomy, where the bladder sits on top of the prostate with considerably less contact area, as shown in Fig. 6-4 (c). It should be noted here that the prostate of Patient 3 contains small holes (which are assumed to be filled with fascia in the FE model) due to the brachytherapy treatment, which would potentially reduce its overall strength.

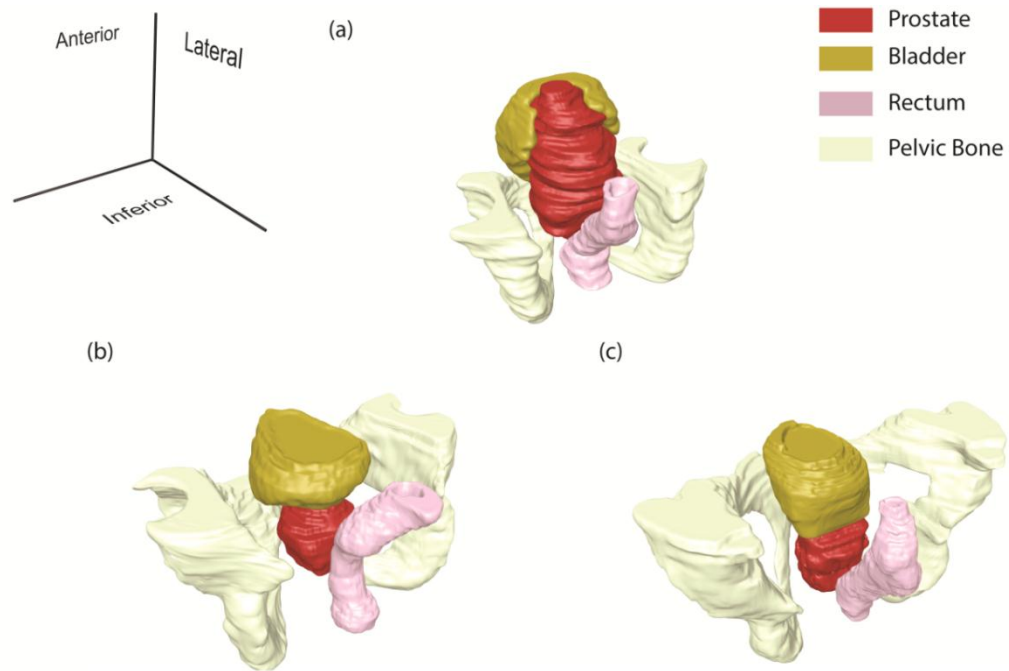


**Figure 6-4.** Reconstructed 3D models of three selected patients from MRI scans. (a) Patient 1; (b) Patient 2; and (c) Patient 3. Convergent hybrid, tetrahedral meshes were used in the model with 1198539 elements for Patient 1, 922988 for Patient 2 and 1022059 for Patient 3.

Fig. 6-5 shows the force feedback from the instrumented digital rectal examination with low intrabladder pressure when the pelvic bone is modelled for each of the patients with each of the two prostate tissue conditions. The force feedback is significantly higher for patients 1 and 2 when the IBP is high. In patient 3 due to his unique anatomical structure where the bladder sits on top of the prostate the influence of IBP is minimized. In fact, the force feedback for Patient 1 and 3 become similar when IBP is reduced. The curves for the force feedback of the fully healthy and fully cancerous tissue act as the lower and upper bounds of possible outcome of an IDRE test. The result of any test on a prostate with a cancerous nodule inside would lie within these two bounds so it represents the

“diagnosis window” against which resolution of the volumetric fraction of cancerous tissue could be assessed. The results for Patients 1 and 3 are similar when the indentation depth is small, even though the overall stiffness of the prostate of Patient 3 is reduced due to the brachytherapy. This is potentially caused by the indentation being performed at the end part of the rectum, where only the inferior part of the prostate can be reached (even in DRE upper parts of the rectum are hardly reachable by the finger unless anaesthesia is used). For larger depths of indentation the palpation force in Patient 2 becomes higher since a thicker region of the prostate is palpated. It can be seen that, although the reaction forces in the cancerous scenario are higher than in the healthy case, the relative difference between the cancer and healthy results remains approximately constant between different patients. Such results could be due to the fact that the same mechanical properties are used for all three patients. However, the force feedback obtained during palpation does not depend only on the mechanical properties but also on the topology of the sample, especially in the cases where the cancerous nodules are close to the indenter. This suggests that the effects of inter-patient differences in the topology of the rectal wall (e.g. thickness) are negligible. When high intrabladder pressure is present, the differences between patients are intensified as shown in Figs. 6-5 (a) and 6-5 (b). It is important to note that the diagnostic distinguishability of cancerous nodules during IDRE can be estimated by the vertical gap of force data between healthy and cancerous cases at certain indentation depth. Further discussion is required here regarding the indentation depth. As previously described in Chapters 3 and 4 there are some limitations regarding the maximum depth of indentation which is constrained by patient discomfort and the possibility of causing damage to the tissue. However, very superficial indentations may lead to some uncertainties. First the indentation has to be sufficiently deep so that the prostate is felt and not only the rectal wall. Secondly, the force feedback recorded during the contact-finding phase may be comparable to that of the actual indentation and

therefore the signal to noise ratio would be unfavourable compared to deeper indentations. This problem would be further increased by any involuntary movements of the patient during the procedure. Therefore, it is clearly shown that the diagnosis would benefit from deeper palpation and also the presence of high intrabladder pressure.

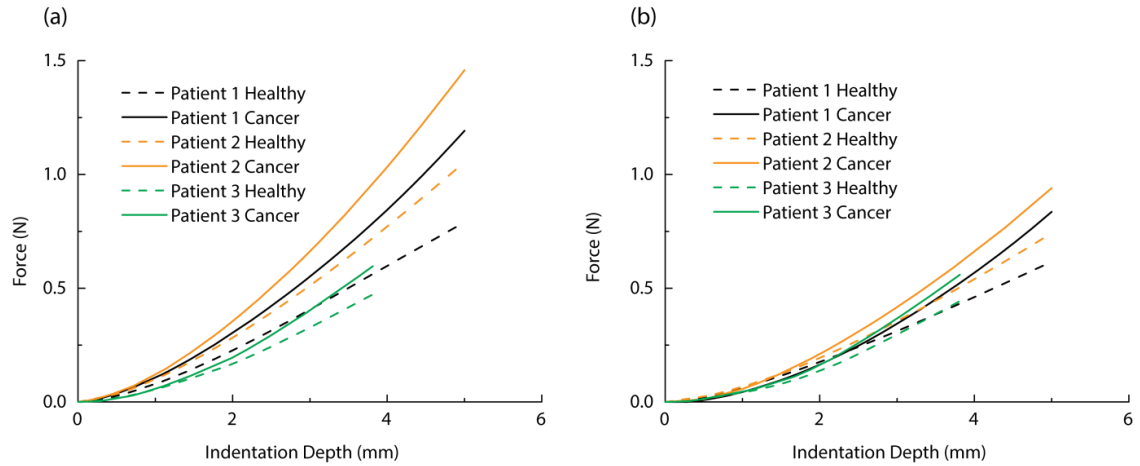


**Figure 6-5.** Changes in palpation force of three patients during IDRE subjected to (a) high intrabladder pressure and (b) low intrabladder pressure when the pelvic bone is considered.

It should be noted here that, at the beginning of the modelling, the indenter is not necessarily in contact with the rectum. This can result in that, at the very early stages of the indentation, no contact is registered, especially in the case of low intrabladder pressure. This is why the final indentation depth from the rectum is less than the 5 mm in the case of patient 3.

### 6.5 Influence of intrabladder pressure: is it possible to increase its sensitivity preparing the patient?

In this section the role of intrabladder pressure (IBP) in the sensitivity of IDRE will be investigated. The displacement fields for the three patients in IDRE tests when the intrabladder pressure is high are shown in Fig. 6-6. It is therefore possible to explore how a change in IBP influences the interaction between organs thus affecting the outcome and sensitivity of IDRE. Patient 1 has an enlarged prostate with the bladder surrounding it. This pushes the prostate towards the rectal wall which improves the probing efficacy. A

similar phenomenon is seen in Patient 2, whose bladder surrounds the prostate which also results in a displacement towards the rectal wall when high intrabladder pressure is present. Patient 3 has a considerably different geometry where the bladder sits on top of the prostate without enveloping it. This causes a displacement of the prostate towards the anterior direction in the high intrabladder pressure condition. In all cases, the presence of IBP moves the prostate towards the inferior direction leading to an increased palpation area. For patients suffering from pollakiuria due to the enlargement of the prostate, performing the examination with higher IBP would be beneficial for the examination. More importantly, performing IDRE multiple times over a period of time with different IBP levels may help determine whether the bladder is being compressed by the prostate due to e.g. benign prostatic hyperplasia or a malignant neoplastic process, which may eventually have great influence in the sensitivity of IDRE.

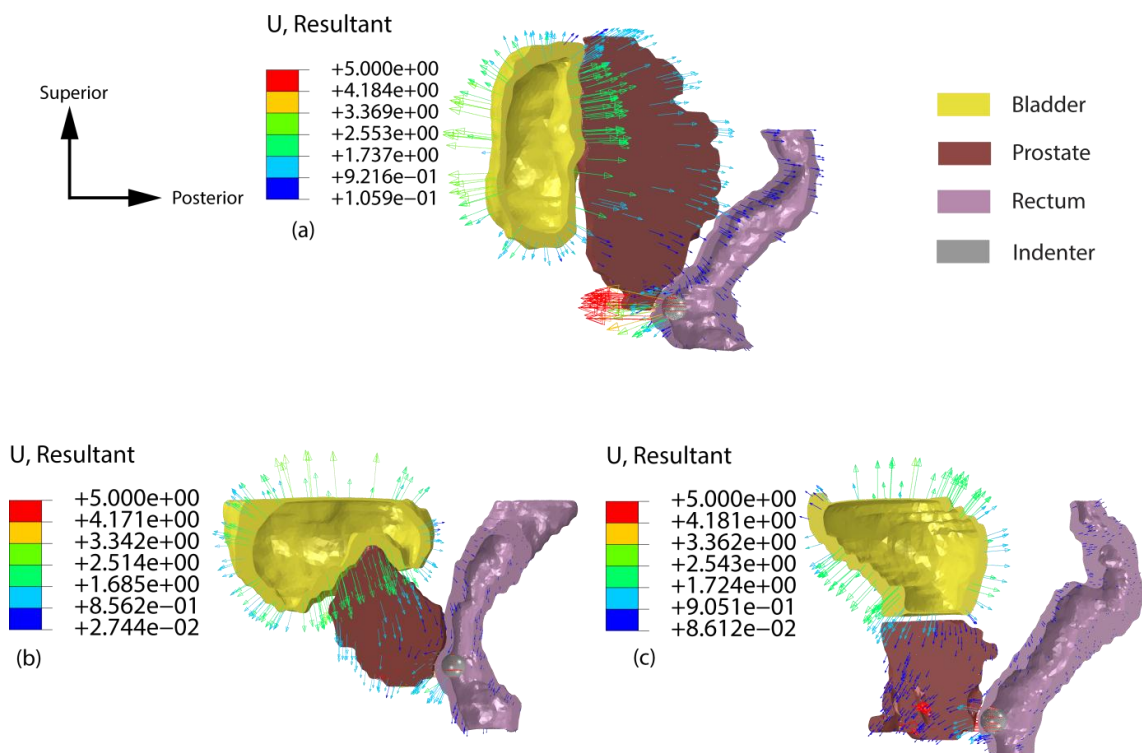


**Figure 6-6.** Displacement fields in mm of three patients subjected to IDRE when LIBP is present. (a) Patient 1; (b) Patient 2; and (c) Patient 3. In these cases, the pelvic bone is not modelled and the prostate is assumed to be healthy and the pelvic bone is not modelled.

Fig. 6-7 shows the force feedback for the 3 patient models subjected to IDRE, comparing the healthy and cancerous states under either low or high IBP conditions. As might be expected, the palpation force increases when high intrabladder pressure is present. More significantly, the distance between force data in the cancer and healthy cases also increases when IBP becomes higher, leading to improved diagnostic distinguishability of the procedure. This is due to the structure of the pelvic cavity and interactions between organs which push the prostate against the rectal wall when the bladder is more inflated under HIBP condition. In contrast, the Patient 3 model exhibits a different behaviour, in which the reaction forces are lower under the high intrabladder pressure as shown in Fig. 6-7 (b). Furthermore the resolution (i.e. the difference in force between the healthy and cancerous cases) shows a weak dependency on the IBP.

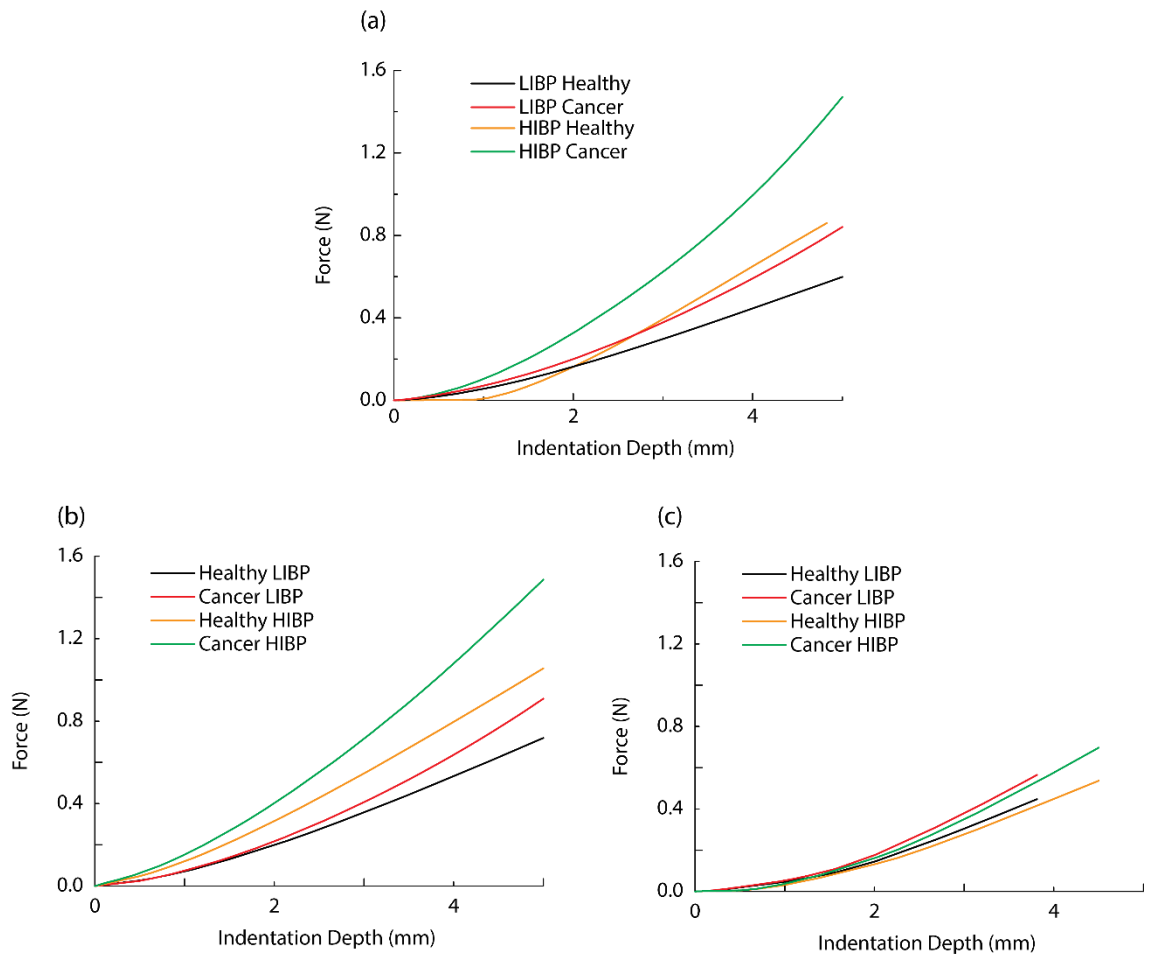


**Figure 6-7.** Reaction forces of Patients 1 (a), 2 (b) and 3 (c) under LIBP and HIBP conditions without the presence of the pelvic bone.

## **6.6 The pelvic bone: to model or not to model**

The aim of this section is to understand the effects of presence of the pelvic bone in the prediction of the proposed patient-specific model and determine if there are circumstances under which it needs to be modelled to obtain more accurate results. In this way, it will be possible to reduce unnecessary numerical problems associated with the inclusion of a stiff material in a soft matrix as well as reducing the uncertainty in the model.

Figs. 6-8 (a) and (b) show the displacement map of Patient 1 when the pelvic bone is present and absent, respectively. In this particular case the bladder sits on top of the pelvic bone therefore the anteroposterior axis is not highly constrained by the bone except in the inferior part. This is critical in this particular case, because the prostate is moved along the inferoposterior direction, whereas, without the pelvic bone, the prostate is pushed directly towards the rectum. The effect of modelling the pelvic bone in Patient 2 is more significant in the inferior zone of the bladder that expands more freely when the pelvic bone is not considered. However, the deformation in the anteroposterior axis is not greatly influenced, due to the fact that bladder is located over the bone so that its expansion is not highly constrained. The bladder, which partially envelops the prostate, forces it to move towards the rectum, with little constraints from the bone, since the bladder and prostate interact along the craniocaudal and anteroposterior axes. Patient 3, again, has a different structure, where the bladder anterior side is surrounded by the pelvic bone, which hinders its movement and causes a larger displacement of the prostate towards the bottom of the pelvic bone, as shown in Figs. 8 (c) and (d). For this patient, it is important to note that weak bladder-prostate interaction in the anteroposterior axis causes only small displacements of the prostate along this axis. Figs. 6-9 (a) and (b) show the palpation force data for Patient 1 under high and low IBP conditions, respectively. The effect of modelling the pelvic bone is small, especially when the IBP is low, but becomes more



significant when high intrabladder pressure is present. For the Patient 2 little difference can be seen when the pelvic bone is not modelled as shown in Figs. 6-7 (c) and (d). Therefore, for this patient, in whom the bladder wraps around and on top of the prostate forcing it to move towards the area where palpation is performed, the presence of the pelvic bone would have little influence in the outcome of instrumented DRE, making it unnecessary to be taken into account in the patient-specific model.

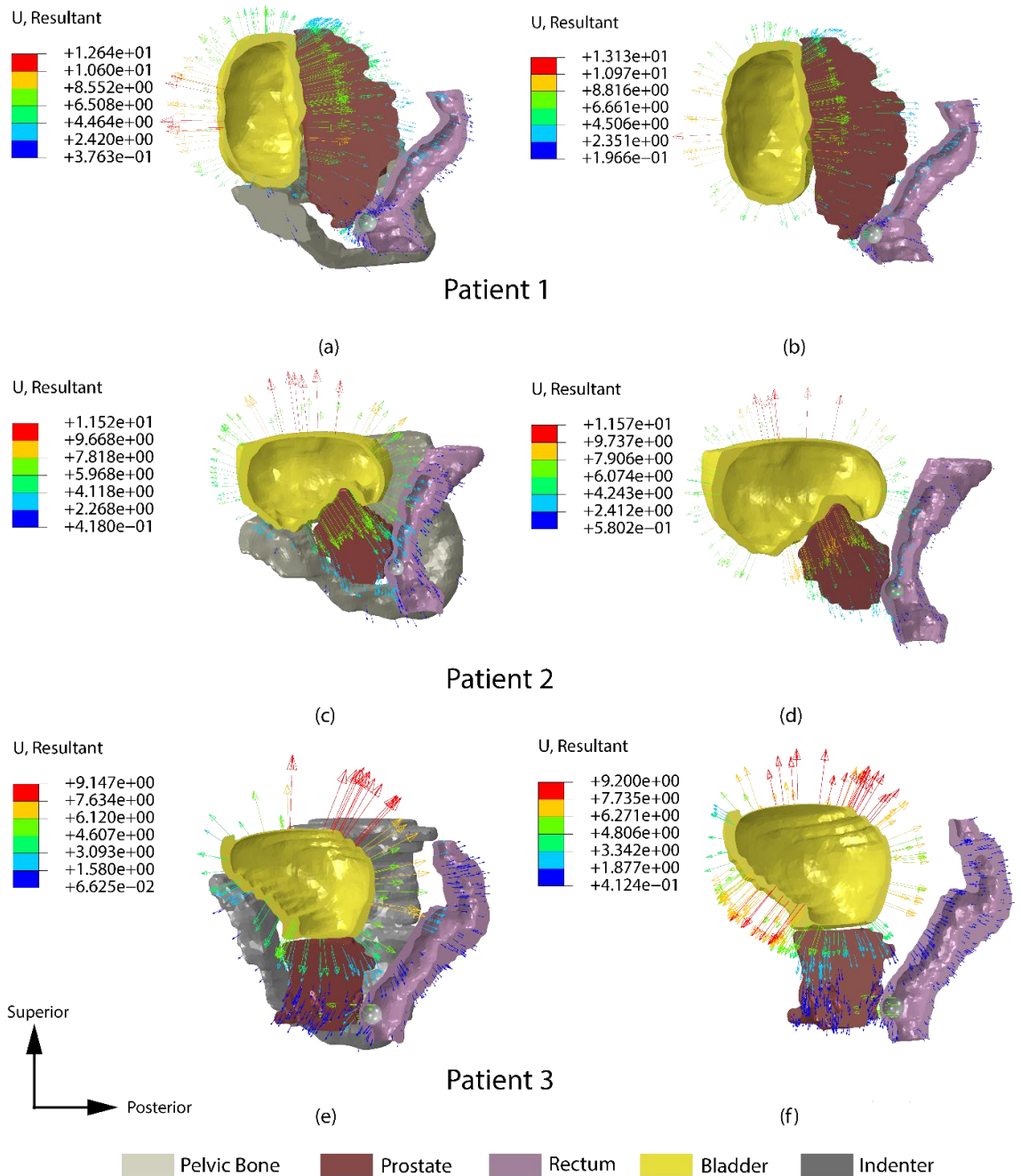


**Figure 6-8.** Displacement fields of Patients 1, 2 and 3, comparing the influence of the pelvic bone in IDRE under HIBP condition. The prostate is assumed to be completely healthy. (a) and (b): Patient 1 with and without pelvic bone, respectively; (c) and (d): Patient 2 with and without pelvic bone, respectively; (e) and (f): Patient 3 with and without pelvic bone, respectively.

Finally, for Patient 3 the differences are very small under the low intrabladder condition. On the other hand, for high intrabladder pressure, the force feedback of the instrumented DRE significantly increases due to the aforementioned effect of the pelvic bone hindering the expansion of the bladder along the anteroposterior axis. For the purpose of clinical practice it would be useful to determine *a priori* whether the pelvic bone needs to be

considered or not. Based on the evidence gathered in this section the pelvic bone should be modelled when high intrabladder pressure is considered especially if the prostate and pelvic bone wrap around the prostate.

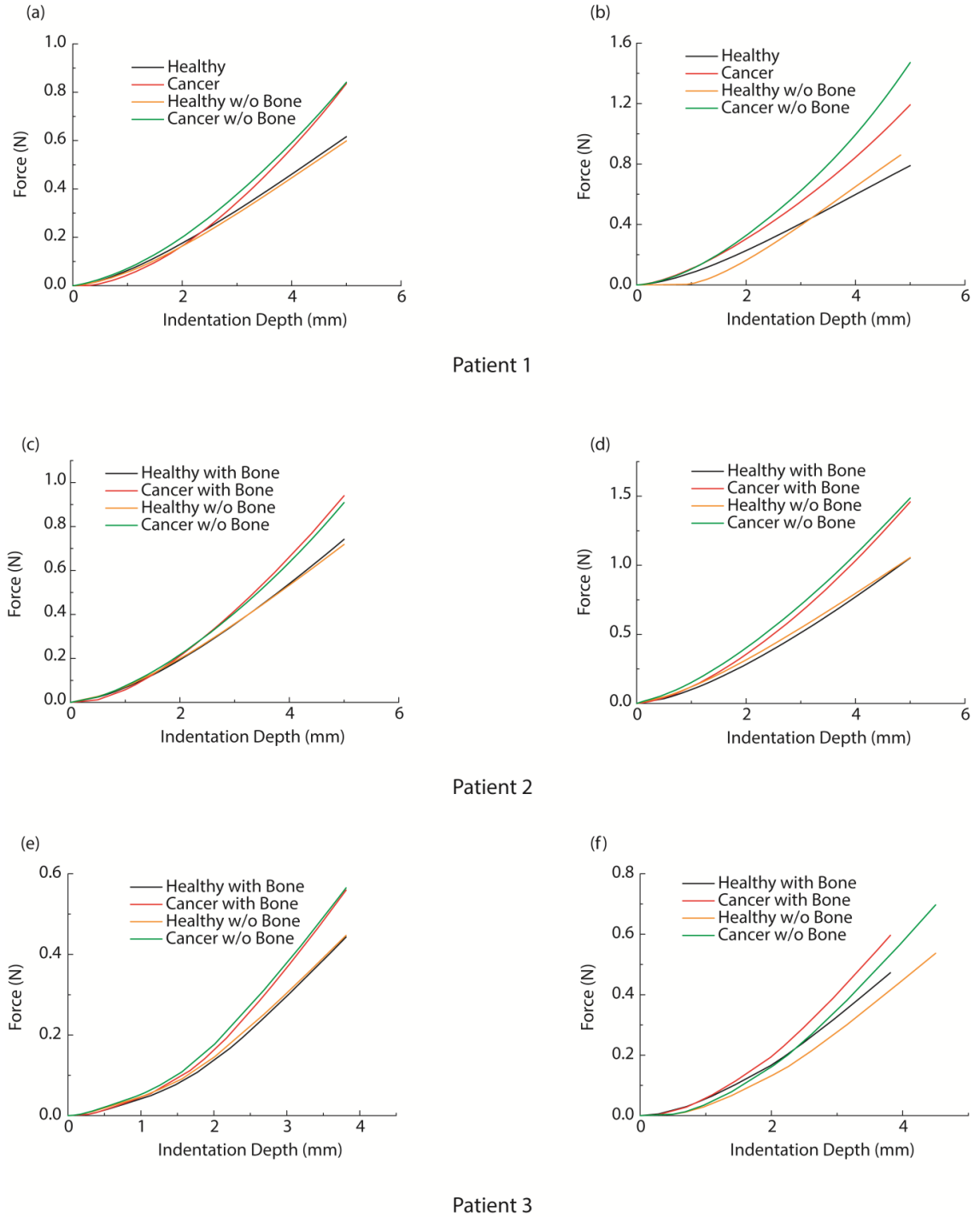


**Figure 6-9.** Comparison of the palpation forces of all three patients under low intrabladder pressure (left column) and high intrabladder pressure (right column) conditions. (a) and (b): Patient 1; (c) and (d): Patient 2; and (e) and (f): Patient 3. The results show a significant difference when the pelvic bone is not present.

## 6.7 Concluding remarks

This Chapter aims to study the effects of patient specific features, e.g. organ geometry and intrabladder pressure, in the outcome of instrumented digital rectal examination. The following key conclusions are highlighted below:

- Higher intrabladder pressure, which could be achieved by asking the patient to retain urine prior to the examination, would improve the sensitivity of the procedure;
- The pelvic bone significantly affects the force feedback of the IDRE therefore needs to be modelled, especially when high intrabladder pressure is present;
- Subject specific structural features (e.g. caused by previous treatments) could influence the outcome of diagnosis, and need to be accounted for in the framework of patient-specific modelling as well as quantitative diagnostic procedures;
- The relative position of the bladder and prostate significantly affects the force feedback and, consequently, the sensitivity of the procedure, in particular when high intrabladder pressure is present.

The proposed framework has certain limitations as it stands. Some organs, like the seminal vesicles, urethra and neuromuscular bundle were not considered because the resolution of the MRI images obtained from standard clinical protocol is insufficient to obtain an accurate representation of them. Complex interactions such as slip between fat and organs and muscle-bone connections are not taken into account due to the impracticality of doing so for the purpose of clinical diagnosis. Furthermore, it was assumed that the tissues are isotropic and the intra-patient variations of their properties are not taken into account in this chapter. It is hoped that, as a part of future work, the clinical validation of this framework will be conducted once all the data from the instrumented digital rectal examination has been collected. Ultimately, it is expected that

such an approach will allow a reduction in the number of expensive and invasive biopsies and clinical scans.

## A multiscale, mechano-morphological approach to soft tissue mechanics: application in prostate cancer diagnosis

### Contents

7.1	Summary .....	111
7.2	Modelling patient histological data .....	112
7.3	Homogenization formulation .....	114
7.4	Tissue diagnosis using SVM .....	119
7.5	Comparison between the traditional and new method. ....	120
7.6	Effects of RVE size in the distribution of the mechanical properties .....	123
7.7	Inter-patient difference in tissue elasticity .....	127
7.8	Support Vector Machines: A tool for quantitative tissue diagnosis.....	128
7.9	Concluding remarks .....	130

### 7.1 Summary

In previous chapters the importance of biomechanical features at different length scales within the framework of tissue diagnosis has been presented. However linking the changes in the microstructure caused by different conditions at lower length scale with the mechanical properties at higher length scales is still a complex task. This is of critical importance to diagnosis since probing is often made at higher length scale (i.e. organ or tissue). However, choosing the optimal probing method or sensor size to quantitatively

assess tissue quality is still challenging, especially considering constraints imposed by clinical practice: patient discomfort, testing times etc.

In this chapter a deeper look into tissue microstructure is investigated to understand how the mechanical properties at the microstructure influence the macroscopic behaviour of tissue. In particular the mechanical properties are obtained using numerical homogenization applying periodic boundary conditions (PBC) to the regions of interest. First, computational models are built using histological samples of prostatic tissue from different patients. Due to the complexity of the finite element meshes obtained, applying periodic boundary conditions using the traditional approaches was impossible. Therefore a novel method to impose PBC on arbitrary meshes is proposed in this chapter. Then the statistical distributions of the mechanical properties of different tissue samples are studied for each patient. It is shown that there exists an overlap between the distribution of the mechanical properties of healthy and cancerous tissue that could potentially hinder the effectiveness of the diagnosis. To resolve this problem the use of Support Vector Machines (SVM) is proposed and tested for different sizes of samples. It is expected that these results will help to determine the optimal size of the probing so that specific devices and protocols can be optimized. It is also hoped to increase the number of patients in the database to improve the accuracy of the diagnosis and transfer the proposed technique into clinical practice in due course.

## **7.2 Modelling patient histological data**

To compare the effects of inter-patient difference and various pathological conditions in the mechanical properties of prostatic tissue two patients were selected in this chapter. Histopathological samples were obtained from their prostate excised during total prostatectomy using the laparoscopic approach.<sup>5</sup> The pathological analysis of Patient 1's

---

<sup>5</sup> This is to acknowledge Dr. M O'Donnell (Consultant Uropathologist, Western General Hospital, UK) for the pathohistological analysis of the images used in this Chapter.

prostate revealed acinar adenocarcinoma with Gleason 3+4 and a PSA of 10.1 *ng/ml* and a prostate volume of 158cc, whilst Patient 2 was diagnosed with a more aggressive acinar adenocarcinoma with a Gleason 4+3 grade albeit a lower PSA level of 9.1 *ng/ml*. Fig. 7-1 shows histological samples of both patients where the coloured region represents the solid phase and the white region the fluid phase. To generate the finite element model the geometry was reconstructed using Scan-IP (Simpleware Ltd., Exeter, UK). First, the images were converted to grayscale. Then a threshold of 0 and 180 was used to identify the solid and fluid phases, respectively. To remove noise from the image and obtain improved meshes a Gaussian recursive filter and island removal filter were used. In this analysis small strains were considered. The solid phase was modelled with an elastic modulus of 17kPa and a Poisson's ratio of 0.3. For the liquid phase a softer and nearly incompressible material with a bulk modulus of 2GPa was considered [168].

Considering various RVE sizes allows the analysis of the changes in the apparent mechanical properties when the size of the RVE varies. Additionally it allows a quantitative analysis of acini volume which can be related to conditions such as BPH and prostate cancer. Three different sizes (i.e 0.68mm, 1.34mm and 2.68mm) were used to discretize the histological images into RVEs. It should be noted that the RVEs that contain the background of the histological image were discarded. With such considerations, a total of 1274 healthy and 290 cancerous samples for RVE size of 0.68mm (50×50 pixels), 383 healthy and 59 cancerous samples for size 1.34mm (100×100 pixels), 89 healthy and 11 cancerous samples for size 2.68 mm (200×200 pixels) were obtained for patient 1. For patient 2 the sample numbers are 1966 and 997 (0.68mm), 443 and 217 (1.34mm) and 84 and 39 (2.68mm) for healthy and cancer, respectively. A summary of the RVE selections considered in the study is shown in Table 7-1.



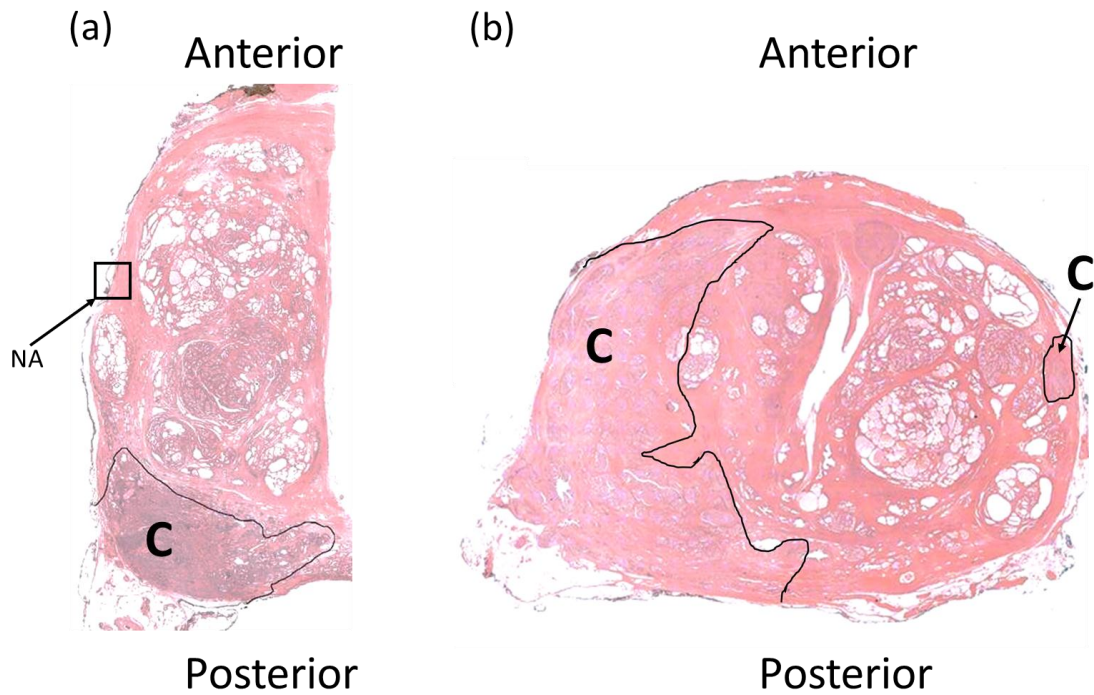


**Figure 7-1.** The apparent mechanical properties are obtained for two different patients. (a) shows the a histological sample from Patient's 1 prostate stained with haematoxylin and eosin (H&E). The cancerous nodule is located at the posterior left side and marked with 'C'. NA indicates an example of an RVE which would not be unacceptable since it contains part of the background. (b) shows a histological images stained with H&E from Patient 2. This patient has two different cancerous nodules located in the left and right sides of the prostate.

**Table 7-1.** Summary of the number of samples and sizes considered throughout the study.

RVE Size	0.68 mm (50 × 50)		1.34 mm (100 × 100)		2.68 mm (200 × 200)	
Number	Healthy	Cancer	Healthy	Cancer	Healthy	Cancer
Patient 1	1274	290	383	59	89	11
Patient 2	1966	997	443	217	84	39

### 7.3 Homogenization formulation

Different boundary conditions have been proposed to obtain the apparent mechanical properties of an RVE. Kinematic uniform boundary conditions (KUBC) consist of a set of prescribed displacement fields and often provide upper bounds for the apparent stiffness, whereas static uniform boundary conditions (SUBC) often results in a lower

bound by imposing a stress field instead [169]. Periodic boundary conditions (PBC) constrain the displacement at the boundaries to be periodic and then strain fields in the vertical, horizontal and shear components are imposed [63].

To impose periodicity at the boundary of RVE, meshes with matching nodes at opposite sides of the RVE are often used. However, obtaining such periodic meshes may be difficult or require extremely fine meshes especially when the geometry is reconstructed from medical images with complex topologies. Different methods that use, among others, Lagrange polynomials and spline interpolations have been reported in the literature to overcome such complication [79, 80]. However, they have certain constraints in the topology of the sample or in their compatibility with Finite Element Analysis codes where accessing the stiffness matrix is complex or impossible. Additionally they may significantly increase the number of variables and consequently the computational cost.

The solution of a traditional finite element analysis is the displacement at each node of the domain. Using the interpolation functions it is then possible to obtain other variables (displacement, strain etc.) at any point over the domain and, in particular, at the boundaries. In this study it is proposed to consider a finite number of control points at each boundary located periodically but not necessarily corresponding with nodes from the Finite Element mesh. The constraints (see [63, 79] for details) that impose the periodic displacements at the boundaries are considered at these points instead of at the Finite Element nodes. Using the same interpolation functions as the ones used in the finite element analysis (linear in this example), the displacements at the control points can be expressed as a linear combination of the nodal displacements. Fig. 7-2 (a) shows a traditional periodic mesh where every node in the boundary (e.g. node 'a') has a matching node at the opposite boundary (e.g. node 'b'). In arbitrary meshes as the one shown in Fig. 7-2 (b) that is not always the case as demonstrated by point 'c', which does not have a matching node at the opposite side. The following equations exemplify the boundary

conditions on nodes ‘a’ and ‘b’ of a periodic mesh when a vertical compression test is considered.

$$U_x^a = U_x^b \quad (7-20)$$

$$U_y^a = U_y^b \quad (7-21)$$

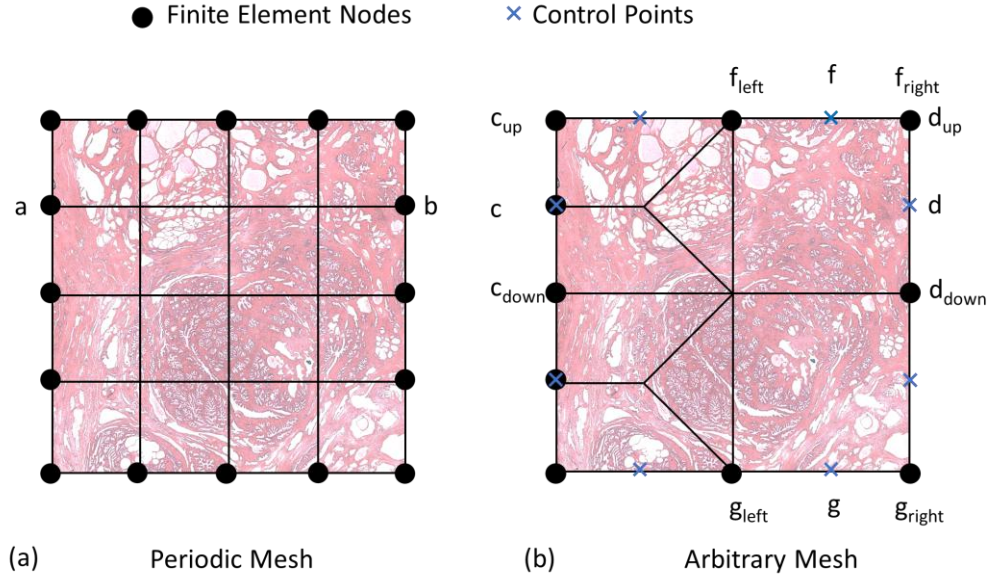


**Figure 7-2.** (a) Example of a periodic mesh where nodes in all the faces have a matching node at the opposite faces. (b) shows an arbitrary mesh where some nodes (for instance c) do not have a matching node on the opposite face.

With the proposed methodology the constraints are imposed at points ‘c’ and ‘d’ instead in Fig. 7-2 (b) as follows:

$$U_x^c = U_x^d \quad (7-22)$$

and

$$U_y^c = U_y^d \quad (7-23)$$

However, the displacements at the control point ‘d’ are not a variable of the FE problem, therefore it has to be expressed as a function of those variables. In this particular case, without loss of generality, the same linear interpolation used in the FE analysis is considered

$$U_x^c = \frac{(U_x^{d_{up}} - U_x^{d_{down}})}{l} \cdot \frac{l}{2} + U_x^{d_{down}} \quad (7-24)$$

and similarly for the y axis

$$U_y^c = \frac{(U_y^{d_{up}} - U_y^{d_{down}})}{l} \cdot \frac{l}{2} + U_y^{d_{down}} \quad (7-25)$$

In general, however, the control points are not coincident with the Finite Element nodes and, therefore, the displacements at both controls points also need to be expressed as a function of the FE nodal values.

$$\frac{(U_x^{f_{left}} - U_x^{f_{right}})}{l} \cdot \frac{l}{2} + U_x^{f_{right}} = \frac{(U_x^{g_{left}} - U_x^{g_{right}})}{l} \cdot \frac{l}{2} + U_x^{g_{right}} \quad (26-7)$$

and

$$\begin{aligned} \frac{(U_y^{f_{left}} - U_y^{f_{right}})}{l} \cdot \frac{l}{2} + U_y^{f_{right}} \\ = \frac{(U_y^{g_{left}} - U_y^{g_{right}})}{l} \cdot \frac{l}{2} + U_y^{g_{right}} + \epsilon_0 \end{aligned} \quad (7-27)$$

where  $\epsilon_0$  is the global displacement applied along the y axis.

Using the same variables (i.e. nodal displacements) to impose boundary conditions in arbitrary meshes has the advantage of resulting in a reduced computational cost since only the linear constraints need to be calculated, which is negligible compared with the computational cost of increasing the dimension of the stiffness matrix of the FE problem.

To test the methodology an RVE topology often used as a benchmark test for periodic structures is considered [79]. It consists of 4 circular inclusions embedded into a softer matrix. Different tests are considered here to demonstrate the robustness and accuracy of the method. First, a comparison of the stress fields obtained using the traditional and novel method is considered under the small strain hypothesis. The Young's modulus of the matrix is 1MPa and that of the inclusion 100MPa. Such stiffness values are arbitrary and

the large stiffness ratio between the matrix and the inclusion only aims at creating a complex stress distribution to demonstrate the ability of the methodology. Both materials have a Poisson's ratio of 0.3. In this test the part is mesh with 100 nodes each side and 80 controls points each side are considered. In order to derive the apparent stiffness tensor using homogenization, three tests were carried out: tensile tests in x and y axis and a shear test. In the small strain scenario a 10% strain was considered. In each test the average strain  $(\epsilon_{xx}, \epsilon_{yy}, \epsilon_{xy})$  and stress  $(\sigma_{xx}, \sigma_{yy}, \sigma_{xy})$  were calculated over the volume of the RVE. Thus to obtain the 9 components of the stiffness tensor shown below, a set of linear equations has to be solved so that Eq. (7-10) is satisfied:

$$C_{ij} = \begin{pmatrix} C_{11} & C_{12} & C_{13} \\ C_{21} & C_{22} & C_{23} \\ C_{31} & C_{32} & C_{33} \end{pmatrix} \quad (7-28)$$

$$\langle \sigma \rangle = C_{ij}^{effective} \langle \epsilon \rangle \quad (7-29)$$

where  $\langle \sigma \rangle$  is the average stress in the RVE,  $C_{ij}^{effective}$  is the effective stiffness tensor and  $\langle \epsilon \rangle$  the average strain in the RVE. Using the same methodology, the influence of the number of control points in the estimated apparent stiffness when finite strains are considered is analysed. In this case global tensile strains of up to 100%, larger than those often used in clinical diagnosis, are considered to validate the methodology. The mechanical properties of the matrix and inclusions are modelled as Neo-Hookean Eq. (7-11) for both materials,  $C_1=0.02$ ,  $D_1=0.001$  and  $C_2=0.06$ ,  $D_2=0.001$ , respectively. This leads to approximately  $\nu=0.5$ ,  $E_1=120\text{kPa}$  and  $E_2=360\text{kPa}$ .  $\bar{I}$  is the first deviatoric strain invariant,  $J$  is the elastic volume ratio and  $C$  and  $D$  are material parameters.

$$\Psi = C(\bar{I} - 3) + \frac{1}{D}(J - 1)^2 \quad (7-30)$$

It should be noted here that the mechanical properties used in this example are arbitrary as the aim is to analyse the convergence of the method. For that reason a Neo-hookean material model, which is stable independently of the stress and strain state, is used. When large strains and non-linear materials are considered the 9 components of the stiffness tensor are calculated at different strain magnitudes (i.e. 1%, 2%, 5%, 10%, 15%, 20%, 40%, 60%, 100% in this study).

The aim of varying the size of RVEs is to determine whether there is a characteristic size (i.e. length scale) at which the mechanical characterization of tissue should be performed taking into account a balance between accuracy and computational cost.

#### **7.4 Tissue diagnosis using SVM**

Clinical practice often requires binary decisions: action or wait, treatment or palliative care, surgery or medications, which are often based on binary diagnosis: healthy or diseased, live or necrotic etc. However, obtaining such dichotomic diagnosis could be challenging and certainly subject to inter-clinician variation. Therefore a mathematical tool that is able to reliably determine whether a set of data corresponds to a certain class (i.e. healthy or diseased) would be useful for diagnostic purpose.

Support vector machines (SVM) are a popular class of algorithms used for classifications and regression analysis. The objective of the algorithm is to find the hyperplane or hypersurface that maximizes the distance between the different classes, which are either quantitative or qualitative results from an experiment usually with multiple variables. First the SVM is trained with a set of data whose inputs and outputs are known (e.g. the cancerous or healthy diagnosis is known *a priori* for each stiffness tensor). Then the SVM can be used to predict the outputs for new inputs whose condition (i.e healthy or cancer) is unknown. To avoid overfitting without compromising the accuracy, data validation is required. 100-fold cross validation is used when the number of samples is greater than

100 and the hold-one-out approach otherwise [170]. Radial basis functions are used as the kernel of the SVM [171].

### **7.5 Comparison between the traditional and new method.**

The traditional method to impose periodic boundary conditions (PBC) requires identical meshes at opposite RVE faces. In this section a comparison study between the apparent properties of a RVE obtained using the traditional method and the proposed one, free from that meshing constraint, is carried out. Figs. 7-4(a) and (b) show the stress distribution in the RVE subject to the tensile test in the vertical direction when PBC are imposed using the traditional and the proposed methods, respectively. The main differences, although small, occur at the boundaries around the control points due to the stress concentration caused by the nodal forces required to enforce the periodic boundary conditions. However, to obtain the apparent properties, which is the main focus of the methodology, only the average stress and strains are critical. Fig. 7-5 shows the apparent properties obtained at different strains and the convergence towards the solution calculated using the traditional PBC method. Due to the symmetries of the RVE the material can be considered orthotropic therefore only some components of the stiffness tensor are shown. When a low number of points, compared to the 100 nodes per edge in this particular model, is used the resulting values of the different components, especially the diagonal ones, is lower than those calculated using the traditional method. This could be caused by the strain being applied effectively in a local manner where only a few boundary nodes are subjected to nodal forces rather than globally, when most (if not all) of the boundary nodes are subjected to nodal forces. Therefore the stiffer insertions, located relatively far away from the control points, would have little influence. Increasing the number of control points the solution converges to one obtained using the traditional method.  $C_{11}$  and  $C_{22}$  follow a similar trend and the error is within 5.2% when using 40 control points (compared to 100 nodes per side in the mesh used in the traditional

method). The traditional solution and the new one are effectively the same when more than 80 control points are used.  $C_{21}$ , however, decays with increasing strains and needs more control points to achieve the same level of accuracy as  $C_{11}$  or  $C_{22}$ . On the contrary  $C_{33}$  is less sensitive to changes in the number of control points. It can be seen that increasing the number of control points would further reduce error. However, the number of control points cannot be increased without a limit since only one control point between the nodes of an element should be selected. If a greater number of control points is used the resulting constraints become linearly dependent. This leads to numerical instabilities that cause the displacements to become zero or close to zero. As a result the stiffness of the sample is artificially increased. This imposes a constraint in the mesh on the faces where the aspect ratio of elements should be reasonably close to 1. In this particular example, without loss of generality, 3-node triangular plane stress elements with linear interpolation are used. However, it should be noted that the method would be also applicable with square elements or a mix of both. Such flexibility allows to use square elements in areas of simple geometry to increase the accuracy and efficiency and triangular elements areas of complex geometry without worrying about the type of element present on the surfaces. Therefore automatic meshing algorithms can be used with the associated advantages (i.e. reduction in pre-processing of simulations and cost). Such constraint, which may appear strict, is often satisfied since most meshing algorithms have elements with aspect ratios close to 1 to avoid numerical instabilities. It should be noted here that the number of control points could be less than the number of nodes at each side without compromising the accuracy. This would result in a lower number of constraints and therefore a lower computational cost, especially when nonlinear methods such as the Lagrange multipliers are used to solve the FE problem. More importantly, the same numerical method used to impose the constraints with periodic meshes (matrix row and column deleting, Lagrange multipliers etc.) can still be used and no further



mathematical manipulation of the stiffness matrix or load vector is required. This results in a simplification of the coding and a reduced computational cost.

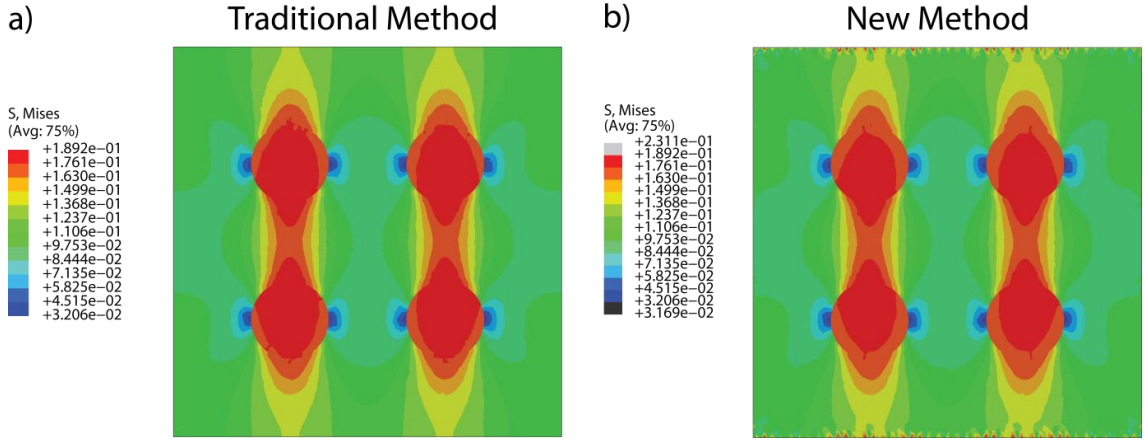


**Figure 7-4.** Von Mises stress distribution in MPa when the traditional method (a) and the new method (b) are used to impose periodic boundary conditions in a tensile test with 80 control points.

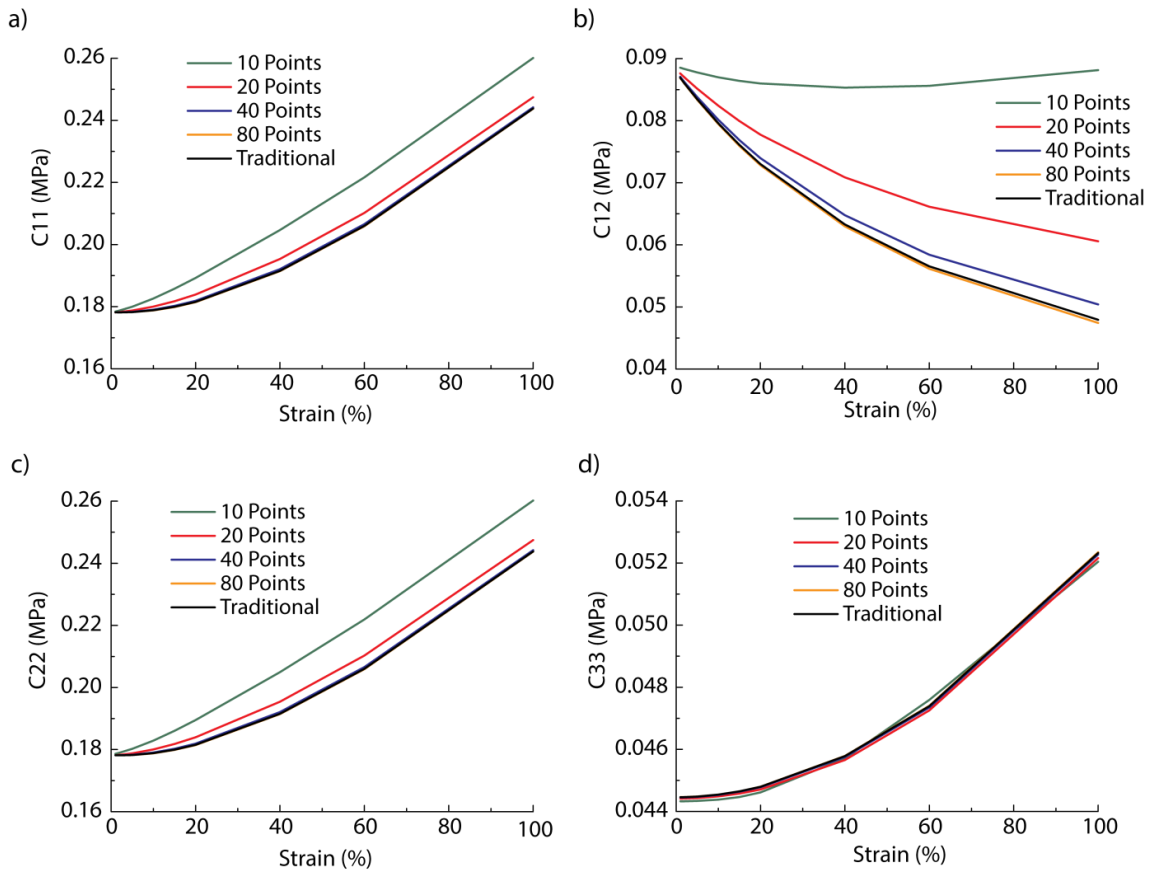


**Figure 7-5.** Convergence results toward the traditional PBC solution for increasing number of control points. (a) shows the results for the component  $C_{11}$  and (b)-(d) for  $C_{12}$ ,  $C_{22}$  and  $C_{33}$  respectively.

## 7.6 Effects of RVE size in the distribution of the mechanical properties

The aim of this section is twofold: (i) to investigate the influence of RVE size and convergence of the mechanical properties at different length scales and (ii) to analyse the changes in the distribution of mechanical properties. First, the eigenvalues of all the stiffness tensors are calculated to ensure that they are positive thus physically feasible. Fig. 7-6 shows the components of the apparent stiffness tensor for both patients, with two categories, i.e. cancerous and healthy tissue. The results are also listed in Table 7-2. It should be noted that the average stiffness values of healthy tissues are always below those of cancerous tissue. This would imply that, on average, it is possible to distinguish the properties of both phases (i.e. cancer and healthy). However, the standard deviation is significantly higher in the healthy samples. In fact the standard deviation of the different components overlap in all cases except in one,  $C_{11}$  for size 1.34mm (100×100) in Patient 1. This highlights that considering just one elastic constant and a certain threshold to distinguish between healthy and cancer may lead to inaccurate diagnosis. Therefore more sensitive techniques (such as support vector machines (SVM) which will be discussed later) should be used to discriminate between healthy and cancerous tissue. The average apparent stiffness observed in Patient 2 is slightly higher than Patient 1 (measured by  $C_{11}$ ,  $C_{22}$  and  $C_{33}$ ), which suggests a lower amount of acini and potentially a more aggressive cancer in Patient 2 [41]. In the case of Patient 1 the average values of the stiffness tensor components tend to converge when the size of RVE is greater than 1.34 mm. Patient 2 shows a similar trend although interestingly the difference between the distribution of the stiffness components of RVEs with sizes of 0.68 mm and the 1.34 mm is smaller. This can also be observed in Fig. 7-1 where a greater number of smaller acini in Patient 2 than in Patient 1 can be seen.

Most tissue samples present a high degree of anisotropy, close to orthotropic with a lower stiffness in the y-axis. Such difference is rather obvious in the case of the healthy tissue,

particularly for samples in size of 0.68mm. It has been found, in literature, the stromal fibres present certain directionality in prostatic tissue [141], which suggests a certain degree of anisotropy the healthy tissue possesses. This correlates well with the aforementioned results. However, in the cancerous case, the tissue appears to be isotropic since the average values of the diagonal components  $C_{11}$  and  $C_{22}$  become equal. This would indicate that the stroma is randomly oriented and has little directionality. Such disorganized structure could be directly linked to Gleason score assigned to the histopathological samples. The detailed results for the average mechanical properties can be found in Tables 7-2 and 7-3.

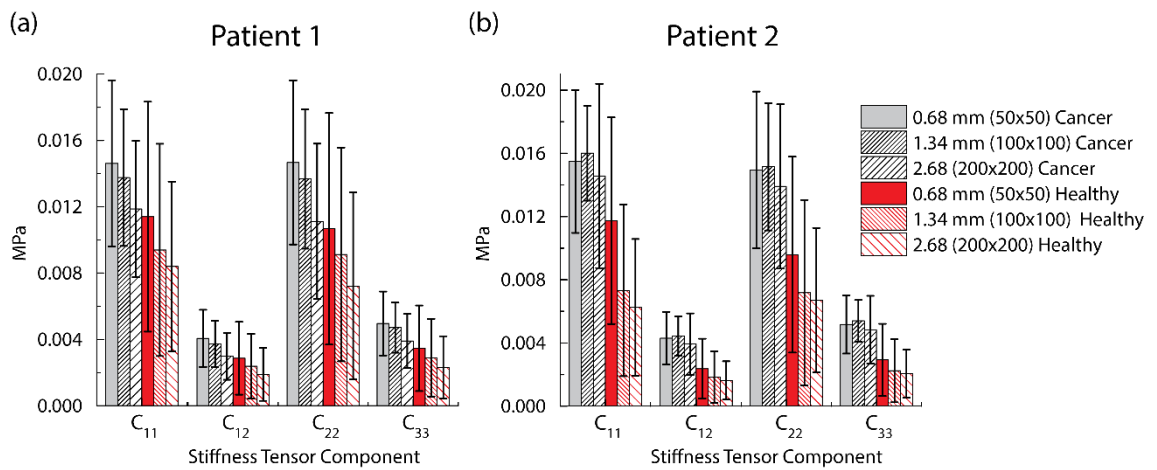


**Figure 7-6.** Average mechanical properties of the healthy and cancerous RVE's from patient 1(a) and 2(b) and their respective standard deviations.

**Table 7-2.** Results of the average stiffness tensor for different RVE sizes in Patient 1. All the elements are shown to depict the quasi orthotropic behaviour of the material. Terms C31,C32, C13 and C23 are much smaller than the rest and close to zero.

	<b>Cancer</b> <b>(0.68mm)</b>	<b>Cancer</b> <b>(1.34 mm)</b>	<b>Cancer</b> <b>(2.68mm)</b>	<b>Healthy</b> <b>(0.68 mm)</b>	<b>Healthy</b> <b>(1.34mm)</b>	<b>Healthy</b> <b>(2.68mm)</b>
<b>c11</b>	1.55E-02	1.60E-02	1.46E-02	1.17E-02	7.33E-03	6.25E-03
<b>c21</b>	4.29E-03	4.44E-03	3.89E-03	3.37E-03	1.85E-03	1.65E-03
<b>c31</b>	3.21E-05	1.82E-05	-3.66E-05	3.93E-05	-3.52E-05	-1.56E-05
<b>c12</b>	4.30E-03	4.44E-03	3.93E-03	2.37E-03	1.84E-03	1.63E-03
<b>c22</b>	1.50E-02	1.51E-02	1.39E-02	9.59E-03	7.19E-03	6.71E-03
<b>c32</b>	5.52E-05	2.89E-05	-1.97E-05	-3.22E-05	-5.28E-05	-4.64E-05
<b>c13</b>	3.23E-05	1.71E-05	-2.21E-05	-3.47E-05	-3.52E-05	-1.46E-05
<b>c23</b>	5.65E-05	2.70E-05	-1.89E-05	-3.48E-05	-5.59E-05	-4.92E-05
<b>c33</b>	5.18E-03	5.40E-03	4.84E-03	2.93E-03	2.25E-03	2.05E-03

**Table 7-3.** Results of the average stiffness tensor for different RVE sizes in patient 2. All the elements are shown to depict the quasi orthotropic behaviour of the material.

	<b>Cancer</b> <b>(0.68mm)</b>	<b>Cancer</b> <b>(1.34 mm)</b>	<b>Cancer</b> <b>(2.68mm)</b>	<b>Healthy</b> <b>(0.68 mm)</b>	<b>Healthy</b> <b>(1.34mm)</b>	<b>Healthy</b> <b>(2.68mm)</b>
<b>c11</b>	1.46E-02	1.38E-02	1.19E-02	1.14E-02	9.40E-03	8.40E-03
<b>c21</b>	4.07E-03	3.72E-03	2.98E-03	3.08E-03	2.38E-03	1.87E-03
<b>c31</b>	-4.07E-05	-1.10E-04	-9.02E-05	1.65E-05	-7.55E-06	-3.53E-06
<b>c12</b>	4.06E-03	3.73E-03	2.99E-03	2.87E-03	2.38E-03	1.89E-03
<b>c22</b>	1.47E-02	1.37E-02	1.11E-02	1.07E-02	9.12E-03	7.22E-03
<b>c32</b>	-4.00E-05	-1.10E-04	-9.68E-05	-6.45E-05	-2.65E-05	-3.41E-05
<b>c13</b>	-3.93E-05	-1.10E-04	-9.91E-05	-4.55E-06	-6.32E-06	1.24E-05
<b>c23</b>	-4.01E-05	-1.00E-04	-9.93E-05	-1.16E-05	-2.74E-05	-2.46E-05
<b>c33</b>	4.96E-03	4.71E-03	3.91E-03	3.47E-03	2.90E-03	2.31E-03

Fig. 7-7 shows the relative frequency of the magnitude of components  $C_{11}$ ,  $C_{22}$  and  $C_{33}$  of the apparent stiffness tensor of tissue samples from Patient 1 when different RVE sizes are considered. Monotonic convergence of the mechanical properties is not observed in the healthy samples when the RVE size varies. For the smallest sample size a wide range of apparent stiffness is observed as shown in Figs. 7-7(b). However, Fig. 7-7 (a) shows a peak around 15 kPa which is not present at the higher scales. Such peak is related to areas

with lower concentration of acini which are more compliant than solid areas. For the cancerous tissue their stiffness tensors are significantly different. For RVE sizes smaller than 1.34mm the mechanical properties are similar, especially for higher stiffness values as seen in Figs. 7-7(c) and (d) which show that the stiffness of cancerous tissue tends to be higher. It should be noted here that the distribution of the tissue stiffness could be correlated to the statistical distribution of acini size in the tissue microstructure. Both the stroma (i.e. solid part of the tissue) and acini (i.e. fluid phase) contribute to the apparent tissue stiffness, and it would be interesting, as a potential future work, to quantitatively relate the apparent tissue stiffness to the volume fractions of both phases for diagnosis purpose.

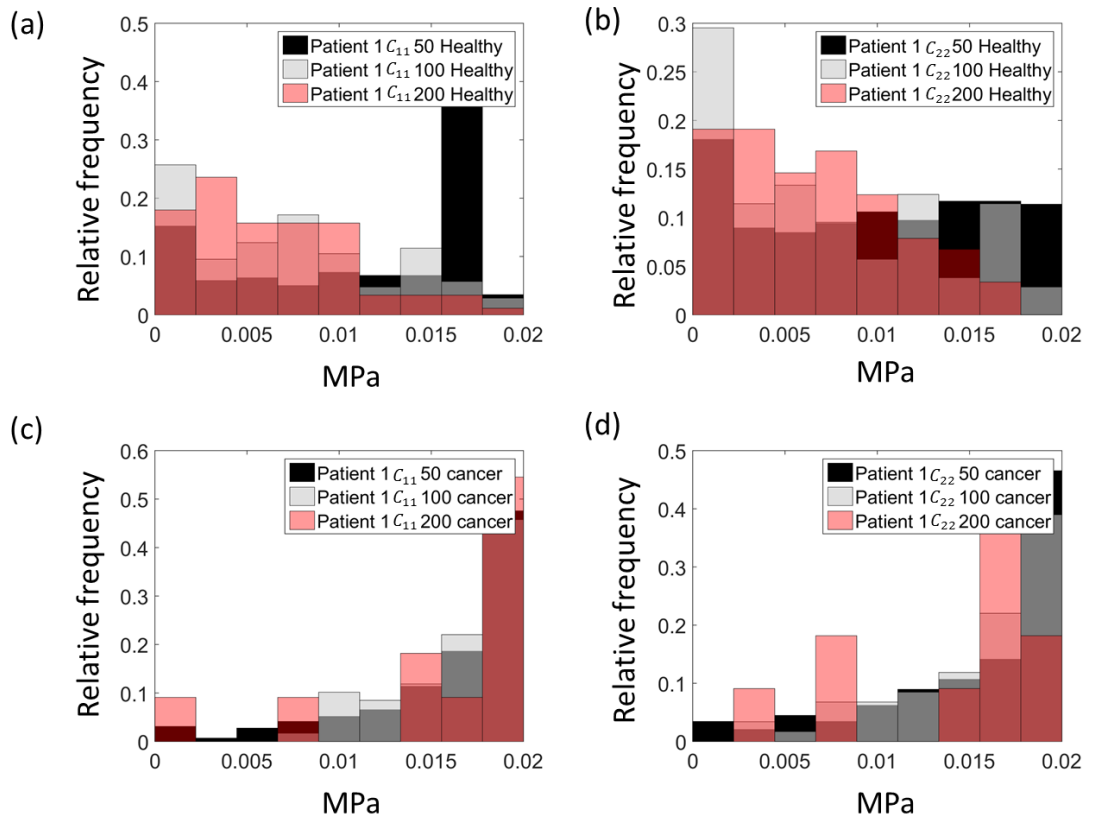


**Figure 7-7.** Comparison of the relative frequency of the magnitude of components  $C_{11}$  and  $C_{22}$  of the stiffness tensor for different RVE sizes and different conditions: healthy and cancer for Patient 1.

## 7.7 Inter-patient difference in tissue elasticity

Figs. 7-8 and 7-9 show the relative frequency of the three diagonal terms of the stiffness tensors of tissue samples from both patients when three different RVE sizes (i.e. 0.68, 1.34 and 2.68 mm) are considered. The distribution of apparent stiffness is similar for  $C_{11}$  and  $C_{22}$  especially when the smallest RVE is used. A similar trend is observed for the intermediate RVE size. However when the largest RVE is used, the distribution of their stiffness components is considerably different. It should be remarked that in the healthy case the mechanical properties for the medium RVE are significantly different as opposed to the cancerous case. This could be related to a different pathophysiological condition (i.e. prostatitis, BPH etc.) or to inter-patient variability. Patient 2, who had a more aggressive adenocarcinoma (Gleason 4+3 as opposed to Gleason 3+4 for Patient 1) has a wider range of stiffness values which suggests a less organized tissue microstructure associated with a higher Gleason score.

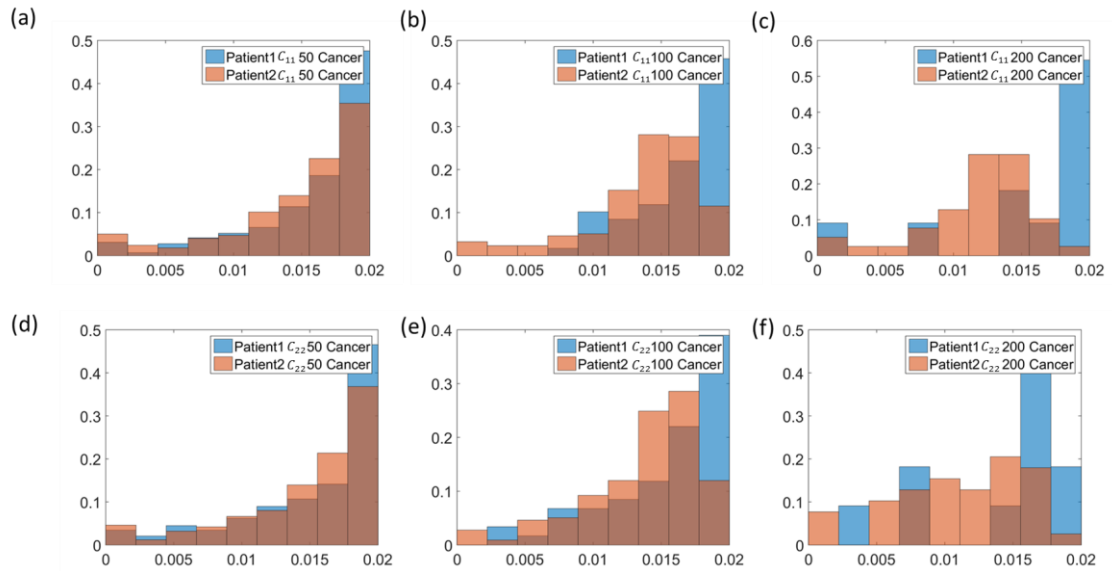


**Figure 7-8.** Inter-patient comparison of the relative frequency of the apparent mechanical properties of RVE for different sizes when only cancerous tissue is considered.

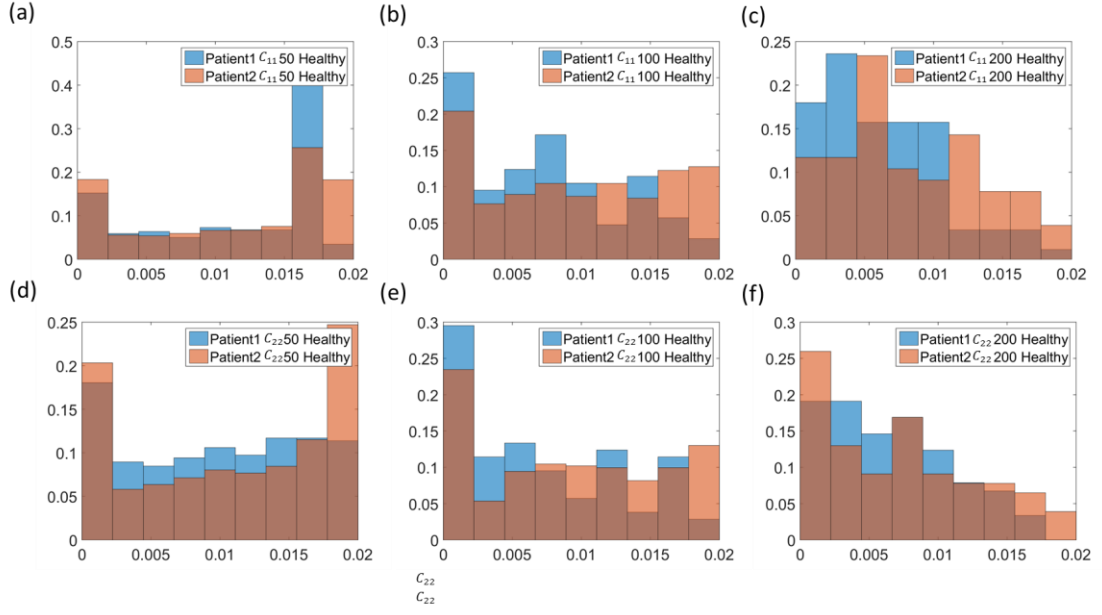


**Figure 7-9.** Inter-patient comparison of the relative frequency of the apparent mechanical properties of RVE for different sizes when only healthy tissue is considered.

It is worth highlighting that the structural features in tissue at lower length scale (i.e. 0.68mm size) are more affected by the pathology, whereas at higher length scale (i.e. 2.68mm size) the difference in tissue microstructure is mainly caused by inter-patient variation. This would imply that a measurement at a larger scale could provide useful information about unique features such as the presence of BPH or variations in the volume of stroma which can be related to the shape of acini [172]. On the other hand a lower scale measurement could be more useful to assess tissue quality where patient specific features may be less relevant when the mechanical properties are considered as a continuum, as in elastography or palpation. These results suggest that with a sufficiently large database it would be possible to construct benchmark histograms for different types of pathologies at lower scales, against which clinical measurements could be employed to determine the presence of certain diseases.

## 7.8 Support Vector Machines: A tool for quantitative tissue diagnosis.

In the previous sections it is shown that the mechanical properties of both cancerous and healthy tissues spread over a wide range. At the same time they have certain overlap in a

certain range of stiffness over which diagnosis is difficult to carry out. The aim of this section is to evaluate the feasibility of using Support Vector Machines (SVM) to determine whether diagnosis can be conducted using the apparent stiffness tensor of the tissue sample.

Fig. 7-10 shows the diagnosis results obtained using SVM. First a dummy case is considered, where the classified dataset is also used for training. Results from this case provide a qualitative insight to the differences between the mechanical properties of healthy and diseased tissue. If an accuracy of 100% is obtained then the classes (healthy and diseased) could be perfectly distinguished from each other. Figs. 7-10(a) and (b) show the results for this scenario which are below 100%, especially for the cancerous tissue in Patient 2 when the size of the RVE tested and the one used to train the SVM are different. This is caused by an overlap in the distribution of the mechanical properties of healthy and cancerous samples as previously shown in Figs. 7-8 and 7-9. Figs. 7-10(c) show the results where Patient 1 is diagnosed by the data trained from Patient 2 and Fig. 7-10(d) where Patient 2 is diagnosed with data trained from Patient 1. In healthy tissue the results for the largest RVE have an accuracy of over 70% however, for the medium size RVE the diagnosis is significantly worse, especially for Patient 2. Finally a database with data from both patients is constructed to train the SVM. Characterization of healthy tissue is performed with an accuracy of over 80% except in one scenario, which corresponds to training the learning machine with data from the smallest RVE (1.34mm) to diagnose the biggest one (2.68 mm). This means that knowing the size of the sample being tested is critical. The largest RVE appears to be preferable for diagnosis as its accuracy is higher in most of the scenarios attempted. However in diagnosis of cancer tissue the accuracy is less. As a result a diagnosis using SVM based on healthy tissue could provide a higher level of confidence.



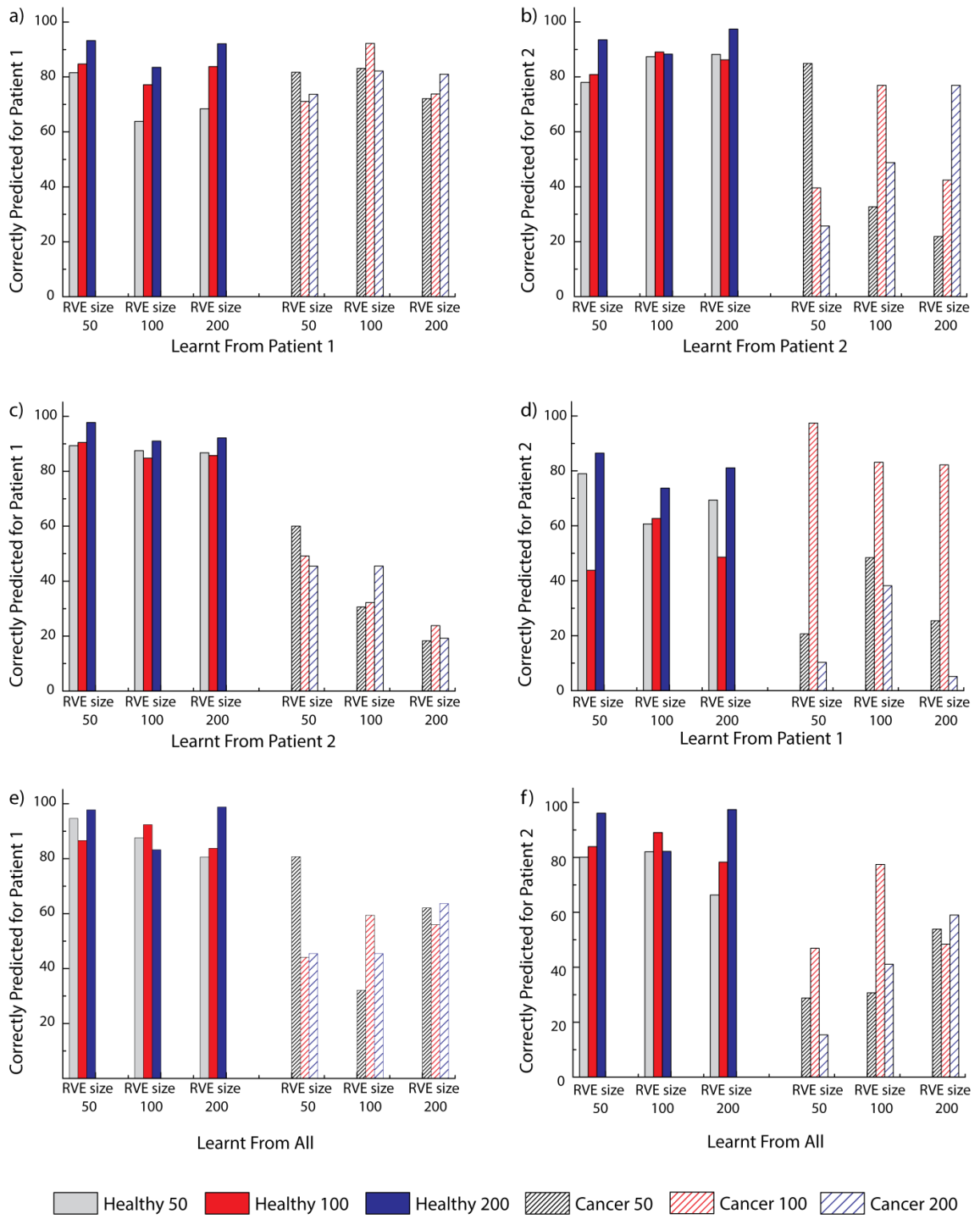


**Figure 7-10.** Results from the SVM prediction using the stiffness tensor as input. X-axis shows the dataset used to train the SVM and the Y-axis the results of the classes correctly predicted.

## 7.9 Concluding remarks

The objective of this chapter was threefold: **(a)** to propose a novel method to impose periodic boundary conditions on arbitrary meshes, **(b)** to analyse how changes in the

microstructure of prostatic tissue influence its apparent stiffness and (c) to investigate the possibility of using support vector machines as a diagnostic tool.

In this chapter it has been shown that the proposed methodology to impose periodic boundary conditions on arbitrary meshes results in similar accuracy as the traditional one where symmetric meshes are enforced at the boundaries. This result has been validated under the hypothesis of small and finite strains. By using the aforementioned methodology to analyse the apparent mechanical properties of tissues, it has been shown that cancerous tissue appears to be, on average, statistically isotropic although each different region of interest may have certain anisotropic behaviour. On the other hand healthy tissue shows a certain degree of anisotropy which could be related to stroma orientation and could be further correlated to the pathophysiological conditions. The size of the sample being tested has been proved to be critical. At higher length scale (i.e. when the RVE size is larger), inter-patient variation has more dominant influence than pathological conditions in the apparent tissue stiffness. However, results from lower length scales (i.e. when the RVE size is smaller) better describe tissue quality. In the case of cancerous tissue the statistical distribution of mechanical properties is similar for RVE sizes of 0.68mm and 1.36mm. This suggests that an RVE or a set of RVEs with mechanical properties that mimic such statistical distribution could be defined as a benchmark result for tissue stiffness for the purpose of diagnosis. Finally, Support Vector Machines have been adopted to perform quantitative diagnosis based on the apparent mechanical properties of tissue samples. In the analysis carried out in this chapter SVM have been used to classify the data into two classes: healthy and cancer. However, it would be even more beneficial for clinical use to differentiate between multiple pathologies such as BPH or the Gleason score of a certain sample. To predict such details the SVM should be trained with a larger database with data from multiple pathologies. It could be further enriched with other data such as PSA level.

The methodology presented here has some limitations as it stands. First both tissues phases (solid and liquid) are considered as a continuum solid. Although this assumption has been thoroughly used in literature it is hoped to perform a similar analysis using a realistic fluid structure interaction analysis. The number of patients in this study is limited due to the complexity of obtaining complete histological images from patients that have undergone a complete prostatectomy. It is expected to increase such database which would result in a better understanding of the changes in the mechanical properties caused by different diseases at different stages, which would subsequently allow a better training of the Support Vector Machine. The ultimate objective would be to increase the understanding of the changes in the mechanical properties of tissues so that improved early diagnostic techniques can be put in place to improve the life expectancy and quality of patients with reduced medical costs.

## Heterogeneity in Tissue Diffusivity: An Application in Drug Delivery

### Contents

---

8.1	Summary .....	133
8.2	Histology modelling: homogenisation of diffusivity .....	134
8.3	Formulation of pharmacodynamics – modelling of tissue response .....	139
8.4	Numerical homogenization of tissue diffusivity .....	141
8.5	Sensitivity analysis .....	145
8.5.1	A preliminary analysis of diffusion in soft tissues.....	145
8.5.2	Intravenous drug delivery – sensitivity analysis .....	148
8.5.3	Bolus injection – sensitivity analysis .....	152
8.6	Concluding remarks .....	159

---

### 8.1 Summary

In previous chapters novel techniques have been proposed to perform soft tissue diagnosis considering the mechanical behaviour of the tissue at organ scale (Chapters 3, 4, 5 and 6) and also at the microscale (Chapter 7). In fact, in the preceding chapter the apparent mechanical properties of soft tissue at organ scale have been linked to the underlying microstructures of the tissue. In particular it has been shown that pathological conditions influences the tissue microstructure thus subsequently vary the mechanical properties of the tissue. However, the changes in the microstructure of the tissue not only affect the mechanical properties but also drug diffusion. It is therefore critical to quantify such

changes to evaluate the efficacy of a treatment so it can be tailored in a patient-to-patient basis.

In this chapter changes in the diffusivity of two drugs, commonly used as chemotherapeutic agents (i.e. doxorubicin and paclitaxel), caused by the various conditions of the tissue (i.e. cancer and healthy) and by the inherent properties of the drug (i.e. molecular weight) are analysed. The apparent diffusivity is obtained using numerical homogenization with periodic boundary conditions (PBC) to the different regions of interest from two selected patients. Due to the complex topology of soft tissue microstructures obtaining periodic meshes is complex and inefficient. Therefore the same methodology used in Chapter 7 to impose PBC with arbitrary meshes is adopted in this chapter. The statistical distributions of the tissue diffusivity are analysed for each patient and drug. To evaluate the impact of the drug in the population of healthy and cancerous cells a competition model that considers biological factors such as cell cycle arrest and replication rate is employed. This framework, which brings together patient-specific drug diffusivity and pharmacodynamics, would allow to determine the outcome of a chemotherapeutic treatment before drug is administered to the patient. A patient specific model of a third patient obtained from a histological sample where the blood vessel network was visible was used to illustrate the proposed framework in different scenarios where different drugs were administered intravenously or via a bolus injection following multiple drug concentration profiles. It is hoped that this platform will allow to optimise the treatment of soft tissue diseases especially those such as cancer where the aggressiveness of the drugs limits the maximum dose.

## **8.2 Histology modelling: homogenisation of diffusivity**

Diffusivity of drug in tissues is influenced by different factors such as its molecular weight [173] and its solubility in fat and water [174]. In this study two drugs often used in chemotherapy treatments are considered: paclitaxel and doxorubicin, with molecular

weights of 853.906 *g/mol* and 543.52 *g/mol*, respectively. Swabb *et al.* [173] experimentally determined a relationship to estimate the diffusivity of drugs with different molecular weights in tissues. In this chapter the diffusivity of drugs in the solid phase of prostatic tissue (i.e. stroma) is estimated using that relationship, showed in Eq. (8-1).

$$D_{tissue} = 1.778 \cdot 10^{-4} \cdot MW^{-0.75} \quad (8-31)$$

where  $D_{tissue}$  is the drug diffusivity in  $cm^2/s$  and  $MW$  is the molecular weight of drug in *g/mol*. It is important to note here that the Eq. (8-1) is only used to estimate the drug diffusivity in the solid phase of the tissue. The estimated values of the diffusion coefficient in the solid phase of the tissue for Doxorubicin and Paclitaxel are  $1.58 \cdot 10^{-6} cm^2/s$  and  $1.13 \cdot 10^{-6} cm^2/s$ , respectively. The drug diffusivities in water ( $4 \cdot 10^{-6} cm^2/s$ ) and in blood vessels ( $5 \cdot 10^{-7} cm^2/s$ ) are adopted from [175] and [15] respectively. The diffusivity of drug in blood is assumed to be the same as in water. The apparent diffusivity of the drugs in tissue will be calculated from numerical homogenisation using patient-specific histological models, which later will be demonstrated.

Three patients are considered in this study. Histopathological analysis of Patient 1's prostate revealed acinar adenocarcinoma with Gleason 3+4 and a PSA of 10.1 *ng/ml* and a prostate volume of 158cc. Patient 2 was diagnosed with a more aggressive acinar adenocarcinoma with a Gleason 4+3 grade albeit a lower PSA level of 9.1 *ng/ml*. Finally Patient 3 has a prostate specific antigen (PSA) concentration of 4.72 *ng/ml*. Histological analysis of the prostate revealed acinar adenocarcinoma with a Gleason score of 7 (3+4) which invades 5% of the prostate volume and is present in both lobes and the apex. Fig. 8-1 (a) and (b) show the histological samples of the patients, which will be later used to estimate the diffusion properties. A high resolution image of Patient 3 is shown in Fig. 8-1(c) where the blood vessels are visible.

To estimate the local diffusive properties in soft tissues the histological samples of Patient 1 and Patient 2 are discretised into square representative volume elements (RVE) of two different sizes: 1.34mm and 2.68mm, respectively. Samples that contain the background of the image are discarded as shown in Fig. 8-1. A summary of the number of samples obtained from each patient is shown in Table 8-1.

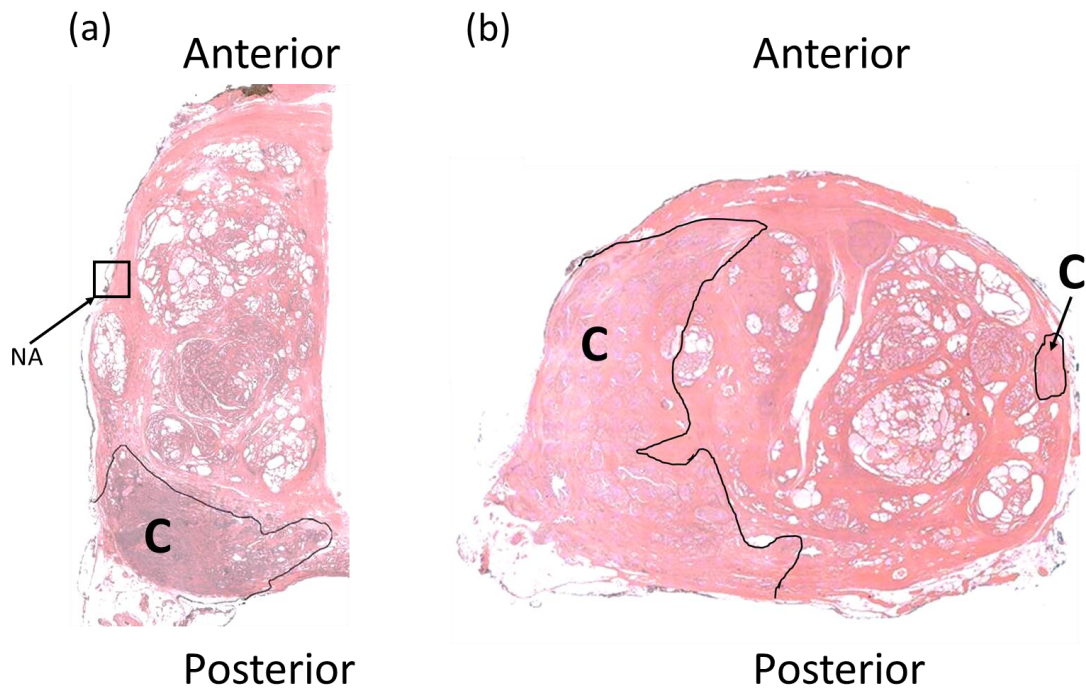


**Figure 8-1.** The histological samples of patient's 1 and 2 used to estimate the apparent tissue diffusion are shown in (a) and (b). NA indicates an unacceptable area to calculate the apparent diffusion tensor since it contains part of the background. C indicates the cancerous areas.

**Table 8-1.** Summary of the number of samples and sizes considered throughout the study.

<b>RVE Size</b>	<b>1.34 mm (100 × 100)</b>		<b>2.68 mm (200 × 200)</b>	
<b>Number</b>	<b>Healthy</b>	<b>Cancer</b>	<b>Healthy</b>	<b>Cancer</b>
<b>Patient 1</b>	383	59	89	11
<b>Patient 2</b>	443	217	84	39

Periodic boundary conditions (PBC) are applied to each RVE to obtain their effective diffusivity tensor. Although periodic meshes are often used to apply PBC they are difficult or impractical to when the models are reconstructed from biological images as in prostatic tissue as shown in Fig. 8-1. In this chapter the methodology proposed in Chapter 7 is used to impose PBC on arbitrary meshes to obtain the effective diffusivity tensor shown in Eq. 8-2. The procedure of applying numerical homogenisation in the framework of FE analysis, is summarised in [63]. For clarity the procedure is illustrated with a periodic mesh as shown in Fig. 8-2.

$$D = \begin{bmatrix} D_{11} & D_{12} \\ D_{21} & D_{22} \end{bmatrix} \quad (8-32)$$



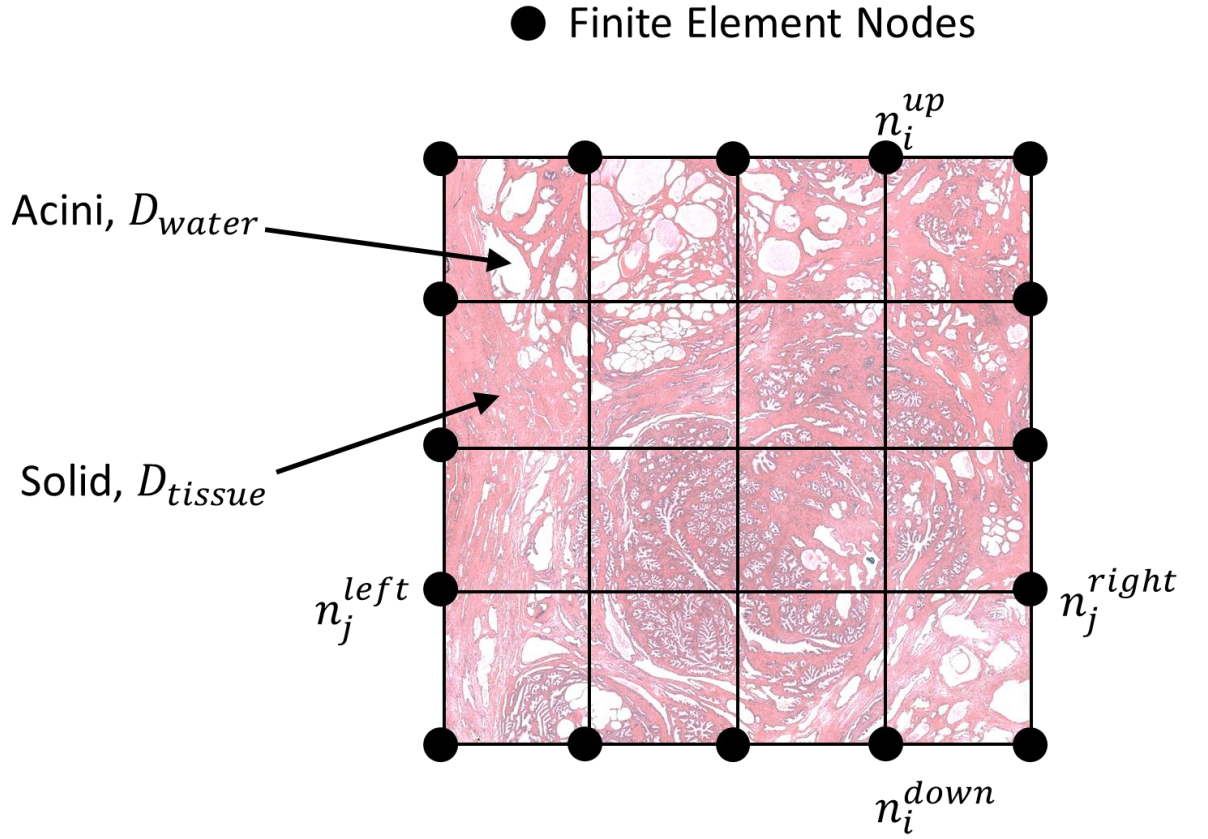


**Figure 8-2.** The histological samples are divided into regions of interest to be analysed. Acini are clusters of cells that contain fluid. For the purpose of the analysis in this chapter the diffusivity properties of such fluid are considered like those of water. The diffusivity properties of the solid phase are calculated from Eq. 8-1.

Two tests are performed to obtain the apparent diffusion properties. First a gradient is imposed in the vertical direction. Periodic boundary conditions require the difference between the values in opposite nodes to be constant (i.e. the concentration gradient  $\Delta Concentration$ ) as shown in Eq. 8-3.

$$n_i^{up} - n_i^{down} = \Delta Concentration \quad (8-33)$$

In the vertical faces the concentration in nodes located at symmetrical position have to be equal as illustrated in Eq. 8-4.

$$n_j^{left} - n_j^{right} = 0 \quad (8-34)$$

Next, a gradient is imposed in the horizontal direction which results in an equation parallel to Eq. 8-3 as seen below in Eq. 8-5

$$n_j^{left} - n_j^{right} = \Delta Concentration \quad (8-5)$$

The equations to impose the periodic boundary conditions in the horizontal faces read now

$$n_i^{up} - n_i^{down} = 0 \quad (8-6)$$

Finally the components of the diffusivity tensor in Eq. 8-1 are obtained so that Eq. 8-7 is satisfied where  $\langle J \rangle$  is the average flux and  $\langle \nabla C \rangle$  the average concentration gradient.

$$\langle J \rangle = D^{effective} \cdot \langle \nabla C \rangle \quad (8-7)$$

### 8.3 Formulation of pharmacodynamics – modelling of tissue response

The efficacy of a chemotherapy treatment depends on various biophysical factors such as blood vessel density, interstitial fluid pressure and tissue diffusivity as well as biochemical factors such as cell drug-resistance and ECM pH. The aim of this chapter is to investigate the role of tissue microstructure (in particular its heterogeneity) in the efficacy of drug delivery. To evaluate how drug influences the population of cancerous and health cells, in this study, the model proposed by Komarova and Wodarz [176] is considered and summarised below:

$$\dot{S} = r_s S(1 - u + \beta \epsilon_s u) + \alpha u r_s S(1 - \epsilon_s) - \phi S \quad (8-8)$$

$$\dot{M} = r_m M(1 - u + \beta \epsilon_m u) + \alpha u r_m M(1 - \epsilon_m) - \phi M \quad (8-9)$$

$$\begin{aligned} \phi = & S r_s [1 - u(1 - \beta \epsilon_s - \alpha(1 - \epsilon_s))] + \\ & + M r_m [1 - u(1 - \beta \epsilon_m - \alpha(1 - \epsilon_m))] \end{aligned} \quad (8-10)$$

where  $S, M$  represent the fractions of healthy and cancerous (mutated) cells and  $\dot{S}, \dot{M}$  are the temporal derivatives, respectively.  $r_s$  and  $r_m$  are the replication rates of healthy and mutated cells and the probability of a mutant being viable is  $\alpha$ .  $u$  is the probability of a genetic alteration occurring during replication. This parameter is controlled by the

treatments used to combat the disease such as chemotherapy and radiotherapy. In this study the pharmacodynamics parameter,  $u$ , is considered to be equal for paclitaxel and doxorubicin although in practice they may be different, since the main aim of this chapter is to investigate the effects of drug diffusion in heterogeneous soft tissues rather than the different pharmacodynamics properties of the drugs.  $\epsilon_s, \epsilon_m$  are the probabilities that a genetic alteration is repaired in the healthy and diseased cells, respectively.  $\beta$  is associated to the cost (or probability) associated with cell repair. When  $\beta = 0$  the repairing cells never replicate and when  $\beta = 1$  there is no cell cycle arrest.  $\alpha$  is the probability of a mutant being viable. Arbitrary values consistent with the dynamics are found in the literature [176].

In this chapter a modification to the model is introduced and cell cycle arrest of healthy and cancerous cells becomes different so that  $\beta_m < \beta_s$ . Eqs. 8-8 to 8-10 then become:

$$\dot{S} = r_s S(1 - u + \beta_s \epsilon_s u) + \alpha u r_s S(1 - \epsilon_s) - \phi S \quad (8-11)$$

$$\dot{M} = r_m M(1 - u + \beta_m \epsilon_m u) + \alpha u r_m M(1 - \epsilon_m) - \phi M \quad (8-12)$$

$$\phi = S r_s [1 - u(1 - \beta_s \epsilon_s - \alpha(1 - \epsilon_s))] + M r_m [1 - u(1 - \beta_m \epsilon_m - \alpha(1 - \epsilon_m))] \quad (8-13)$$

Two drug delivery scenarios are considered in this study: an intravenous delivery and a bolus injection directly into the tissue. In the first scenario a sinusoidal profile of drug infusion following the equation:  $\sin(\frac{2\pi t}{25}) + 1$  is used. In the case of bolus injection, a single dose and a sinusoidal profile are considered. To model different concentrations of the drug being delivered the parameter  $u$  is multiplied by various amplification factors ( $A_f$ ) accordingly in order to explore how tissue responds to various resulting drug concentrations.

Fig. 8-3 (a) shows a histological sample from Patient 3 where the blood vessels are visible. The cancerous nodule is characterised by small irregular acini compared to the bigger ones in the healthy part. The homogenised model, where healthy and cancerous tissues

are considered as continuum solid materials, is shown in Figs. 8-3 (b) and in 8-3(c) with the area where the bolus is injected highlighted.

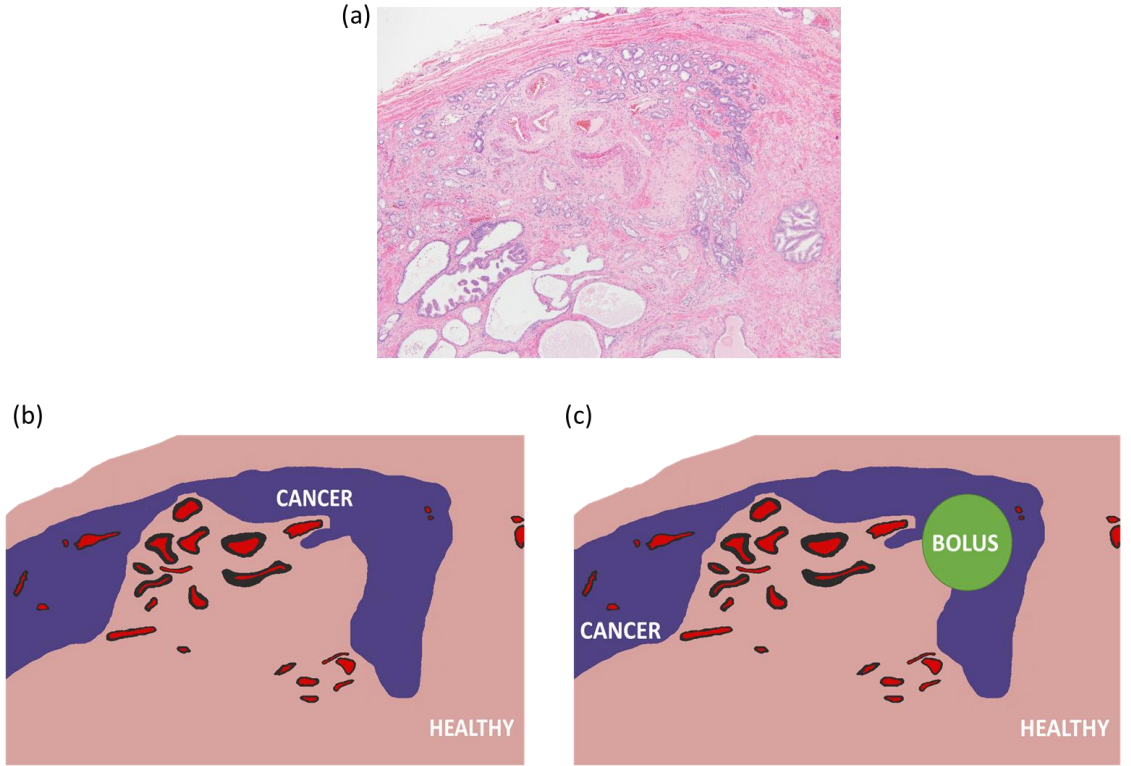


**Figure 8-3.** The histological sample from patient 3 used to illustrate the proposed framework is presented here. (a) shows the histological slice of patient 3 with visible blood vessels. The image shows the multiscale nature of the tissue and therefore the need to obtain apparent mechanical properties to reduce computational time. Images (b) and (c) show the homogenized model and the position of the blood vessels. In (c) the area where the bolus injection is applied is highlighted. Convergent meshes with 156225 3-node linear diffusion elements are used to model the drug diffusivity.

#### 8.4 Numerical homogenization of tissue diffusivity

In this section the influence in drug delivery efficacy of RVE size, administered drug, pathological condition and inter-patient variability is analysed. Fig. 8-4 (a) shows the average apparent diffusivities and the standard deviation obtained for Patient's 1 and 2 from the histological images considering RVE sizes of 1.34 and 2.68mm, respectively. Only the main diagonal components  $D_{11}$  and  $D_{22}$  are plotted here. The minor diagonal elements  $D_{12} = D_{21}$  are orders of magnitude lower ( $\sim 10^4$  times lower) and therefore of limited significance in the results. The effective diffusivity of Doxorubicin in tissue is, as expected, higher than that of Paclitaxel due to its higher molecular weight. The inter-

patient differences are small especially when the healthy smaller RVE (i.e. 1.34 mm) is considered. This result emphasises the hypothesis previously described in Chapter 7 that smaller RVE may contain information relevant to the pathological condition and larger ones to the patient-specific features such as the topology of the tissue microstructure. It should be noted here that major differences are related to the drug being administered and tissue pathological condition rather than inter-patient differences. In fact the influence of using paclitaxel instead of doxorubicin is higher than the changes caused by pathology. On the other hand, the sample size has a small impact in the estimated apparent diffusivity, for both healthy and cancerous tissues. The standard deviation is smaller in the larger samples than in smaller samples in healthy tissue, however the standard deviation becomes considerably higher in the larger RVE than in the smaller ones in tumour tissue. Although there is a clear trend depicted by the current data set, it should be emphasized here that the number of large samples is relatively small therefore there is a need of carrying out studies on tissue samples from more patients in order to add to the confidence of the statistical analysis.

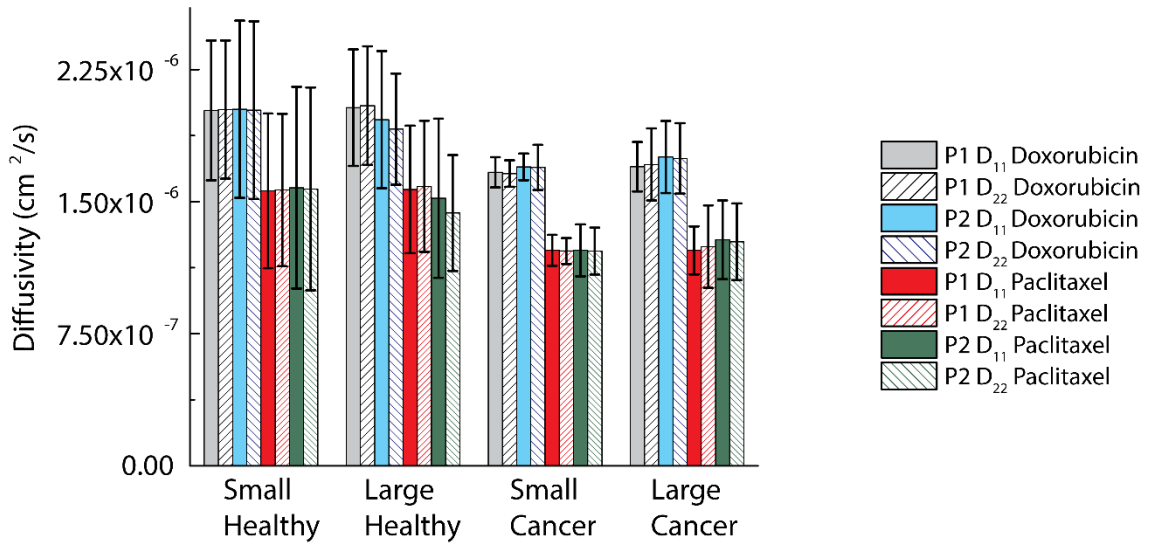


**Figure 8-4.** Statistical distribution of the diffusivity results for the different sizes of RVE considered (i.e. small and large), conditions (i.e. cancer and healthy), drugs (i.e. Paclitaxel and Doxorubicin), patients (Patient 1 and Patient 2) and diffusivity tensor components ( $D_{11}$  and  $D_{22}$ ).

Figs. 8-5 (a) and (b) show, when Doxorubicin is administered, the distribution of the components  $D_{11}$  and  $D_{22}$  of diffusivity for Patient 1 when RVE sizes of 1.34 mm and 2.68mm are considered , and Figs. 8-5(d) and (e) for Patient 2. Independently of the RVE size the cancerous diffusivity mainly ranges between  $1.5\text{e-}6$  and  $2\text{e-}6 \text{ cm}^2/\text{s}$  whereas the healthy one is dispersed in the range  $1.5\text{e-}6$  to  $4\text{e-}6 \text{ cm}^2/\text{s}$ . Such different distributions may lead to potential diagnosis techniques based on measurement of tissue diffusivity. Results show that cancerous tissue has a lower degree of anisotropy since most samples have similar diffusivity along both axes. The healthy samples present higher degree of anisotropy, especially in the case of Patient 2. This, in addition to a drift of the diffusivity toward higher values, can be linked to the health condition of the patient which has bigger acini. Such a high fraction of fluid phase in tissue microstructure increase the effective diffusivity of drug in tissue. This would be of critical importance in older patients who are prone to suffer from BPH. Lower doses of chemotherapy could be given to achieve similar drug concentration in tissue. On the contrary, patients with larger cancerous nodules, whose diffusivity is significantly lower, may require higher drug doses or different drug delivery methods to achieve a sufficient drug concentration to eliminate the malignant cells. The similar results for Paclitaxel are obtained, as shown in Fig. 8-6, where the effective diffusivity is lower than Doxorubicin.

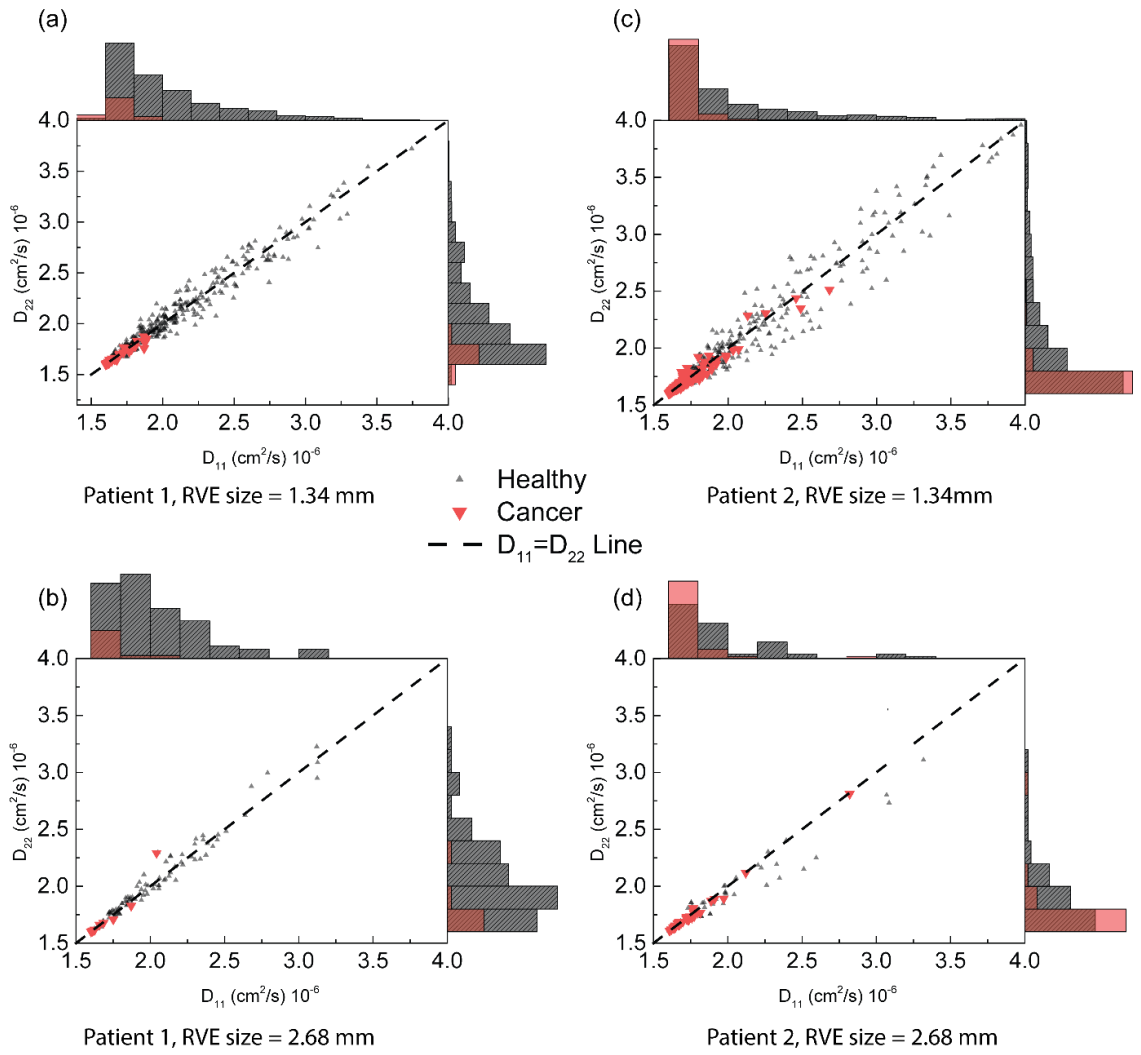


**Figure 8-5.** Comparison of the diagonal components of the effective diffusivity tensor and their distribution for two different RVEs Patient 1(a-b) and Patient 2(c-d) when the drug used is Doxorubicin. Although the results are anisotropic the distribution along the symmetry line (where  $D_{11} = D_{22}$ ) is relatively symmetric. This suggests that the average behaviour of the tissue could be approximately isotropic.

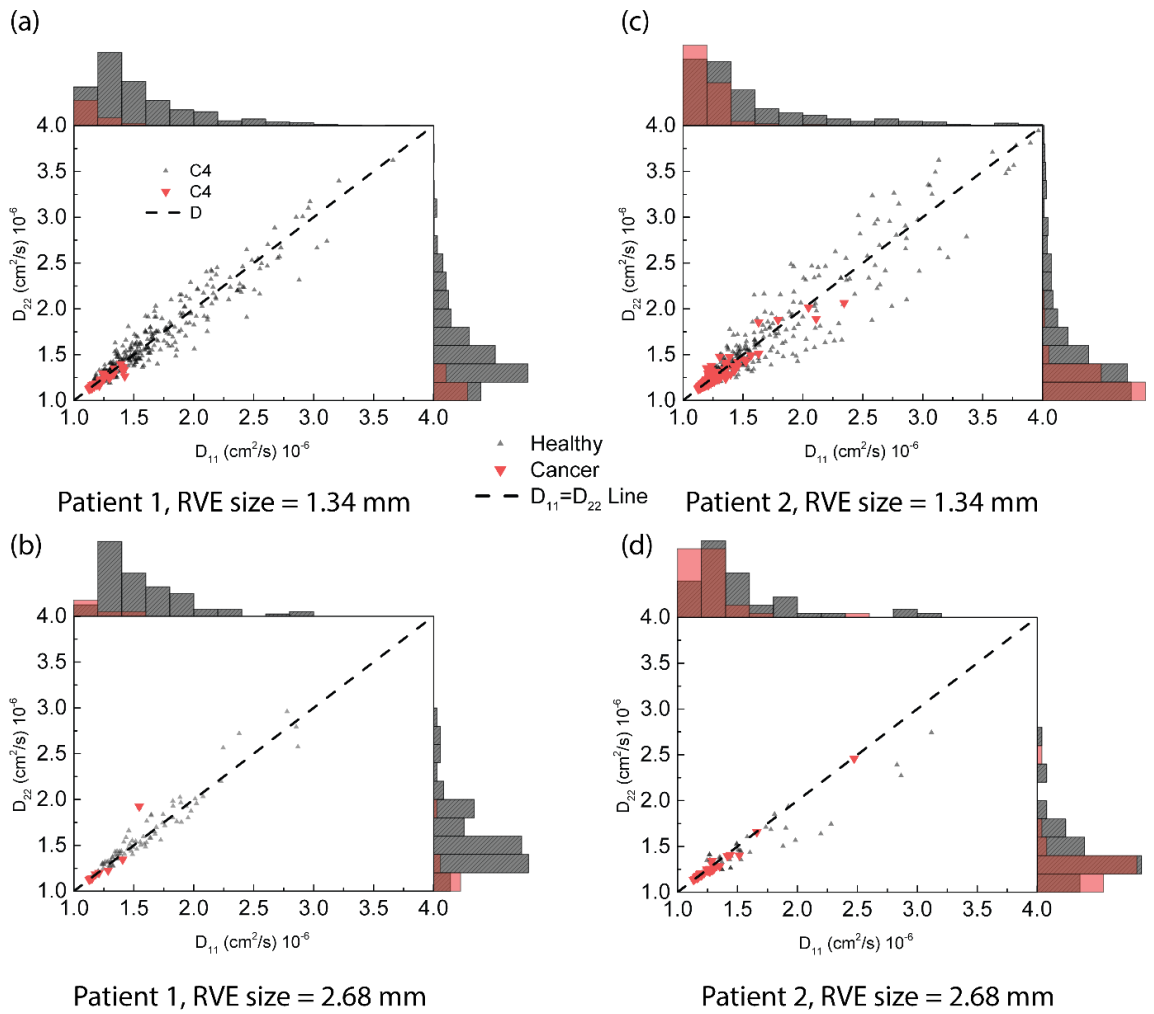


**Figure 8-6.** Comparison of the diagonal components of the effective diffusivity tensor and their distribution for two different RVEs Patient 1(a-b) and Patient 2(c-d) when Paclitaxel is used as a chemotherapeutic agent. The results are qualitatively similar to those shown in Fig. 8-5 for Doxorubicin. Although the results are anisotropic the distribution along the symmetry line (where  $D_{11} = D_{22}$ ) is relatively symmetric. This suggests that the average behaviour of the tissue could be approximately isotropic.

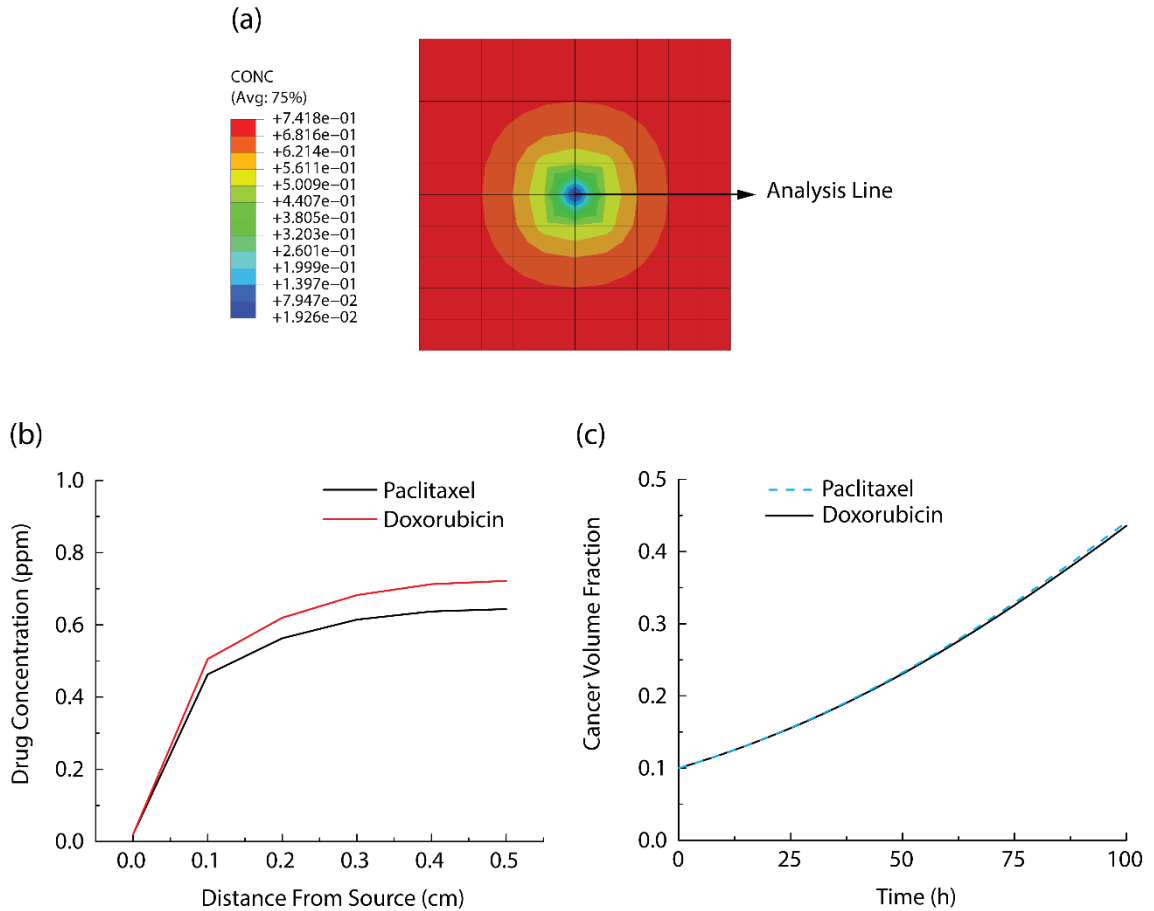
## 8.5 Sensitivity analysis

### 8.5.1 A preliminary analysis of diffusion in soft tissues.

In this section a preliminary analysis of the drug diffusion and drug efficacy problem is presented in a simplified model to better describe and understand why the cancer volume is approximately the same when two different drugs with the same diffusivity are used. Fig. 8-7 (a) shows a 1 cm-sided rectangle with a single point source of drug located in the centre. An initial concentration is considered at  $t=0$ h. The concentration profile after 100h



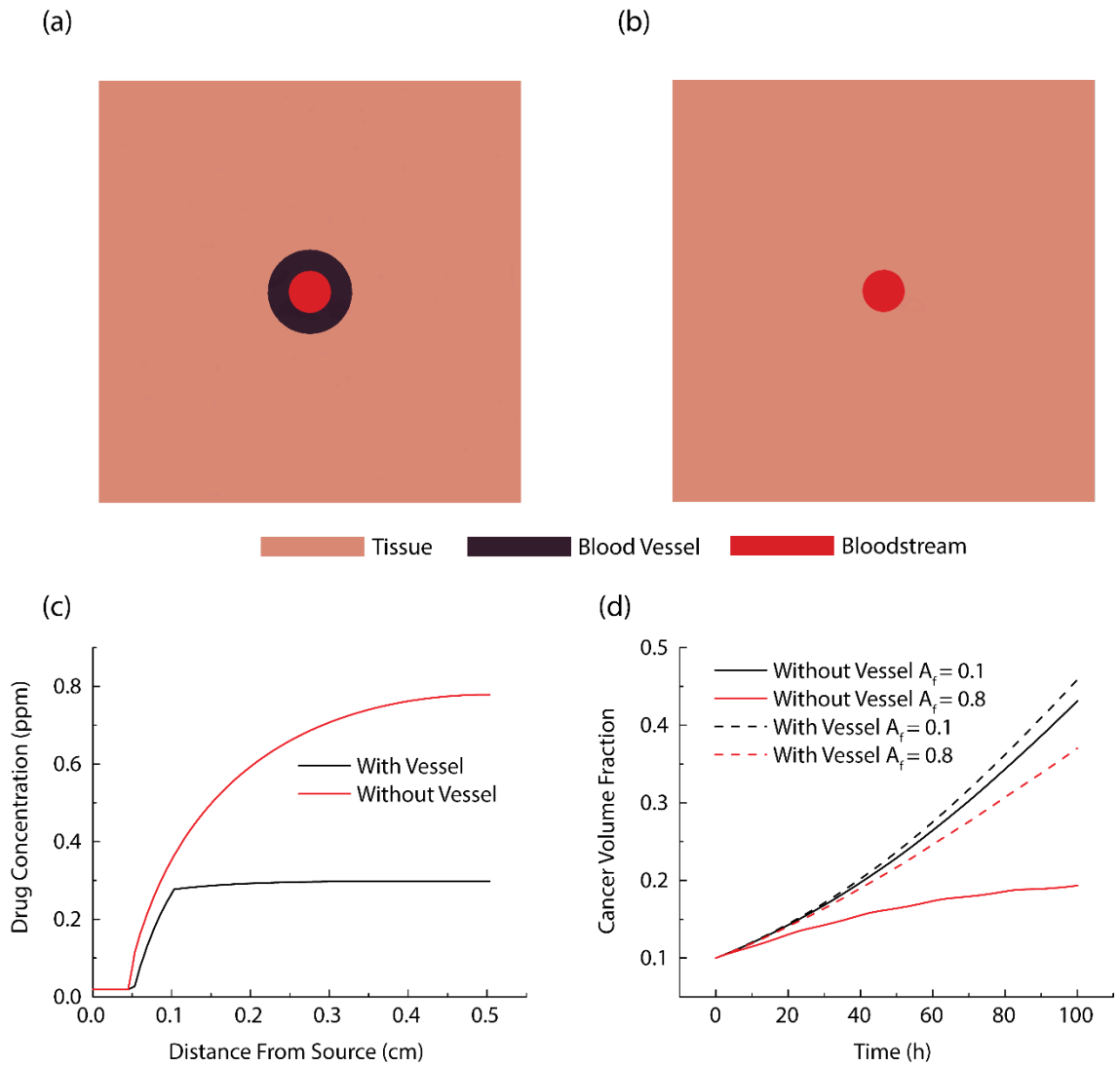
along the analysis line is shown in Fig. 8-7 (b) for the average diffusivities obtained in section 8.4 for Paclitaxel and Doxorubicin.



**Figure 8-7.** A simple model (a) is used to illustrate how drugs with different apparent diffusivities may influence significantly the profile of the drug concentration along the Analysis Line (b) but cancer volume fraction evolution remains similar (c) over time.

Drug concentration is significantly different far away from the source. However, the evolution of the cancerous cell population (the initial condition considered for the cancerous cell population was 10% and  $A_f = 0.1$ ) is very similar as shown in Fig. 8-7. This is caused by the cancerous cells having an insufficient drug concentration when far away from the drug source and, therefore, growing without control. It is therefore necessary to improve the diffusivity of the drug so that areas far away from the delivery point receive a sufficient dose to eliminate the cancerous cells and prevent the cancer from spreading and eventually causing the death of the patient.

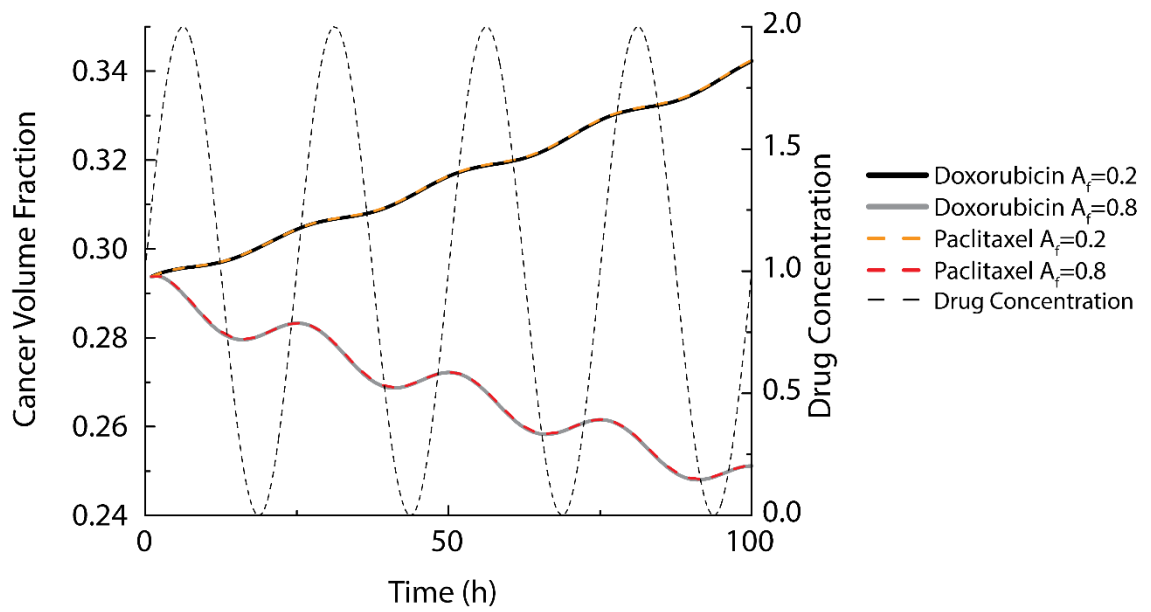
A second simple model is created to highlight the role of the diffusivity of blood vessels in the drug delivery. Fig. 8-8 (a-b) shows the model with and without blood vessel respectively. The drug source is a 0.05cm radius circle in the middle of the model and the thickness of the vessel is 0.05 cm. Fig. 8-8 (c) shows the drug concentration profile from the centre point. The drug concentration is significantly higher in the tissue (i.e. in the distance of 0.1-0.5 cm) when no blood vessel is present. This implies a better drug transportation into the tissue, hence a higher efficacy of such drug treatment. The evolution of the cancerous volume fraction is shown in Fig. 8-8 (d). When the blood vessel is present with a drug dose of  $A_f = 0.8$  the evolution of tumour fraction is similar to the scenario when it is not present during the first 40 hours of the treatment. This result highlights the role of the blood vessel in the dynamic behaviour of the system – to get similar efficacy of drug treatment in both scenarios (i.e. bolus injection and intravenous delivery), drug concentration needs to be 8 times higher to compensate the hindering effect of drug diffusion through blood vessel.



**Figure 8-8.** Simplified model to illustrate the role of the diffusivity of blood vessels in drug delivery efficacy. The models with and without the blood vessel are depicted in (a) and (b) respectively. The drug concentration along the analysis line is significantly greater when no blood vessel is present (c) which results in a reduced population of cancerous cells (d).

### 8.5.2 Intravenous drug delivery – sensitivity analysis

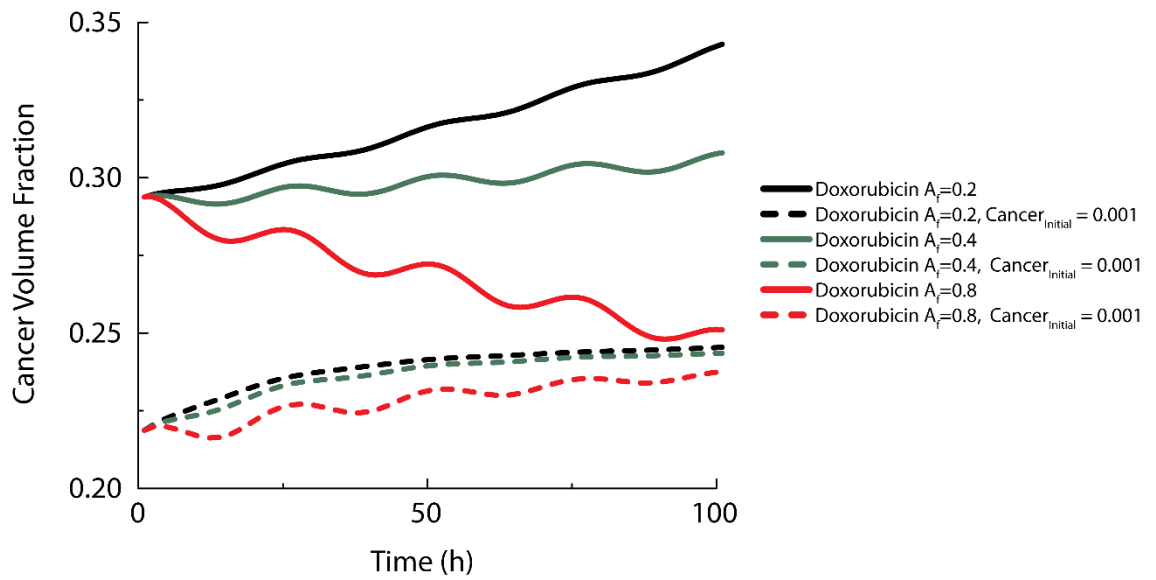
In this section the influence of different parameters involved in drug delivery is analysed when the drug is administered intravenously. A sinusoidal profile of drug concentration in the blood vessel through intravenous delivery is considered, as shown in Fig. 8-9. The subsequent tissue response is illustrated in the same figure, when  $A_f$  (i.e. the amplification factor of the drug concentration) equal to 0.2 and 0.8 respectively are considered for both drugs.



**Figure 8-9.** The drug profile considered is sinusoidal. The results for Paclitaxel and Doxorubicin are very similar independently of the concentration used.

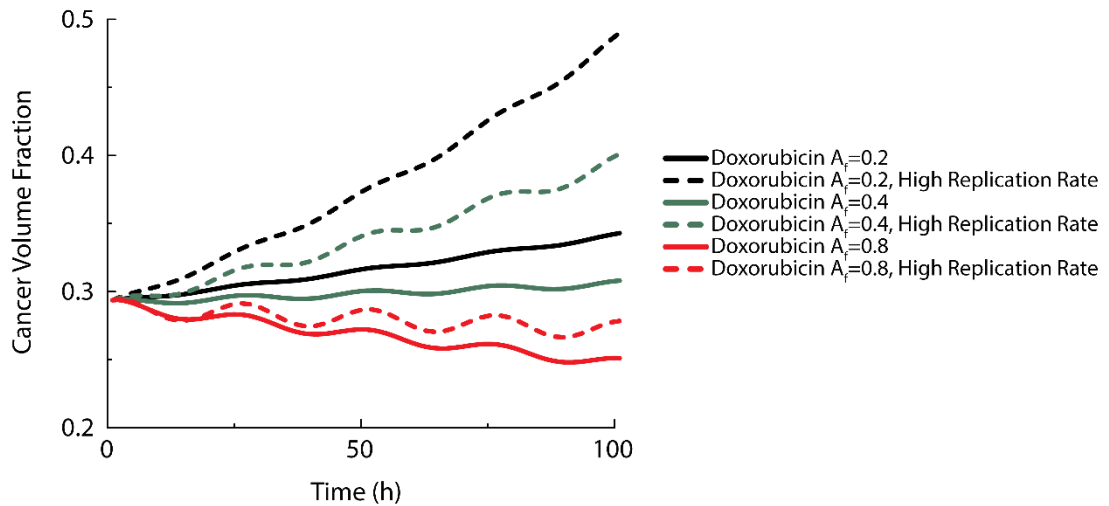
It can be seen that the tumour cells are reduced when highest concentration (i.e.  $A_f=0.8$ ) of drugs is used, however cancer progress is predicted when the lowest drug concentration (i.e.  $A_f=2$ ) is applied. Results show a minimum difference between the tissue responses subject to different drugs. That is due to drug diffusivity into tissue being controlled mostly by the diffusion through blood vessels as previously discussed in section 8.5.1 (illustrated in Fig. 8-8).

Fig. 8-10 shows the influence of the initial concentration of cancerous cells in the healthy part of the tissue on the tissue response to drug delivery. This parameter, which is the initial value of variables  $S$  and  $M$  in Eqs. 8-11 and 8-12 respectively, can be interpreted as the probability of cancer spreading into healthy tissue. The two lower concentrations of drug (i.e.  $A_f = 2$  and 4) do not serve as a prophylactic measure against cancer growing or to kill the existent cancerous cells. Therefore ultimately the cancer spreads to the organ. However, when initial concentration of cancerous cells is reduced to 0.001 chemotherapy is able to stop the tumour from spreading, resulting in much lower tumour fraction compared to other cases where the initial concentration of cancerous cells is higher



**Figure 8-10.** Evolution of cancer volume fraction for different initial concentration of cancerous cells. The prophylactic effect of chemotherapy is only visible for the highest concentration.

Increasing the replication rate of cancerous cells, on the other hand, has a negative effect on the prognosis of the patient, especially when low doses of drug are given to the patient as illustrated in Fig. 8-11.



**Figure 8-11.** Evolution of cancerous cell population when the replication rate of cells is increased.

The effect of increasing the ability of cancerous cells repairing themselves, regulated by parameter  $\epsilon_m$  in Eqs. 8-11 and 8-12, is shown in Fig. 8-12. As opposed to the results in Fig. 8-11, the effects are amplified when higher doses of drug are used. A similar trend is

observed when the arrest cost of cell cycle of cancerous cells is lower than healthy cells, as shown in Fig. 8-13.

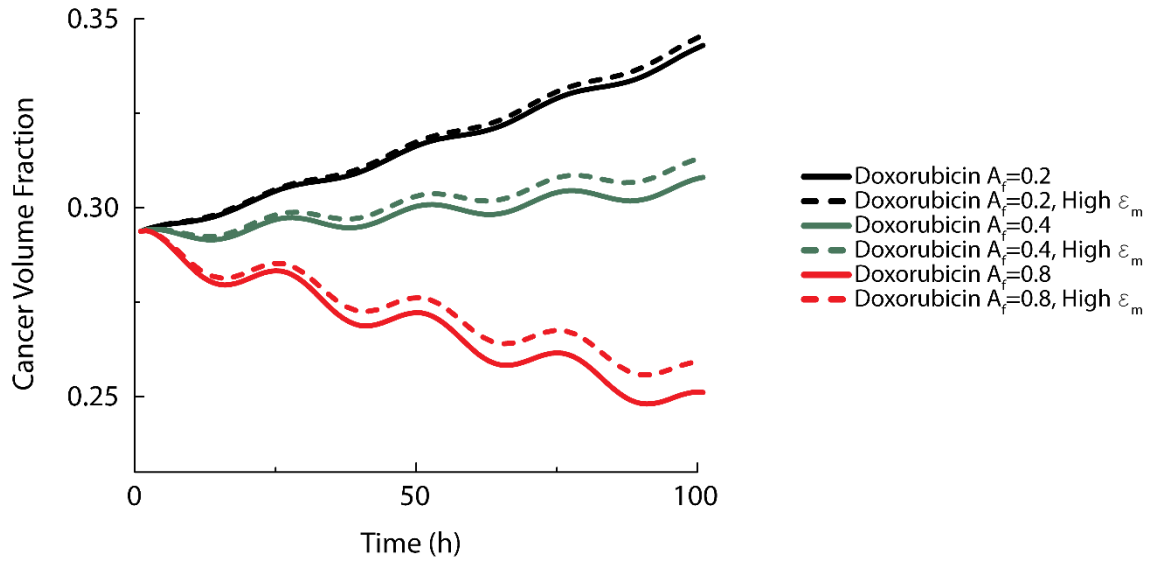


**Figure 8-12.** Evolution of the population of cancerous cell when the ability of cancerous cell to repair,  $\epsilon_m$ , is increased.

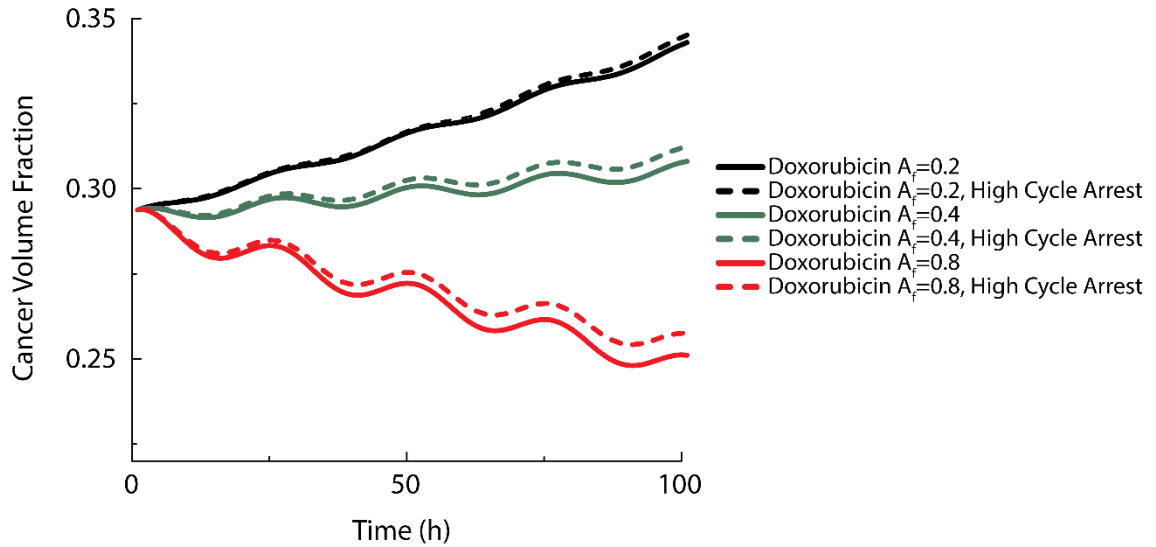


**Figure 8-13.** Evolution of cancer volume fraction for different cell cycle arrest for cancer and healthy cells.

In summary the choice of all these parameters as discussion in this section, specific to the tumour, its development stage and the immune system of the patient, is therefore crucial and needs to be carefully tuned to obtain prediction and subsequently the optimisation of drug delivery with the accuracy required in clinical practice.

### **8.5.3 Bolus injection – sensitivity analysis**

In this section two types of bolus injection are considered. Firstly the case of delivering a single dose is considered. Fig. 8-14 shows the evolution of tumour volume when paclitaxel and doxorubicin are administrated using two amplification factors of drug concentration (i.e. 2 and 8), respectively. In both cases the tumour grows and spreads. It is noted that the tissue response using both drugs is similar and the difference between using a higher or lower dose is less significant than in the previous scenarios when an intravenous treatment was considered. Such finding is believed to be due to diffusion pathway of the drug in tissue since the dose is comparatively low and takes longer to arrive to the rest of the tumour via diffusion, firstly through the blood vessel then through the tissue, therefore the regions of tumour more distant from the injection site have more time to grow before the drug concentration is built up to a critical amount that would hinder the tumour growth. Such hypothesis is in fact in line with what has been shown and discussed in section 8.5.1, in particular Fig. 8-7(c), where it can be seen that the difference in the drug diffusivity is unable to make a notable difference in tumour treatment due to the delay in drug diffusion in comparison to the tumour growth.

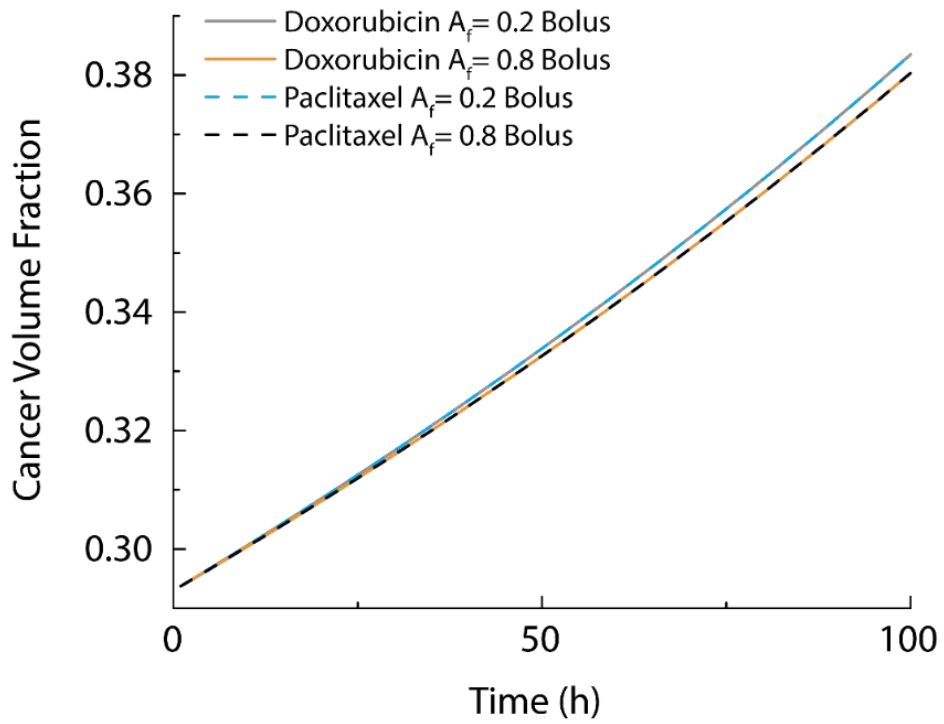


**Figure 8-14.** Comparison of cancer volume fraction evolution over time when two different amplification factors and drugs are considered

Fig. 8-15 shows the influence of reducing the initial amount of cancerous cells present. Such hypothesis is further strengthened by the results shown in Fig. 8-15, where the drug is administered directly into the tissue thus avoiding the hindrance of the blood vessels. The difference between the effects of both drugs is made clear when the bolus treatment lasts longer. In particular it is shown that a higher replication rate of cancerous cells further increases the benefits of the drug with low molecular weight (i.e. Doxorubicin) with respect to the one with higher MW (i.e. Paclitaxel) since the reduced diffusivity allows the drugs to diffuse faster into the tumour nodule.



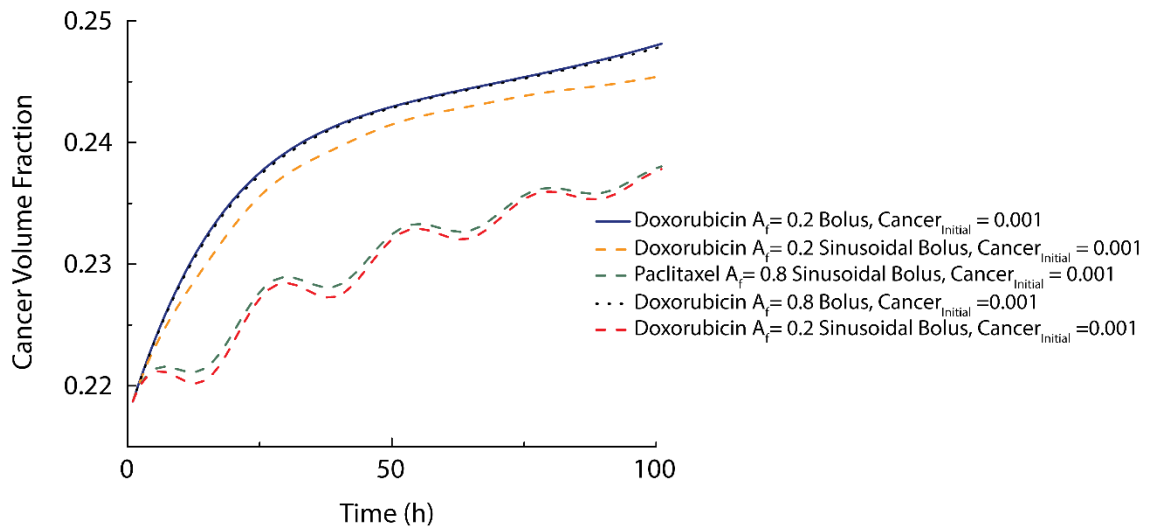


**Figure 8-15.** A comparison of the influence of the initial concentration of cancerous cells in cancer volume fraction over time.

Little difference is observed when the tumour repairing parameter  $\varepsilon_m$ , in Fig. 8-16, when a single bolus injection is considered between use of paclitaxel and doxorubicin. However, the difference is notably higher when a sinusoidal bolus injection is used, as shown in Fig. 8-17 where the cell replication rate parameter  $r_m$  is varied. The difference between the sinusoidal and the single injection cases is that tissue receives more sustained drug dose when sinusoidal drug profile is present, consequently leading to a lower tumour volume at  $t=100$  h.

The comparison between the results obtained using the bolus and intravenous delivery reveal the critical role of drug diffusivity in tissue and the limiting role to drug diffusion that the low diffusivity of blood vessels plays. In fact drug diffusivity appears to be the most critical factor in the outcome of the treatment compared to the biological parameters. Higher drug diffusivities are therefore preferred and result in better clinical outcomes (measured in this chapter by the evolution of cancer volume fraction) especially in bolus treatments. However, the high diffusivity would also cause the drug administered via bolus to reach the bloodstream easily and therefore distribute across the body which could result in worsened side effects. Such result strengthens the hypothesis that to predict the

outcome of the treatment *a priori* and to chose the optimal chemotherapeutic agent the diffusivity of the tissue has to be determined either by experimental or computational approaches.

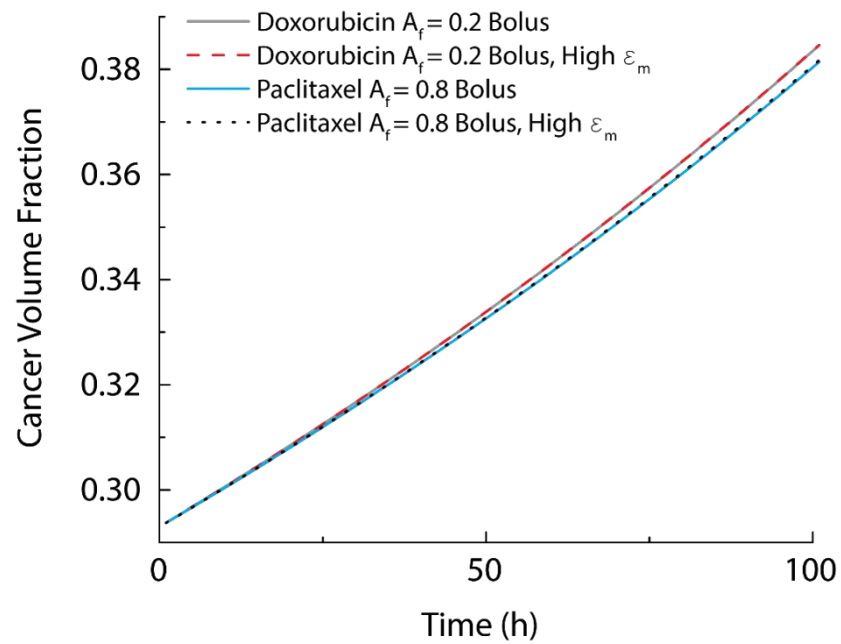


**Figure 8-16.** Impact on cancer volume fraction evolution over time of the ability of cancerous cells to repair themselves when Paclitaxel and Doxorubicin are administered.

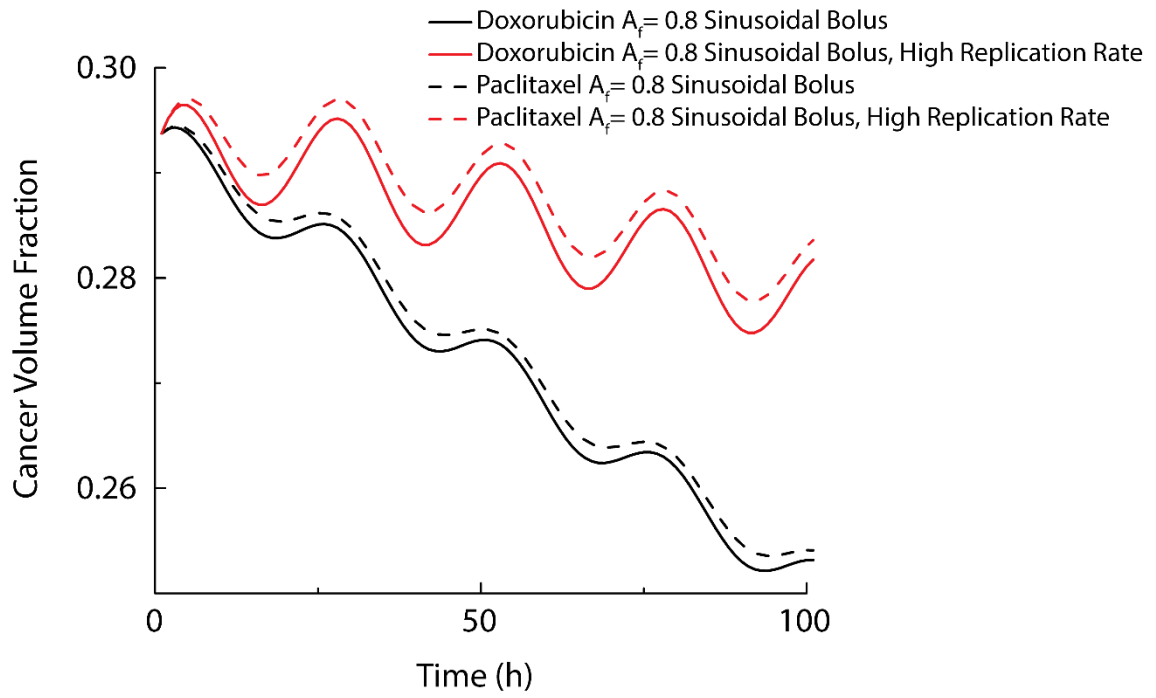


**Figure 8-17.** Comparison of cancer volume fraction evolution over time when two different drugs and cancerous cell replication rate,  $r_m$  are considered.

#### 8.5.4 Influence of drug profile in treatment efficacy

A different drug profile is considered in this section as shown in Fig. 8-18 (a), in addition to the sinusoidal profile used in section 8.5.2, to compare the influence of the drug concentration profile administrated in blood stream. To enable such comparison, both profiles have the same total amount of drug over the time of 100 hours (i.e. the areas under two profiles are the same). Compared to the sinusoidal drug profile the one proposed here has 5 cycles instead of 4 and a more aggressive dosage. Fig. 8-18 (b) shows the comparison of both drugs at the highest concentration considered in this study delivered using the method of bolus injection. Although the final tumour progression is very similar due to the same amounts of drug administered, the evolution is considerably different. In fact the rate at which cancerous cells are killed is significantly different. The exponential drug profile used in this study allows the drugs to reach the tumour nodule faster therefore leading to a faster establishment of effective drug concentration in tumour nodule. This trend is amplified when the drug is administered intravenously as shown in

Fig. 8-18(c). However such behaviour may not be true for high drug dosage rate that is arbitrary, since the diffusivity may become non-linear (i.e. diffusivity may vary depending on local condition) due to saturation, clogging etc. Therefore high doses may become less effective even if they were not toxic for the patient. The higher killing rate has implications regarding the ability of cancerous cells to become immune to chemotherapeutic agents since less malignant cells are given the opportunity to replicate.

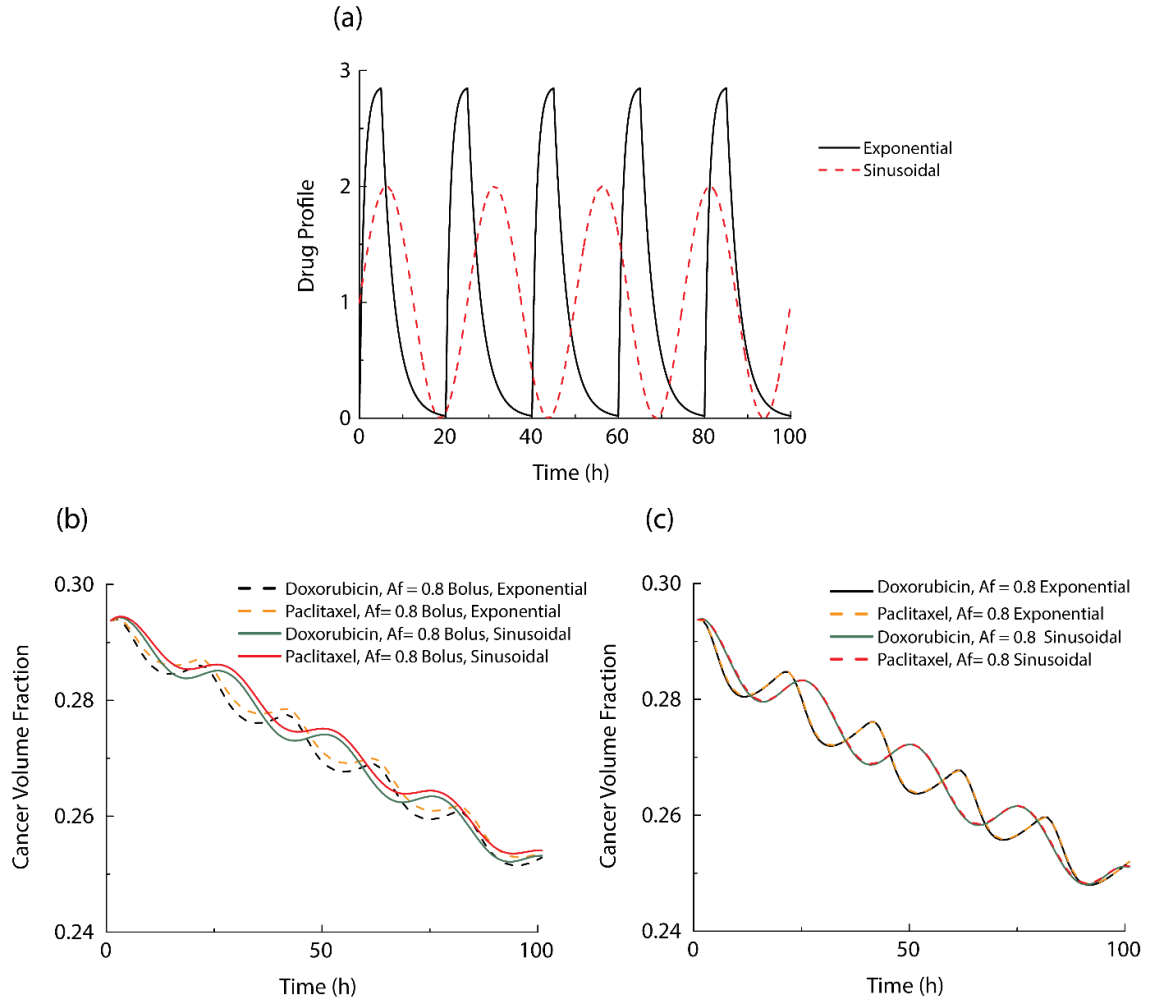


**Figure 8-18.** (a) A different drug concentration controlled by two exponentials is considered in this section. Evolution of cancerous volume fraction when the drug is following a sinusoidal or exponential law via a bolus (b) or through the blood vessels (c).

The evolutions of drug concentration profile and tissue response are illustrated in Fig. 8-19, when a bolus injection of Doxorubicin with sinusoidal drug profile ( $A_f = 0.8$ ) is considered. In particular Fig. 8-19(a) shows the concentration of Doxorubicin 4 hours after the beginning of the treatment. It should be remarked here that high concentrations

are achieved on the healthy and cancerous parts of the tissue. However, the left side of the tumour receives a lower dose at later stages. Therefore cancerous receive less amount of drug and can replicate faster. Fig.8-19 (c) shows the volume fraction of tumour 4 hours after the start of the drug treatment, where it can be seen how cancerous cells start to die from the location where the bolus was injected. The distance that drugs need to travel is critical since longer times may result in ineffective treatment. Figs. 8-19 (b) and (d) show the evolution of the treatment (i.e. drug concentration and tumour status, respectively) after 80 hours. It can be seen that the tumour at the location where the bolus is injected has been successfully treated, as well as much lower fraction of tumour found in other regions. However, if the cancerous cells replicate faster the delay of the drug to get to all the cancerous cells may be critical in determining the success of the treatment.

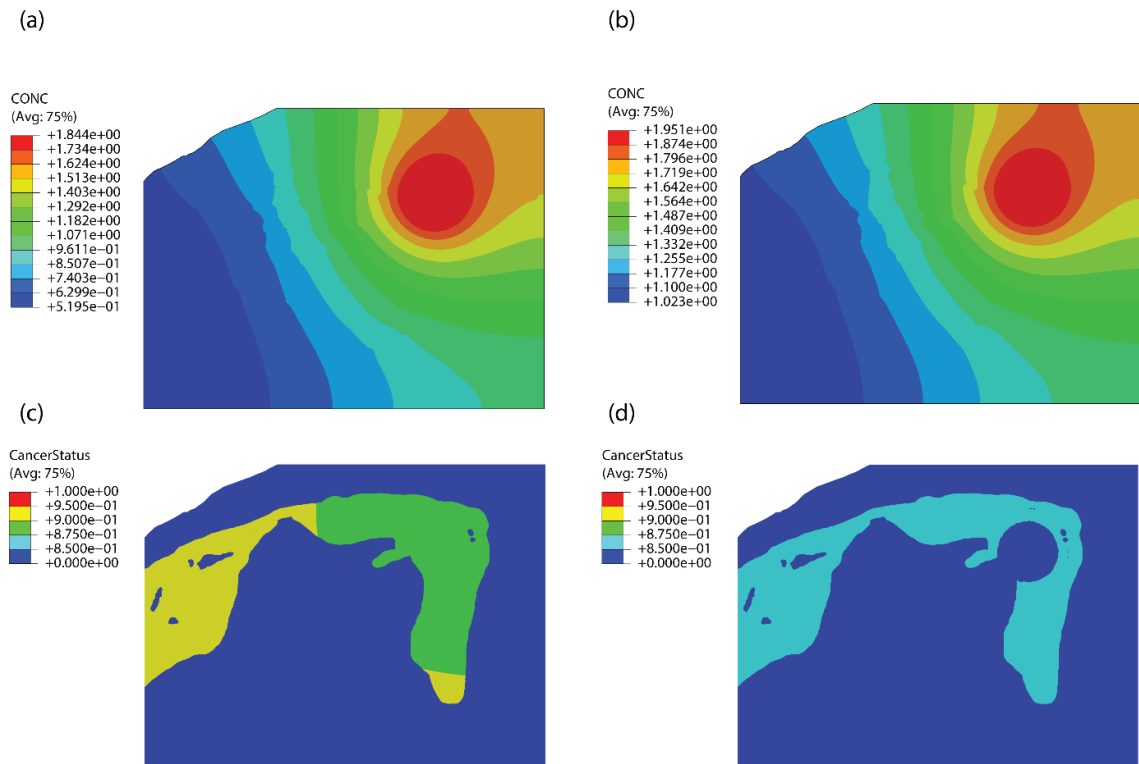


**Figure 8-19.** Drug concentration is shown in (a) and (b) 4 hours and 80 hours after the beginning of the treatment when a sinusoidal bolus injection is considered. The evolution of the cancer status is shown in (c) and (d) after the same period respectively. The area where the bolus sinusoidal injection was applied is identified by the high concentration in (a-b) and by a large reduction in the population of cancerous cells in (d) compared to the same area in (c).

## 8.6 Concluding remarks

Determining the optimal delivery, including the delivery methods and drug concentration profile, of chemotherapy agents such as doxorubicin or paclitaxel is critical. This chapter, closely linked with previous chapters in the concept of tissue microstructural heterogeneity, presents a computationally framework to evaluate the outcome of a drug treatment using data from a biopsy prior to drug being administered to the patient.

First a methodology to calculate the apparent drug diffusivity tensor in soft tissue due to presence of cancer is presented. These results are then used as ‘material properties’ into the patient-specific model that incorporates the blood vessel network to estimate the tissue response using a modified competition model.

The main conclusions of this study are:

- Inter-patient variation, which appears to be less influent in the drug diffusivity than the molecular weight of the drug, is still notable in affecting the efficacy of drug delivery.
- The apparent drug diffusivity in tissue remains approximately constant for the different RVE sizes chosen. This suggests the existence of an RVE that can be used to model the tissue using its effective properties from the information at lower length scale, thus simplifying the model and reducing the computational cost to make the method easier to implement in clinical practice.
- The profile of drug concentration delivered by either intravenous or bolus injection has significant impact on the rate at which malignant cells are killed. This may lead to a more ideal outcome where tumour nodule becomes less resistant to chemotherapeutic treatment due to the short period of time being treated. This is of critical importance in the success of the treatment and therefore needs further investigation.

- The proposed framework would be of particular importance not only to the evaluation of the capability of a chemotherapeutic treatment but also to predict its prophylactic function.

As it stands the proposed methodology has certain limitations: the capillary which also influences the pathway of drug delivery is not considered; the diffusivity of healthy and cancerous tissue are not updated over time and the immune response of cancerous cells is not taken into account in the competition model. It is hoped to overcome this constraints in the future once histological images are available in higher resolution that is able to capture the topological features of capillary vessels. In this chapter it is assumed that Doxorubicin and Paclitaxel, which are widely used in the treatment of solid tumours in breast and prostate, have the same pharmacodynamics properties. However, that is just an assumption since the main objective of the analysis performed in this chapter was to analyse the influence of drug diffusivity. Therefore, to transfer the proposed methodology into clinical practice it would be necessary to quantitatively determine those parameters. A further limitation is that the transport of drug from tissue into the blood vessels when the bolus approach is used is not considered. However, taking into account the relatively low diffusivity of blood vessels the effects of such phenomenon are expected to be negligible. In this chapter bidimensional models are considered as it is hoped that the methodology proposed here can be validated performing drug diffusion analysis in histological samples. However, the methodology is general and could be applied to model drug diffusion in three dimensional geometries. Nevertheless, obtaining such geometries from excised samples is a challenging task at the moment because of two main reasons. First it is complex and expensive to stain and cut in a sufficient number of samples a complete organ. Second pathologists require the organ to be cut in very specific areas and geometries for clinical diagnosis. It is expected to increase the database of patient tissue samples to improve the understanding of inter-patient differences when different grades

of cancer are present. It is hoped that the framework presented here will serve as a basis for a platform that allows predicting and optimising the outcome of a chemotherapeutic treatment before aggressive drug is given to the patient, towards the ultimate goal of personalised medicine.



## Looking back and working forward

### Contents

---

9.1	Looking back.....	162
9.2	Working forward.....	167

---

### 9.1 Looking back

As mentioned at the outset, the synergy between engineering, medical and biological sciences has already led to significant advances in clinical practice such as diagnosis, image guided surgery and reduction of side effects in aggressive treatments such as radiotherapy. It is expected that such multidisciplinary research will continue to increase in pursuit of the aims of improving quality of life and life expectancy. This doctoral thesis aimed to contribute towards deepening such synergies in the areas of soft tissue diagnosis and treatment and also serve as a basis for further interactions between engineering and clinical diagnosis and treatment. In particular, the main aim was to investigate how changes in tissue microstructure caused by various pathophysiological conditions influence the mechanical properties at organ scale, and, more importantly, how to take advantage of these changes for diagnostic purposes using mechanical palpation. Analysing the influence of patient specificity not only in diagnosis but also in drug delivery aspects of treatment is also a major objective of the thesis. Tumour drug delivery is closely linked to the rest of the thesis since both are influenced by changes in the underlying microstructure due to pathological condition, and both need to recognise that

the microstructure and its response to disease are patient-specific. The final goal of this research is therefore to establish a framework that allows accurate, non-invasive, efficient, cost-effective diagnosis that allows planning an adequate and optimized drug delivery treatment.

The specific contributions and conclusions that have been made in this thesis are summarized as follows:

### **Chapter 3: A novel palpation-based method to detect hard cancerous nodules in soft tissues – the computational framework and experimental validation**

- ✓ First work to propose a method for estimating the size and depth of a cancerous nodule using palpation, without *a priori* knowledge of its topology.

The advantage of the framework is that it eliminates the limitations of previous methods that required the knowledge of either the nodule size or depth prior to examination. Furthermore, the methodology is not restricted to idealised cylindrical or circular nodules, but can be applied to nodules with any geometry. This generality is of critical significance in opening up the opportunity for non-invasive palpation-based assessment of a wide variety of tumours, such as colorectal, breast and even liver cancers.

### **Chapter 4: Quantitative tissue quality assessment through viscoelastic characterization using instrumented palpation**

- ✓ Systematic study of the effectiveness of dynamic instrumented palpation on soft tissue, taking into account its viscoelastic behaviour;
- ✓ First work to characterize the viscoelasticity of prostatic tissue, in the presence of cancerous nodules reconstructed from MRI scans, to quantitatively assess the tissue quality using viscoelastic response from dynamic palpation;
- ✓ First work to propose a novel tissue quality index for soft tissue diagnostics, based on its viscoelastic behaviour.

Compared to previous approaches for soft tissue diagnosis which are mainly based on the tissue elasticity, the methodology presented here showed that the viscoelastic response is an adequate index for quantitative assessment of tissue quality, and, more importantly, is less sensitive to changes of nodule depth. Furthermore, is the method does not require *a priori* knowledge of the topology of the cancerous nodule, making it potentially more efficient in terms of the number of medical procedures involved. Consequently, the proposed methodology is seen as a reliable tool for quantitative tissue diagnosis.

**Chapter 5: A novel method for rapid, quantitative, mechanical assessment of soft tissue for diagnostic purposes – a viscoelastic ‘rule of mixtures’**

- ✓ A novel method is proposed to obtain the apparent viscoelastic properties of biphasic materials or tissues
- ✓ A fast mathematical methodology is proposed to relate such apparent properties to the volume fraction of each phase in soft viscoelastic materials with random microstructure.
- ✓ First work to propose a methodology based on realistic mechanical testing scenarios to estimate the cancerous volume fraction in tissue without *a priori* knowledge of nodule topology.

The concept of ‘the rule of mixtures’ has been widely used for heterogeneous engineering materials. However, they are not applicable to estimating the apparent time constants of heterogeneous viscoelastic tissues. The fast numerical rule of mixtures presented here allows an estimation of the volume fraction of each phase regardless of the topology of the inclusion. This implies that, compared to previous methodologies, the framework presented here does not require any complex finite element simulation. Thus the method is particularly attractive for use in clinical practice due to ease of use and fast outcome. Furthermore the proposed methodology could be also applied in other fields such as structural health monitoring (SHM) of heterogeneous engineering materials.

## **Chapter 6: Patient Specific Modelling of Palpation-based Prostate Cancer**

### **Diagnosis: Effects of Pelvic Cavity Anatomy and Intrabladder Pressure**

- ✓ Systematic study of patient-specific modelling (PSM) in biomechanical modelling of the male pelvic cavity;
- ✓ First work to propose a framework for PSM applied to the example of the male pelvic cavity for the purpose of prostate cancer diagnosis using palpation;
- ✓ First work to investigate the effects of changing the intrabladder pressure during palpation-based prostate cancer diagnosis when patient-specificity is considered; Results show that it is possible to increase the sensitivity of the procedure by regulating the bladder content, which can be implemented in clinical practice;
- ✓ First work to explore the effectiveness of incorporating the pelvic bone into the proposed PSM framework for prostate cancer diagnosis.

Compared to previous efforts to model the male pelvic cavity, the framework established here takes into account patient specificity including not only the actual local anatomy but also the outcome of previous treatments to the prostate. The recommendation provided in this chapter for patient preparation prior to digital rectal examination (instrumented or not) would improve the outcome of the procedure. Furthermore the modelling community would benefit from the findings from the study including the pelvic bone, thus reducing the computational cost of future models. More importantly, this work emphasises the benefits of patient specific modelling in general clinical practice.

## **Chapter 7: A multiscale, mechano-morphological approach to soft tissue mechanics: application in prostate cancer diagnosis**

- ✓ First work to systematically analyse the influences of the changes in the mechanical properties of prostatic tissue due to the presence of a cancerous nodule;

- ✓ Novel methodology to impose periodic boundary conditions on arbitrary meshes;
- ✓ First work to introduce the use of support vector machines to classify the apparent mechanical properties of soft tissue in terms of its pathological condition.

Two main contributions are made here. First a novel method involving the imposition of periodic boundary conditions on arbitrary meshes is proposed. This is of special relevance when working with models reconstructed from images obtained from biological samples with highly complex geometries such as histological images, where periodic meshes are complex or even impossible to obtain. More importantly, the method is well suited to commercial software where the stiffness matrix is inaccessible. The second contribution is in the analysis of the changes in the effective properties of soft tissue subjected to different patho-physiological conditions and the associated diagnosis using soft computing techniques. This allows a qualitative diagnosis (i.e. either cancerous or healthy) to be made directly from the mechanical tests performed on the sample, essentially using pattern recognition. Compared to previous methodologies that extract a single feature based on elasticity, e.g. the Young's modulus, the proposed methodology allows improved the diagnosis by introducing more components of the stiffness tensor, thereby acknowledging the significance of tissue anisotropy and its influence on the proposed diagnostic methods.

### **Chapter 8: Heterogeneity in Tissue Diffusivity: An Application in Drug Delivery**

- ✓ First work to analyse the changes in the apparent drug diffusivity in tissue microstructure due to the changes caused by cancer
- ✓ First work to introduce a patient-specific framework that considers drug diffusivity from the local blood vessels and pharmacodynamics to predict the evolution of cancer under drug treatment

In this chapter, two main contributions are made. First, a methodology is presented for calculating the apparent drug diffusivity tensor in soft tissue under various physiological conditions. These results are then transferred into a patient-specific model which, in contrast to previous work, incorporates the vessel network. This enhanced model estimates cancer progression under different treatment strategies using a modified competition model. It is hoped that the framework presented here will serve as the basis for a platform that allows the prediction and optimisation of the outcome of a proposed treatment before any aggressive drug is given to the patient.

## **9.2 Working forward**

It is hoped that the methodologies proposed in this thesis will serve a long term goal in the development of healthcare technology that improves cancer diagnosis and treatment ultimately improving the care, quality of life and life expectancy of patients. The following work is proposed to further advance this thesis to an even higher level that takes into account not only the uniqueness of each patient and pathological condition but also the constraints of the clinical practice (e.g. patient discomfort, economic feasibility).

### **Mechanics-based soft tissue diagnosis:**

**Use of novel diagnostic devices:** The work presented in Chapters 3, 4 and 5 has been based on the use of a single sensor (although *in silico*) to perform the mechanical characterization of the tissue. However, this limits the variety of tests that can be simultaneously performed. It might be of interest, for instance, to pinch, stretch or compress the tissue before performing any palpation to obtain further measurements that would enhance the diagnosis. Such devices would provide the opportunity to improve the diagnosis with novel testing methodologies and data analysis. More importantly they could be introduced into current surgical devices such as pincers, thus facilitating the translation into medical practice. A further challenge that novel diagnostic devices could help to address is quantitatively assessing the need for tissue pre-conditioning under

different loads, especially *in-vivo*. This is of critical relevance to obtain accurate patient-specific mechanical properties.

**Miniaturized sensors:** Although, for the purpose of digital rectal examination, the use of finger-sized probes has proven to be useful, as discussed in Chapters 2, 3, 4 and 5, miniaturising the sensors would give rise to new opportunities such as increasing the sensitivity, maybe even to cellular scale, or accessing other internal organs such as the intestines, lungs, heart and brain. As discussed in Chapters 7 and 8, the mechanical properties may vary significantly in a rather small length scale depending on the pathological conditions. Testing at lower scales would allow a higher resolution diagnosis thus providing much more useful information for certain conditions where microstructural changes associated with the early stage of diseases often occur locally. However, the diagnostic procedures should be extremely sensitive to avoid detecting normal heterogeneities in healthy tissue as abnormalities. The process of classifying such data as healthy or cancerous could be done, for instance, using artificial neural networks (ANN) or Support Vector Machines (SVM). More importantly, it could provide an insight into the vascularization and diffusivity of the tissue, thus paving new roads to optimization of diagnosis and tailoring the treatment on a patient-specific basis.

**Larger database of histological and MR images:** In Chapters 4, 5, 6, 7 and 8, data from different patients have been used to test the proposed computational models either at the microscopic or at organ scale. It is expected that an increase in the database would improve the accuracy of the models, e.g. support vector machines used in Chapter 8, and provide a deeper understanding of the changes in the microstructure caused by various conditions. Morphometric indices could be derived, which could be useful for both clinical diagnosis and multiscale modelling. This objective is undoubtedly ambitious and the cost of performing MRI scans to a large group of patients could be prohibitive. Therefore, it would certainly require a much wider collaboration to obtain such data from

patients with different genotypes and phenotypes. As a result building such database will be a long-term project.

**Multiphase Multiscale models:** The models in this work assume that the tissue behaviour can be modelled as a continuum solid. However, tissues are multiphase materials with solid and aqueous phases. Therefore, using multiphase models including such effects as fluid-structure interaction would allow a better understanding of the influence of the aqueous phase in tissue mechanics. However, such models are computationally expensive and have various limitations. Drug delivery research would also benefit from such models to account for such variables as interstitial fluid pressure that have been reported in cancerous tissue. This would require characterization of such properties, for instance using miniaturized sensors as mentioned above, which represents a challenge in itself. However, a balance between the complexity of the model and its applicability in clinical practice, where constraints such as time-per-patient are critical, has to be considered.

#### **Drug delivery:**

**Diffusivity estimation from mechanical properties:** Current diagnostic techniques require a biopsy to ascertain the presence and grade of a disease. However, the advances in palpation will hopefully reduce the need for such procedures. Although avoiding a biopsy would be advantageous for the patient, the lack of histological images would hinder the estimation of drug diffusivity on a patient-specific basis. Therefore, to avoid invasive procedures and the risks associated with them, it would be necessary to estimate the diffusivity during the palpation procedure. This is directly linked with the need for miniaturized sensors to measure the properties with the required resolution and to the work carried out in Chapters 7 and 8.

**Patient-specific model reduction:** To obtain clinically significant data, it is necessary to include patient-specific information in the drug delivery model. Multiscale modelling has



proven a useful technique to reduce the complexity of such models, but patient-specific models are still complex, laborious to create and therefore adapting them into clinical practice is challenging. It is therefore necessary to reduce their complexity without compromising the accuracy to make computational models readily available in clinical practice. In this regard, it would be especially interesting to reduce the complexity of multiphysics models, for instance using model order reduction techniques, which would improve the analysis of drug delivery into solid tumours.

**Personalized drug delivery optimization:** Current protocols for treatment of diseases such as cancer are very strict regarding dosage and timing and the peculiarities of each patient are not considered. As a result, the opportunity of providing an optimal treatment is lost. Chemotherapy is specially challenging due to the multiple biological constraints in place, such as cardiotoxicity, hepatotoxicity and drug resistance. Therefore it would be critical to establish a platform to predict the outcome of drug treatment and its possible optimization (e.g. design of drug or dosage procedure) before giving any drug to the patient as personalised medicine.

From the proposed ideas for future work and given the opportunity to follow one of them with the adequate support it is believed that personalized drug delivery optimization has the potential to create a higher, long-lasting impact in society within a reduced time frame.

## Bibliography

- [1] Schwartz JM, Denninger M, Rancourt D, Moisan C, Laurendeau D. Modelling liver tissue properties using a non-linear visco-elastic model for surgery simulation. *Medical image analysis* 2005;9:103-12.
- [2] Famaey N, Vander Sloten J. Soft tissue modelling for applications in virtual surgery and surgical robotics. *Computer methods in biomechanics and biomedical engineering* 2008;11:351-66.
- [3] Efstratios Georgakarakos, T. Christian Gasser, Michalis Xenos, Nikolaos Kontopodis, George S. Georgiadis, Ioannou CV. Applying Findings of Computational Studies in Vascular Clinical Practice: Fact, Fiction, or Misunderstanding? *Journal of Endovascular Therapy* 2014;21:434-8.
- [4] Chen Y, Zhou S, Li Q. Microstructure design of biodegradable scaffold and its effect on tissue regeneration. *Biomaterials* 2011;32:5003-14.
- [5] Chen Y, Zhou S, Li Q. Mathematical modeling of degradation for bulk-erosive polymers: Applications in tissue engineering scaffolds and drug delivery systems. *Acta Biomater* 2011;7:1140-9.
- [6] Palacio J, Jorge-Penas A, Munoz-Barrutia A, Ortiz-de-Solorzano C, de Juan-Pardo E, Garcia-Aznar JM. Numerical estimation of 3D mechanical forces exerted by cells on non-linear materials. *Journal of biomechanics* 2013;46:50-5.
- [7] Phipps S, Yang TH, Habib FK, Reuben RL, McNeill SA. Measurement of the mechanical characteristics of benign prostatic tissue: a novel method for assessing benign prostatic disease. *Urology* 2005;65:1024-8.
- [8] Masuzaki R, Tateishi R, Yoshida H, Sato T, Ohki T, Goto T, et al. Assessing liver tumor stiffness by transient elastography. *Hepatology international* 2007;1:394-7.
- [9] Nicolle S, Palierne JF. Dehydration effect on the mechanical behaviour of biological soft tissues: observations on kidney tissues. *Journal of the mechanical behavior of biomedical materials* 2010;3:630-5.
- [10] Sack I, Beierbach B, Wuerfel J, Klatt D, Hamhaber U, Papazoglou S, et al. The impact of aging and gender on brain viscoelasticity. *NeuroImage* 2009;46:652-7.
- [11] Yi A, Cho N, Chang JM, Koo HR, La Yun B, Moon WK. Sonoelastography for 1,786 non-palpable breast masses: diagnostic value in the decision to biopsy. *European radiology* 2012;22:1033-40.
- [12] Salameh N, Peeters F, Sinkus R, Abarca-Quinones J, Annet L, ter Beek LC, et al. Hepatic viscoelastic parameters measured with MR elastography: Correlations with quantitative analysis of liver fibrosis in the rat. *Journal of Magnetic Resonance Imaging* 2007;26:956-62.
- [13] Krouskop TA, Wheeler TM, Kallel F, Garra BS, Hall T. Elastic Moduli of Breast and Prostate Tissues Under Compression. *Ultrason Imaging* 1998;20:260-74.
- [14] Yarpuzlu B, Ayyildiz M, Tok OE, Aktas RG, Basdogan C. Correlation between the mechanical and histological properties of liver tissue. *J Mech Behav Biomed Mater* 2014;29:403-16.
- [15] Groh CM, Hubbard ME, Jones PF, Loadman PM, Periasamy N, Sleeman BD, et al. Mathematical and computational models of drug transport in tumours. *Journal of The Royal Society Interface* 2014;11:20131173.
- [16] El-Kareh AW, Secomb TW. A Mathematical Model for Comparison of Bolus Injection, Continuous Infusion, and Liposomal Delivery of Doxorubicin to Tumor Cells. *Neoplasia* (New York, NY) 2000;2:325-38.
- [17] Bayliss LE, Robertson GW. The visco-elastic properties of the lungs. *QJExp Physiol* 1939;29:27-47.

- [18] Huang CY, Mow VC, Ateshian GA. The Role of Flow-Independent Viscoelasticity in the Biphasic Tensile and Compressive Responses of Articular Cartilage. *Journal of Biomechanical Engineering* 2001;123:410.
- [19] Kerdok AE, Ottensmeyer MP, Howe RD. Effects of perfusion on the viscoelastic characteristics of liver. *J Biomech* 2006;39:2221-31.
- [20] Holzapfel GA. Biomechanics of Soft tissue. In: Lemaitre J, editor. *Handbook of Material Behavior, Nonlinear Models and Properties*: LMT-Cachan, France; 2000.
- [21] Bischoff JE. Reduced parameter formulation for incorporating fiber level viscoelasticity into tissue level biomechanical models. *Annals of biomedical engineering* 2006;34:1164-72.
- [22] Ebihara T, Venkatesan N, Tanaka R, Ludwig M. Changes in Extracellular Matrix and Tissue Viscoelasticity in Bleomycin-induced Lung Fibrosis. *American Journal of Respiratory and Critical Care Medicine* 2000;162:1569-76.
- [23] Garteiser P, Doblas S, Daire JL, Wagner M, Leitao H, Vilgrain V, et al. MR elastography of liver tumours: value of viscoelastic properties for tumour characterisation. *European radiology* 2012;22:2169-77.
- [24] Xu F, Wen T, Seffen KA, Lu TJ. Characterization of Thermomechanical Behaviour of Skin Tissue II. Viscoelastic Behaviour. *World Congress on Engineering* 2007 V. London2007.
- [25] Balleyguier C, Canale S, Ben Hassen W, Vielh P, Bayou EH, Mathieu MC, et al. Breast elasticity: principles, technique, results: an update and overview of commercially available software. *European journal of radiology* 2013;82:427-34.
- [26] Chen LH, Ng SP, Yu W, Zhou J, Wan KW. A study of breast motion using non-linear dynamic FE analysis. *Ergonomics* 2013;56:868-78.
- [27] Sinkus R, Tanter M, Xydeas T, Catheline S, Bercoff J, Fink M. Viscoelastic shear properties of in vivo breast lesions measured by MR elastography. *Magnetic resonance imaging* 2005;23:159-65.
- [28] Sack I, Jöhrens K, Würfel J, Braun J. Structure-sensitive elastography: on the viscoelastic powerlaw behavior of in vivo human tissue in health and disease. *Soft Matter* 2013;9:5672.
- [29] Guo J, Hirsch S, Fehlner A, Papazoglou S, Scheel M, Braun J, et al. Toward an Elastographic Atlas of Brain Anatomy. *PloS ONE* 2013.
- [30] Rashid B, Destrade M, Gilchrist MD. Mechanical characterization of brain tissue in tension at dynamic strain rates. *Journal of the mechanical behavior of biomedical materials* 2014;33:43-54.
- [31] Streitberger K-J, Sack I, Krefting D, Pfueller C, Braun J, Paul F, et al. Brain Viscoelasticity Alteration in Chronic-Progressive Multiple Sclerosis. *PloS ONE* 2012.
- [32] Taylor SL, Lerner AL, Rubens DJ, Parker KJ. A Kelvin-Voigt Fractional Derivative Model For Viscoelastic Characterization of Liver Tissue. *ASME International Mechanical Engineering Congress & Exposition*. New Orleans, Louisiana2002.
- [33] Holzapfel GA, Gasser TC. A viscoelastic model for fiber-reinforced composites at finite strains: Continuum basis, computational aspects and applications. *Computer Methods in Applied Mechanics and Engineering* 2000;190:4379-403.
- [34] Holzapfel GA, Gasser TC, Ogden RW. A New Constitutive Framework for Arterial Wall Mechanics and a Comparative Study of Material Models. *Journal of Elasticity* 2000;61:1-48.
- [35] Soltz MA, Ateshian GA. Experimental verification and theoretical prediction of cartilage interstitial fluid pressurization at an impermeable contact interface in confined compression. *J Biomech* 1998;31:927-34.
- [36] Abdel-Sayed P, Moghadam MN, Salomir R, Tchernin D, Pioletti DP. Intrinsic viscoelasticity increases temperature in knee cartilage under physiological loading. *Journal of the mechanical behavior of biomedical materials* 2014;30:123-30.

- [37] Van Loocke M, Simms CK, Lyons CG. Viscoelastic properties of passive skeletal muscle in compression-cyclic behaviour. *Journal of biomechanics* 2009;42:1038-48.
- [38] Takaza M, Moerman KM, Gindre J, Lyons G, Simms CK. The anisotropic mechanical behaviour of passive skeletal muscle tissue subjected to large tensile strain. *Journal of the mechanical behavior of biomedical materials* 2013;17:209-20.
- [39] Rebelo LM, de Sousa JS, Mendes Filho J, Radmacher M. Comparison of the viscoelastic properties of cells from different kidney cancer phenotypes measured with atomic force microscopy. *Nanotechnology* 2013;24:055102.
- [40] Phipps S, Yang TH, Habib FK, Reuben RL, McNeill SA. Measurement of tissue mechanical characteristics to distinguish between benign and malignant prostatic disease. *Urology* 2005;66:447-50.
- [41] Gleason DF. Histologic grading of prostate cancer: A perspective. *Hum Pathol* 1992;23:273-9.
- [42] Carson WC, Gerling GJ, Krupski TL, Kowalik CG, Harper JC, Moskaluk CA. Material characterization of ex vivo prostate tissue via spherical indentation in the clinic. *Med Eng Phys* 2011;33:302-9.
- [43] Sangpradit K, Liu Hb, Dasgupta P, Althoefer K, Seneviratne LD. Finite-Element Modeling of Soft Tissue Rolling Indentation. *IEEE Transactions on Biomedical Engineering* 2011;58:3319-27.
- [44] Hoyt K, Castaneda B, Zhang M, Nigwekar P, Anthony di Sant'Agnese P, Joseph JV, et al. Tissue elasticity properties as biomarkers for prostate cancer *Cancer Biomark* 2008;4:213-25.
- [45] Atanackovic TM, Janev M, Konjik S, Pilipovic S, Zorica D. Vibrations of an elastic rod on a viscoelastic foundation of complex fractional Kelvin–Voigt type. *Meccanica* 2015;50:1679-92.
- [46] Caputo M. Linear models of dissipation whose Q is almost frequency independent—II. *Geophysical Journal International* 1967;13:529-39.
- [47] Diethelm K, Ford NJ, Freed AD. A Predictor-Corrector Approach for the Numerical Solution of Fractional Differential Equations. *Nonlinear Dynamics* 2002;29:3-22.
- [48] Brinson HF, Brinson LC. *Polymer Engineering Science and Viscoelasticity: An Introduction*: (Springer Science+Business Media, LLC, 233 Spring Street, New York, NY 10013, USA); 2008.
- [49] Yu P, Haddad YM. On the dynamic system identification of the response behaviour of linear viscoelastic materials. *International Journal of Pressure Vessels and Piping* 1994;67:45-54.
- [50] Tran AB, Yvonnet J, He QC, Toulemonde C, Sanahuja J. A simple computational homogenization method for structures made of linear heterogeneous viscoelastic materials. *Computer Methods in Applied Mechanics and Engineering* 2011;200:2956-70.
- [51] Renaud F, Dion JL, Chevallier G, Tawfiq I, Lemaire R. A new identification method of viscoelastic behavior: Application to the generalized Maxwell model. *Mechanical Systems and Signal Processing* 2011;25:991-1010.
- [52] Boyce MC, Arruda EM. Constitutive models of rubber elasticity: A review. *Rubber Chemistry and Technology* 2000;73:504-23.
- [53] Ali A, Hosseini M, Shara BB. A Review of Constitutive Models for Rubber-Like Materials. *American Journal of Engineering and Applied Sciences* 2010;3:232-9.
- [54] Bedal T. Modeling hyperelastic behavior of rubber: A novel invariant-based and a review of constitutive models. *Journal of Polymer Science Part B: Polymer Physics* 2007;45:1713-32.
- [55] Bergstrom JS, Boyce MC. Constitutive modeling of the time-dependent and cyclic loading of elastomers and application to soft biological tissues. *Mech Mater* 2001;33:523-30.

- [56] Parker KJ. A microchannel flow model for soft tissue elasticity. *Phys Med Biol* 2014;59:4443.
- [57] Bates JH. A recruitment model of quasi-linear power-law stress adaptation in lung tissue. *Ann Biomed Eng* 2007;35:1165-74.
- [58] Park SW, Schapery RA. Methods of interconversion between linear viscoelastic material functions. Part I—a numerical method based on Prony series. *Int J Solids Struct* 1999;36:1653-75.
- [59] Gasser TC, Holzapfel GA. A rate-independent elastoplastic constitutive model for biological fiber-reinforced composites at finite strains: continuum basis, algorithmic formulation and finite element implementation. *Comput Mech* 2002;29:340-60.
- [60] Pena E, Alastrue V, Laborda A, Martinez MA, Doblare M. A constitutive formulation of vascular tissue mechanics including viscoelasticity and softening behaviour. *Journal of biomechanics* 2010;43:984-9.
- [61] Anssari-Benam A, Bader DL, Screen HR. A combined experimental and modelling approach to aortic valve viscoelasticity in tensile deformation. *Journal of materials science Materials in medicine* 2011;22:253-62.
- [62] Bergström JS, Boyce MC. Constitutive Modeling of the Large Strain Time-Dependent Behavior of Elastomers. *J Mech Phys Solids* 1997;46:931-54.
- [63] Pahr DH, Zysset PK. Influence of boundary conditions on computed apparent elastic properties of cancellous bone. *Biomechanics and modeling in mechanobiology* 2008;7:463-76.
- [64] Wang M, Pan N. Predictions of effective physical properties of complex multiphase materials. *Mat Sci Eng R* 2008;63:1-30.
- [65] Wong C, Bollampally RS. Thermal conductivity, elastic modulus, and coefficient of thermal expansion of polymer composites filled with ceramic particles for electronic packaging. *J Appl Polym Sci* 1999;74:3396-403.
- [66] Kreher W, Pompe W. Internal stresses in heterogeneous solids: Akademie Verlag; 1989.
- [67] Hamilton R, Crosser O. Thermal conductivity of heterogeneous two-component systems. *Ind Eng Chem Fund* 1962;1:187-91.
- [68] Landauer R. The electrical resistance of binary metallic mixtures. *J Appl Phys* 1952;23:779-84.
- [69] Hashin Z, Shtrikman S. A variational approach to the theory of the elastic behaviour of multiphase materials. *J Mech Phys Solids* 1963;11:127-40.
- [70] Gibiansky LV, Lakes R. Bounds on the complex bulk and shear moduli of a two-dimensional two-phase viscoelastic composite. *Mech Mater* 1997;25:79-95.
- [71] Terada K, Kikuchi N. A class of general algorithms for multi-scale analyses of heterogeneous media. *Computer Methods in Applied Mechanics and Engineering* 2001;190:5427-64.
- [72] Pierard O, Friebel C, Doghri I. Mean-field homogenization of multi-phase thermo-elastic composites: a general framework and its validation. *Composites Sci Technol* 2004;64:1587-603.
- [73] Šmilauer V, Bažant ZP. Identification of viscoelastic C-S-H behavior in mature cement paste by FFT-based homogenization method. *Cement Concrete Res* 2010;40:197-207.
- [74] Liu S, Chen K-Z, Feng X-A. Prediction of viscoelastic property of layered materials. *Int J Solids Struct* 2004;41:3675-88.
- [75] Yi Y-M, Park S-H, Youn S-K. Asymptotic homogenization of viscoelastic composites with periodic microstructures. *Int J Solids Struct* 1998;35:2039-55.
- [76] Lauzon AM, Bates JH, Donovan G, Tawhai M, Sneyd J, Sanderson MJ. A multi-scale approach to airway hyperresponsiveness: from molecule to organ. *Frontiers in physiology* 2012;3:191.

- [77] Hain M, Wriggers P. Numerical homogenization of hardened cement paste. *Comput Mech* 2007;42:197-212.
- [78] Hassani B, Hinton E. Homogenization and structural topology optimization: theory, practice and software: Springer Science & Business Media; 2012.
- [79] Nguyen VD, Béchet E, Geuzaine C, Noels L. Imposing periodic boundary condition on arbitrary meshes by polynomial interpolation. *Computational Materials Science* 2012;55:390-406.
- [80] Tyrus JM, Gosz M, DeSantiago E. A local finite element implementation for imposing periodic boundary conditions on composite micromechanical models. *Int J Solids Struct* 2007;44:2972-89.
- [81] Rezaei A, Salimi Jazi M, Karami G. Computational modeling of human head under blast in confined and open spaces: primary blast injury. *Int J Numer Method Biomed Eng* 2014;30:69-82.
- [82] Van den Berg CA, Van de Kamer JB, De Leeuw AA, Jeukens CR, Raaymakers BW, van Vulpen M, et al. Towards patient specific thermal modelling of the prostate. *Physics in medicine and biology* 2006;51:809-25.
- [83] Goffin JM, Pankaj P, Simpson AH. Are plasticity models required to predict relative risk of lag screw cut-out in finite element models of trochanteric fracture fixation? *Journal of biomechanics* 2014;47:323-8.
- [84] Garijo N, Martínez J, García-Aznar JM, Pérez MA. Computational evaluation of different numerical tools for the prediction of proximal femur loads from bone morphology. *Computer Methods in Applied Mechanics and Engineering* 2014;268:437-50.
- [85] J. Kerner, R. Huiskes, G.H. van Lenthe, H. Weinans, B. van Rietbergen, C.A. Engh, et al. Correlation between pre-operative periprosthetic bone density and post-operative bone loss in that can be explained by strain-adaptive remodelling. *J Biomech* 1999;32:695-703.
- [86] Schileo E, Taddei F, Malandrino A, Cristofolini L, Viceconti M. Subject-specific finite element models can accurately predict strain levels in long bones. *Journal of biomechanics* 2007;40:2982-9.
- [87] Scaife J, Harrison K, Romanchikova M, Parker A, Sutcliffe M, Bond S, et al. Random variation in rectal position during radiotherapy for prostate cancer is two to three times greater than that predicted from prostate motion. *The British journal of radiology* 2014;87:20140343.
- [88] Zhang J, Sandison GA, Murthy JY, Xu LX. Numerical Simulation for Heat Transfer in Prostate Cancer Cryosurgery. *Journal of Biomechanical Engineering* 2005;127:279.
- [89] Hardman D, Semple SI, Richards JM, Hoskins PR. Comparison of patient-specific inlet boundary conditions in the numerical modelling of blood flow in abdominal aortic aneurysm disease. *Int J Numer Method Biomed Eng* 2013;29:165-78.
- [90] Capelli C, Bosi GM, Cerri E, Nordmeyer J, Odenwald T, Bonhoeffer P, et al. Patient-specific simulations of transcatheter aortic valve stent implantation. *Medical and Biological Engineering and Computing* 2012;50:183-92.
- [91] Gasser TC. Bringing Vascular Biomechanics into Clinical Practice. Simulation-Based Decisions for Elective Abdominal Aortic Aneurysms Repair. In: Calvo Lopez B, Peña E, editors. *Patient-Specific Computational Modeling*: Springer Netherlands; 2012. p. 1-37.
- [92] Hardman D, Doyle BJ, Semple SI, Richards JM, Newby DE, Easson WJ, et al. On the prediction of monocyte deposition in abdominal aortic aneurysms using computational fluid dynamics. *Proceedings of the Institution of Mechanical Engineers Part H, Journal of engineering in medicine* 2013;227:1114-24.
- [93] Samady H, Eshtehardi P, McDaniel MC, Suo J, Dhawan SS, Maynard C, et al. Coronary artery wall shear stress is associated with progression and transformation of

- atherosclerotic plaque and arterial remodeling in patients with coronary artery disease. *Circulation* 2011;124:779-88.
- [94] Jackson AS, Reinsberg SA, Sohaib SA, Charles-Edwards EM, Jhavar S, Christmas TJ, et al. Dynamic contrast-enhanced MRI for prostate cancer localization. *The British journal of radiology* 2009;82:148-56.
- [95] Palacio-Torralba J, Jimenez Aguilar E, Good DW, Hammer S, McNeill SA, Stewart GD, et al. Patient specific modeling of palpation-based prostate cancer diagnosis: effects of pelvic cavity anatomy and intrabladder pressure. *Int J Numer Method Biomed Eng* 2015.
- [96] Pallwein L, Mitterberger M, Struve P, Pinggera G, Horninger W, Bartsch G, et al. Real-time elastography for detecting prostate cancer: preliminary experience. *BJU international* 2007;100:42-6.
- [97] Lauren E. J. Thomas-Seale, Dieter Klatt, Pankaj Pankaj, Neil Roberts, Sack I, Hoskins PR. A Simulation of the Magnetic Resonance Elastography Steady State Wave Response through Idealised Atherosclerotic Plaques. *IAENG International Journal of Computer Science* 2011;38:394-400.
- [98] Miyagawa T, Tsutsumi M, Matsumura T, Kawazoe N, Ishikawa S, Shimokama T, et al. Real-time Elastography for the Diagnosis of Prostate Cancer: Evaluation of Elastographic Moving Images. *Jpn J Clin Oncol* 2009;39:394-8.
- [99] Sartor AO, Hricak H, Wheeler TM, Coleman J, Penson DF, Carroll PR, et al. Evaluating localized prostate cancer and identifying candidates for focal therapy. *Urology* 2008;72:S12-24.
- [100] Serfling R SM, Thompson GL, Xiao Z, Benaim E, Roehrborn CG, Rittmaster R. Quantifying the impact of prostate volumes, number of biopsy cores and 5alpha-reductase inhibitor therapy on the probability of prostate cancer detection using mathematical modeling. *The Journal of urology* 2007;177:2352-6.
- [101] Su LM. *Early Diagnosis and Treatment of Cancer*: Saunders Elsevier; 2010.
- [102] Chang DTS, Challacombe B, Lawrentschuk N. Transperineal biopsy of the prostate— is this the future? *Nat Rev Urol* 2013;10:690-702.
- [103] Slapa RZ, Piwowonski A, Jakubowski WS, Bierca J, Szopinski KT, Slowinska-Srzednicka J, et al. Shear wave elastography may add a new dimension to ultrasound evaluation of thyroid nodules: case series with comparative evaluation. *Journal of thyroid research* 2012;2012:657147.
- [104] Wong VW, Vergniol J, Wong GL, Foucher J, Chan HL, Le Bail B, et al. Diagnosis of fibrosis and cirrhosis using liver stiffness measurement in nonalcoholic fatty liver disease. *Hepatology* 2010;51:454-62.
- [105] Daniel GT, V. DS, G. BR, Benjamin C, G. SJ, J RD. US Elastography of Breast and Prostate Lesions. *RadioGraphics* 2009;29:2017-6.
- [106] Oflaz H, Baran O. A new medical device to measure a stiffness of soft materials. *Acta Bioeng Biomech* 2014;16:125-31.
- [107] P. Scanlan, S.J. Hammer, D. Good, S. Phipps, G.D. Stewart, S.A. McNeil, et al. A scalable actuator for the dynamic palpation of soft tissue for use in the assessment of prostate tissue quality. Under review.
- [108] Palacio-Torralba J, Hammer S, Good DW, Alan McNeill S, Stewart GD, Reuben RL, et al. Quantitative diagnostics of soft tissue through viscoelastic characterization using time-based instrumented palpation. *J Mech Behav Biomed Mater* 2014.
- [109] Ahn B, Kim Y, Oh CK, Kim J. Robotic palpation and mechanical property characterization for abnormal tissue localization. *Medical & biological engineering & computing* 2012;50:961-71.
- [110] Lee H, Kim Y, Shin YK, Ahn B, Rha K, Kim J. Localization of abnormality using finite element modeling of prostate glands with robotic system: A preliminary study 4th IEEE RAS & EMBS International Conference Rome2012.

- [111] Kiattisak S, Hongbin L, D. SL, Kaspar A. Tissue Identification using Inverse Finite Element Analysis of Rolling Indentation. 2009 IEEE International Conference 2009.
- [112] Ahn B, Lorenzo EI, Rha KH, Kim HJ, Kim J. Robotic palpation-based mechanical property mapping for diagnosis of prostate cancer. *Journal of endourology / Endourological Society* 2011;25:851-7.
- [113] Murayama Y, Nihon Univ. F, Omata SY, T.; Qiyu Peng; Shishido, K.; Peehl, D.M.; Constantinou, C.E. . High Resolution Regional Elasticity Mapping of the Human Prostate. 29th Annual International Conference of the IEEE. Cite Internationale, Lyon, France 2007. p. 5802-5.
- [114] Miller K, Chinzei K, Orssengo G, Bednarz P. Mechanical properties of brain tissue in-vivo: experiment and computer simulation. *J Biomech* 2000;33:1369-76.
- [115] Ahn B, Kim J. Measurement and characterization of soft tissue behavior with surface deformation and force response under large deformations. *Medical image analysis* 2010;14:138-48.
- [116] Carter FJ, Frank TG, Davies PJ, McLean D, Cuschieri A. Measurements and modelling of the compliance of human and porcine organs. *Med Image Anal* 2001;5:231-6.
- [117] Sasai S, Zhen Y-X, Suetake T, Tanita Y, Omata S, Tagami H. Palpation of the skin with a robot finger: an attempt to measure skin stiffness with a probe loaded with a newly developed tactile vibration sensor and displacement sensor. *Skin Res Technol* 1999;5:237-46.
- [118] Silver-Thorn MB. In vivo indentation of lower extremity limb soft tissues. *Rehabilitation Engineering, IEEE Transactions on* 1999;7:268-77.
- [119] Pailler-Mattei C, Bec S, Zahouani H. In vivo measurements of the elastic mechanical properties of human skin by indentation tests. *Med Eng Phys* 2008;30:599-606.
- [120] Stamey T, McNeal J, Yemoto C, Sigal B, Johnstone I. Biological Determinants of Cancer Progression in Men With Prostate Cancer. *JAMA* 1999;281:1395-400.
- [121] Hosseini SM, Amiri M, Najarian S, Dargahi J. Application of artificial neural networks for the estimation of tumour characteristics in biological tissues. *The International Journal of Medical Robotics and Computer Assisted Surgery* 2007:235-44.
- [122] Li C, Guan G, Ling Y, Hsu Y-T, Song S, Huang JTJ, et al. Detection and characterisation of biopsy tissue using quantitative optical coherence elastography (OCE) in men with suspected prostate cancer. *Cancer Lett* 2015;357:121-8.
- [123] Asbach P, Klatt D, Hamhaber U, Braun J, Somasundaram R, Hamm B, et al. Assessment of liver viscoelasticity using multifrequency MR elastography. *Magn Reson Med* 2008;60:373-9.
- [124] Wex C, Frohlich M, Brandstadter K, Bruns C, Stoll A. Experimental analysis of the mechanical behavior of the viscoelastic porcine pancreas and preliminary case study on the human pancreas. *J Mech Behav Biomed Mater* 2015;41:199-207.
- [125] Good DW, Khan A, Hammer S, Scanlan P, Shu W, Phipps S, et al. Tissue quality assessment using a novel direct elasticity assessment device (the E-finger): a cadaveric study of prostatectomy dissection. *PLoS One* 2014;9:e112872.
- [126] Ahn BM, Kim J, Ian L, Rha KH, Kim HJ. Mechanical property characterization of prostate cancer using a minimally motorized indenter in an ex vivo indentation experiment. *Urology* 2010;76:1007-11.
- [127] Parimi V, Goyal R, Poropatich K, Yang XJ. Neuroendocrine differentiation of prostate cancer: a review. *American Journal of Clinical and Experimental Urology* 2014;2:273-85.
- [128] Carter SM, Williams J, Parker L, Pickles K, Jacklyn G, Rychetnik L, et al. Screening for Cervical, Prostate, and Breast Cancer: Interpreting the Evidence. *Am J Prev Med* 2015;49:274-85.



- [129] Heidenreich A, Bastian PJ, Bellmunt J, Bolla M, Joniau S, van der Kwast T, et al. EAU guidelines on prostate cancer. part 1: screening, diagnosis, and local treatment with curative intent-update 2013. *European urology* 2014;65:124-37.
- [130] Mukerji R, Schaal J, Li X, Bhattacharyya J, Asai D, Zalutsky MR, et al. Spatiotemporally photoradiation-controlled intratumoral depot for combination of brachytherapy and photodynamic therapy for solid tumor. *Biomaterials* 2016;79:79-87.
- [131] Kontopodis E, Kentepozidis N, Christophyllakis C, Boukovinas I, Kalykaki A, Kalbakis K, et al. Docetaxel, gemcitabine and bevacizumab as salvage chemotherapy for HER-2-negative metastatic breast cancer. *Cancer Chemother Pharmacol* 2015;75:153-60.
- [132] Moore HC, Unger JM, Phillips KA, Boyle F, Hitre E, Porter D, et al. Goserelin for ovarian protection during breast-cancer adjuvant chemotherapy. *N Engl J Med* 2015;372:923-32.
- [133] Yu M, Guo F, Tan F, Li N. Dual-targeting nanocarrier system based on thermosensitive liposomes and gold nanorods for cancer thermo-chemotherapy. *Journal of controlled release : official journal of the Controlled Release Society* 2015;215:91-100.
- [134] Willerding L, Limmer S, Hossann M, Zengerle A, Wachholz K, Ten Hagen TL, et al. Method of hyperthermia and tumor size influence effectiveness of doxorubicin release from thermosensitive liposomes in experimental tumors. *Journal of controlled release : official journal of the Controlled Release Society* 2016;222:47-55.
- [135] Kuszyk BS, Corl FM, Franano FN, Bluemke DA, Hofmann LV, Fortman BJ, et al. Tumor transport physiology: implications for imaging and imaging-guided therapy. *Am J Roentgenol* 2001;177:747-53.
- [136] Mura S, Nicolas J, Couvreur P. Stimuli-responsive nanocarriers for drug delivery. *Nat Mater* 2013;12:991-1003.
- [137] Lankelma J, Dekker H, Luque RF, Luykx S, Hoekman K, van der Valk P, et al. Doxorubicin gradients in human breast cancer. *Clin Cancer Res* 1999;5:1703-7.
- [138] Cunningham JJ, Gatenby RA, Brown JS. Evolutionary Dynamics in Cancer Therapy. *Mol Pharm* 2011;8:2094-100.
- [139] Newman NB, Sidhu MK, Baby R, Moss RA, Nissenblatt MJ, Chen T, et al. Long-Term Bone Marrow Suppression During Postoperative Chemotherapy in Rectal Cancer Patients After Preoperative Chemoradiotherapy. *International Journal of Radiation Oncology\*Biophysics* 2016.
- [140] Yan Z, Zhang S, Alam SK, Metaxas DN, Garra BS, Feleppa EJ. Modulus Reconstruction from Prostate Ultrasound Images using Finite Element Modeling. *Proc SPIE 8320, Medical Imaging 2012: Ultrasonic Imaging, Tomography, and Therapy*, 832016 San Diego, California, USA2012.
- [141] McNeal J, Haillot O. Patterns of Spread of Adenocarcinoma in the Prostate as Related to Cancer Volume. *The Prostate* 2001;49:48-57.
- [142] Lawrentschuk N, Lindner U, Klotz L. Realistic anatomical prostate models for surgical skills workshops using ballistic gelatin for nerve-sparing radical prostatectomy and fruit for simple prostatectomy. *Korean journal of urology* 2011;52:130-5.
- [143] Madsen EL, Hobson MA, Shi H, Varghese T, Frank GR. Tissue-mimicking agar/gelatin materials for use in heterogeneous elastography phantoms. *Physics in medicine and biology* 2005;50:5597-618.
- [144] Bouyé S, Potiron E, Puech P, Leroy X, Lemaitre L, Villers A. Transition zone and anterior stromal prostate cancers: zone of origin and intraprostatic patterns of spread at histopathology. *The Prostate* 2009;69:105-13.
- [145] Marquardt DW. An algorithm for least-squares estimation of nonlinear parameters. *Journal of the society for Industrial and Applied Mathematics* 1963;11:431-41.
- [146] Zhang M, Zheng YP, Mak AFT. Estimating the effective Young's modulus of soft tissues from indentation tests—nonlinear finite element analysis of effects of friction and large deformation. *Med Eng Phys* 1997;19:512-7.

- [147] Klatt D, Hamhaber U, Asbach P, Braun J, Sack I. Noninvasive assessment of the rheological behavior of human organs using multifrequency MR elastography: a study of brain and liver viscoelasticity. *Phys Med Biol* 2007;52:7281-94.
- [148] Martinez-Agirre M, Elejabarrieta MJ. Dynamic characterization of high damping viscoelastic materials from vibration test data. *Journal of Sound and Vibration* 2011;330:3930-43.
- [149] Nayar VT, Weiland JD, Nelson CS, Hodge AM. Elastic and viscoelastic characterization of agar. *Journal of the mechanical behavior of biomedical materials* 2012;7:60-8.
- [150] Cleveland WS. Robust Locally Weighted Regression and Smoothing Scatterplots. *Journal of the American Statistical Association* 1979;74:829-36.
- [151] Torlakovic G, Grover VK, Torlakovic E. Easy Method of Assessing Volume of Prostate Adenocarcinoma from Estimated Tumor Area: Using Prostate Tissue Density to Bridge Gap Between Percentage Involvement and Tumor Volume. *Croat Med J* 2005;46:423-8.
- [152] Kiss MZ, Varghese T, Hall TJ. Viscoelastic characterization of in vitro canine tissue. *Phys Med Biol* 2004;49:4207-18.
- [153] Van Looke M, Lyons CG, Simms CK. Viscoelastic properties of passive skeletal muscle in compression: Stress-relaxation behaviour and constitutive modelling. *J Biomech* 2008;41:1555-66.
- [154] Hazanov S. Hill condition and overall properties of composites. *Arch Appl Mech* 1998;68:385-94.
- [155] Heimbach D, Munver R, Zhong P, Jacobs J, Hesse A, MÜLLER SC, et al. Acoustic and mechanical properties of artificial stones in comparison to natural kidney stones. *The Journal of urology* 2000;164:537-44.
- [156] Jalkanen V, Andersson BM, Bergh A, Ljungberg B, Lindahl OA. Indentation loading response of a resonance sensor-discriminating prostate cancer and normal tissue. *J Med Eng Technol* 2013;37:416-23.
- [157] Palacio-Torralba J, Hammer S, Good DW, Alan McNeill S, Stewart GD, Reuben RL, et al. Quantitative diagnostics of soft tissue through viscoelastic characterization using time-based instrumented palpation. *J Mech Behav Biomed Mater* 2015;41:149-60.
- [158] Gasser TC, Auer M, Labruto F, Swedenborg J, Roy J. Biomechanical rupture risk assessment of abdominal aortic aneurysms: model complexity versus predictability of finite element simulations. *Eur J Vasc Endovasc Surg* 2010;40:176-85.
- [159] International Union against Cancer (UICC): TNM Classification of Malignant Tumors. 7th ed. Oxford: Wiley-Blackwell; 2009.
- [160] Paul A. Yushkevich, Joseph Piven, Heather Cody Hazlett, Rachel Gimpel Smith, Sean Ho, James C. Gee, et al. User-guided 3D active contour segmentation of anatomical structures: Significantly improved efficiency and reliability. *NeuroImage* 2006;31:116-28.
- [161] Chiumello D, Tallarini F, Chierichetti M, Polli F, Li Bassi G, Motta G, et al. The effect of different volumes and temperatures of saline on the bladder pressure measurement in critically ill patients. *Critical care* 2007;11:R82.
- [162] Boubaker MB, Haboussi M, Ganghoffer JF, Aletti P. Finite element simulation of interactions between pelvic organs: predictive model of the prostate motion in the context of radiotherapy. *Journal of biomechanics* 2009;42:1862-8.
- [163] Yahia L, Pigeon P, DesRosiers E. Viscoelastic properties of the human lumbodorsal fascia. *Journal of Biomedical Engineering* 1993;15:425-9.
- [164] Nagatomi J, Gloeckner DC, Chancellor MB, Sacks MS. Changes in the biaxial viscoelastic response of the urinary bladder following spinal cord injury. *Ann Biomed Eng* 2004;32:1409-19.

- [165] Arhan P, Faverdin C, Persoz B, Devroede G, Dubois F, Dornic C, et al. Relationship between viscoelastic properties of the rectum and anal pressure in man. *J Appl Physiol* 1976;41:677-82.
- [166] X. Chai, J.B van de Kamer, M. van Herk, M.C.C.M. Hulshof, P. Remeijer, F. Pos, et al. Finite Element-Based Biomechanical Modeling of the Bladder for Image Guided Radiotherapy. In: Dössel O, Schlegel WC, editors. *World Congress on Medical Physics and Biomedical Engineering*. Munich, Germany: Springer.
- [167] J. Middleton, G. Pande, Jones ML. *Computer Methods in Biomechanics and Biomedical Engineering 2*: Gordon and Brach Science Publishers; 1999.
- [168] Mauri A, Ehret AE, De Focatiis DS, Mazza E. A model for the compressible, viscoelastic behavior of human amnion addressing tissue variability through a single parameter. *Biomechanics and modeling in mechanobiology* 2015.
- [169] Hazanov S, Huet C. Order relationships for boundary conditions effect in heterogeneous bodies smaller than the representative volume. *J Mech Phys Solids* 1994;42:1995-2011.
- [170] Chapelle O, Vapnik V, Bousquet O, Mukherjee S. Choosing Multiple Parameters for Support Vector Machines. *Machine Learning*;46:131-59.
- [171] Kim K-j. Financial time series forecasting using support vector machines. *Neurocomputing* 2003;55:307-19.
- [172] De Marzo AM, Marchi VL, Epstein JI, Nelson WG. Proliferative Inflammatory Atrophy of the Prostate: Implications for Prostatic Carcinogenesis. *The American Journal of Pathology* 1999;155:1985-92.
- [173] Swabb EA, Wei J, Gullino PM. Diffusion and convection in normal and neoplastic tissues. *Cancer Res* 1974;34:2814-22.
- [174] Saggarr JK, Yu M, Tan Q, Tannock IF. The Tumor Microenvironment and Strategies to Improve Drug Distribution. *Frontiers in Oncology* 2013;3:154.
- [175] Lankelma J, Fernández Luque R, Dekker H, Schinkel W, Pinedo HM. A Mathematical Model of Drug Transport in Human Breast Cancer. *Microvasc Res* 2000;59:149-61.
- [176] Komarova NL, Wodarz D. Evolutionary Dynamics of Mutator Phenotypes in Cancer Implications for Chemotherapy. *Cancer Res* 2003;63:6635-42.